Title
Add a Pinch of Salt: Effects of Additives for the Development of New Materials

Author
Mak, Wai Han

Publication Date
2020

Peer reviewed|Thesis/dissertation

UNIVERSITY OF CALIFORNIA

Los Angeles

Add a Pinch of Salt:
Effects of Additives for the
Development of New Materials

A dissertation submitted in partial satisfaction of the

requirements for the degree Doctor of Philosophy

in Chemistry

by

Wai Han Mak

2020

ABSTRACT OF THE DISSERTATION

Add a Pinch of Salt:

Effects of Additives for the

Development of New Materials

by

Wai Han Mak

Doctor of Philosophy in Chemistry

University of California, Los Angeles, 2020

Professor Richard B. Kaner, Chair

Something as simple as adding a pinch of salt can make or break a dish. The same can be said for the process of materials development. The field of chemistry and material science is ever expanding and, with it, a call to develop new materials. Challenges include improving existing methods for production and devising new ways to design materials for particular functions. One way to do this is through the use of chemical additives. Adding even a small amount of additives can enhance material properties, aid in kinetics of chemical reactions, and act as templates in the solid state.

The goal of this thesis is to explore the role of additives in materials science through the lens of a chemist. This can be summarized through three parts:

(1) A novel top-down method for the exfoliation of two-dimensional (2D) layered materials was developed using compressible flow. Graphite, hexagonal boron nitride, and molybdenum disulfide were used as representative 2D layered materials. Our process takes advantage of supersonic flow and weak van der Waals forces to mechanically exfoliate 2D materials in seconds. Exfoliated few-layered hexagonal boron nitride produced by our method was used as an additive in polyethylene terephthalate (PET) resulting in an increase in modulus and a decrease in the oxygen permeation rate compared to PET by itself.

(2) Additives can be used to speed up chemical reactions such as for the polymerization of aniline. The addition of oligoanilines can speed up aniline polymerization, with the small molecule acting as a catalyst. Quantitative rate constants were determined using electrochemical polymerization of aniline by adding various oligomers to study the kinetics and growth mechanism of polyaniline.

(3) Carbon additives can be utilized as "templates" in dodecaboride solid solutions to direct surface morphology. The single-phase metal dodecaboride solid solutions, $Zr_{0.5}Y_{0.5}B_{12}$ and $Zr_{0.5}U_{0.5}B_{12}$, were prepared using solid solution alloying. Compared to their parent phases, ZrB_{12} and YB_{12}, $Zr_{0.5}Y_{0.5}B_{12}$ and $Zr_{0.5}U_{0.5}B_{12}$, they have enhanced hardnesses. The addition of carbon into the zirconium–yttrium dodecaboride system causes rapid nucleation of grains causing changes in surface morphology.

The dissertation of Wai Han Mak is approved.

William M. Gelbart

Joseph A. Loo

Alexander Spokoyny

Richard B. Kaner, Committee Chair

University of California, Los Angeles

2020

TABLE OF CONTENTS

LIST OF FIGURES

LIST OF TABLES

ACKNOWLEDGEMENT

First, I would like to thank my advisor, Professor Ric Kaner, for giving me the opportunity to do exciting research in his lab. Thank you for taking a chance on me and for giving me the freedom to pursue science for the sake of curiosity.

I wish to thank my committee members, Professor William M. Gelbart, Professor Joseph A. Loo, and Professor Alexander Spokoyny for their guidance throughout my PhD studies and for giving me constructive feedback on my research and future endeavors.

I especially want to thank my husband, Dr. Cheng-Wei Lin, for always supporting me in my research, in my psychological and physical well-being, and in all areas of my life. I am grateful for all you've done for me and for listening to all my rants, frustration, and tears about research.

I am grateful to all the Kaner group members past and present, and to all my UCLA friends and collaborators. You guys have made the last five years of my life some of the most transformative and fun years of my life.

I want to thank my parents for supporting my goal for higher education and for their sacrifice in moving to the United States so that my brother and I can have a brighter future. I want to thank my brother for his support and for being a cool, chill, older brother (and for the funny memes and Netflix subscription).

I want to thank my community group at Vintage church for being my support network when I didn't know who to go to with my problems. I want to thank God for leading me here and for always listening to my prayers.

Chapter 2 is reprinted (adapted) with permission from (Rizvi, R.; Nguyen, E. P.; Kowal, M. D.; Mak, W. H.; Rasel, S.; Islam, M. A.; Abdelaal, A.; Joshi, A. S.; Zekriardehani, S.; Coleman, M. R.; Kaner, R. B. "High-Throughput Continuous Production of Shear-Exfoliated 2D Layered Materials using Compressible Flows" *Advanced Materials*, 2018, *30*(30), 1800200.) Co-author contributions: R.B.K., R.R., and E.P.N. conceived the idea for the study and designed the experiments. R.R., E.P.N., W.H.M, M.D.K., S.R., and M.A.I. performed the process experiments, characterized, and analyzed the exfoliated nanoparticles. S.R. and A.A. performed the flow simulations. A.S.J., S.Z., and M.R.C. developed and characterized the nanocomposites. R.R. wrote the manuscript with contributions from all authors.

Chapter 3 is reprinted (adapted) with permission from (Lin, C. W.; Mak, W. H.; Chen, D.; Wang, H.; Aguilar, S.; Kaner, R. B. "Catalytic Effects of Aniline Polymerization Assisted by Oligomers." *ACS Catalysis*, **2019**, *9*(8), 6596-6606.) Co-author contributions: Lin, C. W. and Mak, W. H. performed cyclic voltammograms. Chen, D.; Wang, H.; and Aguilar, S. prepared samples. Kaner, R. B. was the Primary Investigator.

Chapter 4 is reprinted (adapted) with permission from (Akopov, G., Mak, W. H.; Koumoulis, D.; Yin, H.; Owens-Baird, B.; Yeung, M. T.; Muni, M. H.; Lee, S.; Roh, I.; Sobell, Z. C.; Diaconescu, P. L.; Mohammadi, R.; Kovnir, K.; Kaner, R.B. "Synthesis and Characterization of Single-Phase Metal Dodecaboride Solid Solutions: $Zr_{1-x}Y_xB_{12}$ and $Zr_{1-x}U_xB_{12}$." *Journal of the American Chemical Society*, **2019**, *141*(22), 9047-9062.) Co-author contributions: Akopov, G. prepared samples and performed Vickers hardness measurements; Mak, W. H. performed XPS analysis; Koumoulis, D. performed solid-state NMR analysis; Yin, H., Roh, I. and Sobell, Z. C. helped with sample preparation and polishing; Owens-Baird, B. performed resistivity measurements; Yeung, M. T. performed SEM/EDS analysis; Muni, M. H. performed UV-vis

analysis; Lee, S. performed DOS calculations; Diaconescu, P. L., Mohammadi, R. and Kovnir, K. helped with manuscript preparation and Kaner, R.B. was the PI.

I would like to acknowledge the Eugene V. Cota-Robles Fellowship, Dean's Scholar Award, and the Thomas and Ruth Jacobs Fellowship for their financial support throughout my doctoral study.

VITA

2015 – 2020	Graduate Student Researcher with Prof. Richard B. Kaner University of California, Los Angeles
2020	Thomas and Ruth Jacobs Fellowship University of California, Los Angeles
2019	Research Showcase Travel Award for the 258rd ACS National Meeting University of California, Los Angeles
2015 – 2019	Eugene V. Cota-Robles Fellowship University of California, Los Angeles
2017	Research Showcase Travel Award for the 253rd ACS National Meeting University of California, Los Angeles
2015	Dean's Scholar Award University of California, Los Angeles
2015	Competitive Edge Summer Research Fellowship University of California, Los Angeles
2011 – 2015	Bachelor of Science in Chemistry (honors) University of California, Santa Cruz
2013 – 2015	Undergraduate Researcher with Prof. Nader Pourmand University of California, Santa Cruz
2011 – 2014	Anderson Endowed Scholarship University of California, Santa Cruz
2012	Amy Beth Snader Memorial Scholarship University of California, Santa Cruz

Publications *equal contribution

1. Rıfat Emrah Özel, Akshar Lohith, **Wai Han Mak** and Nader Pourmand, "Single-cell intracellular nano-pH probes" *RSC Advances*, **2015**
2. Rıfat Emrah Özel, Sina Kahnemouyi, Hsinwen Fan, **Wai Han Mak**, Akshar Lohith, Adam Seger, Mircea Teodorescu, and Nader Pourmand, "Smartphone Operated Signal

Transduction by Ion Nanogating (STING) Amplifier for Nanopore Sensors: Design and Analytical Application" *ACS Sensors*, **2016**

3. Raphael A. S. Nascimento *, Rıfat Emrah Özel *, **Wai Han Mak**, Marcelo Mulato, Bakthan Singaram, and Nader Pourmand "Single Cell "Glucose Nanosensor" Verifies Elevated Glucose Levels in Individual Cancer Cells" *Nano Letters*, **2016**
4. Georgiy Akopov, Michael T. Yeung, Inwhan Roh, Zachary C. Sobell, Hang Yin, **Wai H. Mak**, Saeed I. Khan, and Richard B. Kaner. "Effects of Dodecaboride-Forming Metals on the Properties of Superhard Tungsten Tetraboride." *Chemistry of Materials*, **2018**
5. Reza Rizvi, Emily P. Nguyen, Matthew D. Kowal, **Wai H. Mak**, Sheikh Rasel, Md Akibul Islam, Ahmed Abdelaal, Anup S. Joshi, Shahab Zekriardehani, Maria R. Coleman, Richard B. Kaner. "High-Throughput Continuous Production of Shear-Exfoliated 2D Layered Materials using Compressible Flows." *Advanced Materials*, **2018**
6. Cheng-Wei Lin, **Wai H. Mak**, Brian T. McVerry, Richard B. Kaner, "Separations Using Conjugated Polymers" *Chapter for Handbook of the Conducting Polymers, 4th Edition*, Edited by Skotheim T.A. and Reynolds, J.R. CRC Press, **2018**
7. Cheng-Wei Lin *, Stephanie Aguilar *, Ethan Rao, **Wai H. Mak**, Xinwei Huang, Dukwoo Jun, Na He, Dayong Chen, Paige Curson, Brian T. McVerry, Eric M. V. Hoek, Shu-Chuan Huang, Richard B. Kaner, "A One-Step Antibacterial Surface Modification by Conjugated Tetraaniline for Antifouling Ultrafiltration Membranes" *Chemical Science*, **2019**
8. Georgiy Akopov, **Wai H. Mak**, Dimitrios Koumoulis, Hang Yin, Bryan Owen-Baird, Michael T. Yeung, Mit H. Muni, Shannon Lee, Inwhan Roh, Zachary Sobell, Paula Diaconescu, Reza Mohammadi, Kirill Kovnir, Richard B. Kaner, "Synthesis of Stoichiometric $Zr_{0.5}Y_{0.5}B_{12}$ and Morphological Effects of the Addition of Carbon on $Zr_{1-x}Y_xB_{12}$" *Journal of American Chemical Society*, **2019**
9. Cheng-Wei Lin, **Wai H. Mak**, Dayong Chen, Haosen Wang, Stephanie Aguilar, Richard B. Kaner, "Autocatalytic Effect and Kinetics Study of Aniline Polymerization" *ACS Catalysis*, **2019**
10. Shuangmei Xue, Chenhao Ji, Matthew D. Kowal, Jenna C. Molas, Cheng-Wei Lin, Brian T. McVerry, Christopher L. Turner, **Wai H. Mak**, Mackenzie Anderson, Mit Muni, Eric M. V. Hoek, Zhen-Liang Xu, Richard B. Kaner, "Nanostructured Graphene Oxide Composite Membranes with Ultrapermeability and Mechanical Robustness" *Nano Letters*, **2020**
11. Chenhao Ji, Shuangmei Xue, Cheng-Wei Lin, **Wai H. Mak**, Brian T. McVerry, Christopher L. Turner, Mackenzie Anderson, Jenna C. Molas, Zhen-Liang Xu, Richard B. Kaner, "Ultra-Permeable Organic Solvent Nanofiltration Membranes with Precisely Tailored Support Layers Fabricated Using Thin-Film Lift-Off" *ACS Applied Materials & Interfaces*, **2020**
12. Stephanie Aguilar, Steven Bustillos, Shuangmei Xue, Chen-Hao Ji, **Wai H. Mak**, Ethan Rao, Brian T. McVerry, Erika Callagon La Plante, Dante Simonetti, Gaurav Sant, Richard B. Kaner, "Enhancing Polyvalent Cation Rejection Using Perfluorophenylazide-Grafted-Copolymer Membrane Coatings" *ACS Applied Materials & Interfaces*, **2020**

CHAPTER 1. INTRODUCTION

Advanced materials are materials that have enhanced properties compared to their conventional counterparts. They can be used in all sectors from consumer electronics to aerospace applications, not to mention a wealth of other fields. With the increased demand for new materials, scientists need to devise methods to increase efficiency for materials production and consider new ways to design materials for tailored applications. One method to do this is through the use of additives. For instance, the use of nanocomposites, or the incorporation of nanoparticles into a bulk material matrix, has introduced new ways of creating and designing materials to enhance materials' physical properties. Fillers have long been used in elastomeric materials such as silicone rubber.[1] Recently, two-dimensional nanomaterials have been incorporated into polymer matrices to create polymer nanocomposites. For example, functionalized graphene incorporated into poly(methyl methacrylate) shows improved mechanical and thermal properties at low loading compared to composites made using carbon nanotube fillers.[2] This was attributed to better dispersity by investigating nanofiller to matrix interactions. The use of additives not only can enhance materials properties, but can also aid in the kinetics of chemical reactions, and act as templates in the solid state. The aim of this thesis is to explore the role of additives in materials science through the lens of a chemist by looking at them as aids to the study of materials development.

In Chapter 2, I discuss the development of a new gas phase exfoliation method to mechanically exfoliate bulk graphite, hexagonal boron nitride and molybdenum disulfide.[3] Our collaboratively developed method is a top-down approach that relies on the formation of supersonic flow. Top-down methods involve the separation or "exfoliation" of bulk layered materials into their few layered state. A most notable example is the use of sonication which can

create cavitation bubbles with enough energy to overcome weak van der Waals forces that hold the layered material together.[4] Our gas phase exfoliation process decreases production time from hours to seconds when compared to that of liquid phase exfoliation. The resulting materials were characterized using transmission electron microscopy, ultraviolet-visible spectroscopy, atomic force microscopy, and Raman spectroscopy. Our process appears to produce a higher concentration of exfoliated material compared to conventional methods, with the potential for this process to become a continuous process. We also studied the possible mechanism for our method using computational fluid dynamics (CFD). A shear rate of 10^5 s^{-1} was achieved near the throat of a partially open needle valve. Gas phase exfoliated hexagonal boron nitride was then incorporated into a polyethylene matrix to create a nanocomposite which had superior mechanical and physical properties. The addition of just 0.15 vol% of gas exfoliated boron nitride led to a 26% decrease in the oxygen permeation rate, which can be beneficial for the food and beverage packaging industries.

Chapter 3 turns towards a more fundamental study of additives focusing on the use of catalysts for chemical reactions. In particular, we examine the kinetics of aniline polymerization with the addition of long chain oligomers.[5] Small amounts of additives can be used to skip the formation of aniline dimer which is the rate limiting step, leading to acceleration of aniline polymerization.[6] The quantitative rate constant was determined using electrochemical methods for the electropolymerization of aniline with the addition of an assortment of oligoanilines and oligothiophenes. The progress of polymerization for each additive was observed using an electrochemical method called potential sweep, and by tracking changes in temperature and open-circuit potential.

Finally, in Chapter 4, we examine the role of additives in solid-state chemistry. The single-phase metal dodecaboride solid solutions, $Zr_{0.5}Y_{0.5}B_{12}$ and $Zr_{0.5}U_{0.5}B_{12}$, were prepared using solid solution alloying.[7] Metal dodecaborides normally form as a mixture of phases which can cause a decrease in mechanical properties and thermal conductivity which can limit their use in abrasives.[8] Compared to the parent phases, ZrB_{12} and YB_{12}, $Zr_{0.5}Y_{0.5}B_{12}$ and $Zr_{0.5}U_{0.5}B_{12}$ have enhanced hardness. The synthesized single-phased metallic compounds were characterized using power X-ray diffraction, scanning electron microscopy and solid-state NMR. The addition of carbon into the zirconium–yttrium dodecaboride system causes rapid nucleation of grains causing changes in surface morphology. The effects of added carbon into the dodecaboride system was studied using diffuse-reflectance, X-ray photoelectron spectroscopy and solid-state NMR.

REFERENCES

(1) Bueche, A. M. *J. Polym. Sci.* **1957**, *25* (109), 139–149.

(2) Ramanathan, T.; Abdala, A. A.; Stankovich, S.; Dikin, D. A.; Herrera-Alonso, M.; Piner, R. D.; Adamson, D. H.; Schniepp, H. C.; Chen, X.; Ruoff, R. S.; Nguyen, S. T.; Aksay, I. A.; Prud'Homme, R. K.; Brinson, L. C. *Nat. Nanotechnol.* **2008**, *3* (6), 327–331.

(3) Rizvi, R.; Nguyen, E. P.; Kowal, M. D.; Mak, W. H.; Rasel, S.; Islam, M. A.; Abdelaal, A.; Joshi, A. S.; Zekriardehani, S.; Coleman, M. R.; Kaner, R. B. *Adv. Mater.* **2018**, *30* (30), 1–11.

(4) Hernandez, Y.; Nicolosi, V.; Lotya, M.; Blighe, F. M.; Sun, Z.; De, S.; McGovern, I. T.; Holland, B.; Byrne, M.; Gun'ko, Y. K.; Boland, J. J.; Niraj, P.; Duesberg, G.; Krishnamurthy, S.; Goodhue, R.; Hutchison, J.; Scardaci, V.; Ferrari, A. C.; Coleman, J.

N. *Nat. Nanotechnol.* **2008**, *3* (9), 563–568.

(5) Lin, C. W.; Mak, W. H.; Chen, D.; Wang, H.; Aguilar, S.; Kaner, R. B. *ACS Catal.* **2019**, *9* (8), 6596–6606.

(6) Wei, Y.; Jang, G. W.; Chan, C. C.; Hsueh, K. F.; Hariharan, R.; Patel, S. A.; Whitecar, C. K. *J. Phys. Chem.* **1990**, *94* (19), 7716–7721.

(7) Akopov, G.; Mak, W. H.; Koumoulis, D.; Yin, H.; Owens-Baird, B.; Yeung, M. T.; Muni, M. H.; Lee, S.; Roh, I.; Sobell, Z. C.; Diaconescu, P. L.; Mohammadi, R.; Kovnir, K.; Kaner, R. B. *J. Am. Chem. Soc.* **2019**, *141* (22), 9047–9062.

(8) Paderno, Y. B.; Adamovskii, A. A.; Lyashchenko, A. B.; Paderno, V. N.; Fillipov, V. B.; Naydich, Y. V. *Powder Metall. Met. Ceram.* **2004**, *43* (9–10), 546–548.

CHAPTER 2. HIGH-THROUGHPUT CONTINUOUS PRODUCTION OF SHEAR-EXFOLIATED 2D LAYERED MATERIALS USING COMPRESSIBLE FLOWS

"Reprinted (adapted) with permission from (Rizvi, R.; Nguyen, E. P.; Kowal, M. D.; Mak, W. H.; Rasel, S.; Islam, M. A.; Abdelaal, A.; Joshi, A. S.; Zekriardehani, S.; Coleman, M. R.; Kaner, R. B. "High-Throughput Continuous Production of Shear-Exfoliated 2D Layered Materials using Compressible Flows" *Advanced Materials*, **2018**, *30*(30), 1800200.)

ABSTRACT

2D nanomaterials are finding numerous applications in next-generation electronics, consumer goods, energy generation and storage, and healthcare. The rapid rise of utility and applications for 2D nanomaterials necessitates developing means for their mass production. This study details a new compressible flow exfoliation method for producing 2D nanomaterials using a multiphase flow of 2D layered materials suspended in a high-pressure gas undergoing expansion. The expanded gas–solid mixture is sprayed in a suitable solvent, where a significant portion (up to 10% yield) of the initial hexagonal boron nitride material is found to be exfoliated with a mean thickness of 4.2 nm. The exfoliation is attributed to the high shear rates ($\dot{\gamma} > 10^5$ s^{-1}) generated by supersonic flow of compressible gases inside narrow orifices and converging-diverging channels. This method has significant advantages over current 2D material exfoliation methods, such as chemical intercalation and exfoliation, as well as liquid phase shear exfoliation, with the most obvious benefit being the fast, continuous nature of the process. Other advantages include environmentally friendly processing, reduced occurrence of defects, and the versatility to be applied to any 2D layered material using any gaseous medium. Scaling this process to industrial production has a strong possibility of reducing the cost of creating 2D nanomaterials.

ARTICLE

The field of 2D layered materials has gained significant interest over the last few decades due to unique properties that manifest when a bulk material is reduced to its 2D form. Layered materials that have been widely researched include graphene, transition metal dichalcogenides such as molybdenum disulfide (MoS_2) and tungsten disulfide (WS_2), and hexagonal boron nitride (BN). Their unique properties can include high mechanical strength,[1] high electrical and thermal conductivities,[2,3] high surface areas,[4,5] and exotic quantum-mechanical effects.[6–8] However, these properties are often dependent on the lattice structure and quality of the material, and the number of layers isolated.[9,10] As such, the past decade has seen tremendous research efforts on methods to synthesize and exfoliate high quality 2D materials, while optimizing yields and reducing costs and processing times.

The preparation of 2D materials can be categorized by either a bottom-up or a top-down approach.[11,12] The bottom-up method, as the name suggests, constructs or "puts together" the 2D material from various chemical precursors or sources onto a substrate. Here common methods include chemical and physical vapor deposition. By contrast, the top-down approach focuses on separating or "exfoliating" a bulk 2D material into individual or few layers. This approach is usually favored in certain applications—such as nanocomposites, energy storage, printable electronic inks, etc.—over bottom-up methods because of the higher throughput and hence, scalability. This includes methods such as ion intercalation,[13] liquid phase exfoliation,[14] micromechanical cleavage[15] (i.e., the Scotch tape method), mechanical attrition (e.g., milling),[16] electrochemical exfoliation,[17] and the commonly used Hummer's method for oxidizing graphite,[18] which can then be used for the large scale production of reduced graphene oxide.

The liquid phase exfoliation techniques can be loosely classified into two categories based on the underlying deformation mechanism causing layer separation: 1) sonication, which causes cavitation and 2) shear-based liquid phase exfoliation. In the sonication methods,[19] an ultrasonic transducer is used to induce unstable cavitation bubbles in a liquid medium, which upon their inevitable collapse emanate a shock (pressure) wave. The energy of this shockwave is sufficient to fragment nearby bulk 2D layered powders into smaller lengths as well as thicknesses along the weak, secondary bonded c-axis. The presence of surfactants and other stabilizers helps match the surface tensions[20] of the exfoliated particles to those of the liquid medium thereby stabilizing the colloidal suspension for any further end-use applications. By contrast, the recently introduced shear-based liquid phase exfoliation techniques rely on the viscous deformation of liquids to generate large velocity gradients (shear rates) that assist in layer separation. This was successfully demonstrated in a rotary mixing process by Paton et al.,[21] where a critical shear rate of 10^4 s^{-1} was found necessary for layer separation. Such shear rates can be attained in certain rotary mixers where rotor–stator gaps are on the order of 100 μm. This was followed up with other studies[22–25] where high shear rates in common mixers and household blenders along with surfactants were used to exfoliate 2D layered materials, demonstrating the versatility of this simple technique. However, the scalability and the economic feasibility of these techniques are questionable as these time-based, batch treatments require large volumes of liquids and extensive size separation postprocessing to get 2D nanomaterial yields on the order of a few percent (1–5%). Recently, nonrotary, high-speed liquid flow through narrow channels has been shown to generate sufficient shear rates to cause exfoliation of graphite. Arao et al.[26] used a high-pressure homogenizer with a 10 μm laminar flow channel to generate high shear rates ($\approx 10^6$ s^{-1}) which were sufficient to exfoliate graphite (thickness = 4 nm) in the presence of surfactants. Karagiannidis et al.[27]

demonstrated that extended time microfluidization under turbulent flow conditions with high shear rates ($\approx 10^8$ s^{-1}) results in a ≈ 100% yield (i.e., no need for size separation) of graphite nanoplatelets (thickness = 12 nm). The process required passing surfactant stabilized liquid suspensions of graphite through small orifices (100 μm) using high pressures (up to 200 MPa) for repeated cycles (up to 100 cycles). The process's advantages of impressive yields and no requirements for size separation are offset by the time-based cycling, the use of surface–property modifying surfactants, and a wide size distribution of the final product. A significant inconsistency in shear-based liquid exfoliation studies is the inability to rule out the possibility of cavitation occurring in areas of low pressure during high-speed turbulent flows. Instead, they have the tendency to ascribe the exfoliation to pure shear acting on the 2D materials resulting in adjacent layers sliding relative to one-another due to the self-lubricity property of 2D materials. Paton et al.[21] demonstrated the exfoliation of graphite in a rotating Couette arrangement (100 μm gap) where the only influencing factor seemed to be the cylinder rotational speed (shear rate). At first glance, the likelihood of unstable flow causing cavitation in this parallel plate arrangement with a low Reynolds number of 64–128 would appear slim, since the flow is assumed to be laminar. However, even by the authors own admission, this assumption may not be well grounded, since Couette flows are known to transition into secondary flows (mixed laminar-turbulent) well below their critical Reynolds numbers.[28,29] Arao et al.[26] acknowledge the presence of some cavitation in their experiments but rule it out within the 10 μm gap channel—where exfoliation is assumed to occur—because of the assumption of laminar state of flow. Joseph[30] succinctly describes cavitation to be caused by an extensional fracture of a liquid at a particular principle normal stress, which is proportional to the applied shear rate. Additionally, Furukawa and Tanaka[31] have shown that beyond a certain critical shear rate, the density dependence of viscosity in most Newtonian fluids can lead to a violation of

the incompressibility criterion and cause cavitation. It stands to reason, based on the work of Joseph and later by Furukawa and Tanaka, that onset of flow instability and cavitation cannot be ignored in shear-based liquid phase exfoliations of 2D materials, particularly at high shear rates ($>10^4$ s^{-1}) and within confined geometries. This absence of dialogue on the contribution of cavitation, which is omnipresent in high-speed liquid turbulent flows, is a major gap in our knowledge of scalable top-down nanomanufacturing of 2D materials.

A collection of top-down techniques that are gaining considerable traction recently involve exfoliation using a supercritical fluid gaseous medium. The majority of gas-phase exfoliation studies thus far have used supercritical CO_2 (sCO_2) as the gaseous medium, although other substances such as water vapor and ethanol can also be used. The approach here is motivated by the logic that sCO_2 is a low-surface-tension fluid with a high, liquid like density, thus among liquid solvents it should be most apt for diffusing into the 2D layered materials. Perhaps one of the earliest demonstrations of the exfoliating ability of high-pressure sCO_2 was by Pu et al.[32] in 2009, where a time-based treatment of sCO_2 was carried out on graphite before venting the products into a sodium dodecyl sulfate surfactant solution. Since then, there have been several studies into supercritical gas phase exfoliation of 2D layered materials, with two preferred methods emerging. The first approach is to combine various chemicals/surfactants with supercritical fluids to assist with the layer separation.[33] The second approach is to combine some type of mechanical agitation, either in the form of ultrasonication[34] or high-speed shear,[35] to assist in the breakup of the bulk 2D crystals. A recent review of supercritical fluid exfoliation of graphite[36] accurately captures the state of the emerging research landscape.

Apart from supercritical fluids, there have been very few investigations into the potential of other gaseous substances for exfoliating 2D layered materials. A patent by Jang et al.[37] describes

a batch processing method where a pressure vessel containing 2D layered materials (graphite) is pressurized by various gases, such as hydrogen, helium, argon, carbon dioxide, and water vapor. It is expected that high pressures and high temperatures will improve the driving force for diffusion of gas molecules in between the layers of the 2D bulk crystals. Afterward, the pressure is rapidly released to cause the gas molecules in between the layers to expand and separate the layers. Unfortunately, the authors used data for electrochemically driven lithium-ion diffusion in graphite[38] and incorrectly applied it to support their hypothesis for gas molecule diffusion occurring within 2D material layers. It should be pointed out that the kinetic diameter of gases is more than 3 times the ionic radius of lithium.

It is important to realize that all gas phase processes to our knowledge require bulk processing with many[32,34,39,40] expecting that gas intercalation, being a diffusion problem, will require a certain minimum time to reach completion. Furthermore, once gas diffusion is complete there is the perception that some time-based stimulus in the form of mechanical agitation/shear, ultrasound, or surfactant uptake is required to disturb the layered crystals. However, the initial premise of gas intercalation within 2D materials is highly improbable because of the large kinetic diameters of gases compared to the available interlayer spacing. For instance, the kinetic diameters of He and CO_2 are 2.6 and 3.3 Å, respectively,[41] whereas the interlayer spacing in graphite is only 3.35 Å.[42] A detailed study by Walker et al.[43] of graphite subject to atmospheres of multiple gases at various temperatures found no evidence of any changes to interlayer distances and gaseous penetration.

In a fitting merger of shear-based liquid phase exfoliation and supercritical gas treatment, here we demonstrate the continuous, high-throughput production of exfoliated 2D materials caused by shear due to high velocity flows of compressible gases. In our compressible flow exfoliation

(CFE) process, 2D layered materials are rapidly jettisoned (**Figure 2-1a,b**) through a small orifice using high-pressure gases without the need for any time-based treatment, unlike other shear-based and gas processes. Shear-based exfoliation occurs due to the high velocities that expanding and accelerating gases can achieve in small orifices coupled with viscous friction effects resulting in a high shear rate ($\dot{\gamma} \geq 10^5$ s^{-1}) experienced by the 2D layered particles. We demonstrate the versatility of our method by applying this technique to exfoliate different 2D layered material (**Figure 2-1c**) as well as demonstrate that our method works, irrespective of the carrier fluid used. Our results indicate that shear is an inadvertent exfoliation mechanism in many reported supercritical fluid methods of producing graphene and other 2D layered nanomaterials.

Our method of CFE is capable of creating very fine colloidal suspensions of various 2D layered materials. Some samples of sprayed dispersions achieved after centrifugation are shown in **Figure 2-1c** for boron nitride, few-layer graphene (FLG), and molybdenum disulfide. All solutions were processed using CFE with helium at 14 MPa as the carrier gas flowing through a 0.1 mm gap annular orifice (1/4 turn open Swagelok valve), although other flow geometries, gases, and pressures conditions are possible as detailed below. To demonstrate the fast nature of our CFE process, similar suspensions were made using the popular liquid phase exfoliation (LPE) method by bath sonicating the same initial concentration for 3 h. The details for both the CFE and LPE processes are provided in the Experimental Section. The CFE process was able to achieve high concentrations of colloidal 2D layered particles after the centrifugation process, as indicated by the extensive laser light scattering through the solution known as the Tyndall effect.[44] UV–Vis light scattering profiles for BN are shown in **Figure 2-2a** indicating that suspensions created through the CFE process are able to absorb significantly more light across a wide spectrum of wavelengths, when compared to the popular LPE method produced using bath sonication. It is

important to note that the results of both techniques, CFE and LPE, are reported here without the use of surfactants or other surface energy modifying chemistries, which could result in higher concentrations but at the expense of deteriorating 2D material interface properties.[45] The results for the exfoliation of other layers compounds including graphite and molybdenum disulfide are shown in **Figure 2-S2**.

Using literature standards for each of the three different 2D layered materials, we have compared the absorption at reference wavelengths and computed the concentrations of the suspensions through the Beer–Lambert law: $\frac{A}{l} = \alpha C$, which states that the light absorption, A, in a medium over a certain distance, l, is proportional to the concentration of the absorbing particles, C. The proportionality term is the extinction coefficient, α, which is specific to a particular 2D layered material, solvent, and wavelength. The characteristics of our dispersions mimicked the reference conditions,[14,19] and hence, the wavelength specific extinction coefficient available in the literature could be used for concentration analysis by UV–Vis. Furthermore, the exact concentrations were obtained using gravimetric measurements and are in good agreement with the concentrations found using UV–Vis light scattering (mean error ≤ 5%). Under the same conditions, our method of CFE achieved concentrations of 0.075, 0.028, and 0.026 mg mL^{-1} for BN, graphite, and MoS_2, respectively. These values are comparable to or much better than the control values obtained using liquid phase exfoliation of 0.004, 0.020, and 0.008 mg mL^{-1} for BN, graphite, and MoS_2, respectively.

The few-layer nature of the final product after CFE processing and centrifugal separation was evident through Raman spectroscopy analysis of drop-cast 2D layer flakes. **Figure 2-2b** illustrates the Raman emission intensity spectra obtained using a 633 nm laser excitation in the relevant bandwidths for BN, while **Figure 2-S3** includes the spectra of graphite and MoS_2.

Comparison of the spectral emissions for all three 2D layered materials suggests a significant reduction in the number of layers, when compared with reference information available in the literature. The bulk form of boron nitride exhibits a spectrum consisting of one prominent E_{2g} phonon mode emission peak at 1366 cm^{-1}.[46] The emission peak undergoes a gradual redshift to 1362–1364 cm^{-1} as the number of layers is reduced to bilayer or few-layer. Finally, when monolayer BN is obtained, its emission peak is significantly blue-shifted to 1369 cm^{-1}, which is quite distinct from its bulk emission spectrum. Examination of the acquired Raman spectrum (**Figure 2-2b**) for boron nitride processed using CFE indicates a significant redshift of the peak to 1362 cm^{-1} suggesting a substantial presence of few-layer and bi-layer BN after processing. By contrast, the LPE processed control did not exhibit significant peak shifting indicating that the structure still consists of many stacked layers similar to bulk BN.

The Raman spectrum for bulk graphite (**Figure 2-S3b**), between the wavenumbers of 1500–3000 cm^{-1} exhibits, two characteristic peaks; the G peak occurring at 1580 cm^{-1}, which is the primary in-plane vibrational mode (E_{2g}),[47,48] and the 2D peak occurring at 2690 cm^{-1}. Several differences exist between the Raman spectra of bulk graphite and single layer graphene,[47,48] with the most noticeable being i) the increase in intensity (doubling) of the 2D peak when compared to the G peak, ii) the redshift of the 2D peak, iii) symmetric ordering of the 2D peak, and iv) the reduction of the full-width half maximum (FWHM) width of the 2D peak. Although all of these conditions are necessary to ascertain the presence of monolayer graphene, they may not all be present when analyzing few-layer graphene, or scans of a distribution of graphene with varying layer thicknesses.[14] A comparison of the Raman spectra for both CFE and LPE processed specimens against the spectrum for bulk graphite indicates two main differences; a significant redshift of ≈ 8 cm^{-1}, and an increased symmetry of the 2D peak. It should be mentioned that a

narrow symmetric peak is exclusive to monolayer graphene, however, the observation here of a wide symmetric peak (FWHM: 75 cm^{-1}) indicates the likely occurrence of AB-stacking disorder (turbostratic graphene) due to restacking or folding of sheets.[49] Taken together, these two observations from the Raman spectra indicate, at the very least, a reduction in layer number thickness from bulk graphite powder after being processed by either continuous CFE process or the batch LPE process. The occurrence of a disorder-activated D peak at 1330 cm^{-1} is indicative of defects, in particular those, which disrupt the sp^2 hybridization. Such defects can be interpreted to be either creation of new edges, vacancies, or substitutions (doping and functionalization), with the ratio between the peak intensities of the D to G peaks (I_D/I_G) providing some limited indication of their population.[47,48] It can be seen from **Figure 2-S3b** that CFE processed graphite has the same D to G peak intensity ratios ($I_D/I_G \approx 0.5$) while the LPE processed materials had a significantly higher peak ratio of 1.1 indicating a higher likelihood of sp^2 hybridization disruption due to LPE processing. Such defects could be present because of sonication at extended times, which can result in new edge formations from particle size reduction as well as point defect generation—including oxidation.

The spectra for bulk MoS_2 before and after CFE and LPE processing are shown in **Figure 2-S3c**. Bulk MoS_2 exhibits two strong first order peaks, E^1_{2g} and A_{1g}, whose relative positions strongly correlate with the number of layers present.[50,51] The peak-to-peak wavenumber distance between the two first order peaks is ≈ 26 cm^{-1} for a 633 nm excitation source. Upon subsequent exfoliation to few-layer and to single-layer MoS_2, the peak-to-peak distance gradually reduces to as little as 19 cm^{-1}. The MoS_2 processed using CFE in this study has an E^1_{2g} and A_{1g} peak-to-peak distance of 22.8 cm^{-1}, which according to a detailed description of MoS_2 Raman signatures by Li et al.[52] corresponds to a 3–4 layer thickness of the particles. The MoS_2 processed using the LPE

technique also undergoes layer thickness reduction, albeit with weaker effect, as indicated by a peak-to-peak separation of 24.0 cm^{-1}, which corresponds to a thickness of 4 or more layers.[52]

The structure of BN nanoparticles was characterized by atomic force microscopy (AFM) after CFE processing with a representative flake shown in **Figure 2-2c**. The flake exhibits a thickness of 2 nm and a width of 350 nm, giving an aspect ratio of 175. At an interlayer spacing of 0.32 nm,[53] a thickness of 2 nm corresponds to 6 layers of BN that were isolated. Further AFM characterization of additional BN particles reveals a distribution of particle thicknesses (**Figure 2-2c**, inset) and lengths (**Figure 2-S4**) when subject to the CFE process. Typically, higher driving pressures in CFE result in better flake quality. For instance, BN produced using He gas at 5.5 MPa (**Figure 2-S4a**) have an average flake thickness of 5.7 nm and length of 160 nm, giving an aspect ratio of 28, while at a pressure of 10 MPa (**Figure 2-S4b**) the flake thickness and length were 4.2 and 276 nm, corresponding to an aspect ratio of 66. Furthermore, ≈ 27% of the flakes processed at 5.5 MPa had a thickness less than 3.2 nm (corresponding to 10 layers or less) with this proportion increasing to 43% at a higher pressure of 10 MPa.

The structures of CFE processed BN, FLG, and MoS_2, as imaged by transmission electron microscopy (TEM), are shown in **Figure 2-2d**. The size of these particles typically ranges from 100 to 800 nm indicating a reduction of particle size compared to the starting particle sizes of 13 μm for BN and 1 μm for graphite and MoS_2. These particles are sufficiently thin after exfoliation, as indicated by their electron-transparency. Furthermore, some flakes appear to be single crystals, while others appear polycrystalline on the basis of their electron diffraction patterns (**Figure 2-2d**, insets). The polycrystallinity is indicative of basal plane rearrangement (turbostraticity), further evidence for which is found in the Moiré patterns occasionally observed during TEM of BN (**Figure 2-S5**). Similar Moiré imaging projections have been observed during restacking of planes

when drying from suspension,[54] or from the mechanical folding and shifting of individual planes during shear processing.[55] Further TEM images of CFE processed 2D nanomaterials are provided in **Figure 2-S6** along with their LPE counterparts. Clear differences in the shape and surface topology characteristics between the two processes are evident such as straighter edges in CFE processed BN (**Figure 2-S6a**), compared to LPE processed BN (**Figure 2-S6d**), which consists of more rounded out edges. Furthermore, CFE processed 2D layered materials contain fewer residual small particle debris compared to the LPE processed particles, which we attribute to the harsher conditions experienced during ultrasonication for extended times in LPE processing. Ultrasonication for extended times (hours, days) has been known to cause structural damage, in particular particle size reduction, of many nanomaterials including carbon nanotubes and 2D layered materials such as graphene,[56,57] BN,[58] and MoS_2.[59] Residual small particle debris with sizes less than 50 nm are quite prominent in the particles processed using LPE, whereas their CFE equivalents are nearly void of such small-scale residuals. Furthermore, despite some restacking and visual aggregation, the CFE processed suspensions are for the most part still stable after 6 months of storage (**Figure 2-S6g**).

The material characterization results presented thus far indicate that CFE is equal to or better than the comparable top-down technique of LPE in terms of 2D nanomaterial concentrations, layer thickness, and structural defects. In regards to processing, the advantages of CFE over LPE include the rapid, high-throughput and continuous nature of the process as well as the use of environmentally friendly gasses instead of handling potentially hazardous solvents in LPE. In contrast to the time-based treatment in ultrasound and shear based LPE processes, the CFE process works with a rapid, single pass of the 2D layered materials through a fine nozzle/orifice. Recently, a microfluidization technique[27] that forces surfactant suspended graphite in an

incompressible liquid through a fine orifice at high pressures was shown to be effective at creating 2D nanosheets of graphite. The process required an intensifier pump and multiple passes through the orifice in order to achieve a 100% yield. Although no postprocess centrifugation was required, the technique is still time dependent and required the use of surfactants, which can be detrimental to the interfacial properties of 2D materials. Similar to several existing top-down processes, both CFE and microfluidization rely on imparting shear forces on the particles to cause layer separation. However, to our knowledge CFE is the only process that utilizes the stored potential energy in high pressure compressed gases to achieve supersonic velocities that generate the shear required for layer separation, while simultaneously utilizing the gas phase for suspending the exfoliated particles during the brief process.

A series of controlled experiments (**Figure 2-3**) were performed to quantify the effect of various process parameters such as the upstream gas pressure, starting BN amount, process time, gas type, and flow geometry. Initial experiments were carried out using a Swagelok needle valve partially opened at a 1/4 turn to create an annular gap of ≈ 0.1 mm along with a converging portion just before the gap and a diverging portion right after the gap (**Figure 2-S7**). Other valve settings were experimented with as well, with larger openings giving lower process yields due to insufficient shear, while smaller openings resulted in the valve being clogged and the complete restriction of flow. Experiments with flow through constant area stainless steel channels (30 cm length) with varying inner diameters (1.3, 2.1, 3.1, 3.8, and 4.6 mm) were also performed to clarify the role of shear during CFE processing. The effect of the amount of starting bulk 2D material on the final 2D nanomaterial concentration obtained is shown in **Figure 2-3a**. The initial concentration is defined as the ratio of BN powder fed into the gas flow to the volume of liquid solvent that it sprays into after the CFE process is complete. The final concentrations are based on

gravimetric measurements after centrifuging and careful drying. Regardless of the flow geometry (valve or tube), an increase in the initial concentration results in a concomitant rise in the final concentration with only 2 s of process run time. However, this effect is limited at higher BN loading amounts, particularly for the valve, where the flow is restricted because of clogging from the highly packed BN powder. The ratio between the final and initial concentrations in **Figure 2-3a** can be interpreted as the yield of the process, which for CFE is between 5 and 10%. This yield is comparable, if not better than most liquid phase processes that do not rely on surfactants or surface functionalization[19] (a comparison is provided in **Table 2-S1**). As can be seen from **Table 2-S1**, the CFE method, detailed here, is able to exfoliate in a matter of seconds (2 s), as opposed to several minutes or hours required in other comparable processes. Furthermore, if this process is run continuously then the yield can be driven up further through material recovery and recycling.

The effect of varying inner diameters on the final concentration for the straight tube flow configuration at 5.5 MPa is shown in **Figure 2-3c**. As the tube diameter is increased, there is a rapid increase in the final concentration peaking at 0.11 mg mL^{-1} at a diameter of 2.1 mm followed by a gradual decrease. Smaller tube diameters of 0.5 and 0.1 mm were also tested, but they significantly impeded the flow at the applied pressures. The final series of experiments investigated the effect of various gases used in CFE with the results summarized in **Figure 2-3d**. Helium, nitrogen, and carbon dioxide at a common pressure of 5.5 MPa through both valve and straight tube configurations were tested. The final concentrations using helium flowing through the valve were significantly better (0.15 mg mL^{-1}) than nitrogen (0.03 mg mL^{-1}) and carbon dioxide (0.03 mg mL^{-1}). A similar trend was observed for the straight tube configuration. Other carrier gases such as argon, a heavier monatomic gas, and compressed air, a gaseous mixture, had similar results as nitrogen and were significantly lower than those obtained using helium.

It is well known that within certain pressure differentials, compressible fluids passing through a converging–diverging channel achieve supersonic velocities governed by a differential relation based on the conservation of mass and momentum[59]

$$\frac{dV}{V}[M^2 - 1] = \frac{dA}{A}$$

where dV/V is the fluids relative change in instantaneous velocity (V), dA/A is the relative change in the flow channel's instantaneous area, and M is the fluid's Mach number, defined as its velocity V relative to the velocity of the speed of sound, V_s. Specifically, the average flow velocity in the narrowest portion (the "throat") of the channel (dA/A = 0) is equal to the speed of sound in that fluid. Depending on the design of the channel exit (diverging portion), it can achieve even higher velocities (supersonic) after leaving the throat. This increase in velocity is concomitant with a rapid pressure drop (flow expansion) in the diverging portion of the CD nozzle. Using this simple picture of supersonic compressible flows and the assistance of computational fluid dynamics (CFD), we can examine in detail the geometry specific nature of the flow through a partially open needle valve and elucidate the mechanisms responsible for the observed exfoliation of 2D nanomaterials. CFD simulations were performed in COMSOL Multiphysics v5.3 (High Mach Number—Fluid Physics Model) with the 2D geometry modeled (**Figure 2-S7**) using CAD software as per the supplier's dimension of the needle valve. Typical results of flow simulations are shown in **Figure 2-4**, which describes the case of helium gas at 5.5 MPa flowing through the partially open needle valve (0.1 mm gap). The velocity surface plots (**Figure 2-4a**) demonstrate that the valve acts as an adjustable converging–diverging nozzle capable of achieving supersonic flows within the pressure range of interest. The surface plots indicate significant regions after the throat of the nozzle where the velocities exceed 1600 m s^{-1}, corresponding to Mach 1.6 (the speed of sound in helium at room

temperature is ≈ 1000 m s^{-1}). Other regions of high Mach flow are also present in the valve; however, the primary region of interest is the throat portion where rapid changes in velocities occur within small flow cross-sections. These changes in velocities, V, can be understood through its spatial gradient, the shear rate, $\dot{\gamma}$, defined as $\dot{\gamma} = \frac{dV}{dx}$, which for the simulated flow is plotted in **Figure 2-4b**. This surface plot indicates that shear rates in excess of 10^5 s^{-1} are easily achieved for rapidly accelerating flows through a fine CD-nozzle. A line scan profile (**Figure 2-4c**) along the throat portion of the nozzle (red line in **Figure 2-4b**) indicates that the shear rate starts out highest near the wall at 4×10^5 s^{-1}, before rapidly decreasing to 1×10^5 s^{-1} and then gradually rising again to 3×10^5 s^{-1}. This skewed profile of the shear rate along the throat is attributed to the asymmetric channel profile. Regardless, it can be seen that the entire flow, including suspended BN and other 2D layered particles, is subject to shear rates in excess of 10^5 s^{-1}. This key observation is a link between the exfoliation results using compressible gases in CFE to the shear dominated exfoliation mechanisms utilized in other liquid-based top-down 2D nanomaterial production processes.[21–27] The instantaneous changes in momentum acting on the suspended 2D particles in a multiphase gas flow subject to such shear rates would significantly alter the kinetic energy of the particles, some of which would be dissipated as work done toward overcoming the secondary c-axis bonds of the 2D layered materials. The layer shear mechanism involved in CFE is equivalent to that observed in liquid phase exfoliation by high-speed shearing.[21] In this comparable method, effective exfoliation of 2D nanomaterials occurs provided that the shear-rates are higher than a critical value of 10^4 s^{-1} and that the material is subjected to that shear-rate (i.e., cycled) for a sufficient amount of time. In the present CFE process, the 2D layered materials are easily subject to shear rates higher than 10^5 s^{-1} and make only one pass through the nozzle with a very small residence time thus making it a continuous, high-throughput operation.

Other conditions, representative of the valve experiments in **Figure 2-3b**, but at various pressures, were simulated in CFD (**Figures 2-S8 and 2-S9**) to provide insights into the shear rates developed in supersonic flows through fine orifices. It can be seen that the shear rate distribution in the valve evolves as the pressure is increased from 1.4 to 2.8 and 5.5 MPa while remaining more or less steady at 14 MPa. At low pressures, areas of high shear ($\dot{\gamma} > 10^4$ s^{-1}) exist only near the wall in the diverging portion of the CD nozzle inside the valve. As the upstream pressure driving the flow is doubled to 2.8 MPa, shear rates of 10^5 s^{-1} or greater are experienced throughout the CD nozzle. Further doubling of the pressure to 5.5 MPa (**Figure 2-S9c**) causes the regions of high shear ($\dot{\gamma} > 10^5$ s^{-1}) to further enlarge. Raising the pressure beyond 5.5 MPa did not significantly change the distribution and magnitude of the high shear zones inside the valve. The evolution of the shear zones as predicted by the simulations can be directly correlated with the experimentally observed dependence of the final concentration on the upstream pressure (**Figure 2-3b**). The final concentration more than triples from 0.04 to 0.15 mg mL^{-1} as the pressure is increased from 1.4 MPa to 5.5 MPa, after which it slowly increases to 0.2 mg mL^{-1} at 11 MPa.

It is important to point out that supersonic flows and changing area profiles may not be a necessary requirement in CFE. Rather, the shear rate, which is related to the overall flow velocity and the flow channel width, is of considerable importance. The advantage of using gases for shearing 2D layered materials is their inherent compressibility, which can be utilized to accelerate to and decelerate from high velocities across short distances, thereby imparting a high shear rate on any suspended solids including 2D materials. Perhaps the most straightforward demonstration of this effect is the straight tube experimental results of **Figure 2-3b,c**. The flow profiles in these experiments are within the consideration of Fanno flow, which describes the adiabatic expansion of a compressible gas inside a constant area duct with a known friction factor.[60] For considerably

long ducts, gas expansion during flow causes maxima in the mass flow rate and a state of choked flow exists where the flow velocity reaches the speed of sound (Mach 1). Once choked flow is achieved, no further increase in the upstream pressure will cause faster velocities. This understanding of Fanno flow correlates well with the achieved final concentrations in **Figure 2-3b** for straight tubes, which become invariant with pressures of 5.5 MPa and higher. Despite the doubling of pressure, velocities faster than the speed of sound are unattainable in these straight tubes and hence the maximum shear rate and shear rate distribution experienced by the multiphase flow remains unchanged.

Aside from velocity, the shear rate experienced by the flow is dependent on channel width considerations. Assuming friction effects at the wall (no-slip condition), the shear rate should be highest at the walls and lower at the center of the flow. Complicating this simple explanation is the consideration of turbulent flows, as in the case here, where analytical expressions of velocity and shear rate profiles are nonexistent. The Reynolds number, characterizing the laminar-turbulent flow classification based on the fluid's velocity, V, channel diameter, D and the fluid's kinematic viscosity, ν is given by the relation: $Re = \frac{VD}{\nu}$.46 For the case of helium at Mach 1 through a 2.1 mm channel, the Reynolds number is 18 000, which is well above the turbulent-laminar flow boundary (Re = 2300). Thus, in addition to wall friction, a further contribution to the high shear rates experienced in turbulent flows comes from the sudden, erratic changes in the local velocity profile arising from the stochastic generation of eddies. These changes in velocity over a short span would give rise to the high shear rates experienced in the centerline of the flow profile (e.g., **Figure 2-4c**). In the straight tube experiments, the channel width has an effect in imparting shear on the 2D layered materials, and hence, on the final concentration achieved. It is evident from **Figure 2-3c** that reducing the tube diameter from a starting value of 4.6 mm tends to improve the

final concentration, and hence, the overall yield of the CFE process. This effect can be explained in terms of shear rate where a reducing tube diameter at the same velocity will impart greater shear rates on the flow because of an increased fraction of the wall (zone of high shear rate) relative to the overall flow cross-section. Almost halving the tube diameter from 4.6 to 2.1 mm has the effect of increasing the concentration to 0.11 mg mL^{-1}—an improvement by a factor of 5.4 times. However, further reduction of the tube diameter to 1.3 mm has the unintended effect of severely decreasing the concentration to 0.045 mg mL^{-1}. At this diameter, the flow did not achieve the choked condition as per Fanno flow and it was audibly apparent that the exit flow velocities were considerably less than Mach 1. Friction effects tend to dominate at smaller tube diameters resulting in considerably lower flow velocities and hence shear rates. For instance, changing the tube diameter from 2.1 to 1.3 mm for helium flowing at Mach 1 increases the friction factor from 0.028 to 0.035, as per the Moody–Colebrook relationship.[60] In addition to wall friction, the reduced diameter lowers the Reynolds number from 18 000 to 11 000, thus reducing the turbulent nature of the flow and the effectiveness of eddies to generate high shear rates.

Perhaps the most convincing demonstration of the compressible gas dynamic principles at work in the CFE process is by varying the carrier gas. This was experimentally observed and is summarized in **Figure 2-3d**, which shows that the final concentration obtained by helium is almost 5 times better than those using nitrogen or carbon dioxide in both straight tube and valve (CD nozzle) configurations. At 293 K, the speed of sound in helium is roughly 1000 m s^{-1}, while nitrogen and carbon dioxide are considerably lower at 350 and 270 m s^{-1}, respectively. Provided choked flow (Mach 1) is achieved for these gases, helium being the lighter and faster gas imparts sufficiently higher shear rates than the other heavier gases. Hydrogen gas would serve as an even better medium for exfoliating 2D layered materials, since it is a lighter gas than helium, having a

higher speed of sound (1270 m s^{-1}), as well as being more abundant and cost-effective. However, safety considerations prevented us from evaluating high-pressure hydrogen in CFE processing of 2D layered materials.

To demonstrate the utility of our ultrafast compressible flow exfoliation method, we considered improving the barrier properties of poly(ethylene terephthalate) (PET) by reinforcing it with the exfoliated 2D layered nanomaterials. PET is commonly used for food and beverage packaging where the simultaneous requirements of high optical transparency and limiting oxygen transport have proven to be a technical challenge. Numerous inorganic compounds such as mineral particles,[61] nanoclays,[62,63] and 2D nanomaterials[64] have been investigated as a potential reinforcing phase to improve the oxygen barrier properties. However, most studies show significant improvements only at high inorganic volume content where the optical transparency as well as mechanical strength and ductility of PET become compromised. Other approaches such as using layer-by-layer fabrication[65] have proven to be useful for improving barrier properties at low inorganic volume content while maintaining decent optical transmissivity. However, these techniques are still far from being demonstrated for mass-production and so the scalability of such a layer-by-layer approach, especially for low-value consumer packaging applications, is questionable.

In the present application, concentrated suspensions of CFE-BN and bulk-BN powder were added to a powdered PET resin by evaporating the isopropanol in the presence of the resin followed by mixing in the melt phase at 265 °C (details in the Experimental Section) and extruding into continuous films. The melting temperature (T_m) and enthalpy of melting (ΔH_m) of PET, as measured by a second differential scanning calorimetry (DSC) heat trace, was found to remain unchanged at 246 °C and 40 J g^{-1}, respectively, regardless of the type and amount of BN added

(**Table 2-S2**). The addition of BN to PET did increase the apparent glass transition temperature of PET by ≈ 1.5–2 °C with no significant differences observed for the type of BN (CFE or bulk) or the amount (0.017 or 0.15 vol%). The PET composites show a crystallization peak during cooling that resulted in the disappearance of cold crystallization during the second heating trace (**Figure 2-S10**). While cooling from the melt (10 °C min^{-1}), the crystallization peak for PET was at 198 °C, which increased to 207 °C for PET containing 0.017 and 0.15 vol% of CFE-BN. In comparison, the crystallization peak for bulk BN was at 203 and 206 °C for 0.017 and 0.15 vol%, respectively, indicating slower crystallization kinetics of the bulk BN particles compared to the exfoliated BN, which can be attributed to the heterogeneous nucleation effect of nanomaterials.[64,66] The final PET films were optically transparent (94% transmittance) and remained transparent (>90%) when 0.017 and 0.15 vol% of CFE-BN or bulk-BN powder were added (**Figure 2-5a**). The transmitted light when subject to wide-angle scattering (>2.5° from normal) is defined as optical haze, and this was found to be smaller for the exfoliated 2D nanomaterials than the bulk BN nanomaterials (**Table 2-S3**).

At a low volume content of 0.017 vol% BN, there was no noticeable difference in the tensile Young's modulus of the PET films (888 MPa) for either the nanoparticles or the bulk particles (**Figure 2-5b**). Addition of 0.15 vol% CFE-BN resulted in an improvement in the modulus of PET by 21% to 1072 ± 15 MPa. By contrast, the same amount of bulk-BN to PET resulted in only a 12% improvement in the modulus (993 ± 55 MPa). No significant variations in PET's tensile strength and strain at failure were observed (**Table 2-S4**) for the type of BN (CFE or bulk) or the amount (0.017 or 0.15 vol%), which is likely due to the low amounts that were added. Prior to the oxygen permeation measurements, the PET and PET–BN films were biaxially stretched down to a 20 μm thickness at a low stretch speed and temperature (Supporting

Information), where concerns surrounding strain induced crystallization can be neglected.[67] Similar to the mechanical properties, a low volume content (0.017 vol%) of either the CFE-BN or bulk-BN did not result in any change to PET's steady-state oxygen permeation rate (OPR), which was 0.27 ± 0.01 cm^3 cm m^{-2} d atm. Adding 0.15 vol% of the compressible flow exfoliated BN resulted in the OPR dropping by 26% to 0.20 ± 0.01 cm^3 cm m^{-2} d atm. Interestingly, the same amount of bulk-BN to PET caused the OPR to increase to 0.37 ± 0.08 cm^3 cm m^{-2} d atm, which would be detrimental to any barrier packaging applications. It is suspected that larger layered aggregates in the PET–bulk-BN films could have delaminated during the stretching phase to open up new low resistance pathways for permeation. An SEM image (**Figure 2-5d**) shows thin sheets of CFE-BN protruding out of a freeze-fractured surface of 0.15 vol% PET–BN nanocomposites, viewed at a tilt, indicating some dispersion of the BN nanoparticles. The significantly improved mechanical and barrier properties of the CFE-BN nanocomposites are attributed to the exfoliation of the layered BN particles into thin sheets, which can be easily dispersed and result in a more efficient load transfer across the polymer–particle interface as well as creating a more tortuous pathway for permeation.

Here we have introduced a new method—CFE—for exfoliating 2D layered materials by compressible fluids flowing through fine nozzles in a continuous manner. The underlying principle is based on accelerating multiphase flows of 2D layered materials suspended in a compressible media to supersonic velocities whereby sufficient shear rates ($\dot{\gamma} > 10^5$ s^{-1}) are generated to cause layer reduction and exfoliation. Using helium gas and boron nitride particles, the CFE process was able to create suspensions of 2D nanomaterials in isopropanol that have an average thickness of 4.2 nm, and an average length of 276 nm (aspect ratio ≈ 65). The CFE process is capable of exfoliating other 2D nanomaterials such as few-layer graphene and molybdenum disulfide, using

a multitude of gases such as helium, nitrogen, or carbon dioxide. Apart from the high concentrations (0.2 mg mL^{-1}) and yields (10%) achieved in a short duration, the advantages of CFE include the ability to isolate the exfoliation and suspension stabilization processes from each other, environmentally friendly processing and reduced occurrence of defects that might otherwise arise in comparable liquid phase, time-based treatments. Nanocomposites produced using CFE processed boron nitride had significantly improved mechanical and barrier properties when used in the plastic PET compared to neat PET and bulk-BN counterparts, all the while preserving the optical properties. Using a continuous flow of compressible gasses for high-throughput 2D nanomaterials production could represent a paradigm shift in their economic feasibility for mass manufacturing.

EXPERIMENTAL

Three types of 2D layered materials were used to investigate the compressible flow exfoliation (CFE) method. The first was natural graphite flake, an electrically conductive layered material, provided by Sigma Aldrich (Milwaukee, WI), which had a reported powder size of 1-2 μm. The second was molybdenum disulfide (MoS_2), a transition metal dichalcogenide with topologically insulating characteristics, purchased from Alfa Aesar (Milwaukee, WI), which had a reported powder size of 1 μm. The third was hexagonal boron nitride (BN), an insulating layered compound, provided by Momentive Performance Materials (Waterford, NY), which had a reported size of 13 μm. Helium, carbon dioxide and nitrogen compressed gases were used as the carrier fluids and obtained from Airgas Inc. (Radnor, PA) with greater than 99.99% purity. The solvent isopropanol (IPA) from Fisher Scientific (Waltham, MA) was used to suspend BN, while N-methyl-2-pyrrolidone (NMP) from Sigma Aldrich (St. Louis, MO) was used to suspend graphite and MoS_2.

Compressible Flow Exfoliation Process

The compressible flow exfoliation (CFE) method involves bulk 2D layered materials that are suspended in a gas, which passes through a flow compression channel (e.g. a small orifice, converging channel, thin tube, etc.) and then allowed to expand into ambient conditions. The flow velocity and expansion pressures can be controlled through the appropriate design of an exit channel, such as a converging diverging (de Laval) nozzle. During this process, the gaseous medium achieves supersonic (Mach 1 or greater) velocities which coupled with large viscous friction effects in narrow channels generate the high shear rate environment for 2D particle exfoliation. In a typical CFE experiment, 0.1 to 0.5 g of a 2D layered material is charged in a 50 mL, high-pressure vessel and sealed (**Figure 2-1b**). The high-pressure fluid, with upstream (stagnant) pressures in the range of 1.4 MPa to 14 MPa (200-2000 psi), is then released into the vessel and the mixture of carrier fluid and 2D material is allowed to flow through a narrow channel or orifice capable of compressing and expanding (accelerating) the gas. From our experience, a partially open Swagelok needle valve (SS-1KS4, Swagelok Corp.) can be used as an annular shaped CD nozzle with an adjustable throat distance. When partially opened (0.25 turns), the valve has an annular orifice gap of 0.1 mm, which we have found to be sufficient for exfoliation from parametric studies.

After passing through the channel, the multiphase jet is vented into a large collection bottle or flask containing 50-100 ml of an appropriate solvent. From prior studies and experience, the appropriate solvents were IPA for BN, and NMP for graphite and MoS_2. The total process lasts only 2 s in time and could be extended for longer times (continuous operation) if there are no concerns for expending the gas or evaporating the solvent. Orientation of the spray nozzle with respect to the collection vessel is critical for maximizing the retention and yield, with the optimum configuration being a cyclonic flow tangential to the collection vessel walls (**Figure 2-S1**).

The sprayed solution, containing the 2D layered material, is then centrifuged at high speeds of 1400 rpm (rcf. = 420 G) for 90 min in order to separate the bulk and multi-layered 2D materials from the few layered 2D nano-materials (supernatant), which is a commonly employed protocol in top-down 2D materials research.[68] For comparison, equivalent dispersions of few layered 2D materials were prepared by liquid phase exfoliation with the assistance of ultra - sonication. In a typical process, 0.1 g of bulk 2D materials were mixed with 100 ml of the appropriate solvent (see above) and were bath sonicated for 3 h using a VWR Scientific B2500A-DTH Ultrasonic Cleaner (42 kHz – Elec. Spec. 117V, 210 W). All other handling of the liquid phase exfoliation suspensions, including centrifuging, was carried out in the exact same manner as the CFE suspensions.

CFD Flow Simulation

Computational Fluid Dynamics (CFD) simulations of the compressible flow exfoliation (CFE) process were carried out in the COMSOL Multiphysics 5.3 (COMSOL Inc.) simulation package. The high Mach flow module was utilized with the turbulence accounted for through the κ-ε turbulence model. The simulations consisted of flow analysis around the partially opened needle valve, which acts as a fine orifice in our process.

Exfoliated Nanoparticle Characterization

The absorption characteristics of the exfoliated 2D nanomaterial suspensions were measured by a UV-Vis spectrophotometer (Shimadzu UV-3101PC) scanned from wavelengths of 190 to 900 nm. The Raman spectra of the exfoliated 2D nanomaterials was obtained using a Renishaw inVia Qontor Raman Microscope, 50x lens and 633 nm laser. A 10 μL drop of the suspension was vacuum dried on a clean silicon wafer substrate prior to measurements. The 2D nanomaterial's

thickness and lateral dimensions were quantified using a Veeco Nanoscope III Multimode Atomic Force Microscope (AFM). Prior to AFM measurements, a 10 μL drop of the suspension was dried rapidly by casting on a mica substrate heated to 150 °C. The 2D nanomaterials were also viewed on a Hitachi HD-2300 Scanning Transmission Electron Microscope (TEM) at an accelerating of 200 kV. Prior to TEM observations, a 10 μL drop of the suspensions was cast onto lacey Formvar/carbon-coated grids.

Polymer Nanocomposites Preparation

The utility of the CFE process was demonstrated by fabricating polymer nanocomposites for oxygen barrier and mechanical properties. Polyethylene terephthalate (PET; Laser+7000) with an intrinsic viscosity of 0.84 ± 0.02 dl/g (DAK Americas) was used as the resin. The PET pellets were cryogenically ground to make a fine powder with mean particle size of 700 microns. Different volumes of compressible flow exfoliated BN (CFE-BN) solution in isopropanol (0.11 mg/ml of solution) were mixed with PET powder to make 0.017% and 0.15% v/v nanocomposites. For comparison, bulk-BN was mixed with PET powder and IPA to make the same volume content composites. A PET control sample was prepared by making a slurry of PET powder with an equivalent amount of IPA. The slurries of CFE-BN and bulk-BN with PET were vacuum dried for an extended period at room temperature to evaporate the solvent. Dried PET powders coated with CFE-BN and bulk-BN were extruded with a RCP 0250 microtruder single screw extruder (Randcastle Extrusion Systems Inc., USA) at 265 °C and 140 rpm. A slit die and a cooling roll was used to make nanocomposite films with a thickness and width of 70 microns and 3 cm, respectively.

Polymer Nanocomposite Characterization

Thermal transitions were studied using DSC-7 differential scanning calorimeter (Perkin Elmer Inc, USA). Samples of about 10 mg were first melted and quench cooled (using an ice bath) under a nitrogen environment to erase the thermal history and then heated from 40 °C to 300 °C at 10 °C/min heating rate followed by cooling at 10 °C/min. Tensile measurements were carried out according to ASTM D638-10 using an Instron universal tester (Instron Corp., USA) at a strain rate of 25 mm/min (100%/min). Tensile bars were cut from the nanocomposite films using a Specimen V die cutter. Oxygen transport studies of a control PET and nano-composites were measured using an Oxysense 5250I instrument with an Oxyperm permeation chamber (Oxysense Inc, USA) according to ASTM F3136–15. All the films were thinned down to ~20 μm thickness with a biaxial film stretcher (T.M. Long Co. Inc, USA) for permeation measurements at a temperature of 100 °C at a rate of 2.5 mm/s and a 200% biaxial extension ratio. Air (20.8 % oxygen) was used as the transmission gas and the oxygen permeation rate (OPR) was calculated using the dynamic accumulation method [69]. The permeability coefficient is the steady-state OPR value, which accounts for the thickness of the sample. Percent haze of the PET-BN nanocomposite films was determined using a Haze-gard Plus hazemeter (BYK Gardner Inc, USA) following ASTM 1003-95.

ACKNOWLEDGEMENT

R.R. would like to acknowledge support from the Canadian NSERC Postdoctoral Fellowship and from the University of Toledo (University Startup Funds). E.P.N. would like to acknowledge support from the Australian Endeavour Research Fellowship. W.H.M. would like to acknowledge support from the UCLA Cota-Robles Fellowship.

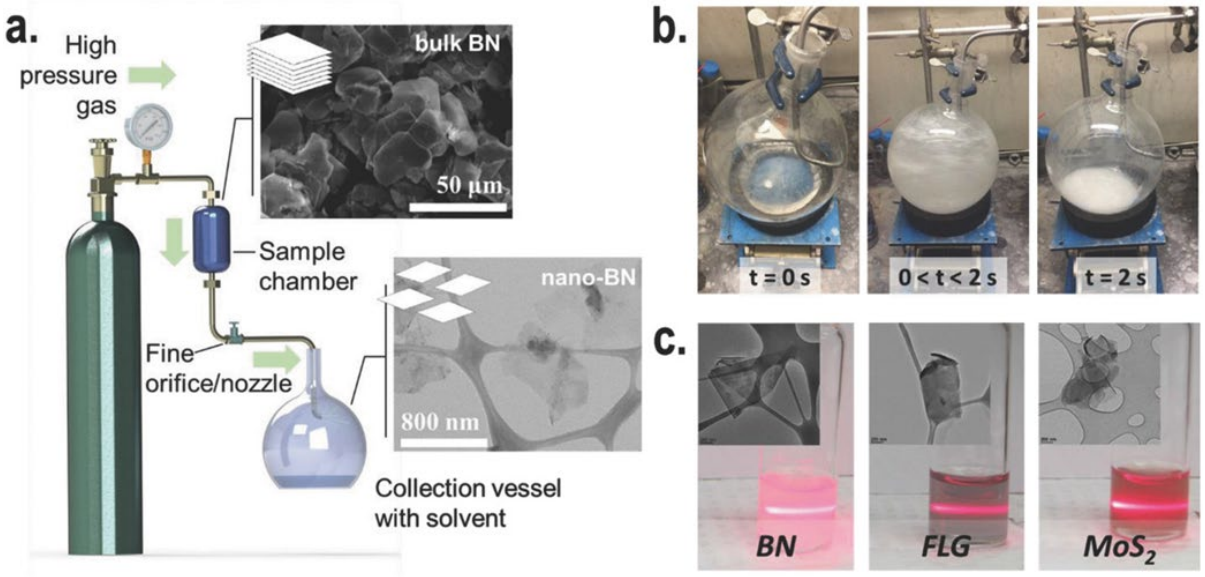

Figure 2-1. a) Process schematic of the compressible flow exfoliation setup including a description of the critical components and the initial and final structures of the BN powder. b) Still images of the collection vessel before, during, and after the CFE process for BN powder. c) Exfoliated suspensions of various 2D layered nanomaterials after centrifugation.

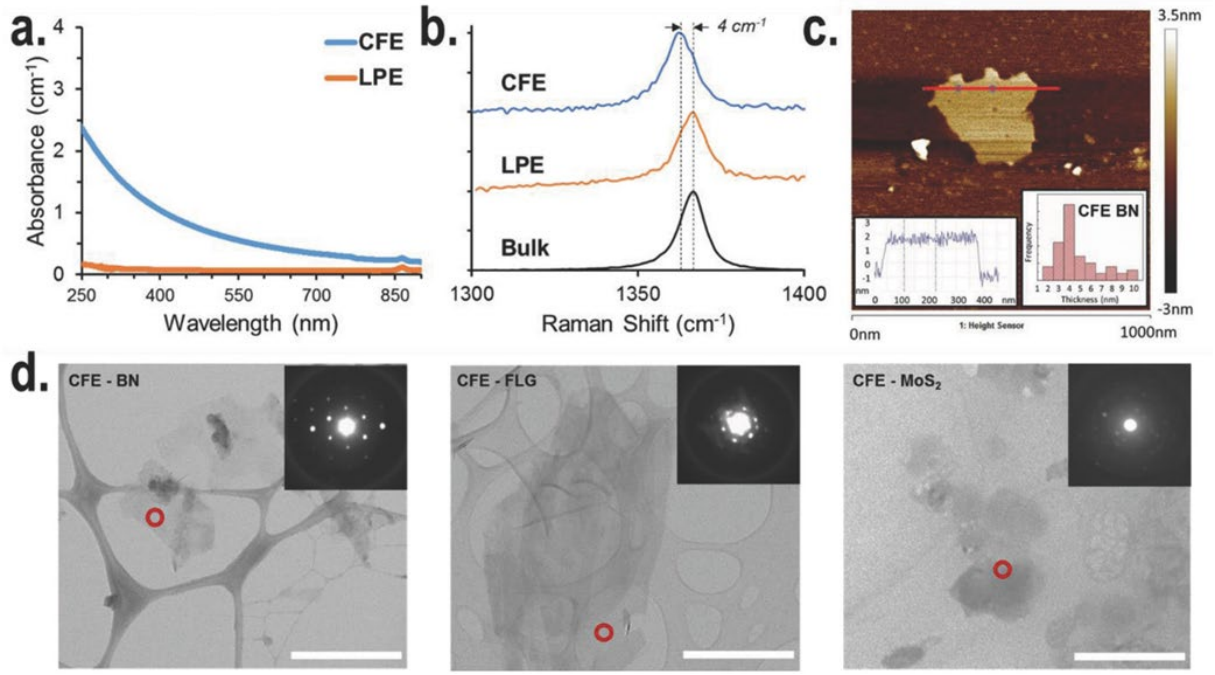

Figure 2-2. The a) UV–Vis and b) Raman spectra for BN produced using continuous flow exfoliation (CFE) and the comparable liquid phase exfoliation technique. c) The AFM scan image of a BN flake isolated after CFE with insets showing the height profile of the flake and the thickness distribution of several flakes. d) The TEM images (scale bar: 800 nm) for various 2D materials produced by CFE along with their diffraction patterns (inset) at the marked spot—shown here are BN (left), graphite (middle), and MoS2 (right).

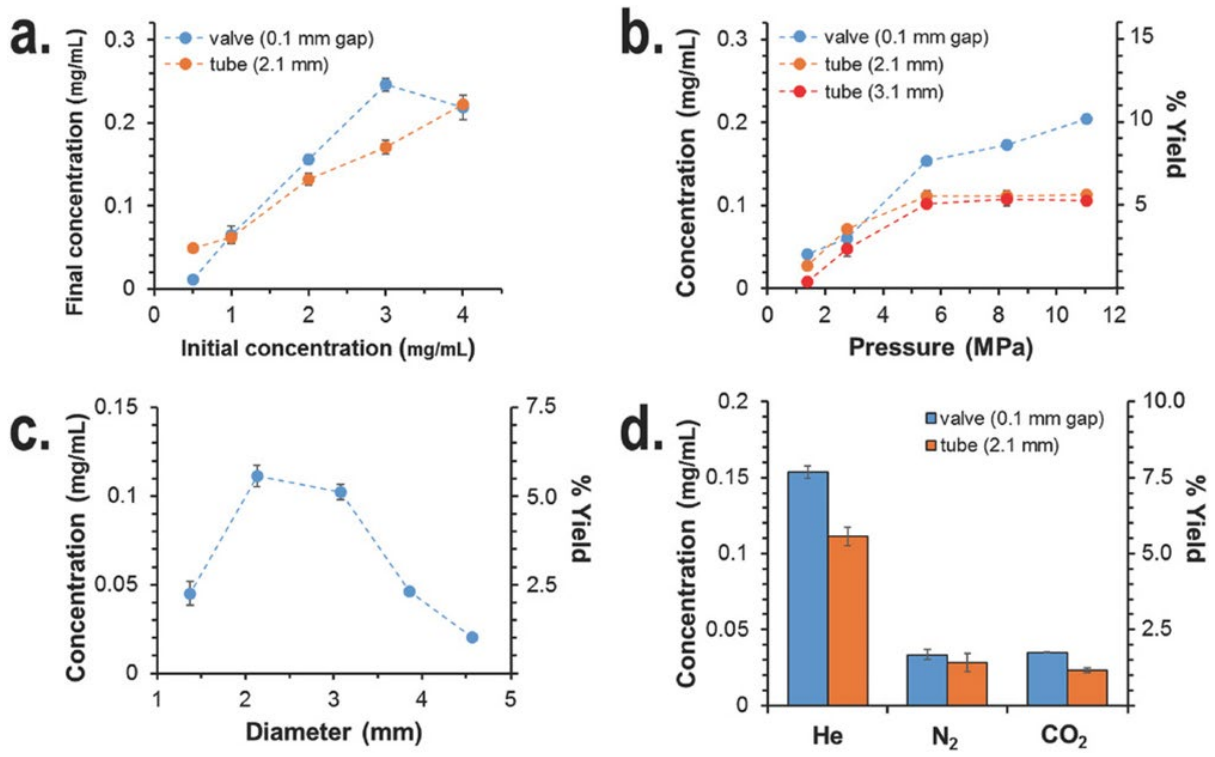

Figure 2-3. a–d) Plots showing the effects of initial BN concentration (a), upstream gas pressure (b), flow geometry (tube diameter) (c), and carrier gas type (d) on the final BN concentration and yield in CFE. All error bars represent the standard deviation (n = 3).

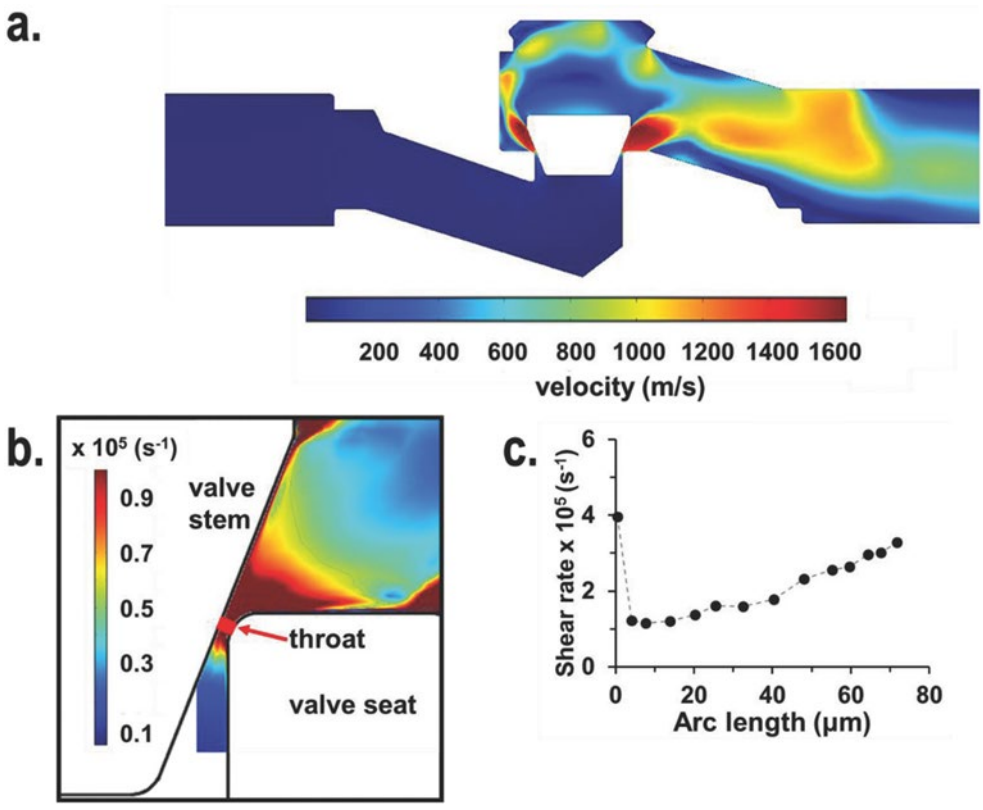

Figure 2-4. CFD simulation results showing: a) a surface plot of velocity variations, b) a surface plot of shear rate variations near the throat, and c) a line scan profile of the shear rates at the minimum cross-section (red line in Figure 4b). The simulation conditions are for BN particles in helium gas at an upstream pressure of 5.5 MPa and a gap of 0.1 mm.

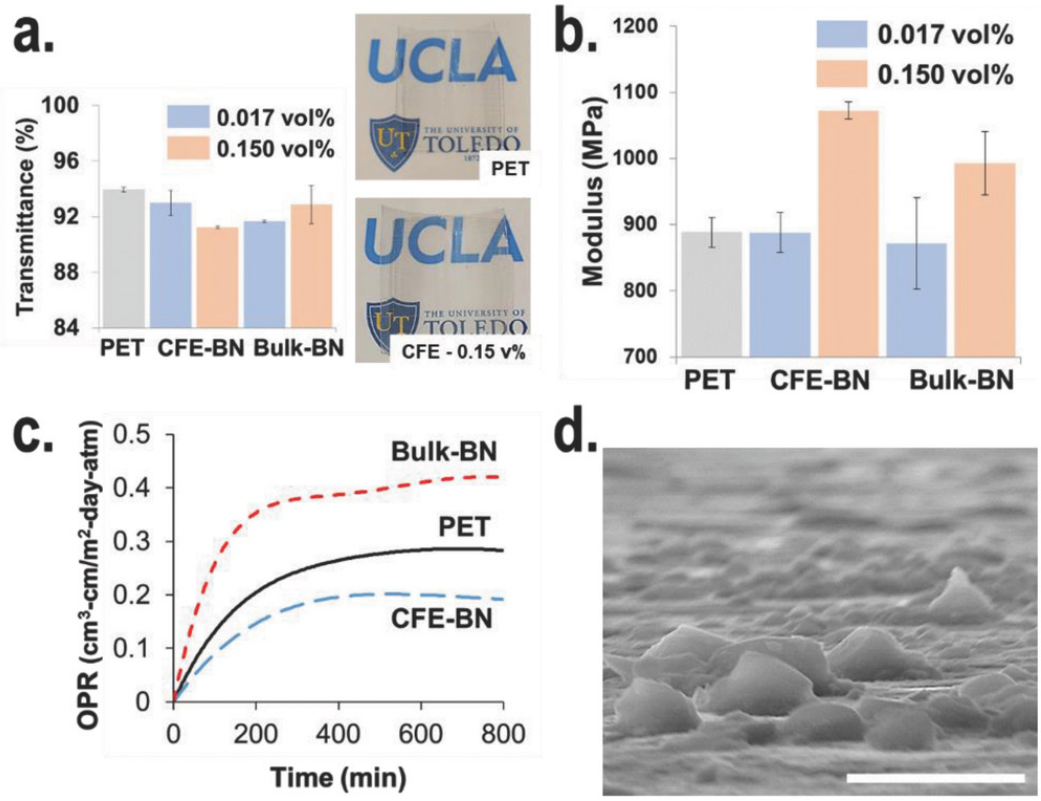

Figure 2-5. PET–BN nanocomposites prepared using CFE exfoliated and bulk boron nitrides at 0.017 and 0.15 vol% of boron nitride and their: a) visual light transmittance, b) tensile Young's modulus, and c) oxygen permeation rate (OPR) at 0.15 vol% BN. d) A tilted view of a freeze-fractured cross-section of PET–CFE-BN 0.15 vol% showing the protruded boron nitride particles (scale bar: 10 μm). All errors represent the standard deviation (n = 3).

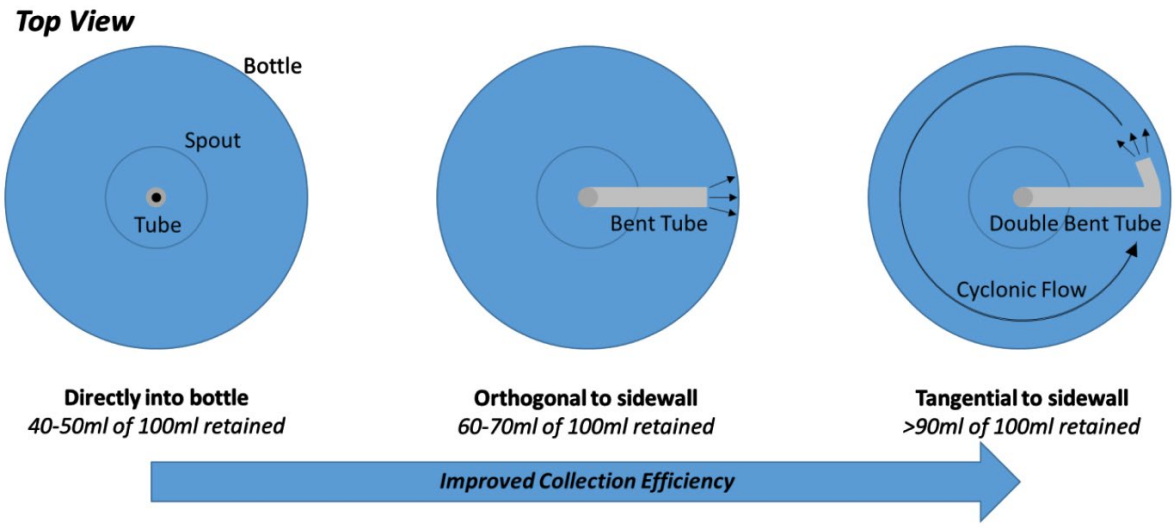

Figure 2-S1. Various collection configuration for 2D nano-materials along with their collection efficiency (defined as the percent solvent retained) used in the compressible flow exfoliation (CFE) process

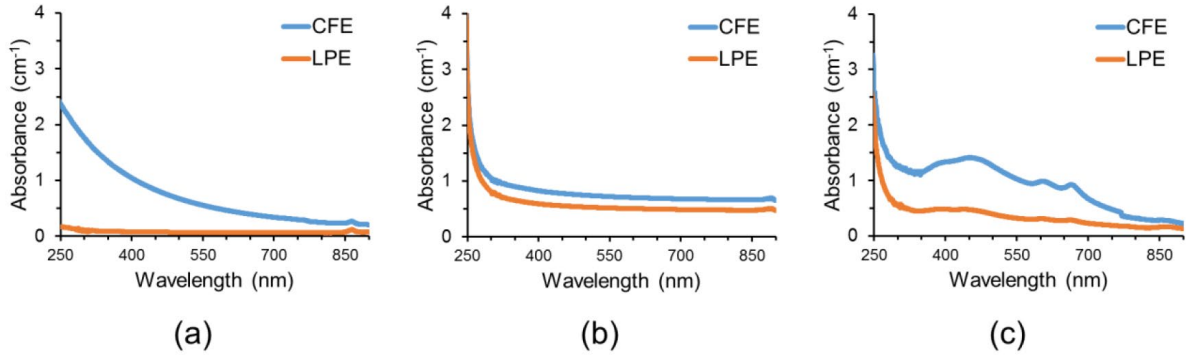

Figure 2-S2. UV-Vis spectra for suspensions of compressible flow (CFE) and liquid phase (LPE – bath sonication) exfoliation of (a) boron nitride, (b) graphite, (c) molybdenum disulfide.

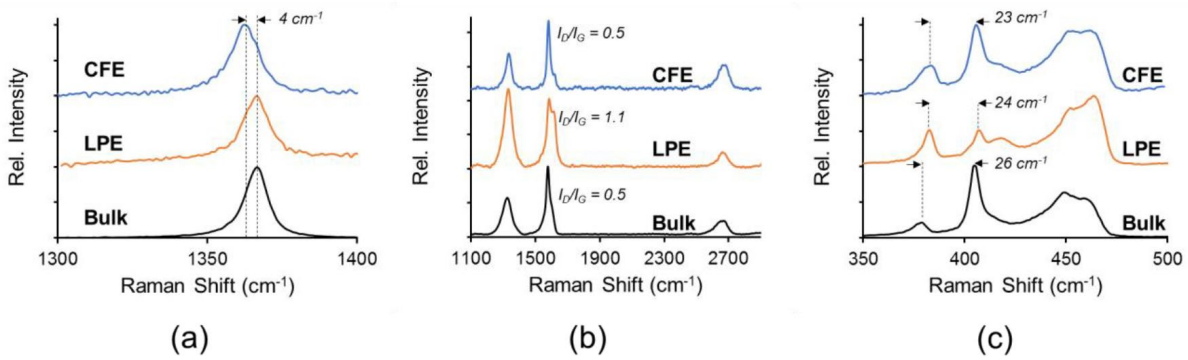

Figure 2-S3. The Raman spectra for suspensions of compressible flow (CFE) and liquid phase (LPE – bath sonication) exfoliation of (a) boron nitride, (b) graphite, (c) molybdenum disulfide.

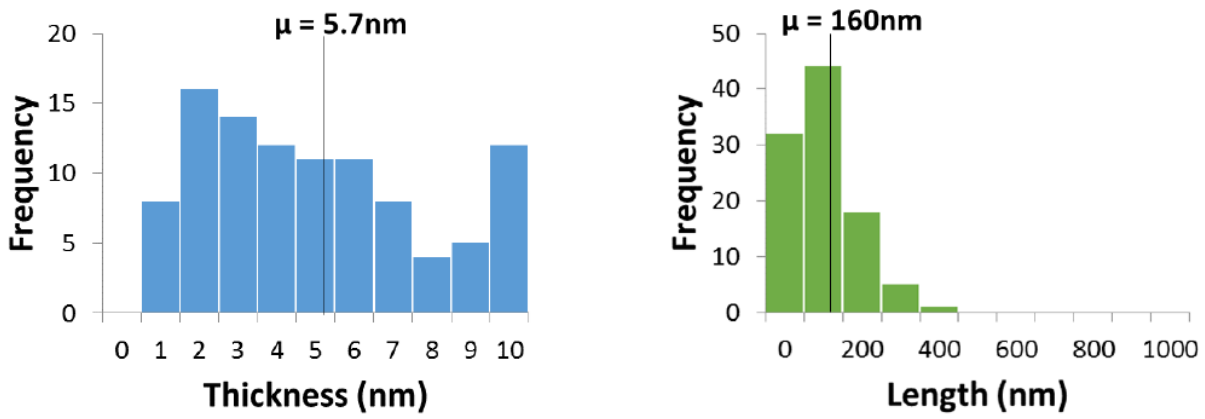

(a)

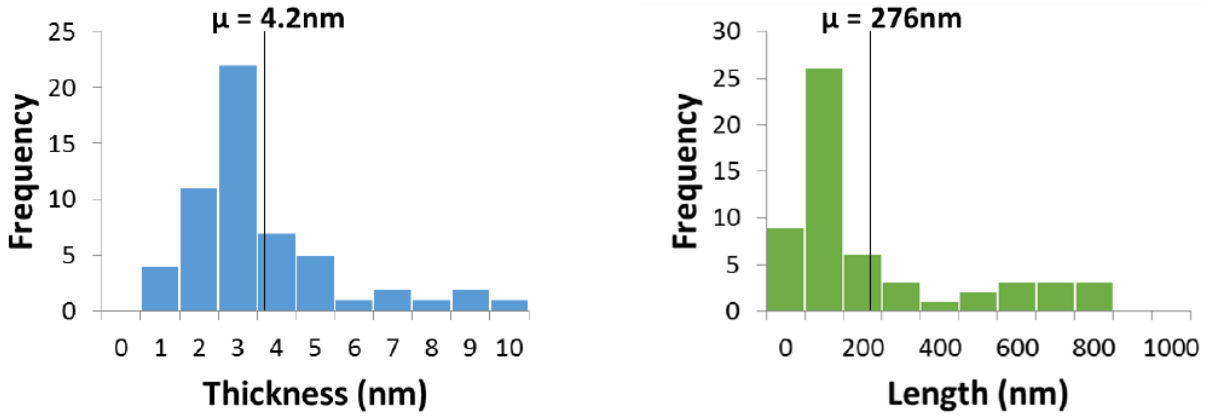

(b)

Figure 2-S4. The AFM histograms showing the thickness (left) and length (right) distributions of CFE processed BN at a He driving pressure of (a) 5.5 MPa, and (b) 10 MPa.

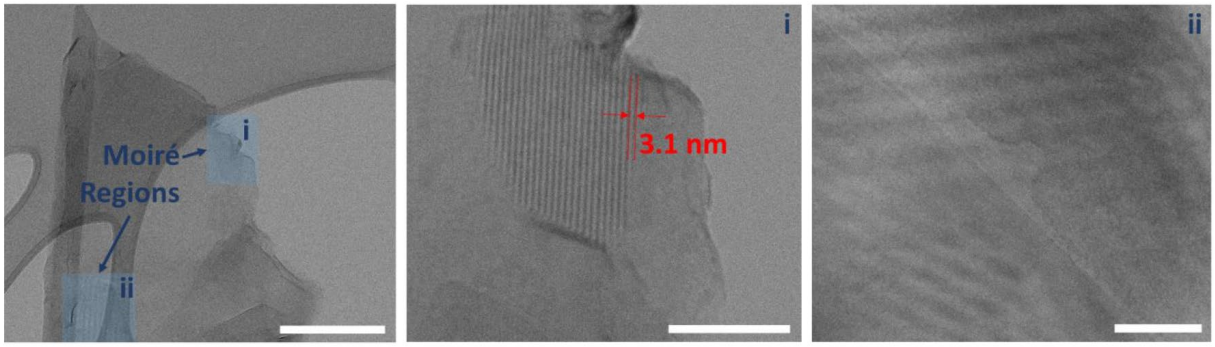

Figure 2-S5. TEM images of (a) a re-stacked BN nanosheet showing two regions, (b) i, and (c) ii, with well established Moiré patterns. Scale bars are (a) 300 nm, (b) 60 nm, and (c) 20 nm.

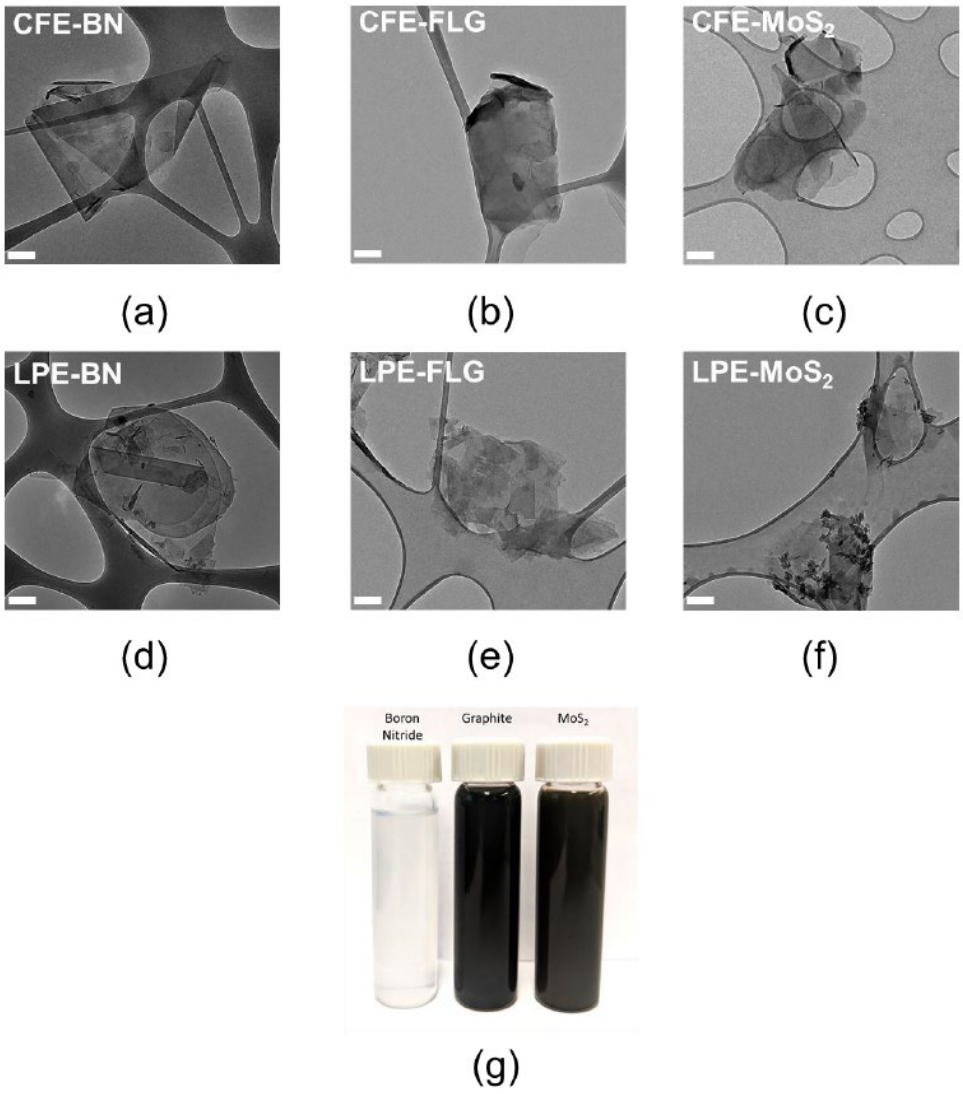

Figure 2-S6. Representative structure of 2D layered materials when viewed in TEM (scale bar: 200 nm). Shown here are CFE processed (a) boron nitride, (b) few-layered graphene, and (c) molybdenum disulfide, as well as their counterpart LPE processed (d) boron nitride, (e) few-layered graphene, and (f) molybdenum disulfide. (g) Solutions of (left to right) boron nitride in IPA, and graphite and molybdenum sulfide in NMP, showing a stable suspension after 6 months of storage.

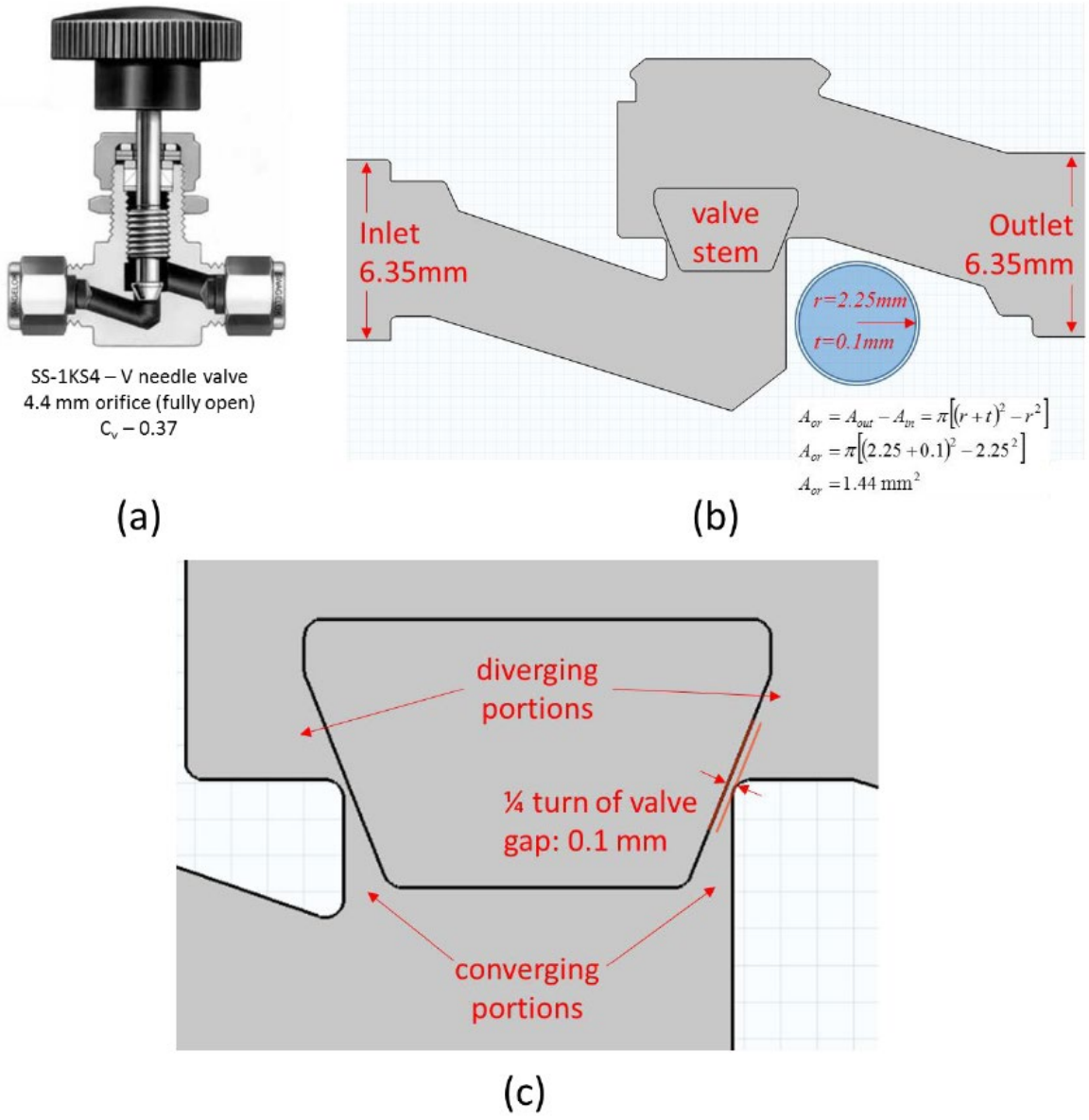

Figure 2-S7. (a) Schematic representation of the needle valve used in the CFE experiments, along with (b) the modeled geometry of the valve stem and flow channel, which at a ¼ turn of the valve creates an annular orifice with a gap of 0.1 mm.

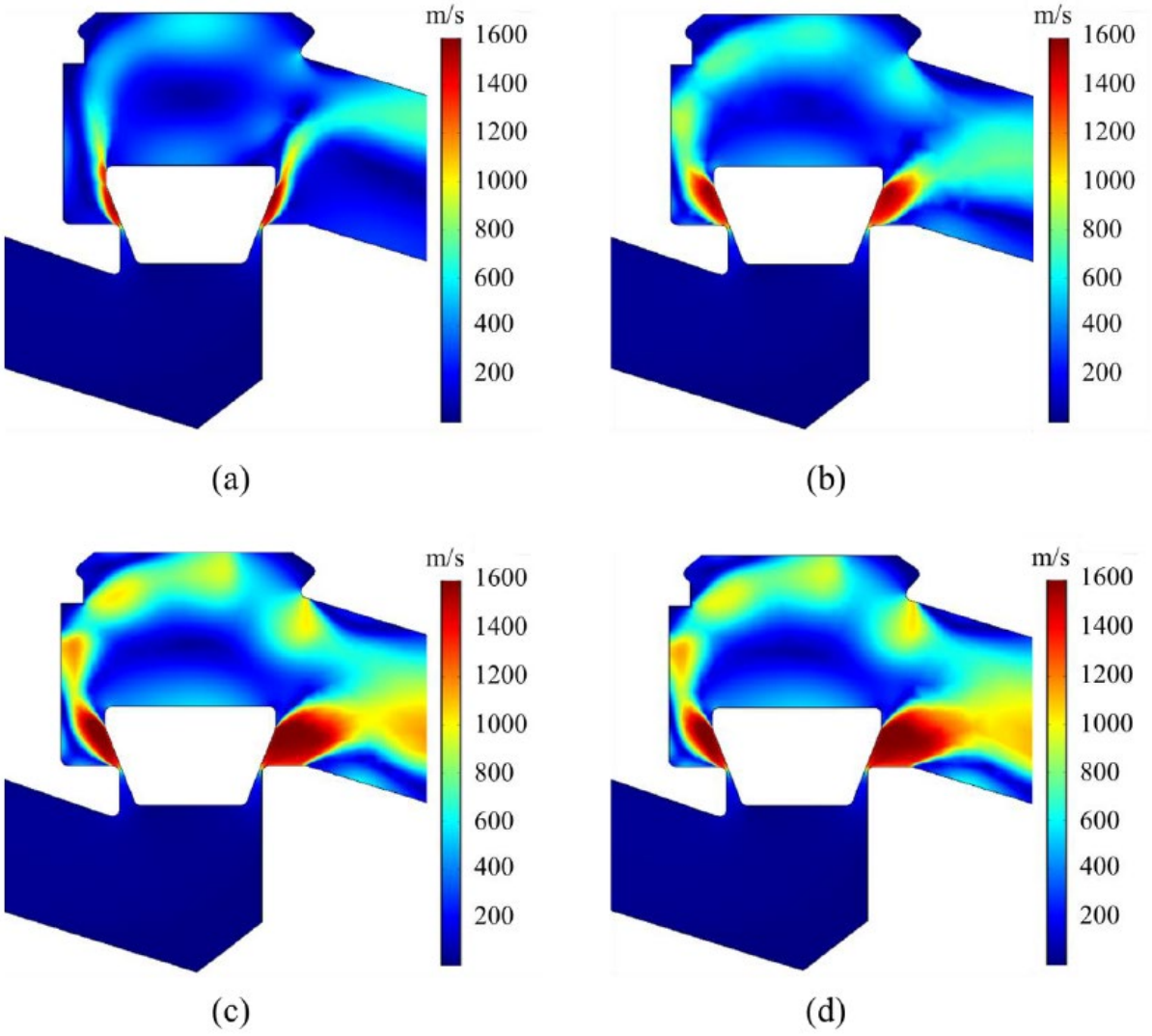

Figure 2-S8. Surface plots depicting the CFD predicted velocities of helium flowing through a partially open needle valve at upstream pressures of (a) 1.4, (b) 2.8, (c) 5.5, and (d) 14 MPa.

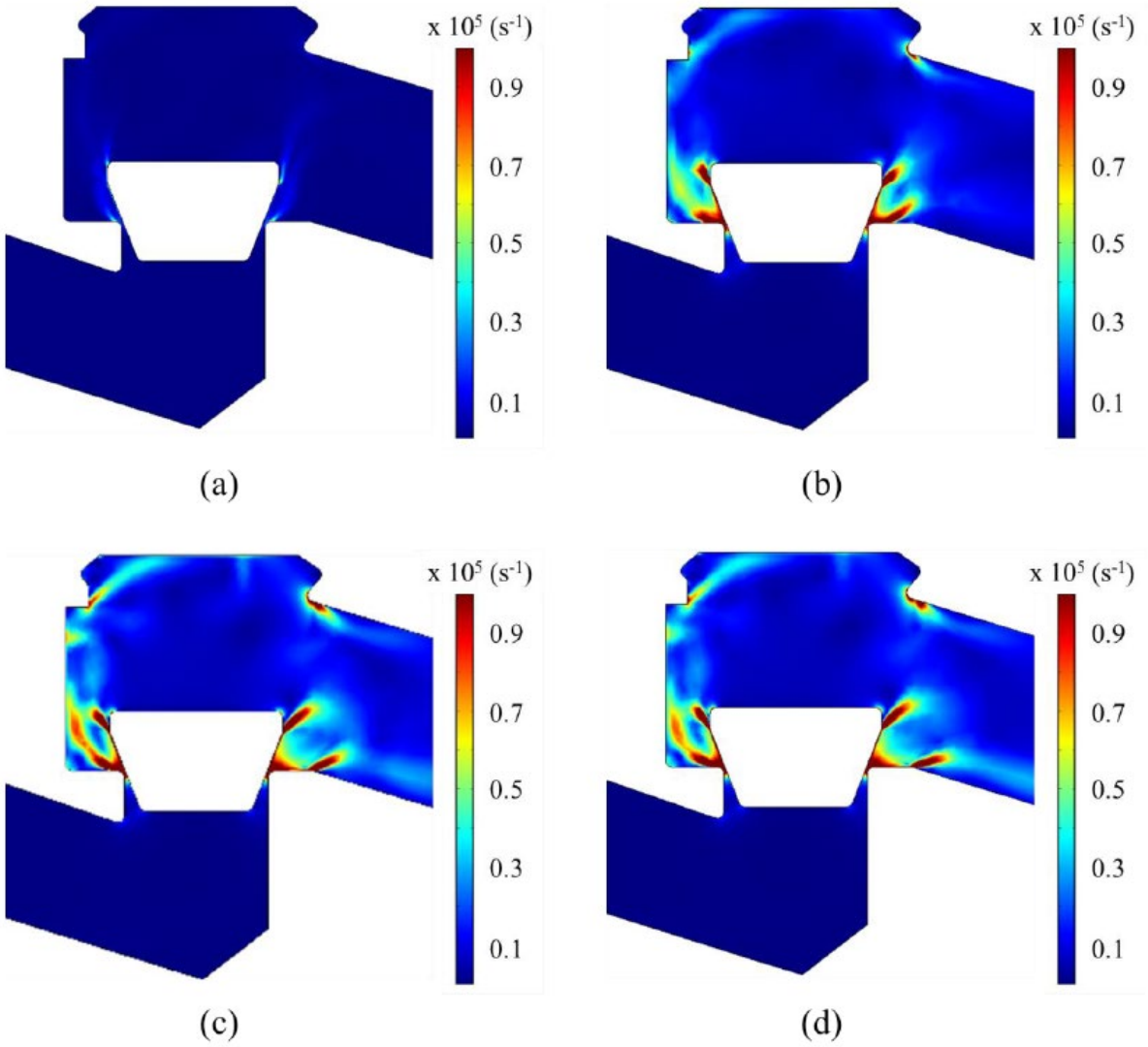

Figure 2-S9. Surface plots depicting the CFD predicted shear rates of helium flowing through a partially open needle valve at upstream pressures of (a) 1.4, (b) 2.8, (c) 5.5, and (d) 14 MPa.

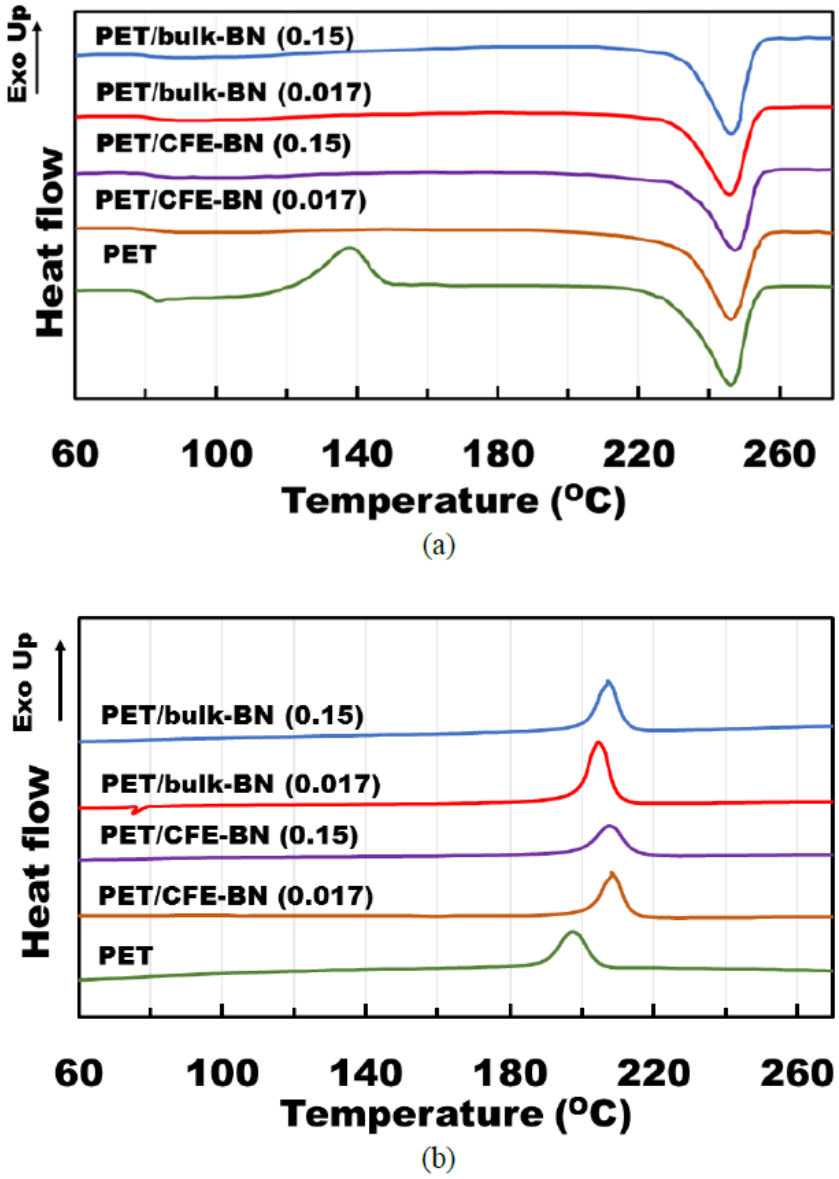

Figure 2-S10. Differential Scanning Calorimetry (DSC) (a) second heating, and (b) first cooling traces for PET containing various types (CFE-BN or bulk-BN) and amounts (0.017 or 0.15 vol%) of BN.

Table 2-S1. Comparison of Boron Nitride Exfoliation Methods with Reported Yields

Starting / Final amounts (concentration or mass)	Yield reported / calculated	Method	Protocol (times)	Surfactant | Chemical process?	Reference
1.0 | 0.06 (mg/mL)	6%	liquid sonication	**1h** sonication → centrifuge @ 500rpm for **90 min** in IPA	No | No	[19]
83.3 | N/A (mg/ml)	9%	low energy liquid ball milling	**15h** low energy ball milling → centrifuge @ 10000rpm for **0.5 h** in benzyl benzoate	No | No	[74]
2.0 | 0.3 (mg/ml)	15%	liquid sonication	**8 h** sonication → centrifuge @ 4000 rpm for **90 min** in methanesulfonic acid (MSA)	No | No	[71]
2.0 | 0.36 (g)	18%	hydroxide-assisted ball milling	**24 h** hydroxide-assisted ball milling → **1 h** sonication → centrifuge @ 2000 rpm for **0.5 h**	No | Yes	[72]
N/A –	85%	urea-assisted, high-energy ball mill processing	1:60 BN:urea ratio – **20 h** high energy ball milling → **1 week** dialysis (urea removal)	No | Yes	[70]
30.0 | 0.18 (mg/ml)	0.6%	sonication with non-ionic surfactants	**5 h** sonnication w. dodecyl ether → centrifuge @ 1500rpm for **20 min**	Yes | No	[73]
2.0 | 0.2 (mg/ml)	10%	compressible flow exfoliation (**This work**)	**2** s (continuous) high pressure helium gas flow → 1400 rpm for **90 min**	No | No	This work

Table 2-S2. Summary of Thermal Transitions of PET and PET Composites from DSC Studies

Sample		Heating (10 °C/min)			Cooling (10 °C/min)	
	vol% BN	T_g (°C)	T_m (°C)	ΔH_m (J/g)	T_c (°C)	ΔH_c (J/g)
PET Control	0	78.5 ± 0.1	245.5 ± 0.2	39.6 ± 1.9	197.6 ± 0.4	42.8 ± 2.1
PET / CFE-BN	0.017	80.1 ± 0.6	245.9 ± 0.1	38.8 ± 2.0	207.7 ± 0.3	41.1 ± 2.2
PET / CFE-BN	0.15	80.5 ± 0.6	245.9 ± 0.9	37.4 ± 2.6	207.1 ± 0.1	37.3 ± 0.7
PET / bulk-BN	0.017	80.9 ± 0.5	245.8 ± 0.3	39.8 ± 2.5	203.4 ± 0.8	38.4 ± 5.9
PET / bulk-BN	0.15	80.6 ± 0.7	246.1 ± 0.3	41.9 ± 1.5	206.3 ± 0.5	42.1 ± 2.2

Table 2-S3. Summary of Optical and Oxygen Permeation Properties of PET and PET Composites

Sample		Haze (%)	Luminous transmittance (%)	OPR (cm^3-cm/m^2-day)
	vol% BN			
PET Control	0	2.8 ± 0.7	94.0 ± 0.2	0.27 ± 0.01
PET / CFE-BN	0.017	5.7 ± 1.1	93.0 ± 0.9	0.28 ± 0.01
PET / CFE-BN	0.15	24.2 ± 2.8	91.2 ± 0.1	0.20 ± 0.01
PET / bulk-BN	0.017	7.5 ± 1.2	91.7 ± 0.1	0.28 ± 0.01
PET / bulk-BN	0.15	36.1 ± 3.0	92.9 ± 1.4	0.37 ± 0.08

Table 2-S4. Summary of Mechanical Properties of PET and PET Composites from Tensile Studies

Sample		Elastic modulus (MPa)	Tensile strength (MPa)	Strain at break (%)
	vol% BN			
PET Control	0	888 ± 23	38 ± 15	256 ± 39
PET / CFE-BN	0.017	888 ± 30	35 ± 3	263± 18
PET / CFE-BN	0.15	1072 ± 13	37 ± 16	247 ± 31
PET / bulk-BN	0.017	872 ± 69	36 ± 11	245 ± 65
PET / bulk-BN	0.15	993 ± 48	37 ± 13	270 ± 40

REFERENCES

(1) Lee, C.; Wei, X.; Kysar, J. W.; Hone, J. *Science* **2008**, *321* (5887), 385–388.

(2) Balandin, A. A.; Ghosh, S.; Bao, W.; Calizo, I.; Teweldebrhan, D.; Miao, F.; Lau, C. N. *Nano Lett.* **2008**, *8* (3), 902–907.

(3) Bolotin, K. I.; Sikes, K. J.; Jiang, Z.; Klima, M.; Fudenberg, G.; Hone, J.; Kim, P.; Stormer, H. L. *Solid State Commun.* **2008**, *146* (9–10), 351–355.

(4) Stankovich, S.; Dikin, D. A.; Dommett, G. H. B.; Kohlhaas, K. M.; Zimney, E. J.; Stach, E. A.; Piner, R. D.; Nguyen, S. B. T.; Ruoff, R. S. *Nature* **2006**, *442* (7100), 282–286.

(5) Xu, Y.; Lin, Z.; Zhong, X.; Huang, X.; Weiss, N. O.; Huang, Y.; Duan, X. *Nat. Commun.* **2014**, *5* (1), 1–8.

(6) Zhang, Y.; Tang, T. T.; Girit, C.; Hao, Z.; Martin, M. C.; Zettl, A.; Crommie, M. F.; Shen, Y. R.; Wang, F. *Nature* **2009**, *459* (7248), 820–823.

(7) Trauzettel, B.; Bulaev, D. V.; Loss, D.; Burkard, G. *Nat. Phys.* **2007**, *3* (3), 192–196.

(8) Kane, C. L.; Mele, E. J. *Phys. Rev. Lett.* **2005**, *95* (22), 226801.

(9) Nagashio, K.; Nishimura, T.; Kita, K.; Toriumi, A. *Appl. Phys. Express* **2009**, *2* (2), 025003.

(10) Li, H.; Wu, J.; Yin, Z.; Zhang, H. *Acc. Chem. Res.* **2014**, *47* (4), 1067–1075.

(11) Tour, J. M. *Chem. Mater.* **2014**, *26* (1), 163–171.

(12) Huang, X.; Zeng, Z.; Zhang, H. *Chem. Soc. Rev.* **2013**, *42* (5), 1934–1946.

(13) Viculis, L. H.; Mack, J. J.; Kaner, R. B. *Science* **2003**, *299* (5611), 1361.

(14) Hernandez, Y.; Nicolosi, V.; Lotya, M.; Blighe, F. M.; Sun, Z.; De, S.; McGovern, I. T.; Holland, B.; Byrne, M.; Gun'ko, Y. K.; Boland, J. J.; Niraj, P.; Duesberg, G.; Krishnamurthy, S.; Goodhue, R.; Hutchison, J.; Scardaci, V.; Ferrari, A. C.; Coleman, J. N. *Nat. Nanotechnol.* **2008**, *3* (9), 563–568.

(15) Novoselov, K. S.; Geim, A. K.; Morozov, S. V; Jiang, D.; Zhang, Y.; Dubonos, S. V.; Grigorieva, I. V; Firsov, A. A. *Science* **2004**, *306* (5696), 666–669.

(16) Zhao, W.; Fang, M.; Wu, F.; Wu, H.; Wang, L.; Chen, G. *J. Mater. Chem.* **2010**, *20* (28), 5817–5819.

(17) Abdelkader, A. M.; Cooper, A. J.; Dryfe, R. A. W.; Kinloch, I. A. *Nanoscale* **2015**, *7* (16), 6944–6956.

(18) Stankovich, S.; Dikin, D. A.; Piner, R. D.; Kohlhaas, K. A.; Kleinhammes, A.; Jia, Y.; Wu, Y.; Nguyen, S. B. T.; Ruoff, R. S. *Carbon* **2007**, *45* (7), 1558–1565.

(19) Coleman, J. N.; Lotya, M.; O'Neill, A.; Bergin, S. D.; King, P. J.; Khan, U.; Young, K.; Gaucher, A.; De, S.; Smith, R. J.; Shvets, I. V.; Arora, S. K.; Stanton, G.; Kim, H. Y.; Lee, K.; Kim, G. T.; Duesberg, G. S.; Hallam, T.; Boland, J. J.; Wang, J. J.; Donegan, J. F.; Grunlan, J. C.; Moriarty, G.; Shmeliov, A.; Nicholls, R. J.; Perkins, J. M.; Grieveson, E. M.; Theuwissen, K.; McComb, D. W.; Nellist, P. D.; Nicolosi, V. *Science* **2011**, *331* (6017), 568–571.

(20) Lotya, M.; King, P. J.; Khan, U.; De, S.; Coleman, J. N. *ACS Nano* **2010**, *4* (6), 3155–3162.

(21) Paton, K. R.; Varrla, E.; Backes, C.; Smith, R. J.; Khan, U.; O'Neill, A.; Boland, C.;

Lotya, M.; Istrate, O. M.; King, P.; Higgins, T.; Barwich, S.; May, P.; Puczkarski, P.; Ahmed, I.; Moebius, M.; Pettersson, H.; Long, E.; Coelho, J.; O'Brien, S. E.; McGuire, E. K.; Sanchez, B. M.; Duesberg, G. S.; McEvoy, N.; Pennycook, T. J.; Downing, C.; Crossley, A.; Nicolosi, V.; Coleman, J. N. *Nat. Mater.* **2014**, *13* (6), 624–630.

(22) Varrla, E.; Backes, C.; Paton, K. R.; Harvey, A.; Gholamvand, Z.; McCauley, J.; Coleman, J. N. *Chem. Mater.* **2015**, *27* (3), 1129–1139.

(23) Varrla, E.; Paton, K. R.; Backes, C.; Harvey, A.; Smith, R. J.; McCauley, J.; Coleman, J. N. *Nanoscale* **2014**, *6* (20), 11810–11819.

(24) Majee, S.; Song, M.; Zhang, S. L.; Zhang, Z. Bin. *Carbon* **2016**, *102*, 51–57.

(25) Yi, M.; Shen, Z. *Carbon* **2014**, *78*, 622–626.

(26) Arao, Y.; Mizuno, Y.; Araki, K.; Kubouchi, M. *Carbon* **2016**, *102*, 330–338.

(27) Karagiannidis, P. G.; Hodge, S. A.; Lombardi, L.; Tomarchio, F.; Decorde, N.; Milana, S.; Goykhman, I.; Su, Y.; Mesite, S. V.; Johnstone, D. N.; Leary, R. K.; Midgley, P. A.; Pugno, N. M.; Torrisi, F.; Ferrari, A. C. *ACS Nano* **2017**, *11* (3), 2742–2755.

(28) Coles, D. *J. Fluid Mech.* **1965**, *21* (3), 385–425.

(29) Gollub, J. P.; Swinney, H. L. *Phys. Rev. Lett.* **1975**, *68* (4), 927–930.

(30) Joseph, D. D. *J. Fluid Mech.* **1998**, *366*, 367–378.

(31) Furukawa, A.; Tanaka, H. *Nature* **2006**, *443* (7110), 434–438.

(32) Pu, N. W.; Wang, C. A.; Sung, Y.; Liu, Y. M.; Ger, M. Der. *Mater. Lett.* **2009**, *63* (23), 1987–1989.

(33) Xu, S.; Xu, Q.; Wang, N.; Chen, Z.; Tian, Q.; Yang, H.; Wang, K. *Chem. Mater.* **2015**, *27* (9), 3262–3272.

(34) Gao, Y.; Shi, W.; Wang, W.; Wang, Y.; Zhao, Y.; Lei, Z.; Miao, R. *Ind. Eng. Chem. Res.* **2014**, *53* (7), 2839–2845.

(35) Li, L.; Xu, J.; Li, G.; Jia, X.; Li, Y.; Yang, F.; Zhang, L.; Xu, C.; Gao, J.; Liu, Y.; Fang, Z. *Chem. Eng. J.* **2016**, *284*, 78–84.

(36) Gao, H.; Hu, G. *RSC Adv.* **2016**, *6* (12), 10132–10143.

(37) Jang, B. Z.; Zhamu, A.; Guo, J. USPTO Patent US7785492B1, 2010.

(38) Levi, M. D.; Aurbach, D. *J. Phys. Chem. B* **1997**, *101* (23), 4641–4647.

(39) Wang, W.; Wang, Y.; Gao, Y.; Zhao, Y. *J. Supercrit. Fluids* **2014**, *85*, 95–101.

(40) Sim, H. S.; Kim, T. A.; Lee, K. H.; Park, M. *Mater. Lett.* **2012**, *89*, 343–346.

(41) Mehio, N.; Dai, S.; Jiang, D. E. *J. Phys. Chem. A* **2014**, *118* (6), 1150–1154.

(42) Bacon, G. E. *Acta Crystallogr.* **1951**, *4* (6), 558–561.

(43) Walker, P. L.; McKinstry, H. A.; Wright, C. C. *Ind. Eng. Chem.* **1953**, *45* (8), 1711–1715.

(44) Li, D.; Müller, M. B.; Gilje, S.; Kaner, R. B.; Wallace, G. G. *Nat. Nanotechnol.* **2008**, *3* (2), 101–105.

(45) Lotya, M.; Hernandez, Y.; King, P. J.; Smith, R. J.; Nicolosi, V.; Karlsson, L. S.; Blighe, F. M.; De, S.; Wang, Z.; McGovern, I. T.; Duesberg, G. S.; Coleman, J. N. *J. Am. Chem. Soc.* **2009**, *131* (10), 3611–3620.

(46) Gorbachev, R. V.; Riaz, I.; Nair, R. R.; Jalil, R.; Britnell, L.; Belle, B. D.; Hill, E. W.;

Novoselov, K. S.; Watanabe, K.; Taniguchi, T.; Geim, A. K.; Blake, P. *Small* **2011**, *7* (4), 465–468.

(47) Ferrari, A. C.; Meyer, J. C.; Scardaci, V.; Casiraghi, C.; Lazzeri, M.; Mauri, F.; Piscanec, S.; Jiang, D.; Novoselov, K. S.; Roth, S.; Geim, A. K. *Phys. Rev. Lett.* **2006**, *97* (18), 187401.

(48) Ferrari, A. C.; Basko, D. M. *Nat. Nanotechnol.* **2013**, *8* (4), 235–246.

(49) Hao, Y.; Wang, Y.; Wang, L.; Ni, Z.; Wang, Z.; Wang, R.; Koo, C. K.; Shen, Z.; Thong, J. T. L. *Small* **2010**, *6* (2), 195–200.

(50) Lee, C.; Yan, H.; Brus, L. E.; Heinz, T. F.; Hone, J.; Ryu, S. *ACS Nano* **2010**, *4* (5), 2695–2700.

(51) Nguyen, E. P.; Carey, B. J.; Daeneke, T.; Ou, J. Z.; Latham, K.; Zhuiykov, S.; Kalantar-Zadeh, K. *Chem. Mater.* **2015**, *27* (1), 53–59.

(52) Li, H.; Zhang, Q.; Yap, C. C. R.; Tay, B. K.; Edwin, T. H. T.; Olivier, A.; Baillargeat, D. *Adv. Funct. Mater.* **2012**, *22* (7), 1385–1390.

(53) Shi, Y.; Hamsen, C.; Jia, X.; Kim, K. K.; Reina, A.; Hofmann, M.; Hsu, A. L.; Zhang, K.; Li, H.; Juang, Z. Y.; Dresselhaus, M. S.; Li, L. J.; Kong, J. *Nano Lett.* **2010**, *10* (10), 4134–4139.

(54) Liao, Y.; Cao, W.; Connell, J. W.; Chen, Z.; Lin, Y. *Sci. Rep.* **2016**, *6*, 26084.

(55) Han, W. Q.; Wu, L.; Zhu, Y.; Watanabe, K.; Taniguchi, T. *Appl. Phys. Lett.* **2008**, *93* (22), 223103.

(56) Quintana, M.; Grzelczak, M.; Spyrou, K.; Kooi, B.; Bals, S.; Tendeloo, G. Van; Rudolf,

P.; Prato, M. *Chem. Commun.* **2012**, *48* (100), 12159–12161.

(57) Khan, U.; O'Neill, A.; Lotya, M.; De, S.; Coleman, J. N. *Small* **2010**, *6* (7), 864–871.

(58) Kouroupis-Agalou, K.; Liscio, A.; Treossi, E.; Ortolani, L.; Morandi, V.; Pugno, N. M.; Palermo, V. *Nanoscale* **2014**, *6* (11), 5926–5933.

(59) Muscuso, L.; Cravanzola, S.; Cesano, F.; Scarano, D.; Zecchina, A. *J. Phys. Chem. C* **2015**, *119* (7), 3791–3801.

(60) Munson, B. R.; Young, D. F.; Okiishi, T. H. *Fundam. Fluid Mechanics*; John Wiley and Sons: Hoboken, NJ, USA, 1990.

(61) Unalan, I. U.; Cerri, G.; Marcuzzo, E.; Cozzolino, C. A.; Farris, S. *RSC Adv.* **2014**, *4* (56), 29393–29428.

(62) Frounchi, M.; Dourbash, A. *Macromol. Mater. Eng.* **2009**, *294* (1), 68–74.

(63) Wang, K. H.; Choi, M. H.; Koo, C. M.; Choi, Y. S.; Chung, I. J. *Polymer* **2001**, *42* (24), 9819–9826.

(64) Xie, S.; Istrate, O. M.; May, P.; Barwich, S.; Bell, A. P.; Khan, U.; Coleman, J. N. *Nanoscale* **2015**, *7* (10), 4443–4450.

(65) Priolo, M. A.; Gamboa, D.; Holder, K. M.; Grunlan, J. C. *Nano Lett.* **2010**, *10* (12), 4970–4974.

(66) Calcagno, C. I. W.; Mariani, C. M.; Teixeira, S. R.; Mauler, R. S. *Polymer* **2007**, *48* (4), 966–974.

(67) Zekriardehani, S.; Jabarin, S. A.; Gidley, D. R.; Coleman, M. R. *Macromolecules* **2017**,

50 (7), 2845–2855.

(68) Backes, C.; Higgins, T. M.; Kelly, A.; Boland, C.; Harvey, A.; Hanlon, D.; Coleman, J. N. *Chem. Mater.* **2017**, *29* (1), 243–255.

(69) Abdellatief, A.; Welt, B. A. *Packag. Technol. Sci.* **2013**, *29*, 281–288.

(70) Lei, W.; Mochalin, V. N.; Liu, D.; Qin, S.; Gogotsi, Y.; Chen, Y. *Nat. Commun.* **2015**, *6* (1), 1–8.

(71) Wang, Y.; Shi, Z.; Yin, J. *J. Mater. Chem.* **2011**, *21* (30), 11371–11377.

(72) Lee, D.; Lee, B.; Park, K. H.; Ryu, H. J.; Jeon, S.; Hong, S. H. *Nano Lett.* **2015**, *15* (2), 1238–1244.

(73) Guardia, L.; Paredes, J. I.; Rozada, R.; Villar-Rodil, S.; Martínez-Alonso, A.; Tascón, J. M. D. *RSC Adv.* **2014**, *4* (27), 14115–14127.

(74) Li, L. H.; Chen, Y.; Behan, G.; Zhang, H.; Petravic, M.; Glushenkov, A. M. *J. Mater. Chem.* **2011**, *21* (32), 11862–11866.

CHAPTER 3. CATALYTIC EFFECTS OF ANILINE POLYMERIZATION ASSISTED BY OLIGOMERS

"Reprinted (adapted) with permission from (Lin, C. W.; Mak, W. H.; Chen, D.; Wang, H.; Aguilar, S.; Kaner, R. B. Catalytic Effects of Aniline Polymerization Assisted by Oligomers. *ACS Catalysis*, **2019**, *9*(8), 6596-6606.)

ABSTRACT

Polyaniline was first confirmed as a dark green precipitate on an electrode during the electrochemical polymerization of aniline in 1862. Since then, scientists have been studying the kinetics and growth mechanisms of polyaniline through the electrochemical approach. Studies have shown that p-phenylenediamine, p-aminodiphenylamine, and other aromatic small molecules may serve as initiators for accelerating the polymerization reaction due to the autocatalytic effect of polyaniline. However, little research has been focused on the catalytic effects of introducing oligoanilines. In this paper, quantitative rate constants for the electrochemical polymerization of aniline in both HCl and acetonitrile/HCl solutions with 0.5 mol % of added oligoanilines including diphenylamine, N-phenyl-p-phenylenediamine, 1,4-phenylenediamine, N,N′-diphenyl-1,4-phenylenediamine, 4,4′-diaminodiphenylamine, and tetraaniline in both emeraldine and leucoemeraldine states are reported. Among all the rate constants, N-phenyl-p-phenylenediamine, 1,4-phenylenediamine, and 4,4′-diaminodiphenylamine are shown to be the most effective catalysts for aniline polymerization. Tetraaniline is likely the intermediate species where the polymerization process starts to slow down, while diphenylamine and N,N′-diphenyl-1,4-phenylenediamine decelerate the reaction. Additionally, adding in oligothiophenes is confirmed to reduce the reaction rate. It is also shown that the rate constants measured are consistent with two other methods: (1) monitoring the open-

circuit potential and (2) measuring the temperature of the solution. These methods were used previously to qualitatively compare the speed of the polymerization reactions. Additionally, the existence of both agglomerated and nanofibrillar polymer morphologies for reactions with slow rate constants is revealed.

INTRODUCTION

Polyaniline, one of the most studied conducting polymers, was first discovered by Ferdinand Runge as a blue dye from coal tar in 1834.[1,2] Years later, an English chemist, Henry Letheby, conducted the first electrochemical reaction of aniline and confirmed that the dark green precipitate on the electrode as polyaniline.[2,3] Although some research was carried out on polyaniline during the early twentieth century, it was not until the 1970s when MacDiarmid, Heeger, and Shirakawa's discovery of its electrical conducting properties did extensive research on it burgeon.[4–7] To investigate the growth mechanism and kinetics of the aniline polymerization process, electrochemical polymerization in aqueous inorganic acid solutions has been widely conducted.[8–10] This work indicated that the anodic current is directly proportional to the amount of the dark green precipitate deposited on the electrode.[11–14] Hence, scientists were able to quantify the rate of aniline polymerization, which has been found to be an autocatalytic reaction.[15–18]

A reaction can be considered as autocatalytic when one of the products is either a catalyst or reactant; therefore, the rate of the whole reaction should be nonlinear.[19] In 1962, Mohilner et al. reported that the electrochemical polymerization rate of p-aminodiphenylamine (aniline dimer) is faster than that of aniline monomer. This indicates that forming aniline dimers should be the rate-determining step during aniline polymerization, while also implying autocatalysis for the polymerization of aniline.[11] Later in 1990, Wei et al. first introduced small amounts of aromatic

additives including p-phenylenediamine, benzidine, p-aminodiphenylamine, N,N′-diphenylhydrazine, p-phenoxyaniline, hydroquinone, and N,N-diphenylamine into the aniline polymerization system to avoid the slow step, i.e., the formation of aniline dimer. By fitting the variations of the anodic peak current up to 16 mA, rate constants for each additive under various concentrations were able to be quantified.[12] Other ways to qualitatively evaluate the rate of aniline polymerization reported by Wei et al. include monitoring the open-circuit potential (OCP) and the temperature versus time during the chemical oxidation reaction of aniline by adding ammonium persulfate. The time duration for the chemical potential and the temperature to reach their maximum readings due to the consumption of ammonium persulfate was found to be inversely proportional to the rate of polymerization.[20]

However, kinetic studies on incorporating additives into the aniline polymerization system have dwindled as a great deal of research has turned to the field of morphology, because of the discovery of nanofibers in 2003.[21,22] In 2004, Li and Wang reported enhancing chirality of polyaniline nanofibers with the assistance of aniline oligomers.[23] Tran et al. thereafter demonstrated the intimate relationship between the rate of polymerization and the nanofibrillar morphology and expanded the concept to different conjugated systems including polypyrrole and polythiophene.[24] However, no research to our knowledge has yet discussed the kinetics of introducing oligoanilines with longer chains into the aniline polymerization reaction. As the oxidizing potential is known to be lower for more units of oligoanilines,[25–28] the catalytic effect should not only take the oxidizing potential, i.e., the ease of generating radicals, into consideration, but also factor in the probability of radical transfer.[29]

In this study, we performed thorough electrochemical polymerizations of aniline in the presence of a variety of linear aniline oligomers in both HCl and acetonitrile/HCl solutions. By fitting to

the change of anodic peak current over time with higher-order polynomial equations, catalytic effects of each additive under different ranges of potential sweep were quantified. Additionally, variations of temperature and the open-circuit potential (OCP) of solutions over time are compared to the quantified numbers of rate constant, demonstrating the consistency and practical feasibility of these two methods for measuring reaction rates. Furthermore, the kinetics of placing thiophene oligomers into the aniline system were investigated. Insights associated with the catalytic phenomena and polymer morphologies, along with the characteristics of additives, are also addressed in the following sections.

RESULTS AND DISCUSSIONS

Aniline Polymerization in HCl Solutions

To meticulously investigate the influence of additives, the following oligoanilines were used: aniline, N,N-diphenylamine, p-aminodiphenylamine, p-phenylenediamine, N,N′-diphenyl-1,4-phenylenediamine, 4,4′-diaminodiphenylamine, and tetraaniline in both emeraldine and leucoemeraldine states, denoted as 1A, 1′A, 2A, 2′A, 2″A, 3′A, 4A(EB), and 4A(LEB), respectively, where the first number stands for the numbers of nitrogens, the single prime the amino-ended molecules, and the double prime the phenyl-capped molecules (**Figure 3-1**). Electrochemical polymerization conditions similar to a previous report, i.e., 0.2 M aniline monomer and 1.0 mM additives in a 30 mL 1.0 M HCl solution, were carried out for comparison. Potential sweeps ranging from −0.2 to 0.8, 0.9, and 1.0 V versus Ag/AgCl were tested at a scan rate of 25 mV s^{-1}.[12]

In a typical cyclic voltammetry of the electrochemical polymerization of aniline, it is known that there are two oxidizing peaks and two reducing peaks, which correspond to the transitions from

the reduced state (leucoemeraldine) to emeraldine, and emeraldine to the oxidized state (pernigraniline), and vice versa.[9] In this study, the first anodic peak current was targeted since previous reports confirmed its linear relationship with the amount of polyaniline deposited on the platinum working-electrode during the electrochemical polymerizations of aniline. The first anodic (oxidizing) peak was reported to be located at ~0.17 V versus the saturated calomel electrode (SCE). In our work, the first anodic peak is located at ~0.215 V against the Ag/AgCl reference electrode.[9,30] In **Figure 3-2a**, the first anodic peak appears at ~0.215 V versus Ag/AgCl and gradually increases with more scans as the potential is swept from −0.2 to 0.8 V. Likewise, the cyclic voltammetry with a potential sweep range from −0.2 to 0.9 V (**Figure 3-2b**) shows an increasing anodic peak current with increasing numbers of scans. However, the first anodic peak increases as the oxidizing potentials shift to higher voltages. This phenomenon is known because of the thick layer of the polyaniline film deposited on the electrode.[12] As the polyaniline layer grows thicker on the electrode, the resistance, i.e., the *iR* drop, of the polyaniline film increases; hence, higher voltages for oxidations and lower potentials for reductions are needed for further precipitation. By observing the anodic peak current readings of the last (40th) scan in both **Figure 3-2a** and **Figure 3-2b**, the extremely low current for **Figure 3-2a** indicates that polyaniline does not tend to polymerize under the potential range from −0.2 to 0.8 V (against Ag/AgCl), which is in agreement with previous studies; therefore, no *iR* drop nor shifts in potential are observed. Experimentally, little precipitate was found on the electrode with the potential sweep ranging from −0.2 to 0.8 V, while thick cakes of deposition were observed for electrodes operated between −0.2 to 0.9 V and −0.2 to 1.0 V. Note that electrochemically polymerized polyaniline under high applied voltages, i.e., overoxidation, is believed to cause degradation, cross-linking, the appearance of additional functional groups, and the formation of

benzoquinone.[12,31,32] These changes may also result in a decrease in conductivity that leads to the shift of the anodic peak.

According to reports published around 1990, the rate of aniline electrochemical polymerization can be expressed as

$$R = k[M]i^n \qquad (1)$$

where i is the anodic peak current at ~0.17 V; R can be obtained from the derivatives of the anodic peak current versus scan, i.e., di/dt; k is the rate constant; [M] is the concentration of monomer; and n was determined empirically as 0.5.[12,18] As cyclic voltammetry curves of aniline electrochemical polymerization with and without oligoanilines were recorded under potential sweeps from −0.2 to 0.8 V (**Figure 3-S1**), −0.2 to 0.9 V (**Figure 3-S2**), and −0.2 to 1.0 V (**Figure 3-S3**), the relationships between the anodic peak current, i, and the number of scans can be plotted and fitted with higher-order polynomial equations to have every coefficient of determination greater than 0.999 (**Figures 3-S4–S6**). **Figure 3-3a** shows plots of i against the number of scans, for aniline electrochemical polymerization with and without aniline oligomers, with the potential swept from −0.2 to 0.9 V. By simply taking derivatives of the equations fitted in **Figure 3-S5**, the rate of polymerization, *R*, can be plotted against the number of scans (**Figure 3-3b**) and the anodic peak current (**Figure 3-3c**). It is evident that each polymerization reaction reaches its own maximum rate at different numbers of scans and anodic peak current, indicating distinct catalytic effects caused by the additive. Note that all curves in **Figure 3-3a** are S-shaped, which is symbolic of typical autocatalytic processes. As it is known that the polymerization process of polyaniline is autocatalytic,[15–18] it is expected that oligomers-assisted polymerizations are autocatalytic as well. Since decelerations are likely due to the thick layers of polyaniline formed on the electrode, it would be much more meaningful for us to focus on data points before

reaching the polymerization rate maxima. Note that all reactions reach their rate maximum at anodic peak currents equal to or greater than ∼50 mA, which is consistent with the range of anodic peak currents reported previously.[12]

By truncating the parts after the polymerization rate maxima, the anodic peak currents of aniline polymerization with the sweep range between −0.2 and 0.9 V against the number of scans are plotted in **Figure 3-4a**. Intuitively, on the basis of the plot of rate versus number of scans (**Figure 3-4b**), the rate of polymerization can be considered to follow the order 3′A > 2A ≈ 2′A > 4A(LEB) > 4A(EB) ≈ 1A > 1″A > 2″A. In **Figure 3-4c**, we found that the plots of rate versus the anodic peak current fit well with eq 1 as multiples of k and [M] alter the amplitude of those curves, showing different levels of catalysis. Similar plots for the potential sweep range between −0.2 to 0.8 V and −0.2 to 1.0 V can be found in **Figures 3-S7** and **3-S8**. To carefully examine the rate constant, plots of rate versus the square root of the anodic peak current are plotted. On the basis of eq 1, the slope of the plot should be a multiple of the rate constant, k, and the concentration of aniline, [M]. As shown in **Figure 3-5**, two slopes were fitted for $i < 9$ mA and $i > 9$ mA for better fittings, indicating that two mechanisms likely exist for the electrochemical polymerization of aniline with the potential sweep range from −0.2 to 0.9 V. However, only a single polymerization kinetics seems to apply on the basis of the fitting of one certain slope for each curve in the graphs of rate versus the anodic peak current for −0.2 to 0.8 V and −0.2 to 1.0 V. The reason may be attributed to the electrochemical polymerization processes that tend not to occur when the potential is swept between −0.2 and 0.8 V. Hence, the anodic peak readings are small (**Figure 3-S9**). On the other hand, applying a high voltage, e.g., 1.0 V, may shorten the time duration to reach high values of anodic current (**Figure 3-S10**). Therefore, both −0.2 to 0.8 V and −0.2 to 1.0 V do not have apparent transitions of slopes.

The rate constants, with the unit of $mA^{1/2}\ M^{-1}\ scan^{-1}$, are plotted in **Figure 3-6**. The rate constants reveal that the electrochemical polymerization of aniline does not tend to form polyaniline when the potential applied is less than 0.8 V against Ag/AgCl as the rate constants at 0.8 V are significantly lower than that at 0.9 and 1.0 V. A higher potential directly leads to a higher rate constant, except for 1″A where the rate constant for 1.0 V is even lower than that for 0.9 V. On the basis of the rate constants at 0.8 V, it is evident that 2A, 2′A, 3′A, 4A(EB), and 4A(LEB) can catalyze the polymerization as the second rate constant, k_2, from −0.2 to 0.9 V and the rate constant, k_2, from −0.2 to 1.0 V; only 2A, 2′A, and 3′A show conspicuous enhancements. Both 4A(EB) and 4A(LEB) show significantly higher rate constants for 0.8 V compared to the system without additives, which may be attributed to the conductive nature of tetraaniline itself,[33,34] but no apparent improvement is observed for 0.9 and 1.0 V compared to the polymerization of aniline without additives. Therefore, we speculate that the polymerization reaction accelerates before the formation of tetramer, which might be the intermediate step during aniline polymerization where the rate begins to decline. It is noteworthy that the first rate constant, k_1, at 0.9 V is much greater than the second rate constant, k_2, for 2A, 2′A, and 3′A, indicating that the catalytic effect initiates a sharp acceleration at the very beginning of the polymerization reaction, followed by a comparatively slower mechanism.

All rate constants and oxidation potentials for each material are listed in **Table 3-1**. The general order of the polymerization rate may be concluded as follow: 3′A > 2′A > 2A > 4A(LEB) ≈ 4A(EB) ≈ no additives > 2″A > 1″A. This order is consistent with what Wei et al. reported where only 2′A, 2A, and 1′A were investigated.[12] To increase the polymerization rate of aniline, Wei et al. concluded that the additives must have a lower oxidation potential than aniline, and at least one sterically accessible amino group should be present. The relatively high oxidation potential

for 1″A and its phenyl-capped structure should therefore cause extremely low rate constants. However, 2″A with a phenyl-capped structure seems not to decelerate the polymerization reaction very much. The reason may be because of the low dispersity of 2″A in a 1.0 M HCl solution. As molecules of 2″A tend to stay at the interface between the aqueous solution and air, 2″A tends to show little influence on the rate constants. In a later section, where a mixture of half acetonitrile and half HCl solution is used, the decrease of the rate constant for 2″A can be readily observed. Also, the measured rate constants, *k*, are not proportional to the oxidation potentials, meaning that oligoanilines with longer chains are not guaranteed to speed up the polymerization reaction as the oxidation potential of oligoanilines is known to decrease with longer chain lengths.

For further elucidation, we first compare 3′A and 2A, where the rate constants for 3′A are greater than for 2A. The oxidation potentials for 3′A and 2A are 0.574 and 0.588 V, respectively, as listed in **Table 3-1**. The huge differences in rate constants should not be solely attributed to the tiny oxidation potential difference (0.014 V). In terms of molecular structures, 3′A possesses amine groups at both ends of the molecule, while 2A only has one accessible amine group. Likewise, the rate constants of 2′A are higher than that of 2A, but the oxidation potential of 2′A (0.670 V) is higher than that of 2A (0.588 V). On the basis of the two above-mentioned cases, we realize that a lower oxidation potential compared to that of aniline is essential for accelerating the reaction, but the structure of the molecule, i.e., phenyl or amino groups, can dramatically affect the rate constant when the oxidation potential of such a molecule is lower than that of aniline.

Another way to compare the rate of electrochemical polymerization of aniline reported is to measure the temperature of the reaction solution over time.[20] This method is based on the

exothermic oxidation expected during aniline polymerization with a fixed amount of oxidizing agent, ammonium persulfate in this case. Theoretically, when the reaction is slower, the oxidizing agent will be consumed more slowly; therefore, it takes more time for the solution to reach its maximum temperature. In **Figure 3-7**, profiles of temperature versus time with and without additives are shown. Instead of just focusing on the time to reach the temperature maximum, we also define the time for the reaction's temperature to start increasing as t_1, and the time duration between the temperature starting to rise and the peak temperature as t_2. Therefore, the time duration t_1 indicates when the oxidation reaction starts, and $t_1 + t_2$ is the time for oxidation reactions to end. In **Figure 3-8**, t_1 is found to be linearly proportional to $t_1 + t_2$, indicating that when the reactants are being oxidized earlier, the reaction is terminated faster. Since the amount of additives is almost negligible compared to the concentration of aniline, i.e., the heat released by the oxidizing additives is not likely to be the reason causing the temperature rise, we postulate that t_1 reflects the generation of radicals on monomers just as they start to polymerize, which is affected by the additives added in. For example, a relatively small t_1 is caused by the introduction of an initiator, meaning that the radicals are easier to generate and propagate for further polymerization; hence, the polymerization should have a higher rate constant.

The third method proposed by Wei et al. is to monitor the open-circuit potential (OCP) versus time.[20] The chemical potential of the oxidizing agent, ammonium persulfate, in a solution can be simply measured through a two-electrode setup. Similar to the above-mentioned temperature measurement, the ammonium persulfate will be consumed sooner if the polymerization reaction is faster. Therefore, as the time durations for the OCP start to decline, t would be an indicator for evaluating the rate of polymerization. In **Figure 3-9**, it is clear that 1″A has the slowest rate of

polymerization, while 3′A has the fastest. By comparing the time, t, for the OCP and $t_1 + t_2$ for the temperature measurement, a linear relationship is found (**Figure 3-10**), showing that these two methods are coherent. To examine whether these two methods can be well-related to the rates of polymerization comparatively, contour mappings with rate constants at 0.8 V (**Figure 3-11a**), 0.9 V (**Figure 3-11b** for k_1, and **Figure 3-11c** for k_2), and 1.0 V (**Figure 3-11d**) were applied. On the basis of those colored mappings, we confirm that the OCP and temperature measurements are directly related to the rate constants measured. Note that the OCP measurements tend to be more intimately correlated, which may be due to human error and time gaps, ∼15 s, between each reading from using a conventional thermometer.

In this system, oligothiophenes and pyrrole monomers were also introduced. By applying the same measurements under identical conditions (**Figures 3-S12 to S17**), rate constants under different voltages applied can be obtained, as shown in **Table 3-2**. Note that the solutions with pyrrole monomers added in do not tend to polymerize; i.e., no precipitate was observed. For oligothiophenes, both temperature and OCP measurements show slower reaction rates than the aniline without additives, except for terthiophene (3T) (**Figure 3-S18**). In **Figure 3-S19**, the contour mappings show consistencies among the temperature, OCP measurements, and rate constants. The reasons for the slow reaction rates for oligothiophenes can be attributed to the high oxidation potentials for thiophene monomers and bithiophenes, and low probabilities for radicals to transfer for terthiophenes and sexithiophenes.[29]

Chemical Polymerizations and Morphologies

The morphology of polyaniline is known to be associated with its mode of nucleation during polymerization.[35] Heterogeneous nucleation tends to result in bulk and granular morphologies, while homogeneous nucleation facilitates the formation of nanofibers. Low temperature,

oxidizing agents with low oxidizing potentials, and the gradual addition of oxidizing agents favor heterogeneous nucleation; i.e., it enhances secondary growth, resulting in granular features. Agitation, rapid mixing, and/or adding initiators to increase the rate of polymerization are believed to suppress the secondary growth of polyaniline; therefore, nanofibrillar morphologies are likely to be generated.[24,36–38] As shown in **Figure 3-12**, aniline polymerized with additives including 2A, 2′A, 3′A, and 4A(EB) forms fiberlike morphologies with thin widths, which is in agreement with the above-mentioned growth mechanism. On the other hand, morphologies of 1″A, 2″A, and 4A(LEB) are more similar to that of pure polyaniline.

For aniline polymerization with pyrrole monomers as the additive, no precipitates were observed. Therefore, a suspension of the reaction is shown in **Figure 3-13a**, which should be granular polypyrrole as pyrrole monomers tend to be oxidized first, but the radicals formed did not tend to transfer onto the aniline monomers. Interestingly, SEM images of aniline with oligothiophenes (**Figure 3-13b to 13e**) show a coral-like morphology. The rates for polymerization of aniline with oligothiophenes possess similar or smaller rate constants than additive-free aniline polymerization but greater than that of 1″A, which is counterintuitive for the fibrillar morphology of 1″A, and the coral-like morphologies of oligothiophenes. Therefore, we speculate that the formation of these nongranular morphologies for slower polymerization rates is because of the high oxidation potential of ammonium persulfate (2.1 eV) and the similar steric structures, i.e., π–π stackings. As the measured rate constants increase with increasing voltage applied, the strong oxidizing agent, ammonium persulfate, may tend to offer faster polymerization rates, which favors homogeneous nucleation. The slower rates for oligothiophenes indicate that the secondary growth was not suppressed; therefore, with 5 s of rapid shaking during the synthesis, a coral-like morphology associated with both homogeneous and heterogeneous nucleation was

formed.[35] On the other hand, the explanation for 1″A with a much slower rate constant but still maintaining a more fibrillar morphology may be attributed to π—π stacking. On the basis of previous studies, the morphology of polyaniline and crystallization of oligoanilines are known to be intimately associated with strong π—π stacking forces between molecules.[34,39–41] The similar molecular structures between 1″A and polyaniline may make 1″A serve as a directional template for growing nanofibers.

Aniline Polymerization in Acetonitrile/HCl Solutions

During the electrochemical polymerization, it is noteworthy that some additives, for example, 1″A, 2″A, and oligothiophenes, are not well dispersible in the 1.0 M HCl solution even though they were predissolved in a trace amount of acetonitrile. Therefore, to have all the materials dispersed well in solution, along with proton resources, we performed each of the above-mentioned electrochemical polymerization experiments in a solution containing 15 mL of 1.0 M HCl and 15 mL of acetonitrile using a sweep range between −0.2 and 1.0 V (referenced to Ag/AgCl). Note that the relationship between the anodic peak current and the amount of polyaniline deposited on the electrode should be different than that in the 1.0 M HCl solution, but here we still follow the same rules simply for comparison. The graphs of anodic peak current versus number of scans, rate versus number of scans, rate versus the anodic peak current, and the fittings between the rate and the square root of the anodic peak current are plotted in **Figures 3-S20 and 3-S21**. In contrast to the aqueous solution, only one voltage range was tested, and two rate constants were found to fit the curves with the cutoff at i = 3 mA, instead of 9 mA for the aqueous experiments.

The rate constants are listed in **Table 3-S1** and plotted in **Figure 3-14**. The trends between each additive are similar to that in the aqueous solutions (**Figure 3-6**). The much higher rate constants

k_1 can be attributed to the fitting range of the anodic peak current that is below 3 mA. On the basis of the second rate constant, k_2, 2A, 2′A, 3′A, 4A(EB), and 4A(LEB) are eligible to catalyze the polymerization reactions. It is possible that the conducting 4A(EB) and 4A(LEB) (after oxidation) contribute a great deal to the current readings as they both dissolved pretty well in such solutions. The rate constants for the acetonitrile/HCl system are much smaller than that in the pure aqueous system at 1.0 V, but closer to the rate constant observed at 0.9 V; the reasons causing this phenomena could possibly be a shift in the reference potential due to different solvents used and, most likely, the acetonitrile dissolving the polyaniline deposited on the electrode more efficiently than 1.0 M HCl so that it takes many more scans for the anodic peak current to reach a certain number, i.e., faster depositions for the HCl system. By plotting the rate constants for this acetonitrile/HCl system and the OCP and temperature over time tested in the pure 1.0 M HCl system, it is clear that values of k_1 are not consistent with the OCP and temperature monitoring, while values of k_2 are closer to the trends measured in the 1.0 M HCl system, except for the rate constant of 2″A which is lower.

CONCLUSIONS

In this study, we have confirmed the autocatalytic effect of polyaniline and the catalytic effect of introducing oligoanilines including 2A, 2′A, and 3′A into the system of aniline polymerization by fitting curves with an established empirical equation up to the maximum values of the polymerization rate. Aniline with and without additives does not tend to polymerize with an applied potential lower than 0.8 V against Ag/AgCl but possesses higher rate constants as the applied potential increases. Tetraaniline in both its emeraldine (4A(EB)) and leucoemeraldine (4A(LEB)) states does not tend to accelerate reactions; hence, the formation of tetraaniline might be the intermediate step during the polymerization of aniline when the rate of polymerization

begins to slow down. On the other hand, 1″A and 2″A can decelerate reactions as their rate constants are smaller than that of additive-free aniline polymerization, because of the high oxidation potential and the phenyl-capped structures. Pyrrole monomer, as an additive, inhibits the polymerization of aniline, while oligothiophenes do not facilitate aniline polymerization. By comparing between the rate constants measured and the time durations $t_1 + t_2$ for temperature and the time duration t for the OCP of solutions, we verify the feasibility of these two qualitative methods for evaluating the speed of aniline polymerization.

EXPERIMENTAL SECTION

Materials and Instrumentation

All chemicals were used as received. Aniline (ACS reagent >99.5%), diphenylamine (1″A), N-phenyl-p-phenylenediamine (2A), 2,2′-bithiophene (2T), 2,2′:5′,2″-terthiophene (3T), α-sexithiophene (6T), and phenylhydrazine (97%) were purchased from Sigma-Aldrich. Ammonium persulfate (98+%), thiophene (99+%), and anhydrous acetonitrile (99.9%, extra dry AcroSeal, 1 L) were purchased from ACROS. N,N′-diphenyl-1,4-phenylenediamine (2″A) and 4,4′-diaminodiphenylamine sulfate hydrate (3′A) were acquired from Tokyo Chemical Industry. 1,4-Phenylenediamine (2′A) was purchased from Fluka. Pyrrole (98+%) and platinum foils (99.9%, 0.025 mm thickness, metal basis) for the working and counter electrodes were obtained from Alfa Aesar. Tetraaniline (4A) in both emeraldine and leucoemeraldine states was synthesized as previously reported.(46) The reference electrode (Ag/AgCl, MR-5275) for aqueous electrolytes was obtained from BASi. SEM images were taken with a JEOL JSM-6700 field-emission scanning electron microscope. All electrochemical data were collected with a Biologic VMP3 workstation. All reactions were performed in air at room temperature.

Electrochemical Polymerization

The setup for electrochemical reactions is shown in **Figure 3-S23**. Platinum foils were used as the working and counter electrodes with an area of ~1.0 cm × 1.0 and 1.0 cm × 2.0 cm, each. The extended electrodes were attached with copper foil and sealed with Kapton tape. A suitable electrolyte, monomers, additives, and a tiny magnetic stirring bar were placed in a 50 mL beaker. All reactions were stirred at 500 rpm. For the aqueous electrochemical polymerization of aniline, an additive (1.0 mM) was predissolved with ~200–400 μL of acetonitrile in a 7 mL glass vial and then pipetted to a 50 mL beaker, which contained aniline monomers (0.2 M) and 1.0 M hydrochloric acid (30 mL). The cyclic potential was swept from −0.2 to 0.8, 0.9, and 1.0 V (referenced against Ag/AgCl) at a scan rate of 25 mV s^{-1} for 40 cycles. For polymerization of aniline in acetonitrile and hydrochloric acid, the electrolyte contained 15 mL of acetonitrile and 15 mL of 1.0 M hydrochloric acid.

Open-Circuit Voltage Measurements

The aniline system was measured in an aqueous environment. First, 20 mL of 1.0 M hydrochloric acid, aniline monomer (1.5 mmol), and an additive (0.03 mmol) predissolved in a small amount of acetonitrile were placed in a 50 mL beaker. In a 20 mL glass vial, 342 mg of ammonium persulfate was dissolved in 10 mL of 1.0 M hydrochloric acid. The electrode setup is the same as described above. The real-time voltage versus an Ag/AgCl reference electrode was recorded about 3 s after one-time pipetting the ammonium persulfate solution into the beaker.

Temperature Monitoring

An additive (0.03 mmol) predissolved in a small amount of acetonitrile was mixed with 20 mL of 1.0 M hydrochloric acid and aniline monomer (1.5 mmol) in a 150 mL glass jar. The jar was

placed in a fume hood, and a conventional thermometer was mounted on the rack to read the temperature of the solution. After the thermometer reading reached equilibrium, a 10 mL solution of 1.0 M hydrochloric acid with predissolved ammonium persulfate (342 mg) was poured into the jar. Temperature readings were recorded every 15 s.

Chemical Polymerization

Aniline monomer (0.8 mmol) was added into a 20 mL 1.0 M hydrochloric acid solution. An appropriate additive (0.02 mmol) was first dissolved in a trace amount of acetonitrile in a 7 mL glass vial and then transferred to the solution. Reactions were shaken for 5 s after adding in 45 mg of ammonium persulfate and left to stand for 24 h with caps sealed. The products were left in a vacuum chamber and collected after centrifugation followed by washing with a copious amount of deionized water.

Cyclic Voltammetry of Materials

Cyclic voltammetry of 1″A, 2A, 2′A, 2″A, 3′A, and 4A was characterized by adding a 10 mM concentration of the material into 30 mL of 1.0 M hydrochloric acid solution and sweeping between −0.2 and 1.0 V, referenced against an Ag/AgCl electrode, at a scan rate of 25 mV s^{-1}.

ACKNOWLEDGEMENT

The authors thank Dr. Dandan Zhang and Prof. Chong Liu for lending us reference electrodes. C.-W.L. thanks Dr. Jeong Hoon Ko for useful discussions, and support from the UCLA Dissertation Year Fellowship. W.H.M. and S.A. would like to acknowledge their UCLA Eugene V. Cota-Robles Fellowships, and R.B.K. would like to acknowledge the support from the Dr. Myung Ki Hong Endowed Chair in Materials Innovation at UCLA.

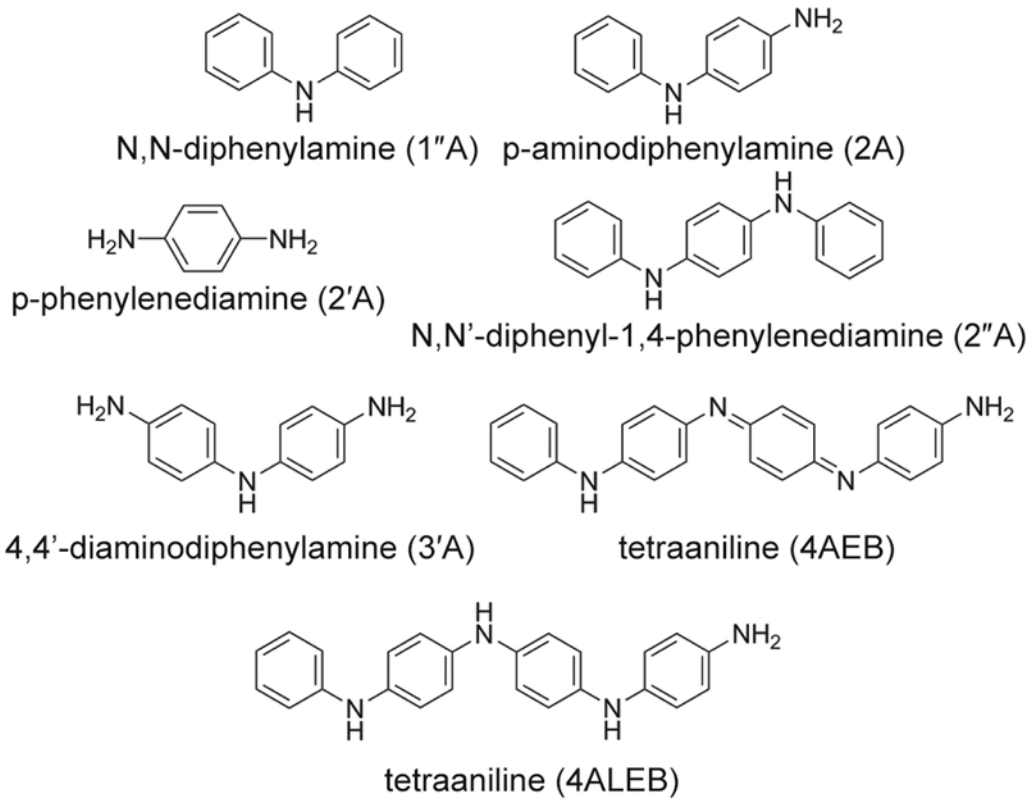

Figure 3-1. Molecular structures of aniline additives and their abbreviations.

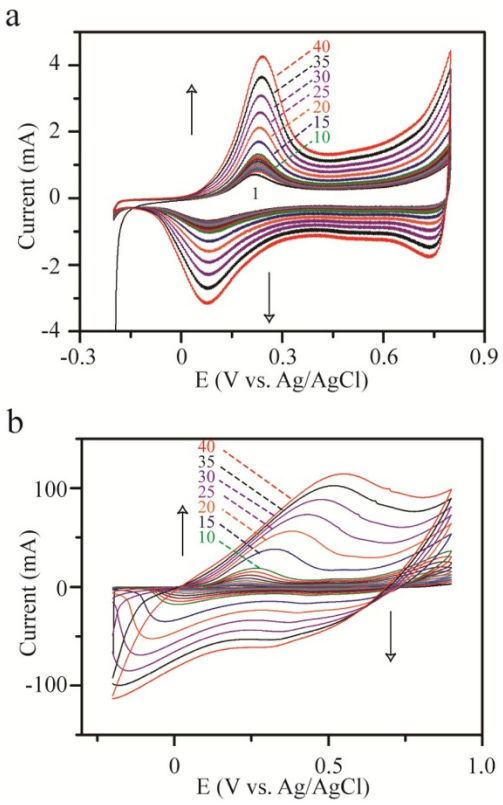

Figure 3-2. Cyclic voltammograms of electrochemical polymerization of 0.2 M aniline in a 1.0 M HCl solution on a platinum electrode from −0.2 V to (a) 0.8 V and (b) 0.9 V versus Ag/AgCl at a scan rate of 25 mV s^{-1}. The number of scans from 1 to 10 and at 15, 20, 25, 30, 35, and 40 are indicated.

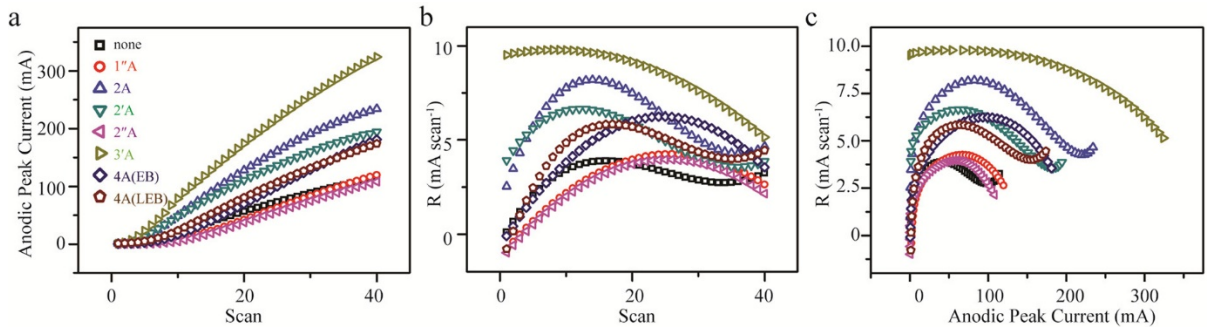

Figure 3-3. Full graphs of (a) anodic peak current versus number of scans, (b) polymerization rate versus the number of scans, and (c) polymerization rate versus the anodic peak current, for aniline electrochemical polymerization with and without oligoanilines. The reactions contain 0.2 M aniline and 1.0 mM additives in a 30 mL 1.0 M HCl solution, with the potential sweep ranges from −0.2 to 0.9 V (against Ag/AgCl) at a scan rate of 25 mV s^{-1}.

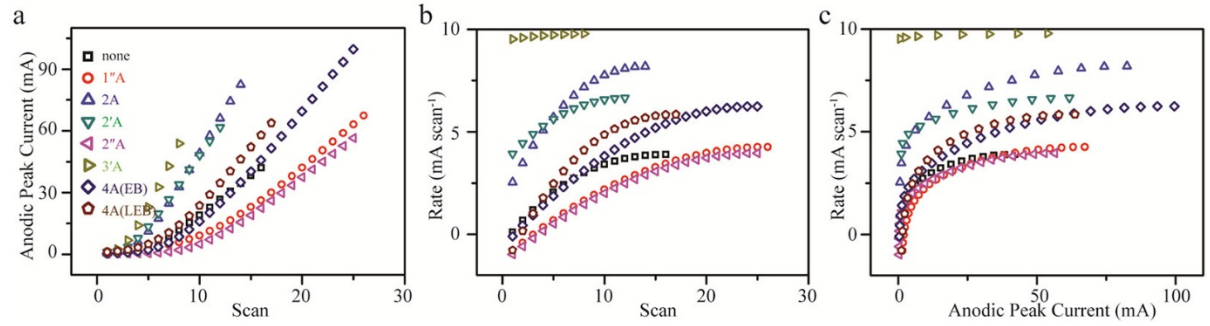

Figure 3-4. Graphs of (a) anodic peak current versus number of scans, (b) polymerization rate versus the number of scans, and (c) polymerization rate versus the anodic peak current, for aniline electrochemical polymerization with and without oligoanilines to reach their maximum rates of electrochemical polymerization. The reactions contain 0.2 M aniline and 1.0 mM additives, 30 mL of a 1.0 M HCl solution, with the potential sweep ranges from −0.2 to 0.9 V (against Ag/AgCl) at a scan rate of 25 mV s^{-1}.

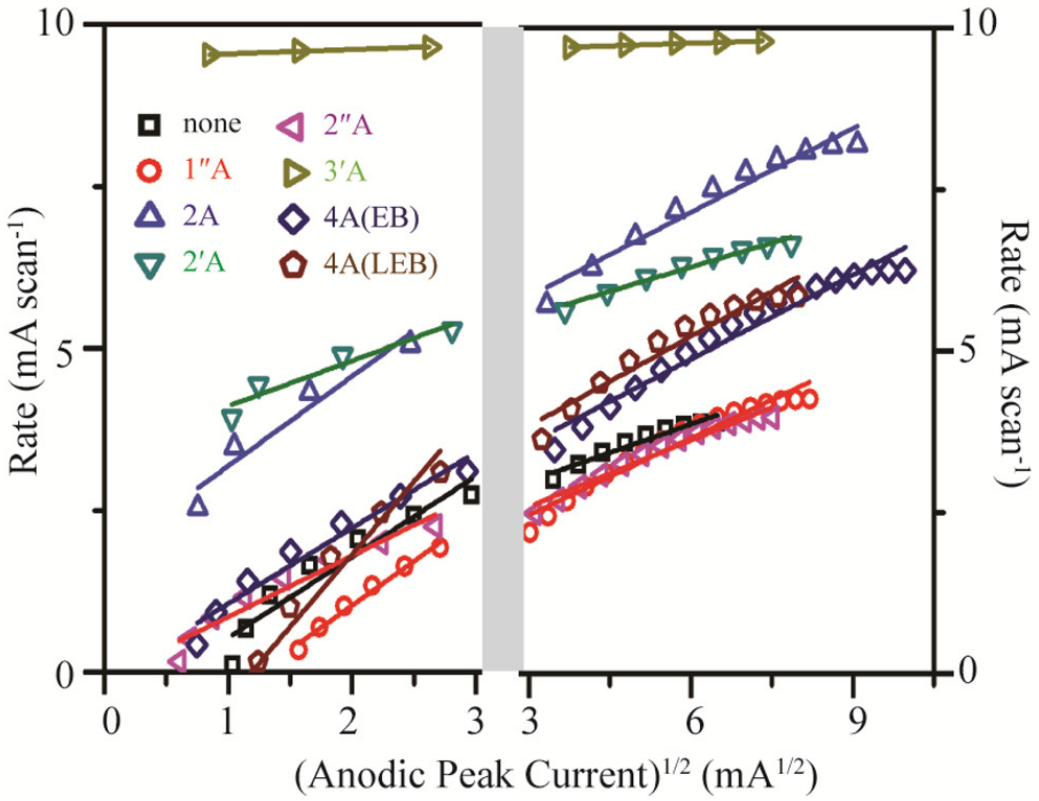

Figure 3-5. Linear relationships of the rate of electrochemical polymerization of aniline with the square root of the anodic peak current. Potential sweep range: −0.2 to 0.9 V (versus Ag/AgCl). Scan rate: 25 mV s^{-1}.

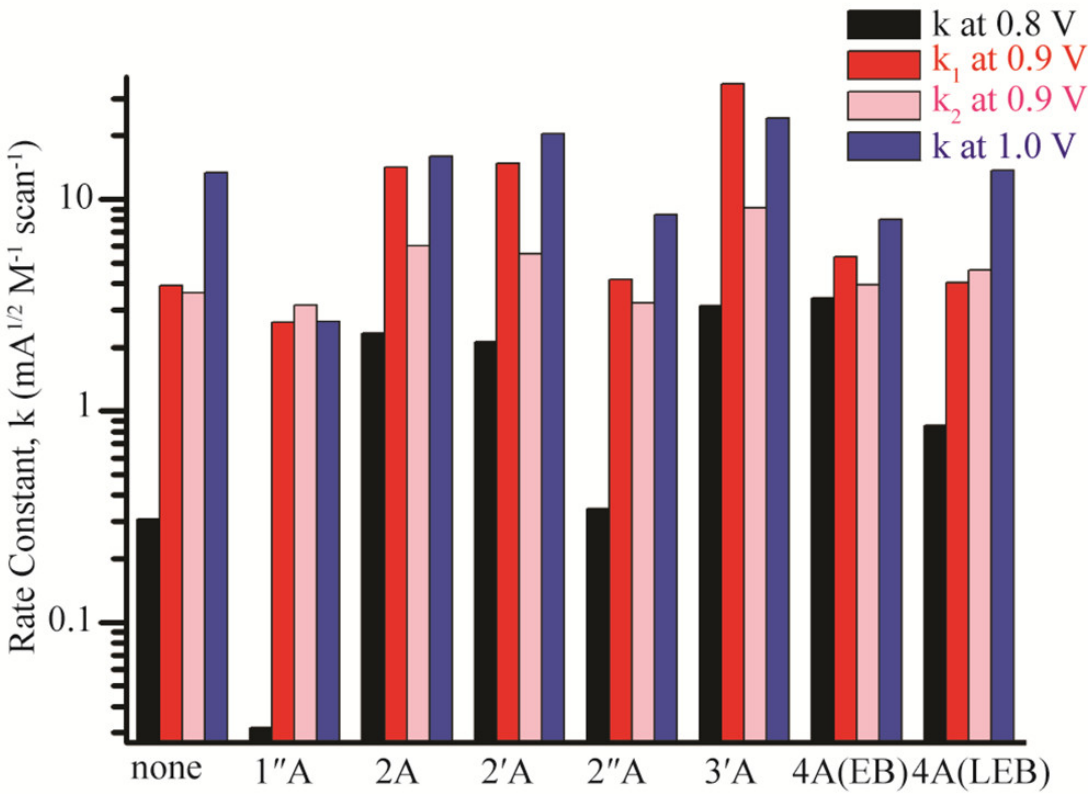

Figure 3-6. Rate constant, *k*, for the electrochemical polymerization of aniline with and without oligoanilines in a 1.0 M HCl solution, with potential sweeps from −0.2 to 0.8, 0.9, and 1.0 V.

Table 3-1. Aniline Electrochemical Polymerization Rate Constant k[a]

additive	k at 0.8 V	k_1 at 0.9 V	k_2 at 1.0 V	k at 1.0 V	E_{ox}[b]
none	0.307	3.90	3.62	13.4	0.785 ([42,43])
1"A	0.0317	2.61	3.15	2.64	0.840
2A	2.32	14.2	6.01	16.0	0.588
2'A	2.11	14.8	5.52	20.5	0.670
2″A	0.343	4.19	3.23	8.45	0.617
3′A	3.12	35.0	9.15	24.1	0.574
4A(EB)	3.41	5.32	3.94	8.05	0.637
4A(LEB)	0.853	4.01	4.60	13.6	0.347

[a]k is given in units of $mA^{1/2}\,M^{-1}\,scan^{-1}$ with and without additives under the potential sweeps of −0.2 to 0.8 V, −0.2 to 0.9 V, and −0.2 to 1.0 V (versus Ag/AgCl). The concentrations of aniline monomer and additives are 0.2 M and 1.0 mM, respectively. The electrochemical polymerization experiments were carried out with a 30 mL 1.0 M HCl solution at a scan rate of 25 mV s^{-1}.

[b]The oxidation potential (E_{ox}) for each material was measured by dispersing 10 mM of materials into a 30 mL 1.0 M HCl solution with a potential swept between −0.2 and 1.0 V versus Ag/AgCl, at a scan rate of 25 mV s^{-1}. Cyclic voltammograms of each material are shown in **Figure 3-S11**.

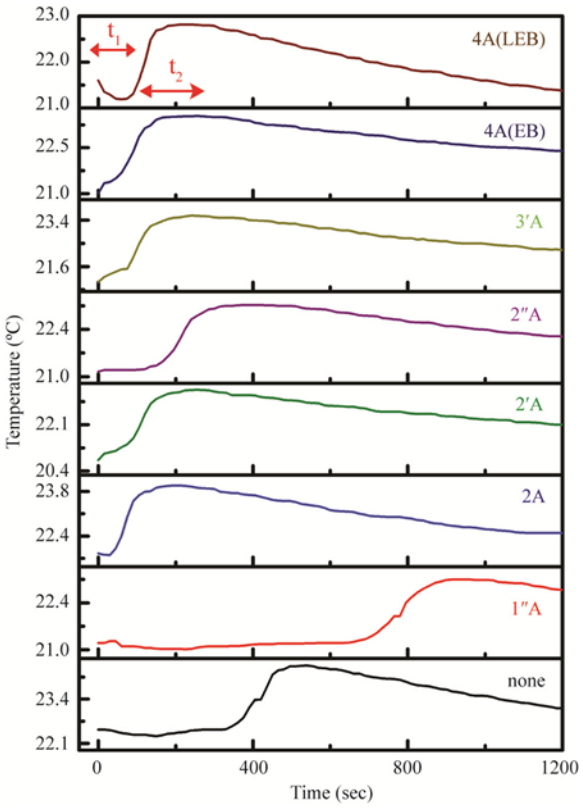

Figure 3-7. Profiles of time versus temperature of a 1.0 M HCl solution containing 0.2 M aniline, 1.0 mM oligoanilines, and 45 mg of ammonium persulfate.

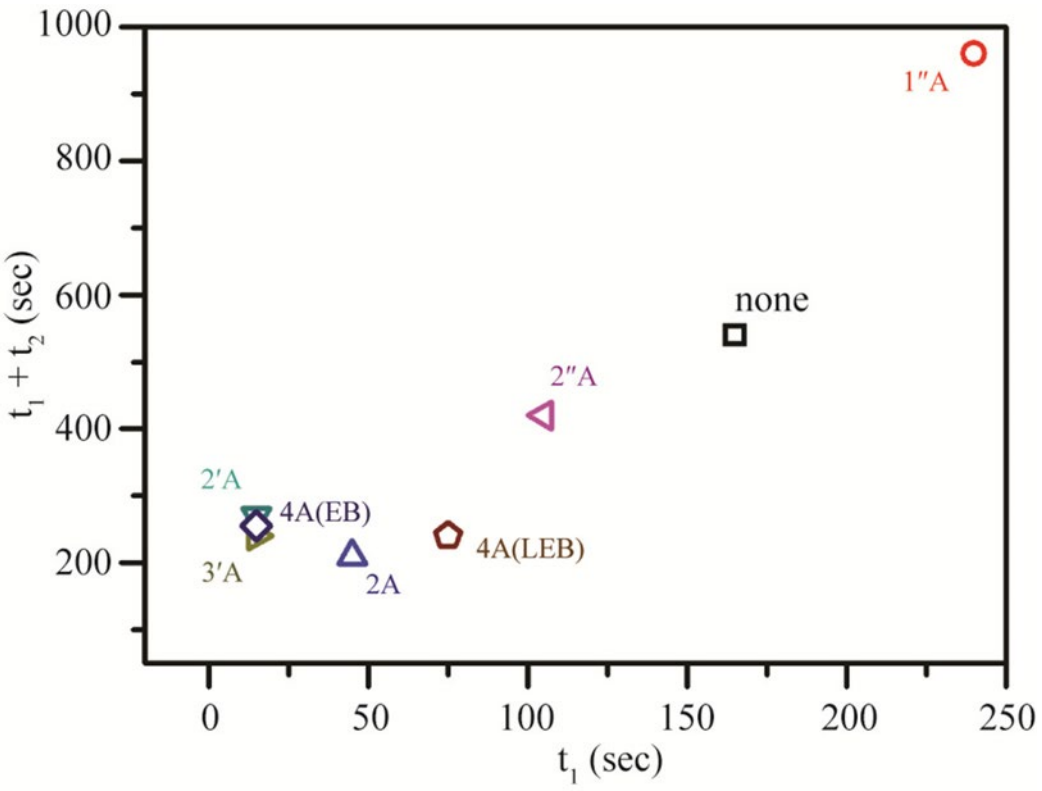

Figure 3-8. Plot of temperature t_1 versus temperature $t_1 + t_2$ for oligoanilines in chemical polymerizations of aniline with ammonium persulfate as the oxidizing agent in a 1.0 M HCl solution.

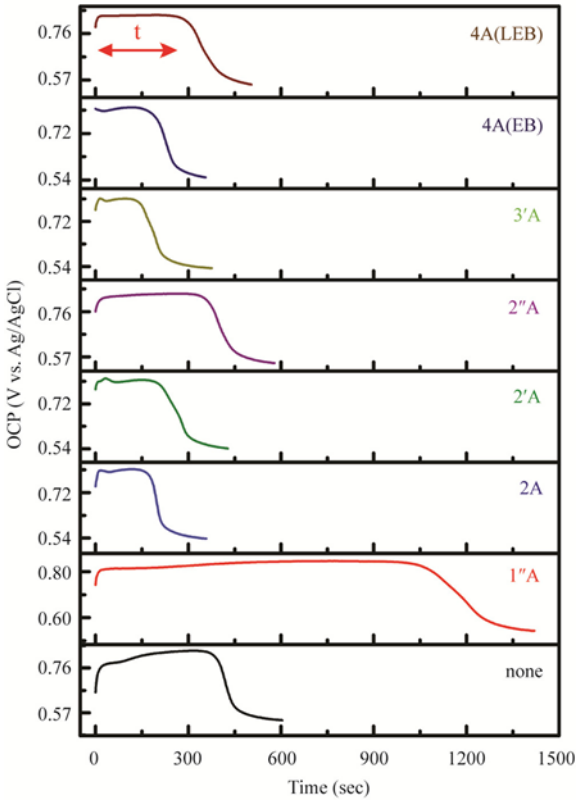

Figure 3-9. Profiles of time versus the open-circuit voltage of a 1.0 M HCl solution containing 0.2 M aniline, 1.0 mM oligoanilines, and 45 mg of ammonium persulfate.

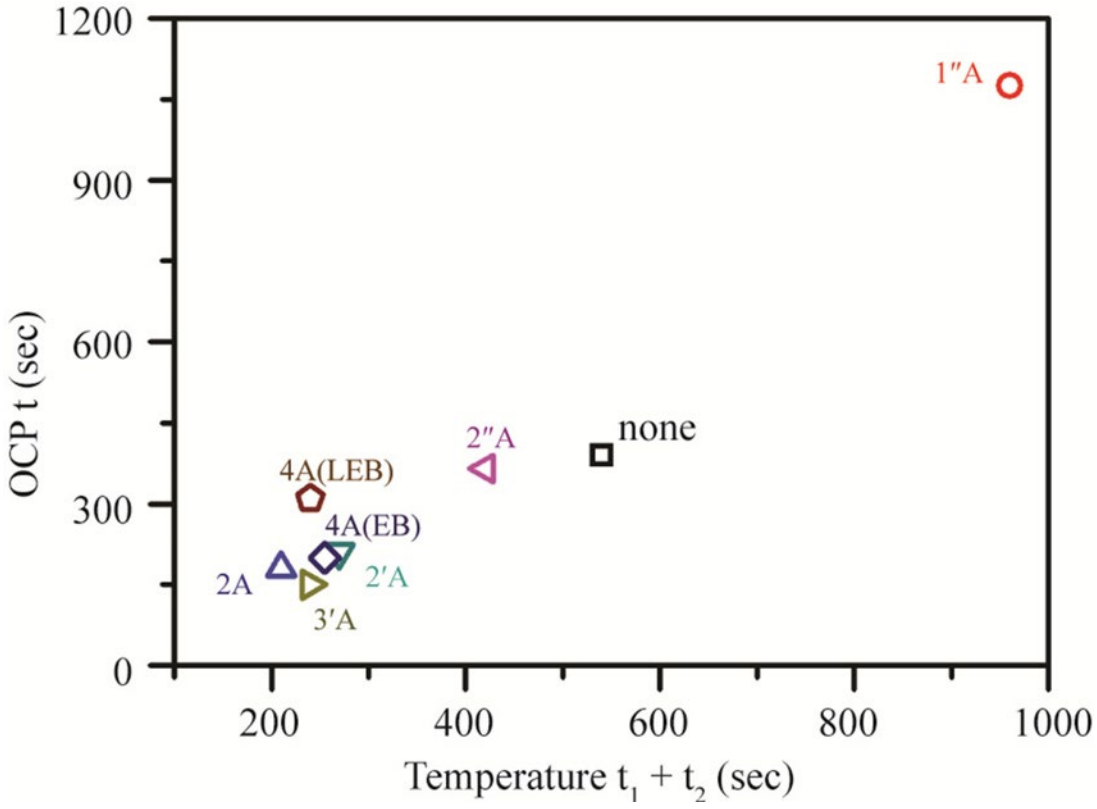

Figure 3-10. Plot of open-circuit potential *t* versus temperature $t_1 + t_2$ for oligoanilines in chemical polymerizations of aniline with ammonium persulfate as the oxidizing agent in a 1.0 M HCl solution.

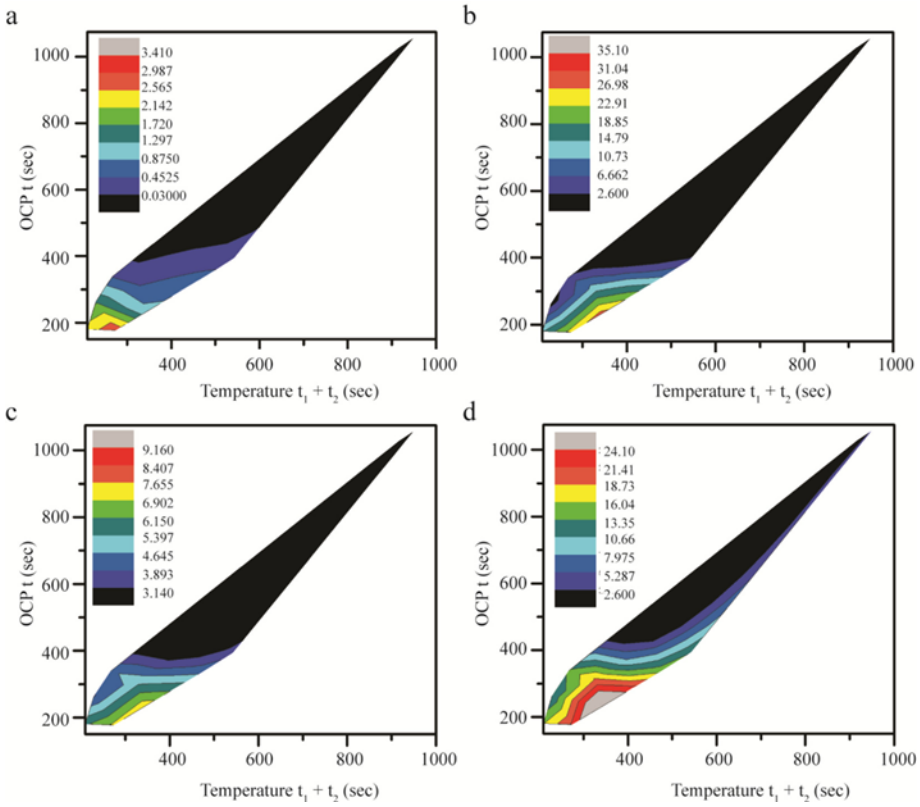

Figure 3-11. Contour plots of t for the open-circuit potential versus the $t_1 + t_2$ duration for temperature profiles, with color mappings for (a) rate constants at 0.8 V, (b) first rate constant, k_1, at 0.9 V, (c) second rate constant, k_2, at 0.9 V, and (d) rate constant at 1.0 V, for introducing oligoanilines into the chemical polymerization of aniline in a 1.0 M HCl solution.

Table 3-2. Electrochemical Polymerization Rate Constant k[a]

additive	***k* at 0.8 V**	**k_1 at 0.9 V**	**k_2 at 0.9 V**	***k* at 1.0 V**	**E_{ox}**
none	0.307	3.90	3.62	13.4	0.800
1T	0.283	4.68	4.28	9.14	1.76 ([44])
2T	0.307	2.85	2.36	8.14	1.00 ([44])
3T	0.317	4.81	4.23	11.2	0.740 ([44])
6T	0.326	7.17	3.82	9.71	0.600 ([44])

[a]*k* is given in units of $mA^{1/2}\ M^{-1}\ scan^{-1}$ with and without oligothiophene additives under the potential sweeps of −0.2 to 0.8 V, −0.2 to 0.9 V, and −0.2 to 1.0 V (versus Ag/AgCl). The concentrations of aniline monomer and oligothiophene additives are 0.2 M and 1.0 mM, respectively. The electrochemical polymerization experiments were carried out with a 30 mL 1.0 M HCl solution at a scan rate of 25 mV s^{-1}.

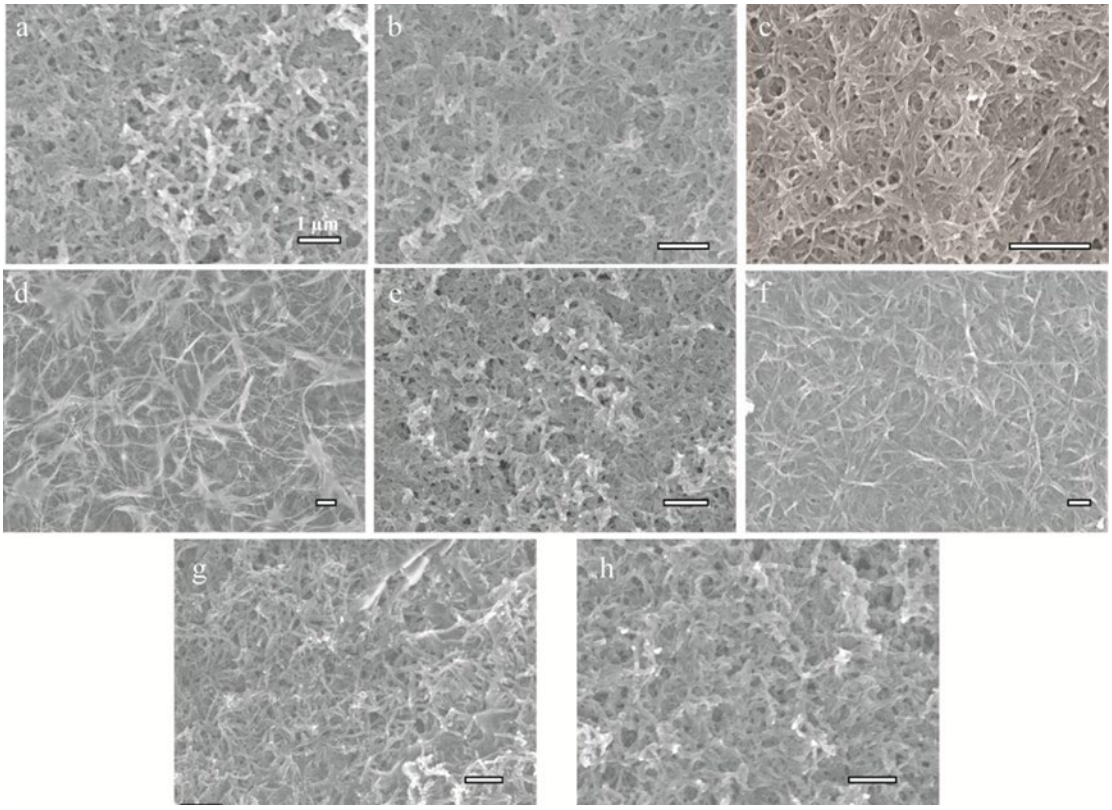

Figure 3-12. Scanning electron microscope images of the chemical polymerization of aniline with (a) no additives, (b) 1″A, (c) 2A, (d) 2′A, (e) 2″A, (f) 3′A, (g) 4A(EB), and (h) 4A(LEB), in a 1.0 M HCl solution.

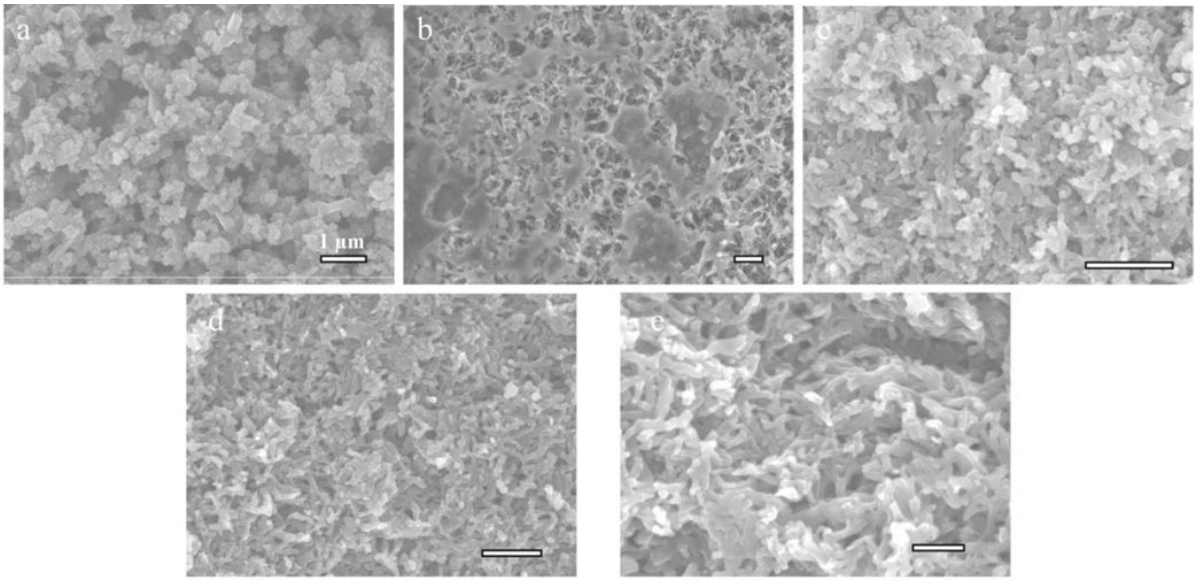

Figure 3-13. Scanning electron microscope images of the chemical polymerization of aniline with (a) pyrrole monomers, (b) 1T, (c) 2T, (d) 3T, and (e) 6T, in a 1.0 M HCl solution.

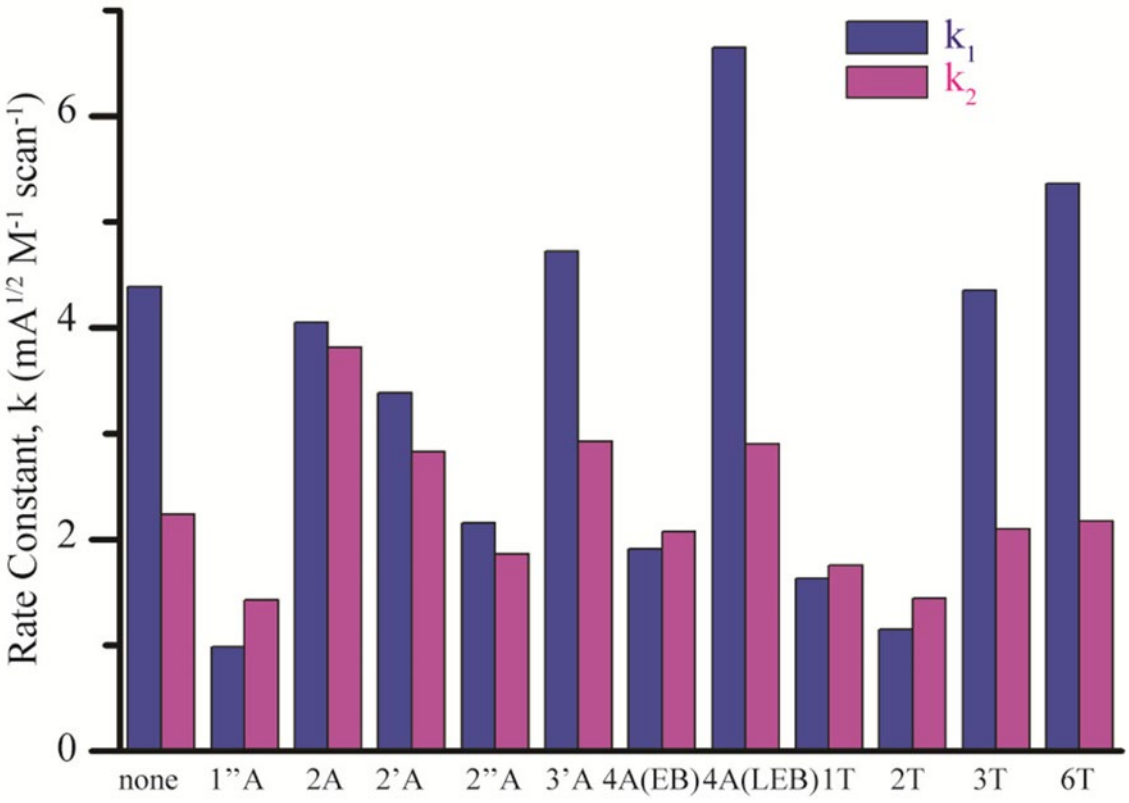

Figure 3-14. Plot showing the first and second rate constants for the electrochemical polymerization of aniline in an acetonitrile/HCl solution, with the potential sweep from −0.2 to 1.0 V, against Ag/AgCl. The scan rate is 25 mV s^{-1}.

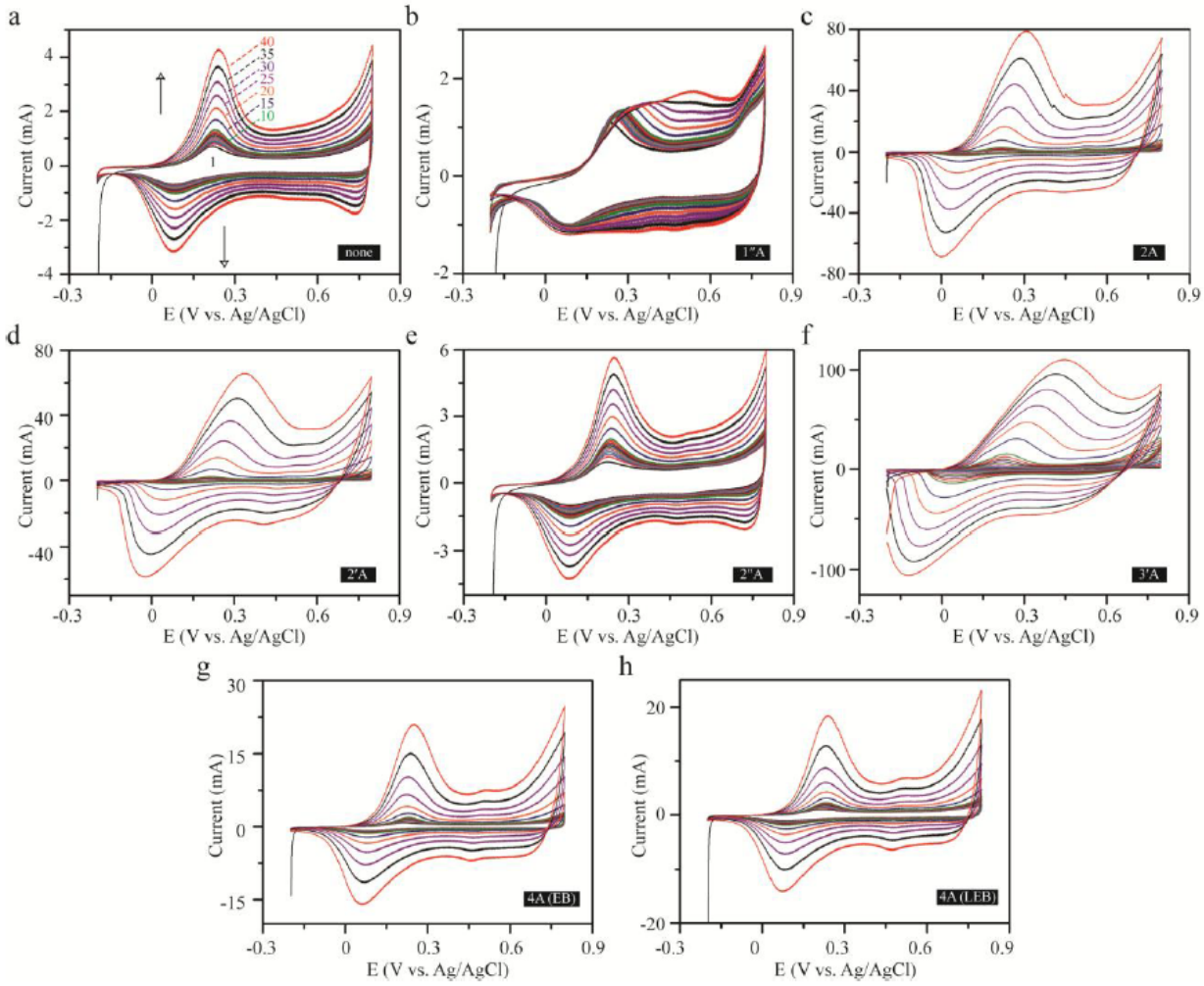

Figure 3-S1. Cyclic voltammograms of electrochemical polymerization of aniline in a 1.0 M HCl solution with (a) no additives, (b) 1″A, (c) 2A, (d) 2′A, (e) 2″A, (f) 3′A, (g) 4A(EB), and (h) 4A(LEB). The reactions contain 0.2 M of aniline and 1.0 mM of additives, with the potential sweep from -0.2 V to 0.8 V (against Ag/AgCl) at a scan rate of 25 mV/s.

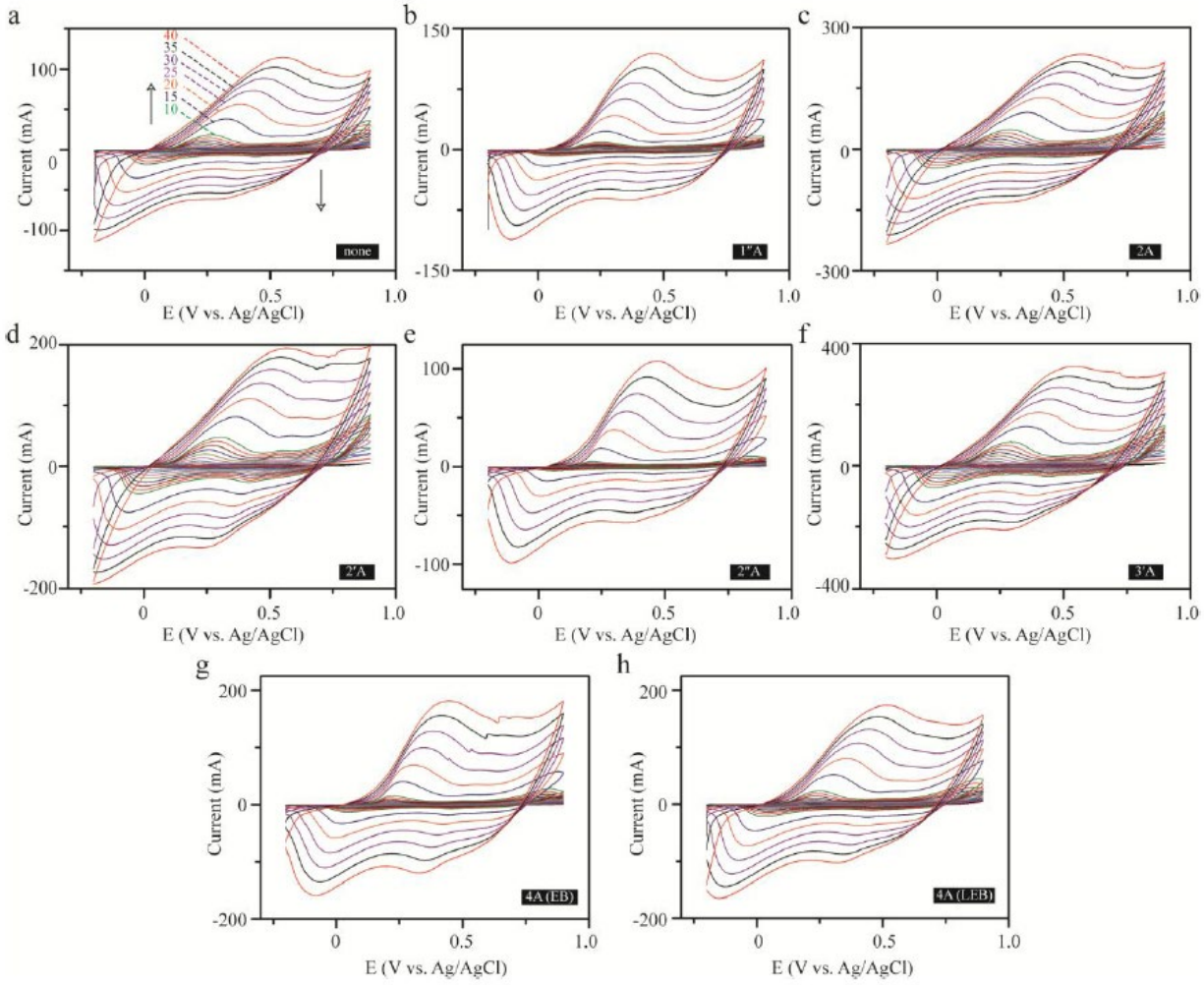

Figure 3-S2. Cyclic voltammograms of electrochemical polymerization of aniline in a 1.0 M HCl solution with (a) no additives, (b) 1″A, (c) 2A, (d) 2′A, (e) 2″A, (f) 3′A, (g) 4A(EB), and (h) 4A(LEB). The reactions contain 0.2 M of aniline and 1.0 mM of additives, with the potential sweep from -0.2 V to 0.9 V (against Ag/AgCl) at a scan rate of 25 mV/s.

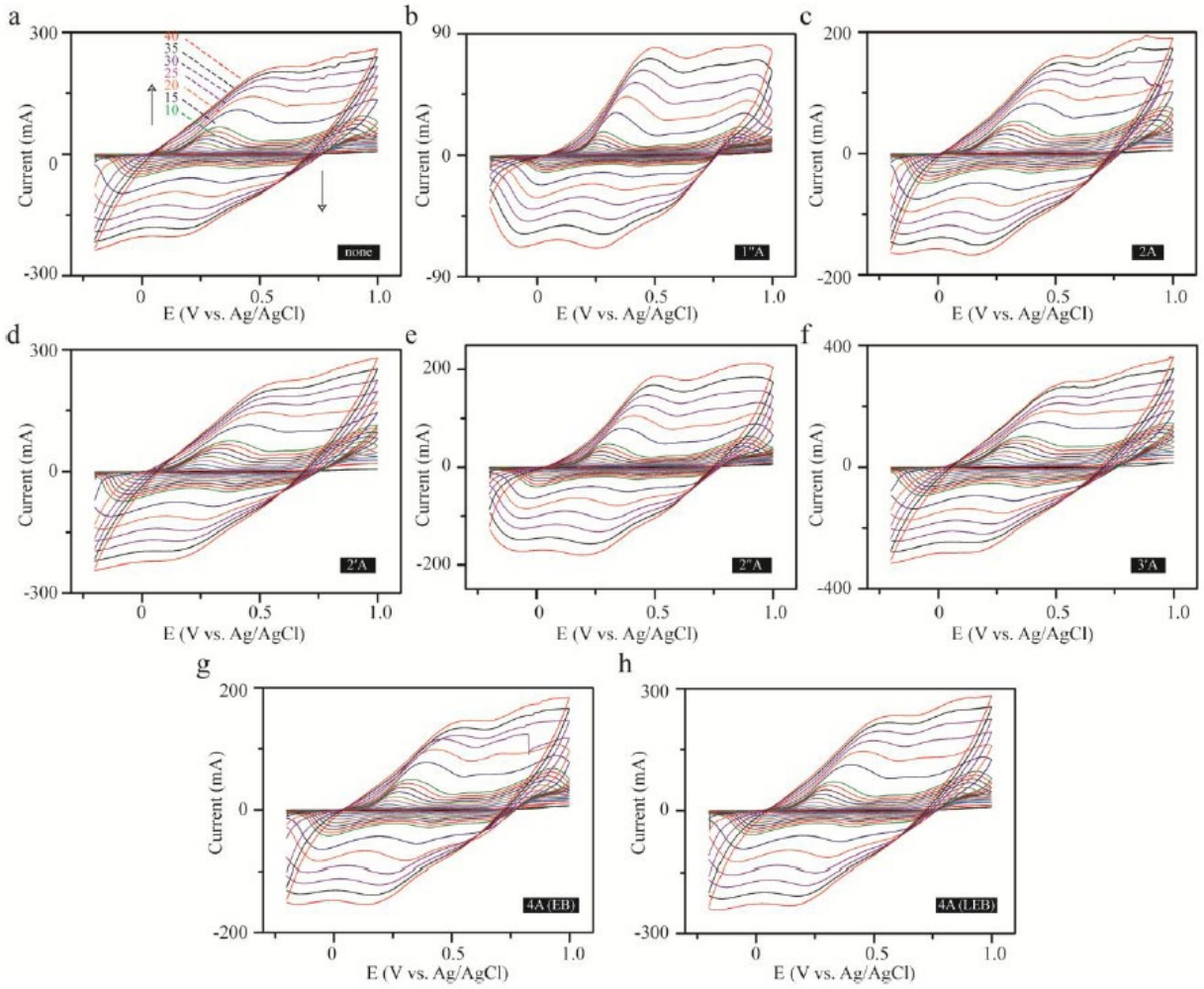

Figure 3-S3. Cyclic voltammograms of electrochemical polymerization of aniline in a 1.0 M HCl solution with (a) no additives, (b) 1″A, (c) 2A, (d) 2′A, (e) 2″A, (f) 3′A, (g) 4A(EB), and (h) 4A(LEB). The reactions contain 0.2 M of aniline and 1.0 mM of additives, with the potential sweep from -0.2 V to 1.0 V (against Ag/AgCl) at a scan rate of 25 mV/s.

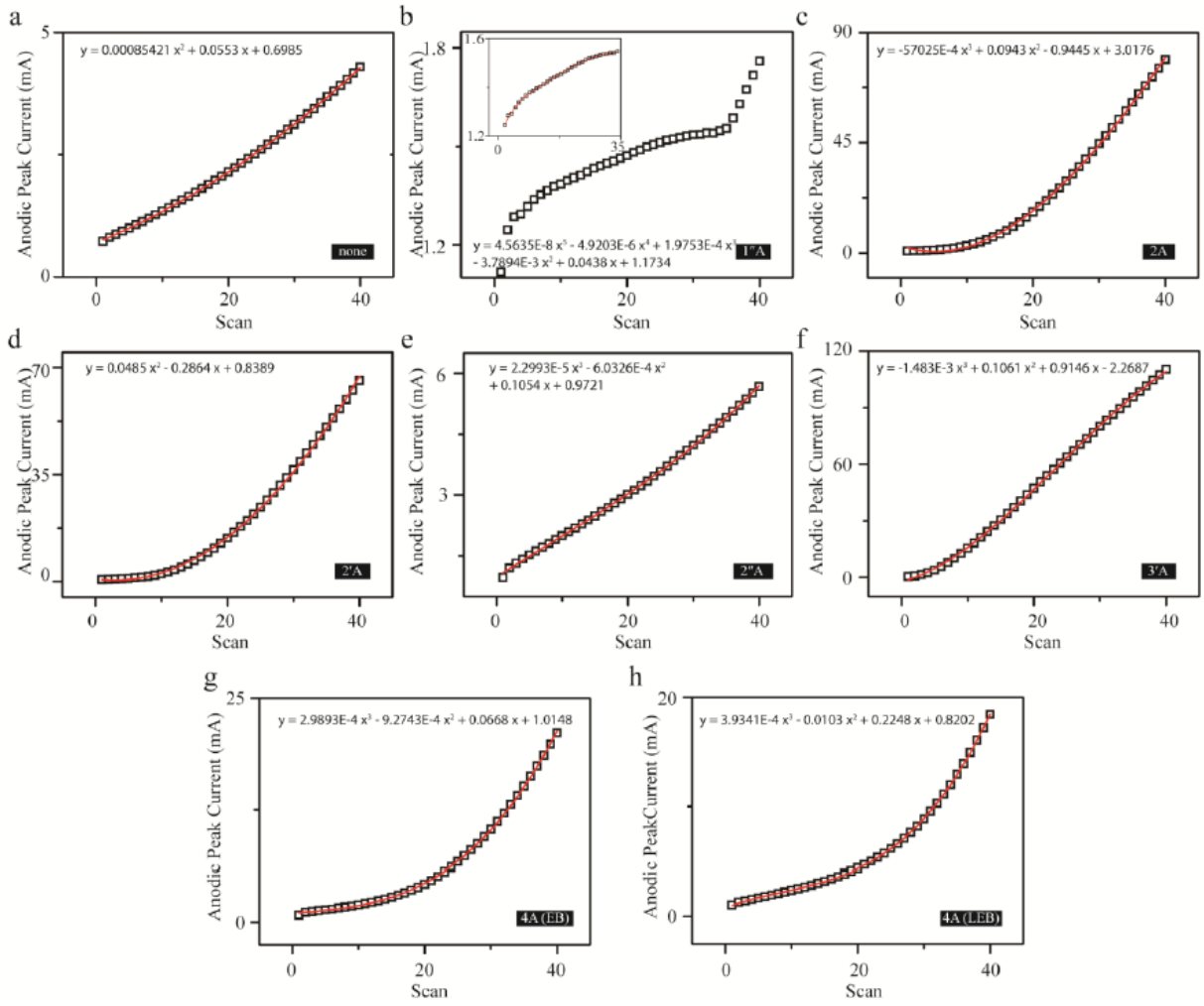

Figure 3-S4. Graphs and polynomial fittings of the anodic peak current versus number of scans for electrochemical polymerization of aniline in a 1.0 M HCl solution with (a) no additives, (b) 1″A, (c) 2A, (d) 2′A, (e) 2″A, (f) 3′A, (g) 4A(EB), and (h) 4A(LEB). The reactions contain 0.2 M of aniline and 1.0 mM of additives, with the potential sweep from -0.2 V to 0.8 V (against Ag/AgCl) at a scan rate of 25 mV/s.

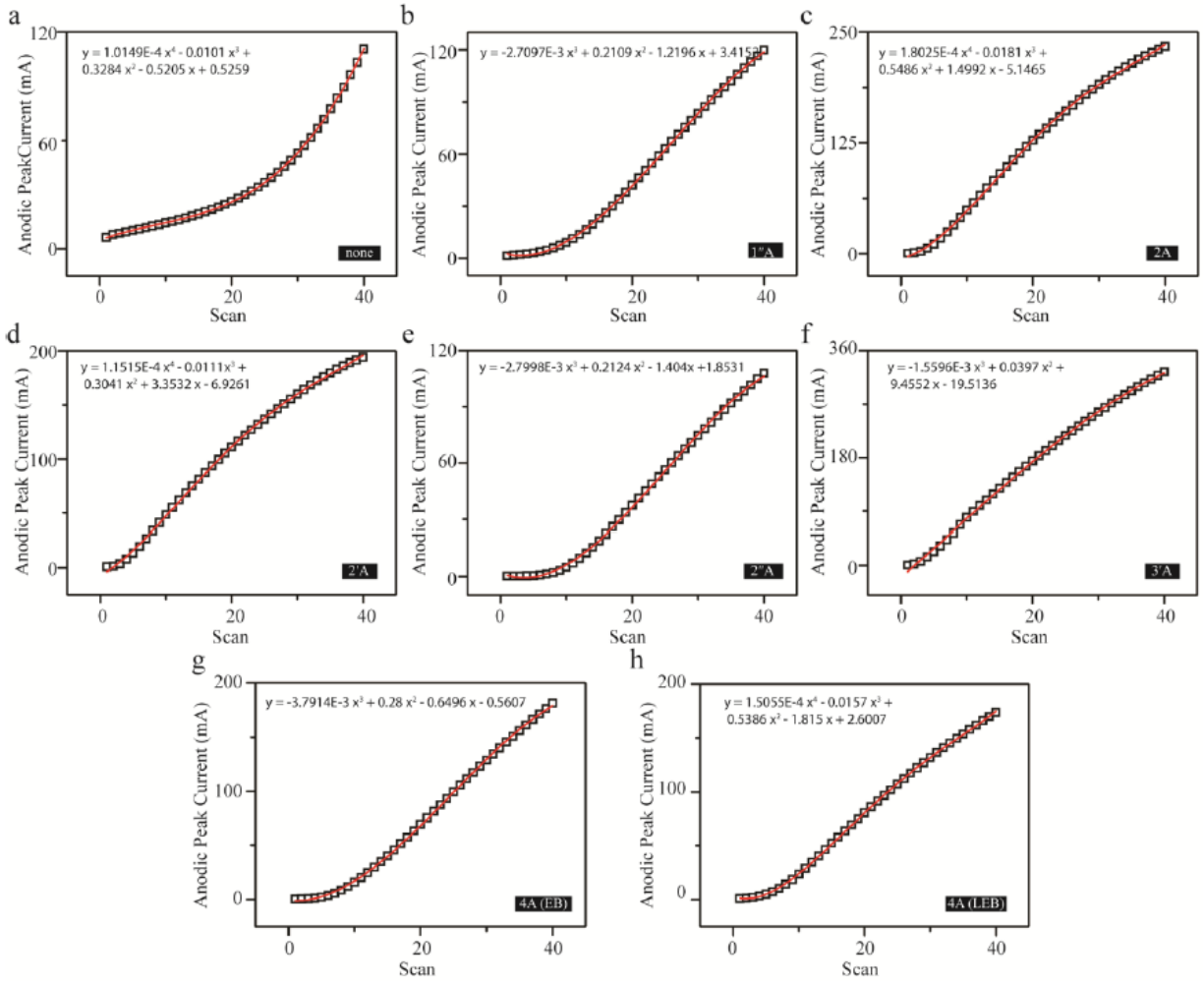

Figure 3-S5. Graphs and polynomial fittings of the anodic peak current versus number of scans for electrochemical polymerization of aniline in a 1.0 M HCl solution with (a) no additives, (b) 1″A, (c) 2A, (d) 2′A, (e) 2″A, (f) 3′A, (g) 4A(EB), and (h) 4A(LEB). The reactions contain 0.2 M of aniline and 1.0 mM of additives, with the potential sweep from -0.2 V to 0.9 V (against Ag/AgCl) at a scan rate of 25 mV/s.

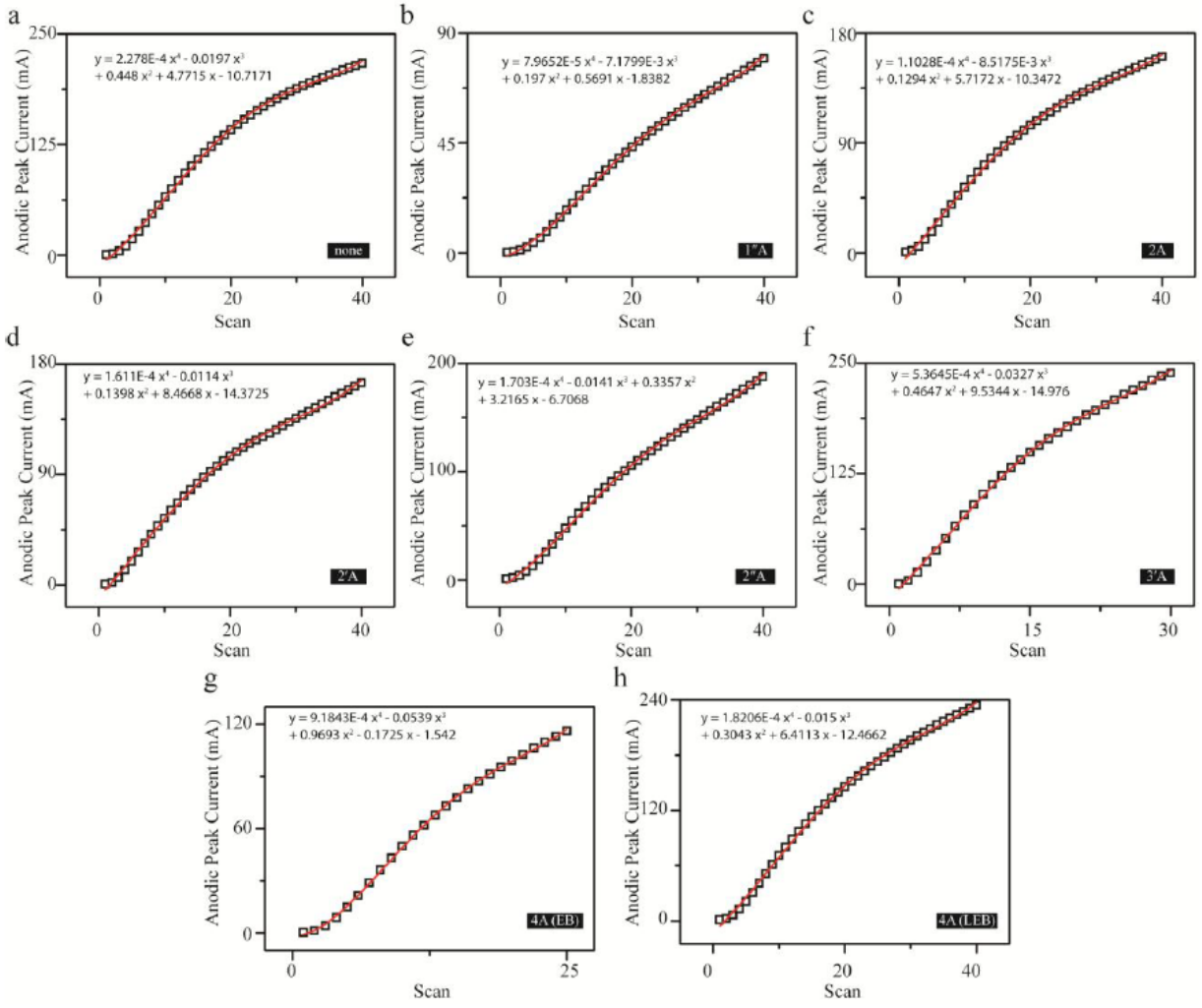

Figure 3-S6. Graphs and polynomial fittings of the anodic peak current versus number of scans for electrochemical polymerization of aniline in a 1.0 M HCl solution with (a) no additives, (b) 1″A, (c) 2A, (d) 2′A, (e) 2″A, (f) 3′A, (g) 4A(EB), and (h) 4A(LEB). The reactions contain 0.2 M of aniline and 1.0 mM of additives, with the potential sweep from -0.2 V to 1.0 V (against Ag/AgCl) at a scan rate of 25 mV/s.

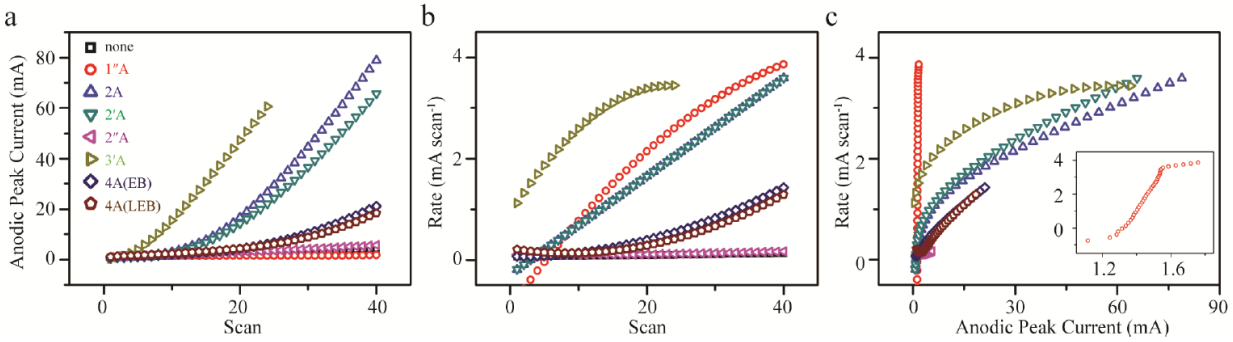

Figure 3-S7. Full graphs of (a) anodic peak current versus number of scans, (b) polymerization rate versus the number of scans, and (c) polymerization rate versus the anodic peak current, for aniline electrochemical polymerization with and without oligoanilines. The reactions contain 0.2 M of aniline and 1.0 mM of additives in a 30 mL 1.0 M HCl solution, with the potential sweep from -0.2 V to 0.8 V (against Ag/AgCl) at a scan rate of 25 mV/s. (Note that the black squares in **Figure 3-S7a** are identical with the anodic peak readings in **Figure 3-2a**)

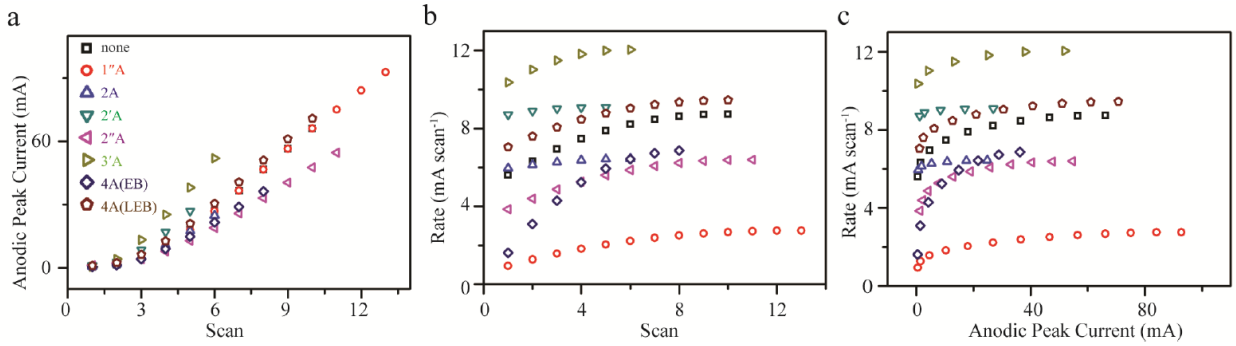

Figure 3-S8. Graphs of (a) anodic peak current versus number of scans, (b) polymerization rate versus the number of scans, and (c) polymerization rate versus the anodic peak current, for aniline electrochemical polymerization with and without oligoanilines. The reactions contain 0.2 M of aniline and 1.0 mM of additives in a 30 mL 1.0 M HCl solution, with the potential sweep from -0.2 V to 1.0 V (against Ag/AgCl) at a scan rate of 25 mV/s

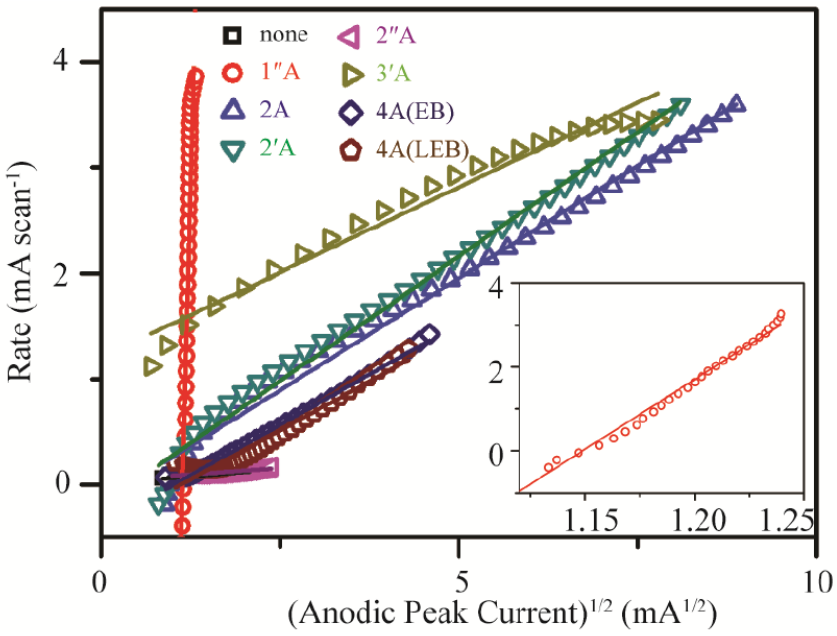

Figure 3-S9. The linear relationship of the rate of electrochemical polymerization of aniline with square root of the anodic peak current. Potential sweep range: -0.2 V to 0.8 V (versus Ag/AgCl). Scan rate: 25 mV/s.

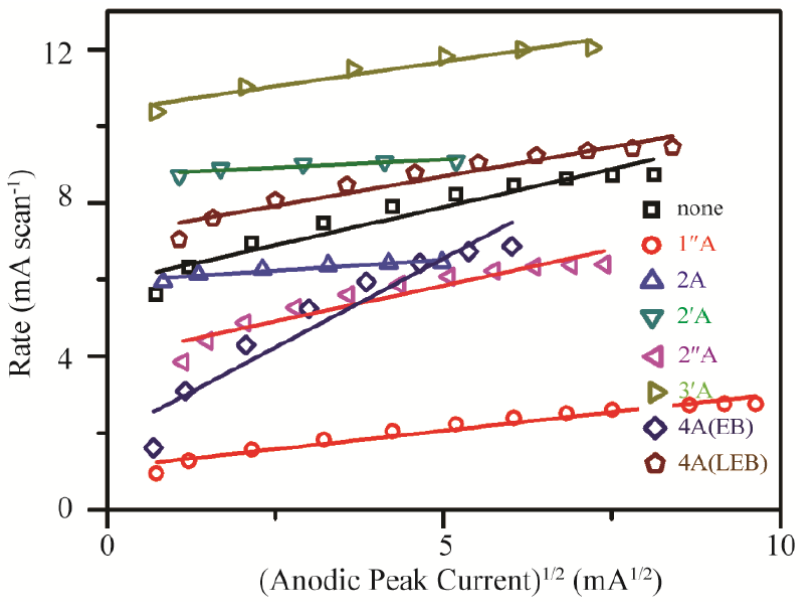

Figure 3-S10. The linear relationship of the rate of electrochemical polymerization of aniline with square root of the anodic peak current. Potential sweep range: -0.2 V to 1.0 V (versus Ag/AgCl). Scan rate: 25 mV/s.

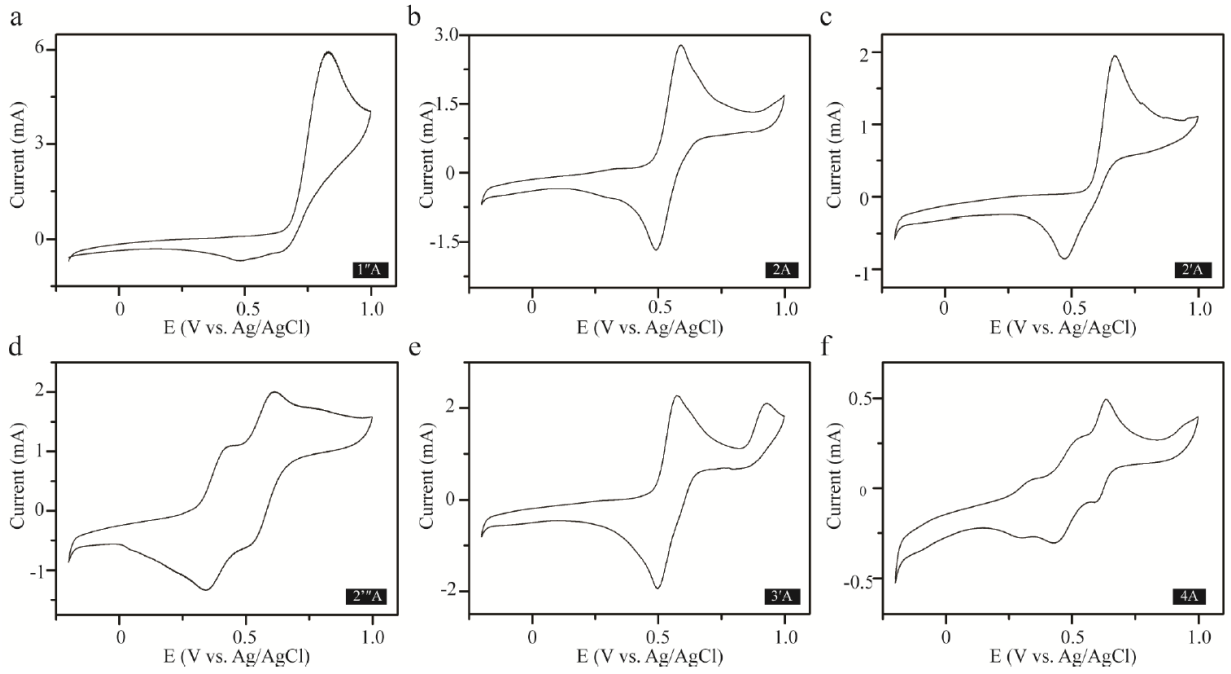

Figure 3-S11. Cyclic voltammograms of 10 mM of (a) 1″A, (b) 2A, (c) 2′A, (d) 2″A, (e) 3′A, and (f) 4A in a 30 mL 1.0 M HCl solution between -0.2 V to 1.0 V (referenced against Ag/AgCl), at a scan rate of 25 mV/s.

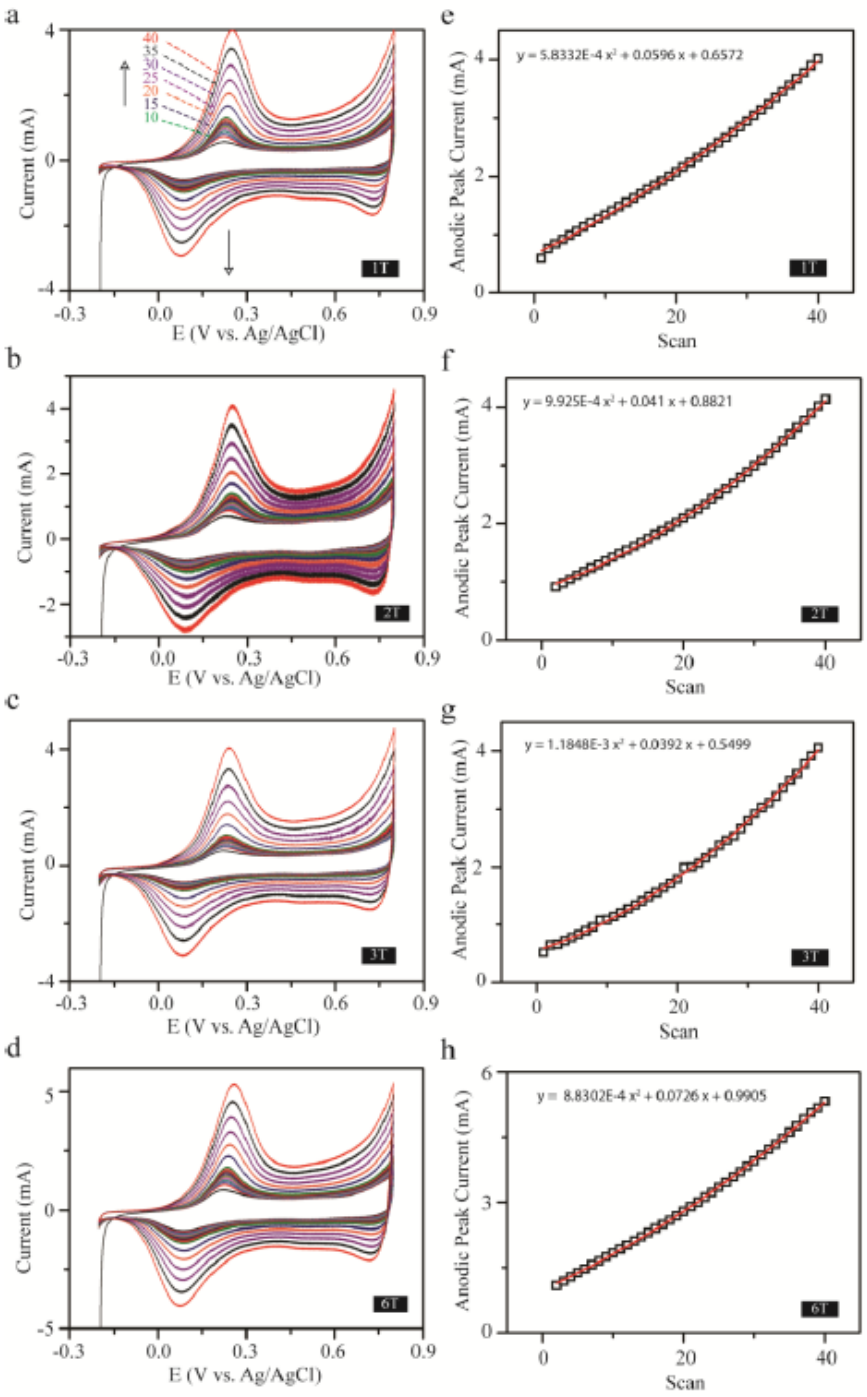

Figure 3-S12. Graphs showing the cyclic voltammograms and the fittings for anodic peak current against number of scans for additives of (a, b) 1T, (c, d) 2T, (e, f) 3T, (g, h) 6T in the electrochemical polymerization of aniline in a 30 mL 1.0 M HCl solution. Sweep range: -0.2 V to 0.8 V (against Ag/AgCl). Scan rate: 25 mV/s.

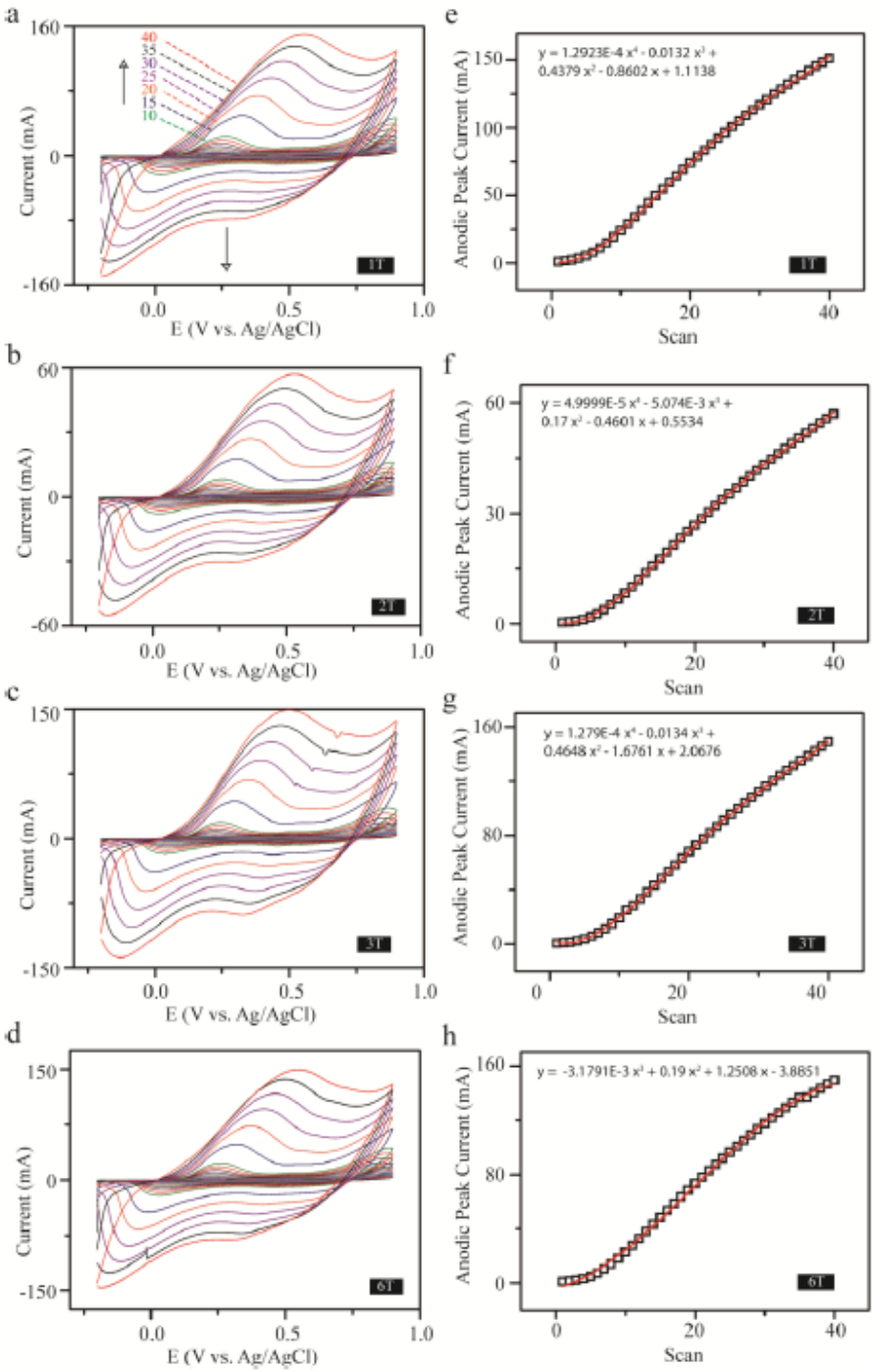

Figure 3-S13. Graphs showing the cyclic voltammograms and the fittings for anodic peak current against number of scans for additives of (a, b) 1T, (c, d) 2T, (e, f) 3T, (g, h) 6T in the electrochemical polymerization of aniline in a 30 mL 1.0 M HCl solution. Sweep range: -0.2 V to 0.9 V (against Ag/AgCl). Scan rate: 25 mV/s.

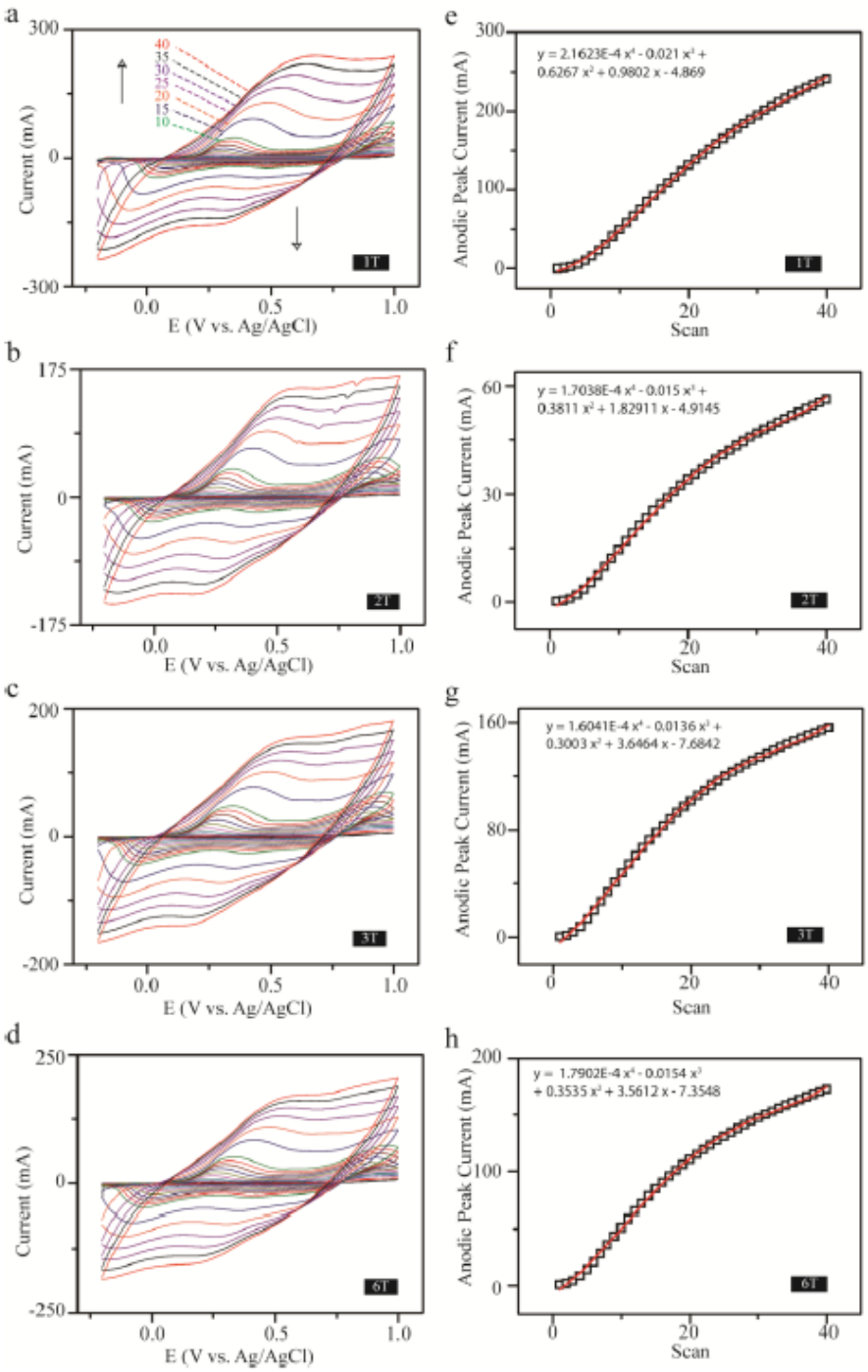

Figure 3-S14. Graphs showing the cyclic voltammograms and the fittings for anodic peak current against number of scans for additives of (a, b) 1T, (c, d) 2T, (e, f) 3T, (g, h) 6T in the electrochemical polymerization of aniline in a 30 mL 1.0 M HCl solution. Sweep range: -0.2 V to 1.0 V (against Ag/AgCl). Scan rate: 25 mV/s.

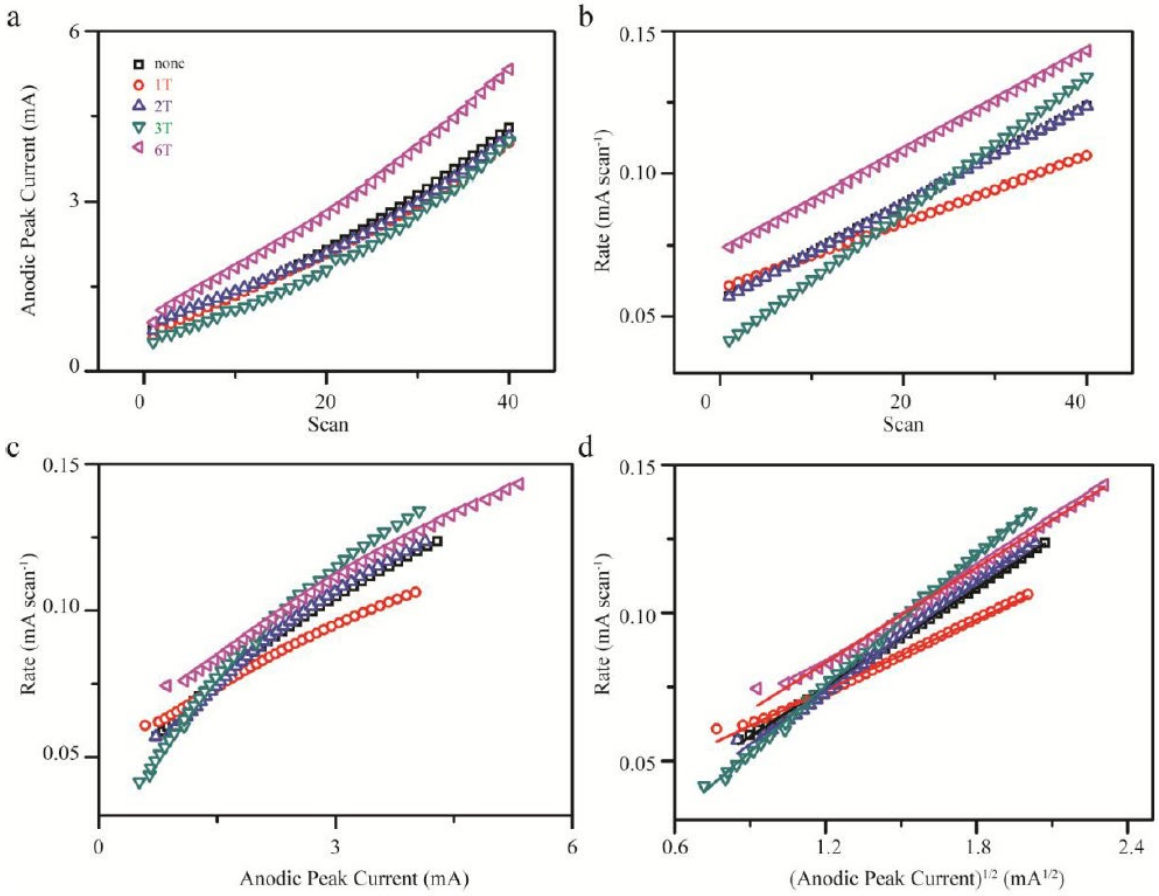

Figure 3-S15. Graphs of (a) anodic peak current versus number of scans, (b) polymerization rate versus the number of scans, (c) polymerization rate versus the anodic peak current, and (d) the fittings for rate versus the square root of anodic peak current, for aniline electrochemical polymerization with and without oligothiophenes. The reactions contain 0.2 M of aniline and 1.0 mM of additives in a 30 mL 1.0 M HCl solution, with the potential sweep from -0.2 V to 0.8 V (against Ag/AgCl) at a scan rate of 25 mV/s.

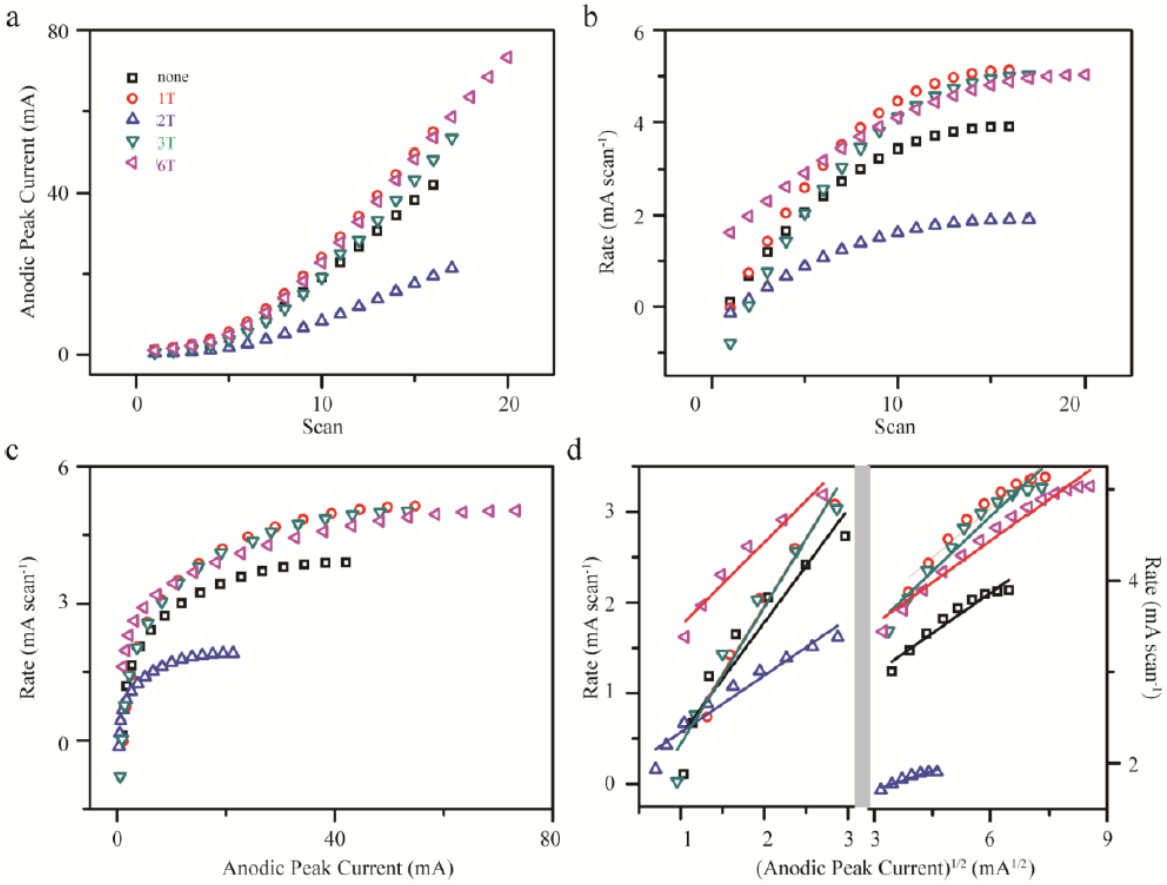

Figure 3-S16. Graphs of (a) anodic peak current versus number of scans, (b) polymerization rate versus the number of scans, (c) polymerization rate versus the anodic peak current, and (d) the fittings for rate versus the square root of anodic peak current, for aniline electrochemical polymerization with and without oligothiophenes. The reactions contain 0.2 M of aniline and 1.0 mM of additives in a 30 mL 1.0 M HCl solution, with the potential sweep from -0.2 V to 0.9 V (against Ag/AgCl) at a scan rate of 25 mV/s.

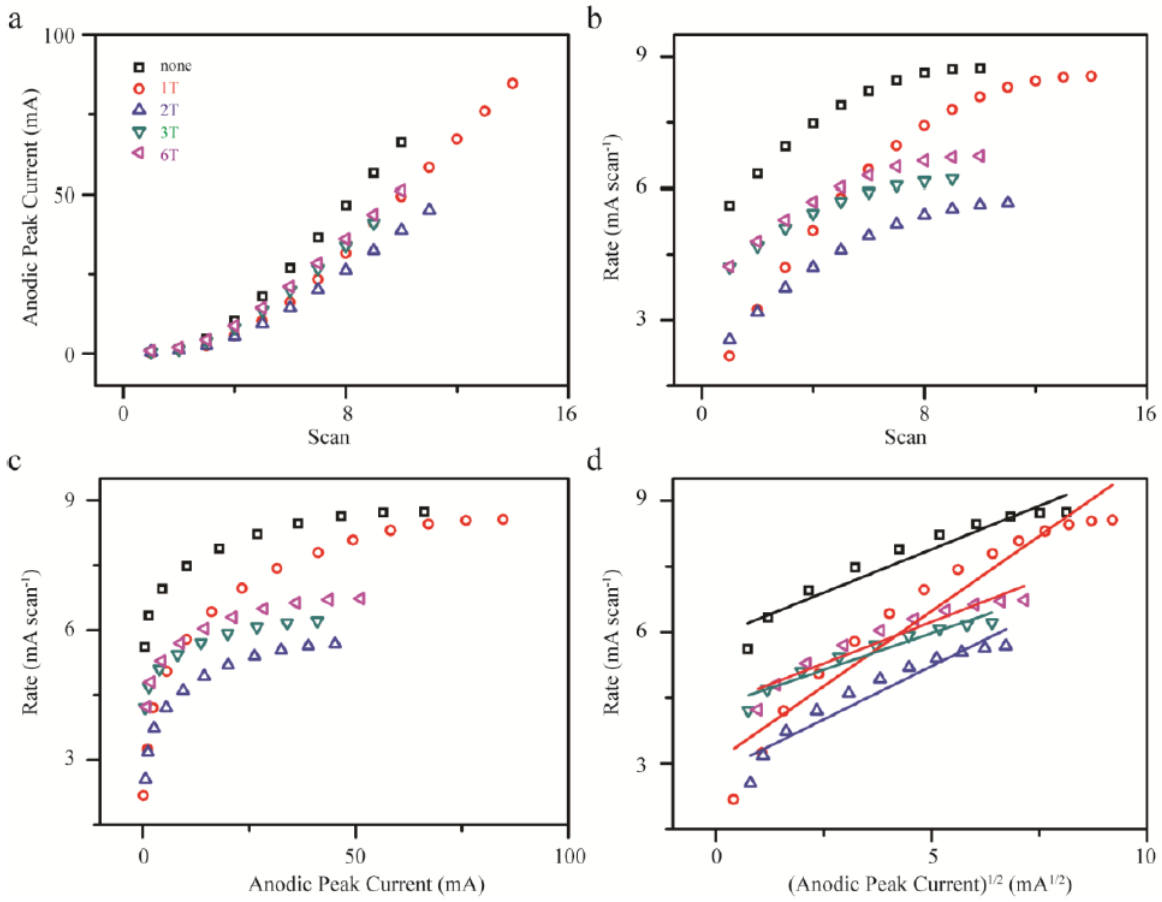

Figure 3-S17. Graphs of (a) anodic peak current versus number of scans, (b) polymerization rate versus the number of scans, (c) polymerization rate versus the anodic peak current, and (d) the fittings for rate versus the square root of anodic peak current, for aniline electrochemical polymerization with and without oligothiophenes. The reactions contain 0.2 M of aniline and 1.0 mM of additives in a 30 mL 1.0 M HCl solution, with the potential sweep from -0.2 V to 1.0 V (against Ag/AgCl) at a scan rate of 25 mV/s.

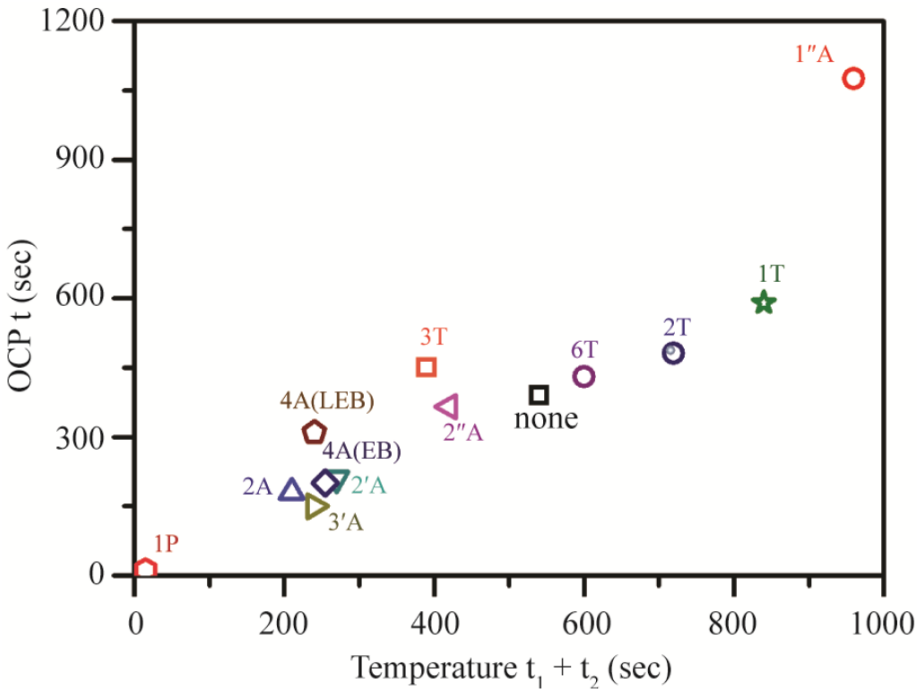

Figure 3-S18. Plot showing t in terms of the open-circuit potential versus $t_1 + t_2$ in terms of temperature for all additives in 1.0 M HCl solutions of chemical polymerization of aniline with ammonium persulfate as the oxidizing agent

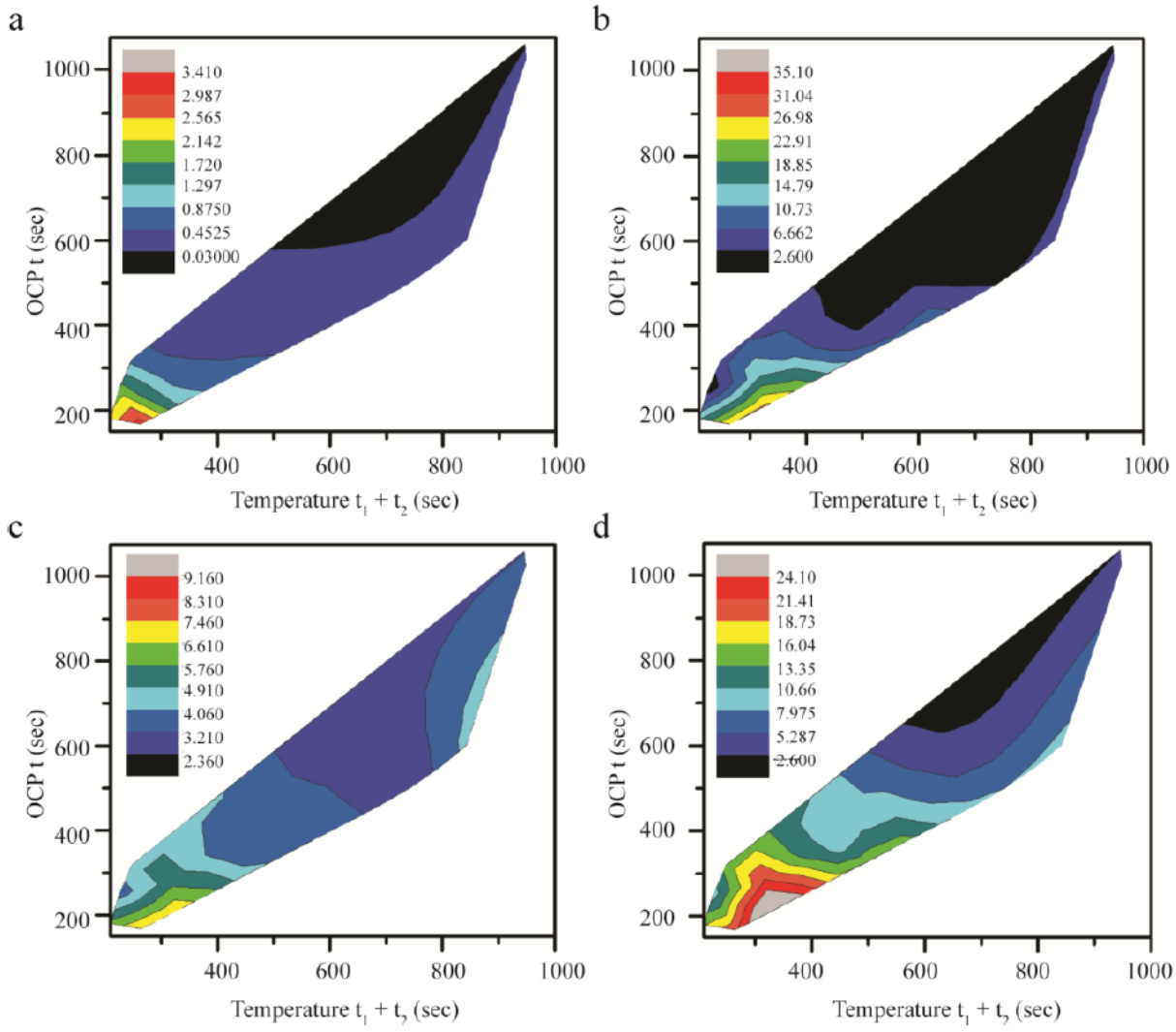

Figure 3-S19. Contour plots of t for the open-circuit potential profiles versus the $t_1 + t_2$ duration for temperature profiles, with color mappings for (a) rate constants at 0.8 V, (b) first rate constant, k_1, at 0.9 V, (c) second rate constant, k_2, at 0.9 V, and (d) rate constant at 1.0 V, for introducing oligoanilines and oligothiophenes into chemical polymerization of aniline in a 1.0 M HCl solution.

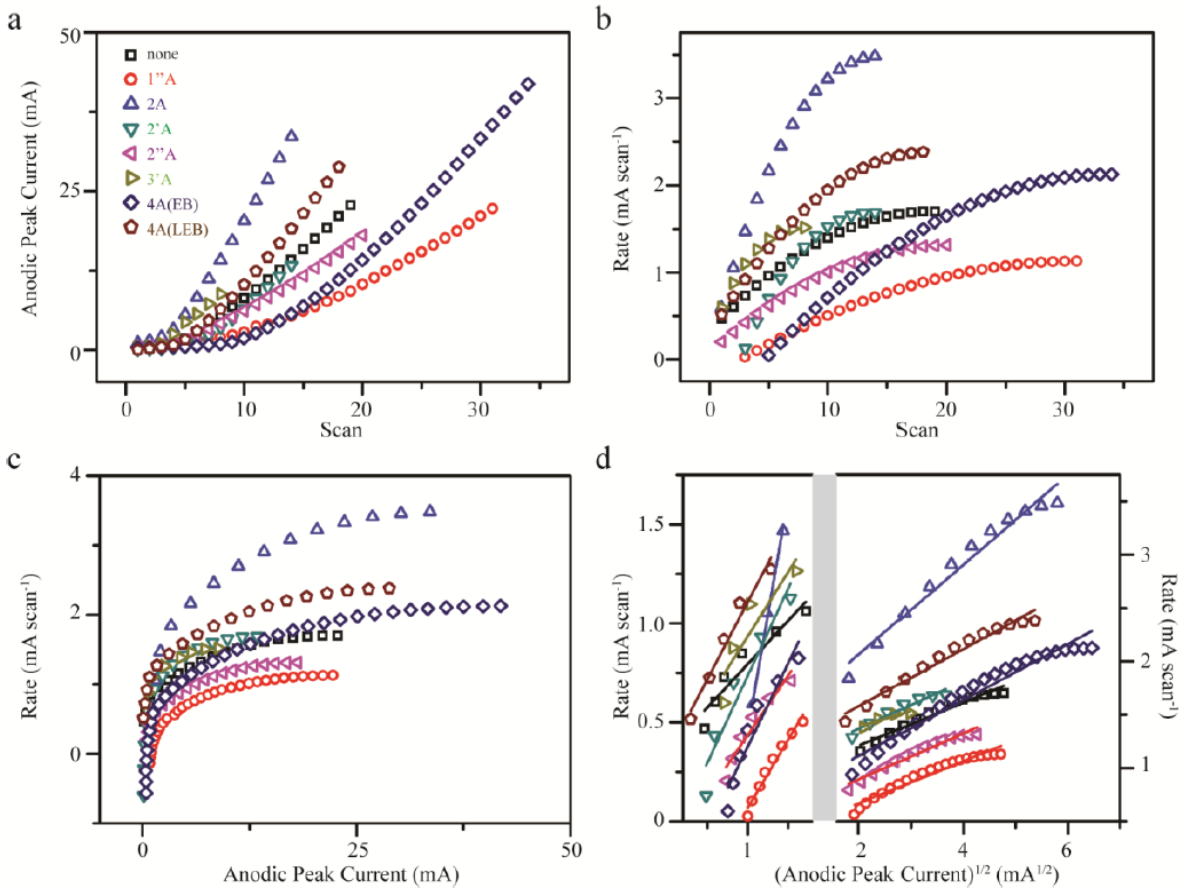

Figure 3-S20. Graphs of (a) anodic peak current versus number of scans, (b) polymerization rate versus the number of scans, (c) polymerization rate versus the anodic peak current, (d) polymerization rate versus the square root of anodic peak current, for aniline electrochemical polymerization with and without oligoanilines to reach their maximum rates of electrochemical polymerization. The reactions contain 0.2 M of aniline and 1.0 mM of additives in a 15 mL 1.0 M HCl and 15 mL of acetonitrile solution, with the potential sweep from -0.2 V to 1.0 V (against Ag/AgCl) at a scan rate of 25 mV/s.

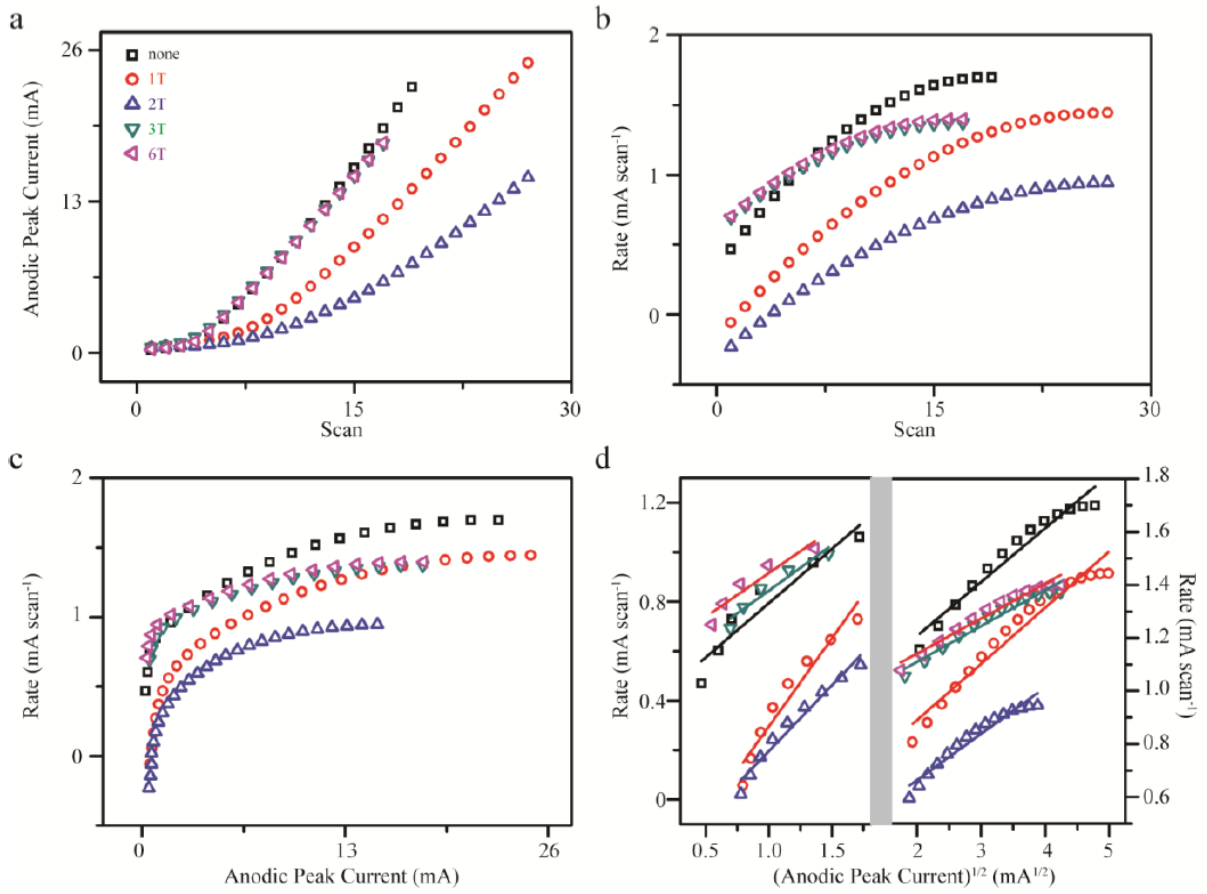

Figure 3-S21. Graphs of (a) anodic peak current versus number of scans, (b) polymerization rate versus the number of scans, (c) polymerization rate versus the anodic peak current, (d) polymerization rate versus the square root of anodic peak current, for aniline electrochemical polymerization with and without oligothiophenes to reach their maximum rates of electrochemical polymerization. The reactions contain 0.2 M of aniline and 1.0 mM of additives in a 15 mL 1.0 M HCl and 15 mL of acetonitrile solution, with the potential sweep from -0.2 V to 1.0 V (against Ag/AgCl) at a scan rate of 25 mV/s.

Table 3-S1. The electrochemical polymerization rate constant k ($mA^{1/2}$ $M^{-1}scan^{-1}$) with and without oligothiophenes and oligoanilines with the potential sweep from -0.2 V to 1.0 V (vs. Ag/AgCl). The concentration of aniline monomer and additives are 0.2 M and 1.0 mM, respectively. The electrochemical polymerization experiments were carried out with a 15 mL 1.0 M HCl and 15 mL acetonitrile solution at a scan rate of 25 mV/s.

additive	k_1 at 1.0 V	k_2 at 1.0 V
none	4.39	2.23
1"A	0.983	1.42
2A	4.05	3.81
2'A	3.39	2.83
2"A	2.16	1.86
3'A	4.72	2.92
4A(EB)	1.91	2.07
4A(LEB)	6.65	2.90
1T	1.63	1.76
2T	1.14	1.44
3T	4.35	2.10
6T	5.36	2.17

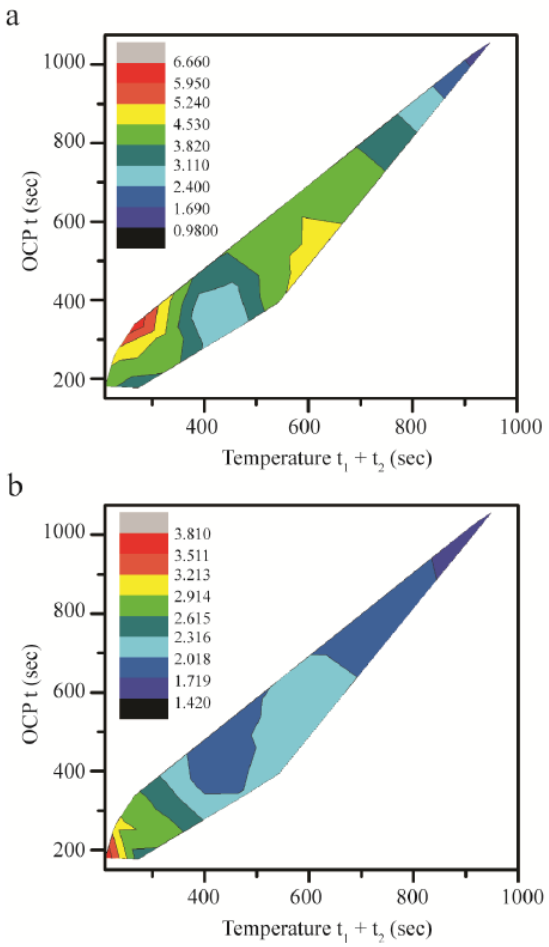

Figure 3-S22. Contour plots of t for the open-circuit potential versus the t_1 + t_2 duration for temperature profiles, with color mappings for (b) first rate constant, k_1, at 1.0 V, and (c) second rate constant, k_2, at 1.0 V, for introducing oligoanilines into chemical polymerization of aniline in a 1.0 M HCl/acetonitrile solution

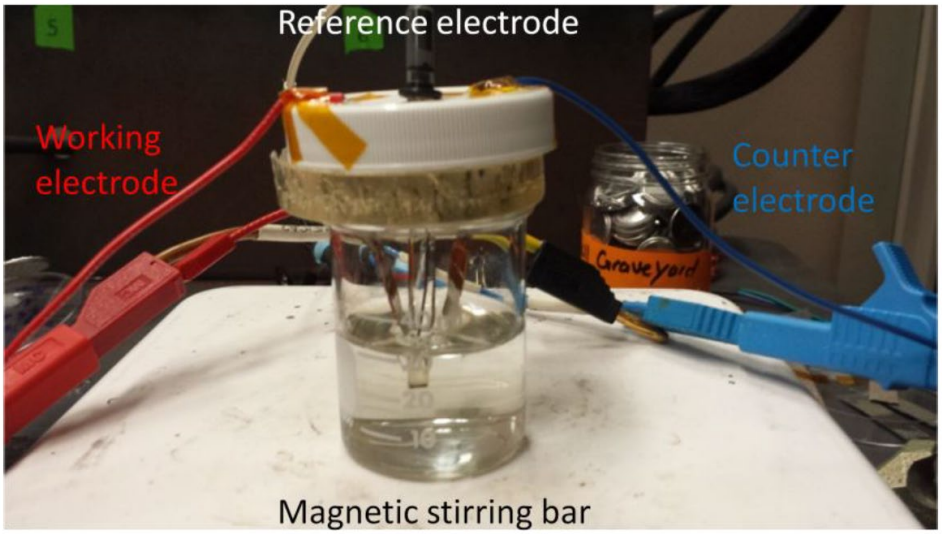

Figure 3-S23. Picture showing the setup for electrochemical reactions

REFERENCES

(1) Runge, F. F. *Ann. Phys.* **1834**, *107* (5), 65–78.

(2) Rasmussen, S. C. *Substantia* **2017**, *1* (12), 99–109.

(3) Letheby, H. *J. Chem. Soc.* **1862**, *15*, 161–163.

(4) MacDiarmid, A. G. *Angew. Chemie - Int. Ed.* **2001**, *40*, 2581–2590.

(5) Heeger, A. J. *Angew. Chemie - Int. Ed.* **2001**, *40*, 2591–2611.

(6) Shirakawa, H. *Angew. Chem. Int. Ed.* **2001**, *40* (14), 2574–2580.

(7) Chiang, J. C.; MacDiarmid, A. G. *Synth. Met.* **1986**, *13* (1–3), 193–205.

(8) Diaz, A. F.; Logan, J. A. *J. Electroanal. Chem. Interfacial Electrochem.* **1980**, *111* (1), 111–114.

(9) Huang, W. S.; Humphrey, B. D.; MacDiarmid, A. G. *J. Chem. Soc. Faraday Trans. 1 Phys. Chem. Condens. Phases* **1986**, *82* (8), 2385–2400.

(10) Tzou, K.; Gregory, R. V. *Synth. Met.* **1992**, *47* (3), 267–277.

(11) Mohilner, D. M.; Adams, R. N.; Argersinger, W. J. *J. Am. Chem. Soc.* **1962**, *84* (19), 3618–3622.

(12) Wei, Y.; Jang, G. W.; Chan, C. C.; Hsueh, K. F.; Hariharan, R.; Patel, S. A.; Whitecar, C. K. *J. Phys. Chem.* **1990**, *94* (19), 7716–7721.

(13) Orata, D.; Buttry, D. A. *J. Am. Chem. Soc.* **1987**, *109* (12), 3574–3581.

(14) Zotti, G.; Cattarin, S.; Comisso, N. *J. Electroanal. Chem.* **1988**, *239* (1–2), 387–396.

(15) Sasaki, K.; Kaya, M.; Yano, J.; Kitani, A.; Kunai, A. *J. Electroanal. Chem.* **1986**, *215* (1–2), 401–407.

(16) Kitani, A.; Yano, J.; Kunai, A.; Sasaki, K. *J. Electroanal. Chem.* **1987**, *221* (1–2), 69–82.

(17) Shim, Y. B.; Park, S. M. *Synth. Met.* **1989**, *29* (1), 169–174.

(18) Wei, Y.; Sun, Y.; Tang, X. *J. Phys. Chem.* **1989**, *93* (12), 4878–4881.

(19) Farmer, J. D.; Kauffman, S. A.; Packard, N. H. *Phys. D Nonlinear Phenom.* **1986**, *22*, 50–67.

(20) Wei, Y.; Hsueh, K. F.; Jang, G. W. *Polymer* **1994**, *35* (16), 3572–3575.

(21) Huang, J.; Virji, S.; Weiller, B. H.; Kaner, R. B. *J. Am. Chem. Soc.* **2003**, *125* (2), 314–315.

(22) Baker, C. O.; Shedd, B.; Innis, P. C.; Whitten, P. G.; Spinks, G. M.; Wallace, G. G.; Kaner, R. B. *Adv. Mater.* **2008**, *20* (1), 155–158.

(23) Li, W.; Wang, H. L. *J. Am. Chem. Soc.* **2004**, *126* (8), 2278–2279.

(24) Tran, H. D.; Wang, Y.; D'Arcy, J. M.; Kaner, R. B. *ACS Nano* **2008**, *2*, 1841–1848.

(25) Cao, Y.; Li, S.; Xue, Z.; Guo, D. *Synth. Met.* **1986**, *16* (3), 305–315.

(26) Kwon, O.; McKee, M. L. *J. Phys. Chem. B* **2000**, *104* (8), 1686–1694.

(27) Zade, S. S.; Zamoshchik, N.; Bendikov, M. *Acc. Chem. Res.* **2011**, *44* (1), 14–24.

(28) D'Aprano, G.; Leclerc, M.; Zotti, G. *Synth. Met.* **1996**, *82* (1), 59–61.

(29) Wei, Y.; Chan, C. C.; Tian, J.; Jang, G. W.; Hsueh, K. F. *Chem. Mater.* **1991**, *3* (5), 888–

897.

(30) Focke, W. W.; Wnek, G. E.; Wei, Y. *J. Phys. Chem.* **1987**, *91* (22), 5813–5818.

(31) Stilwell, D. E.; Park, S.-M. *J. Electrochem. Soc.* **1988**, *135* (2), 2497–2502.

(32) Kobayashi, T.; Yoneyama, H.; Tamura, H. *J. Electroanal. Chem.* **1984**, *177* (1–2), 293–297.

(33) Javadi, H. H. S.; Treat, S. P.; Ginder, J. M.; Wolf, J. F.; Epstein, A. J. *J. Phys. Chem. Solids* **1990**, *51* (2), 107–112.

(34) Wang, Y.; Torres, J. A.; Stieg, A. Z.; Jiang, S.; Yeung, M. T.; Rubin, Y.; Chaudhuri, S.; Duan, X.; Kaner, R. B. *ACS Nano* **2015**, *9* (10), 9486–9496.

(35) Li, D.; Kaner, R. B. *J. Am. Chem. Soc.* **2006**, *128*, 968–975.

(36) Li, D.; Huang, J.; Kaner, R. B. *Acc. Chem. Res.* **2009**, *42* (1), 135–145.

(37) Li, D.; Kaner, R. B. *J. Mater. Chem.* **2007**, *17* (22), 2279–2282.

(38) Huang, J.; Kaner, R. B. *J. Am. Chem. Soc.* **2004**, *126* (3), 851–855.

(39) Zhang, X.; Goux, W. J.; Manohar, S. K. *J. Am. Chem. Soc.* **2004**, *126* (14), 4502–4503.

(40) Wang, Y.; Tran, H. D.; Liao, L.; Duan, X.; Kaner, R. B. *J. Am. Chem. Soc.* **2010**, *132* (30), 10365–10373.

(41) Leng, W.; Chen, M.; Zhou, S.; Wu, L. *Chem. Commun.* **2013**, *49* (65), 7225–7227.

(42) Jonsson, M.; Wayner, D. D. M.; Lusztyk, J. *J. Phys. Chem.* **1996**, *100* (44), 17539–17543.

(43) Sapurina, I. Y.; Stejskal, J. *Russ. J. Gen. Chem.* **2012**, *82* (2), 256–275.

(44) Zotti, G.; Zecchin, S.; Vercelli, B.; Pasini, M.; Destri, S.; Bertini, F.; Berlin, A. *Chem. Mater.* **2006**, *18* (13), 3151–3161.

CHAPTER 4. SYNTHESIS AND CHARACTERIZATION OF SINGLE-PHASE METAL DODECABORIDE SOLID SOLUTIONS: $Zr_{1-x}Y_xB_{12}$ and $Zr_{1-x}U_xB_{12}$

"Reprinted (adapted) with permission from (Akopov, G.; Mak, W. H.; Koumoulis, D.; Yin, H.; Owens-Baird, B.; Yeung, M. T.; Muni, M. H.; Lee, S.; Roh, I.; Sobell, Z. C.; Diaconescu, P. L.; Mohammadi, R.; Kovnir, K.; Kaner, R. B. Synthesis and Characterization of Single-Phase Metal Dodecaboride Solid Solutions: $Zr_{1-x}Y_xB_{12}$ and $Zr_{1-x}U_xB_{12}$. *Journal of the American Chemical Society*, **2019**, *141*(22), 9047-9062.)

ABSTRACT

Single-phase metal dodecaboride solid solutions, $Zr_{0.5}Y_{0.5}B_{12}$ and $Zr_{0.5}U_{0.5}B_{12}$, were prepared by arc melting from pure elements. The phase purity and composition were established by powder X-ray diffraction (PXRD), energy-dispersive X-ray spectroscopy (EDS), X-ray photoelectron spectroscopy (XPS), and ^{10}B and ^{11}B solid-state nuclear magnetic resonance (NMR) spectroscopy. The effects of carbon addition to $Zr_{1-x}Y_xB_{12}$ were studied and it was found that carbon causes fast cooling and as a result rapid nucleation of grains, as well as "templating" and patterning effects of the surface morphology. The hardness of the $Zr_{0.5}Y_{0.5}B_{12}$ phase is 47.6 ± 1.7 GPa at 0.49 N load, which is ∼17% higher than that of its parent compounds, ZrB_{12} and YB_{12}, with hardness values of 41.6 ± 2.6 and 37.5 ± 4.3 GPa, respectively. The hardness of $Zr_{0.5}U_{0.5}B_{12}$ is ∼54% higher than that of its UB_{12} parent. The dodecaborides were confirmed to be metallic by band structure calculations, diffuse reflectance UV–vis, and solid-state NMR spectroscopies. The nature of the dodecaboride colors—violet for ZrB_{12} and blue for YB_{12}—can be attributed to charge-transfer. XPS indicates that the metals are in the following oxidation states: Y^{3+}, Zr^{4+}, and $U^{5+/6+}$. The superconducting transition temperatures (T_c) of the dodecaborides were determined to be 4.5 and 6.0 K for YB_{12} and ZrB_{12}, respectively, as shown by resistivity and superconducting quantum

interference device (SQUID) measurements. The T_c of the $Zr_{0.5}Y_{0.5}B_{12}$ solid solution was suppressed to 2.5 K.

INTRODUCTION

The compositional breadth of metal borides has resulted in a remarkable range of crystal structures.[1,2] This structural diversity yields exciting optical, magnetic and electronic,[3–7] catalytic,[8,9] and mechanical properties.[1,10–12] Metal boride structures range from metal rich subborides[13] (M_4B) to mono-,[14,15] di-,[16,17] and tetraborides,[18–20] to boron rich borides: dodecaborides[21] (MB_{12}) and higher borides[22] (MB_{66}) and β-rhombohedral boron doping phases[23,24] ($MB_{50–100}$); as well as ternary and multinary metal borides.[1,25] Of the aforementioned boride families, metal dodecaborides are interesting due not only to having superior mechanical properties (superhardness),[26–29] but also interesting optical (color)[26–28] and electronic (superconductivity)[30] properties, as well as good oxidation resistance.[26]

Metal dodecaborides can crystallize in two different structures: *cubic*-UB_{12} (*Fm3m*) and *tetragonal*-ScB_{12} (*I4/mmm*) (**Figure 4-1**).[1,21,26,31] The majority of metals form the cubic phase,[1,21] and only Sc, as well as solid solutions based on ScB_{12} (at <5 atom % secondary metal addition), crystallize in the tetragonal structure.[26,31–33] The dodecaboride structure can be thought of as a face-centered cubic (FCC), or body-centered tetragonal (BCT) for ScB_{12}, lattice of 12-coordinate metal atoms, each surrounded by a 24-boron atom cuboctahedron cage. Whether a metal can form a dodecaboride phase is primarily determined by the size of the metal in a 12-coordinate environment; generally, the metal has to have a 12-coordinate radius in between that of zirconium (1.603 Å) and yttrium (1.801 Å).[28,34] Moreover, slight deviations from this range, as in the case of hafnium (1.580 Å)[35] and gadolinium, require high-pressure (6.5 GPa) synthesis[34,35] or ambient pressure stabilization via solid solution formation ($Y_{1–x}Hf_xB_{12}$ and $Zr_{1–x}Gd_xB_{12}$).[27–29]

Most metal dodecaboride phases are incongruently melting and, as such, can either be formed as a mixture of MB_{12} and a lower boride (e.g., ZrB_2 and YB_6) or as MB_{12} and a higher boride or crystalline boron (e.g., YB_{66} and ZrB_{50}).[36,37] This severely limits their potential applications in tooling and as abrasives, due to having either boron-rich phases, which can form boride phases with the binder metals, or having the soft lower boride phases (ZrB_2 and YB_6), which hinder the mechanical properties and also reduce the thermal conductivity of the material and as such heat removal from the tool edge.[38]

Metal dodecaborides can be synthesized as single crystals via zone melting, which is not easily scalable.[38] However, using solid solution alloying, here we have synthesized a single-phase metal dodecaboride phase, $Zr_{0.5}Y_{0.5}B_{12}$ and $Zr_{0.5}U_{0.5}B_{12}$, as confirmed by powder XRD, scanning electron microscopy (SEM) and solid-state NMR spectroscopic data. The fact that these alloys are single phase not only makes it easier to study their properties, but also in the case of mechanical properties has the added benefit of solid solution hardening resulting in enhanced hardness, i.e. 47.6 ± 1.7 GPa at 0.49 N load–a 17% increase in hardness over that of the parent phases (ZrB_{12} and YB_{12}). Furthermore, we have studied the effects of the addition of carbon to the zirconium–yttrium dodecaboride system, as well as provide a possible explanation for the color in metal dodecaborides using diffuse-reflectance, XPS and solid-state NMR (^{10}B and ^{11}B) spectroscopy. Additionally, we studied the magnetic, electronic and thermal properties of the 50/50 atom % solid solution as well as the parent phases. We show that from one single boride structure, subtle variations of stoichiometry can yield a wide range of outcomes, and that careful optimization of even a few atomic percent can yield optimal properties of a superhard, superconducting boride.

For the purposes of this manuscript, boron carbide ($\sim B_{12-x}C_{2-y}$)[39,40] will be referred to as "B_4C" and zirconium carbide ($\sim ZrC_{1-x}$)[41] as "ZrC".

EXPERIMENTAL PROCEDURES

Pellets of the following nominal compositions: $(Zr_{1-x}Y_x):C_z$:13B (x = 0.00, 0.05, 0.25, 0.50, 0.70, 0.75, 0.95 and 1.00; z = 0.0, 0.2, 0.4, 0.5, 0.6, 0.8, and 1.0, C = B_4C + ZrC. Thirteen boron equivalents account for the evaporation of boron during arc-melting; the amount of pure Zr metal was adjusted based on the concentration of ZrC, while the total amount of boron was adjusted based on the amount of boron in B_4C), Zr:C_w:13B and Y:C_w:13B (w = 1.0, 2.0 and 3.0), $(Zr_{0.5}Y_{0.5}):C_z$:13B (z = 0.0, 0.2, 0.4, 0.5, 0.6, 0.8, and 1.0, and C = B_4C, ZrC + B_4C and graphite), and $(Zr_{1-x}U_x)$:20B, (x = 0.00, 0.05, 0.25, 0.50, 0.70, 0.75, 0.95 and 1.00; a metal to boron ratio of 1:20 was used in order to conserve uranium metal, Zr:2.5B, Y:9.0B, boron carbide, (B_4C):zB (z = 2.5, 6, 9, 16, 22 and 36), zirconium carbide, and tungsten carbide were prepared from high-purity metal and boron powders: amorphous boron (99+%, Strem Chemicals, USA), zirconium (99.5%, Strem Chemicals, USA), yttrium (99.9%, Strem Chemicals, USA), depleted uranium metal wire (US Department of Energy), boron carbide (99+%, Strem Chemicals, USA), zirconium carbide (99.5%, Alfa Aesar, USA), tungsten carbide (99.5%, Strem Chemicals, USA) and carbon (graphite, 99+%, Strem Chemicals, USA). In addition, cadmium sulfide (99.999+%, Strem Chemicals, USA), titanium metal (99.9%, Strem Chemicals, USA), chromium metal (99.9%, Strem Chemicals, USA), and potassium permanganate (98%, Alfa Aesar, USA) were used in UV–vis diffuse-reflectance studies. Additionally, ZrB_{12} and YB_{12} samples with a 1:20 metal to boron ratio were prepared for SQUID magnetometry analysis. The amounts of metal were stoichiometrically based on 0.15 g of boron in each sample.

To ensure homogeneous mixing, the weighed powder samples were homogenized in a vortex mixer for ∼1 min and pelletized under a load of 10 tons using a hydraulic press (Carver). The pressed pellets were then placed in an arc melter onto a copper hearth along with oxygen getter

materials (zirconium or titanium metal). The arc-melter chamber was later sealed and evacuated for 20 min followed by purging with argon; this process was repeated four times to ensure that no oxygen was present in the chamber. During arc melting, the getters were melted first to ensure the absorbance of any trace oxygen, and then the samples were heated for $T \sim 1$ to 2 min at $I \sim 145$ A until molten, then allowed to solidify, flipped, and rearced two more times to ensure homogeneity.

The synthesized ingots were cut into two roughly equal pieces using a diamond saw. One half of the ingot was crushed for PXRD using the diamond crusher into a 325 mesh (≤45 μm) powder. PXRD was performed on a Bruker D8 Discover powder X-ray diffractometer (Bruker Corporation, Germany) utilizing a $Cu_{K\alpha}$ X-ray beam (λ_{ave} = 1.5418 Å, $\lambda_{K\alpha1}$ = 1.5406 Å, $\lambda_{K\alpha2}$ = 1.5444 Å, $\lambda_{K\beta}$ is absorbed by a Ni filter) in the 5–100° 2θ range with a scan speed of 0.1055°/s, time per step of 0.3 s. The phases analyzed were cross-referenced against the Joint Committee on Powder Diffraction Standards (JCPDS) database (now International Centre for Diffraction Data (ICDD)). Maud software was used to perform the unit cell refinements.[42–46]

The remaining half of the ingot was mounted in epoxy resin for Vickers hardness measurements and SEM/EDS using an epoxy/hardener set (Allied High Tech Products Inc., USA) and then polished to an optically flat finish on a semiautomated polisher (Southbay Technology Inc., USA) using both silicon carbide abrasive disks of 120–1200 grit (Allied High Tech Products Inc., USA) and 30–1 μm particle-size diamond films (Southbay Technology Inc., USA).

The morphology of the surfaces of the samples was analyzed using an UltraDry EDS detector (Thermo Scientific, USA) and an FEI Nova 230 high-resolution scanning electron microscope (FEI Company, USA). Vickers hardness testing was performed using a MicroMet 2103 Vickers microhardness tester (Buehler Ltd., USA) with a pyramidal diamond indenter tip. Fifteen indents were made at applied loads of 0.49, 0.98, and 1.96 N each, and a minimum of 10 indents were

made at loadings of 2.94 and 4.9 N each. The indents were carried out on randomly chosen spots of the samples. A high-resolution optical microscope (Zeiss Axiotech 100HD, Carl Zeiss Vision GmbH, Germany) with 500× magnification was used to measure the length of the diagonals of each indent. Vickers hardness (H_v) was calculated using eq 1

(1) $H_v = \frac{1854.4F}{a^2}$

where F is the loading force applied in Newtons (N), a is the average of the length of the two diagonals of each indent in micrometers (μm), and H_v is Vickers hardness in gigapascals (GPa).

The reflectance spectra were collected using a diffuse-reflectance attachment on a UV–vis–NIR spectrophotometer (Shimadzu Corp., Japan) in a 400–800 nm range (0.5 nm steps) using $BaSO_4$ powder as background. The acquired reflectance spectra were converted to pseudoabsorbance by applying Kubelka–Munk theory, using eq 2

(2) $A_p = \log\left(\frac{1-\left(\frac{\%R}{100}\right)^2}{2\left(\frac{\%R}{100}\right)}\right)$

where %R is the percent reflectance and A_p is the logarithm of the pseudoabsorbance.

XPS spectra were collected using a Kratos Axis Ultra DLD spectrometer equipped with a monochromatic Al Kα X-ray source. Raw data processing was performed using CasaXPS 2.3 software. Spectral binding energies were calibrated by assigning the C 1s peak with a binding energy of 284.5 eV. For high-resolution XPS, samples were Ar^+ sputter cleaned at an accelerating voltage of 4 kV.

A Bruker AV III 600 (14.10 T) nuclear magnetic resonance (NMR) spectrometer was employed for the acquisition of ^{11}B and ^{10}B NMR signals at frequencies of 192.57 MHz (^{11}B) and 64.51 MHz

(^{10}B), respectively. Specifically, the ^{11}B and ^{10}B NMR spectroscopic data were acquired by using the magic-angle spinning (MAS) technique. The MAS NMR measurements were performed with the use of a 3.2 mm outside diameter zirconia rotor.[47] The NMR spectra were obtained at several spinning rates, ranging from 5 to 17 kHz. The boron background effect resulting from the boron nitride stator in the MAS probe was minimized by the use of the "elimination of artifacts in NMR spectroscopy" pulse sequence.[48] For the ^{11,10}B saturation recovery measurements with MAS at a rate of 17 kHz, the method of pulsing asynchronously to the spinning sample was applied as initially proposed by Yesinowski et al.[49] All samples were washed in dilute HCl/methanol in order to remove any iron content from powderizing. In addition, all samples were mixed with a small amount of NaCl in order to reduce particle-to-particle contacts. The ^{11,10}B chemical shift scales were calibrated using the unified Ξ scale[50] by relating the nuclear shift to the ^{1}H resonance of dilute tetramethylsilane in $CDCl_3$ at a frequency of 600.13 MHz. According to the Ξ scale, the BF_3 etherate compound is the reference for defining zero ppm. The chemical shift referencing was further verified experimentally by acquiring the ^{11,10}B resonance of an aqueous solution of boric acid at pH = 4.4,[51] as well as by measuring a BF_3 etherate sample[50] using a solution-state NMR spectrometer (Bruker AV 600). Analysis and simulations of the MAS NMR spectra were performed by using the Solids NMR Models "sola" in the *TopSpin* software.

The band structures and density of states (DOS) of YB_{12} and ZrB_{12} were calculated using the tight binding-linear muffin tin orbital-atomic sphere approximation (TB-LMTO-ASA) program.[52] The UB_{12} band structure was not calculated due to the presence of correlated f-electrons. The reported crystal structures (YB_{12}: ICSD-23860 and ZrB_{12}: ICSD-409635) were used in the calculations. The calculations used basis sets of Y (5s, 4d), Zr (5s, 5p, 4d), and B (2s, 2p) atomic orbitals, with the 4f and 5p (Y), 4f (Zr), and 3d (B) atomic orbitals downfolded. The band structures and DOS of

each structure were calculated after convergence of the total energy on a dense *k*-mesh of 32 × 32 × 32 points, with 897 irreducible *k* points.

Electrical resistivity was measured from 1.9–300 K using a Physical Property Measurement System (Quantum Design). Arc-melted samples of YB_{12}, ZrB_{12}, and $Zr_{0.5}Y_{0.5}B_{12}$ were cut and polished into regular shapes. Electrical resistivity was measured using the Alternating Current Transport option and a four-probe geometry with 50 μm Pt wires and Ag paste.

SQUID magnetometry was performed in the 2–300 K range initially to narrow down the range of the T_c and in 2–10 K range for other samples with a 0.5 K step size using liquid helium on a Quantum Design Magnetic Properties Measurement System (Quantum Design, USA). The prepared samples were split into pieces, which could fit into a capsule inserted into a plastic sample holder. The samples were treated with HCl, washed with ethanol, and weighed before inserting into the magnetometer. The baseline run of the sample holder was subtracted from the sample signal. All runs were done under an applied field of 10–3 Tesla (10 Oersted).[53]

RESULTS AND DISCUSSION

Previously, the metal dodecaborides were synthesized with a metal to boron ratio of 1:20 in order to prevent the formation of lower boride phases, such as ZrB_2 and YB_6.[26–29] However, in this study we wanted to see whether it is possible to synthesize a single-phase dodecaboride using an almost stoichiometric amount of boron (compensated for the evaporation during arc melting), similar to the case of WB_4, which has to be synthesized using a metal to boron ratio of at least 1 to 8.5[19,54,55] in order to prevent the formation of WB_2 but can be prepared as a single-phase compound by substituting in W for ~32 atom % Ta.[19] Here, we have discovered that a 50/50 atom % solid solution of ZrB_{12} and YB_{12}, prepared with a composition of $(Zr_{0.5}Y_{0.5})13B$, is a single-phase

compound as confirmed by powder XRD (PXRD) (**Figure 4-2**), EDS (**Figure 4-S1**), and ^{11}B NMR spectroscopy (see **Figure 4-10**). As can be seen from the PXRD, the amount of secondary lower boride phases, ZrB_2 and YB_6, decreases with the increased amount of secondary metal, and they are suppressed at the eutectic composition, which can be attributed to the formation of a solid solution. ZrB_{12} and YB_{12} are fully soluble in each other (both being *cubic*- UB_{12} structures) and form solid solutions in the whole range of compositions.[26] This is unsurprising as Zr and Y satisfy all four requirements for solid solution formation according to the Hume–Rothery rules:[56–58] (1) their atomic radii are within ∼15% of each other (r_{Zr} = 1.55 and r_Y = 1.80 Å);[59] (2) they form phases with the same crystal structure (*cubic*- UB_{12} structure type);[1] (3) they have similar electronegativities (1.33 and 1.22 for Zr and Y, respectively);[60,61] and (4) they have similar oxidation states (Zr^{4+} and Y^{3+}).[62] The solid solution formation is also evident in the change of lattice parameters on going from ZrB_{12} (a = 7.411(6) Å) to YB_{12} (a = 7.502(1) Å), closely following Vegard's law[63] as well as in the EDS values for the yttrium concentration being consistent with the nominal composition (**Table 4-1**). Furthermore, the formation of the single-phase compound at the 50/50 atom % composition can be seen in the SEM image in **Figure 4-4** as well as in the results of the NMR spectroscopy discussed later. The ability to synthesize a single-phase metal dodecaboride at stoichiometric metal to boron ratios (accounting for boron evaporation during arc-melting) by means of a solid solution formation allows for much easier synthesis of possible tools and abrasives and their superior properties due to both solid solution hardening (mechanical properties) and better thermal conductivity (due to having only grains of one phase).[38] The only other methods for producing "phase pure" metal dodecaborides are having excess boron (M/B = 1:20), which results in a considerable amount of boron-rich phases; and zone (induction) melting,

although producing single crystals with exact stoichiometry is not easily scalable; furthermore single crystals have inferior mechanical properties than their polycrystalline counterparts.[26–29,38]

Upon the addition of carbon to the dodecaboride system, a change in the relative quantity of the secondary phases can be observed (**Table 4-2, Figure 4-2**). The change of the unit cell parameters for the MB_{12} phase upon the addition of yttrium and carbon can be seen in **Table 4-3**. This is because while carbon does form metal borocarbides[64] for low metal to boron ratios (~1:1), in the case of higher borides and dodecaborides, carbon can be considered an insoluble impurity (**Figure 4-S3**) and as such will preferentially form B_4C, thus reducing the total amount of available boron in the system. However, the addition of carbon has a remarkable effect on the surface morphology of the samples (**Figures 4-3 and 4-4**). Carbon has a similar effect to that of zirconium on tungsten tetraboride[54] in that it causes a rapid cooling and as such very fast nucleation of grains, dramatically reducing their size. This is especially dramatic upon the addition of additional equivalents of carbon, as seen in **Figure 4-3**, where the lower borides, ZrB_2, and B_4C form a lamellar microstructure pattern resulting from an eutectoid transformation of ZrB_2 and B_4C.[65] As can be seen from **Figure 4-4**, upon the addition of carbon, the large "white linear" ZrB_2 and "spiral" YB_6 phases are replaced with a large number of smaller grains. This is similar to the addition of carbide particles to steel, where those particles go to grain boundaries during solidification/annealing and pin the grain boundaries. The full effect of the addition of carbon on the $(Zr_{1-x}Y_x)$:13B solid solution can be seen in **Figures 4-5 and 4-6**. Note that in the case of ZrB_2 a directional grain growth can be seen, where ZrB_2 and B_4C grains are intermixed, which can be attributed to the high melting points of both ZrB_2 and B_4C (~3230 and ~2450 °C, respectively),[36,39] whereas these phases crystallize before the main dodecaboride phase (~2000 °C)[36,37] and serve as "templates"/nucleation points for grain growth, similar to the effect of Ti on WB_4.[54]

In order to investigate whether a source of carbon has any effect on the resulting phase/morphology formation, we performed a study using alloys with a nominal composition of $(Zr_{0.5}Y_{0.5})$:C_z:13 B, where z = 0.2, 0.4, 0.5, 0.8, and 1.0, and the following sources of carbon B_4C, B_4C + ZrC, and graphite (**Figures 4-S10 and 4-S12**). According to the PXRD data in **Figure 4-S10**, in all three cases of different carbon sources, the phase formation is similar, accounting for slight differences in relative intensities of the peaks. Furthermore, optical images in **Figure 4-S12** show that phase formation is indeed independent of the carbon source. On the basis of these facts, it can be inferred that in the case of ZrC as the carbon source ZrC dissociates upon melting into zirconium and carbon, which go on to form the metal dodecaboride and boron carbide phases, respectively; B_4C dissociates into boron and carbon and reforms back into boron carbide; and graphitic carbon (and boron) form boron carbide. These results are important because they show that multiple sources of carbon can be used to form the desired phases, resulting in easier synthesis, especially at low concentrations of carbon addition due to the low molecular weight of carbon.

Figure 4-S6 shows the PXRD of $(Zr_{1-x}U_x)$:20B (1:20 metal to boron ratio was used due to the limited amount of U metal available), which shows the formation of a solid solution between ZrB_{12} and UB_{12} (both being *cubic*- UB_{12} structure).[1] The solid solution formation is also evident in the change of lattice parameters on going from ZrB_{12} (a = 7.411(6) Å) to UB_{12} (a = 7.475(1) Å), closely following Vegard's law[63] as well as in the EDS values for the uranium concentration being consistent with the nominal composition (**Table 4-1**). **Figure 4-S13** shows the morphology of the dodecaboride phases formed for these alloys, which is similar to cases of other dodecaborides prepared at this metal to boron ratio.[26–29]

Vickers hardness for alloys with a composition of $(Zr_{1-x}\ Y_x)$:13B and $(Zr_{1-x}Y_x)$:$C_{1.0}$:13B can be seen in **Figure 4-9**. In both cases, a hardness enhancement can be observed upon increasing the

concentration of secondary metal, culminating at the 50/50 atom % composition. In the case of $(Zr_{1-x}Y_x)$:13B, the hardness increases from 41.6 ± 2.6 and 37.5 ± 4.3 GPa for Zr:13B and Y:13B, respectively, to 47.6 ± 1.7 GPa at 0.49 N load for $(Zr_{0.5}Y_{0.5})$:13B. The low hardness of the Y:13B alloy can be attributed to the large amount of the soft YB_6 phase (27.3 ± 1.2 GPa at 0.49 N load, **Figure 4-S14**). This hardness can be attributed to solid solution hardening effects as outlined by the Hume–Rothery rules discussed above.[56–58] Furthermore, the 50/50 atom % solid solution has an enhanced bulk-modulus of K_0 = 320 ± 5 GPa (k'_0 = 1.2 + 0.1), compared to the parent compounds, Zr:13B and Y:13B, respectively, at K_0 = 276 ± 7 GPa (k'_0 = 2.0 + 0.4) and K_0 = 238 ± 6 GPa (k'_0 = 3.0 + 0.1).[66]The solid solution supports the highest differential stress due to the differences in the radii of Zr and Y and the boron cages.[66]

Upon the addition of 1 equiv of carbon to $(Zr_{1-x}Y_x)$:13B, a similar hardness trend can be observed, culminating at the 50/50 atom % composition. The hardness increases from 46.9 ± 3.7 and 37.8 ± 3.3 GPa, for Zr:$C_{1.0}$:13B and Y:$C_{1.0}$:13B, respectively, to 48.0 ± 3.8 GPa at 0.49 N load for $(Zr_{0.5}Y_{0.5})$:13B. Although, with the addition of carbon, the amount of softer secondary phases increases (27.3 ± 1.2 and 26.0 ± 2.7 GPa at 0.49 N for YB_6 and ZrB_2, respectively, **Figure 4-S14**), it is offset by the formation of superhard B_4C (**Figure 4-S14**), resulting in larger error bars (**Figure 4-7**). A more complete picture of the Vickers hardness change for the $(Zr_{1-x}Y_x)$:C_z:13B system, with the simultaneous variation of both metal and carbon concentrations, can be seen in the 2D contour plots in **Figure 4-13** (complete list of hardness and error values can be seen in **Table 4-S1**). The general trend in hardness here is that samples near the 50/50 atom % metal composition tend to be the hardest, which can be attributed to intrinsic (solid solution) and extrinsic (multiple phases ($Zr_{1-x}Y_xB_{12}$, ZrB_2, YB_6, and B_4C) and grain size (Hall–Petch)[67–70]) hardening.

The hardness for the system with the composition ($Zr_{1-x}U_x$):20B can be seen in **Figure 4-8**. Here again, solid solution hardening can be seen for the 50/50 atom % composition, especially when comparing it to pure UB_{12}. The hardness increases from 41.3 ± 1.1[26,28,29] and 28.1 ± 5.3 GPa for Zr:20B and U:20B, respectively, to 43.4 ± 3.1 GPa at 0.49 N load for ($Zr_{0.5}U_{0.5}$):20B. Again, both zirconium and uranium satisfy the Hume–Rothery[56–58] rules for solid solutions: (1) the atomic sizes are within ∼15% (1.55 and 1.75 Å for Zr and U, respectively),[59](2) ZrB_{12} and UB_{12} crystallize in the same structure (*cubic*- UB_{12}),[1](3) Zr and U have similar electronegativities (1.33 and 1.38 for Zr and U, respectively),(60,61) and (4) Zr and U have similar oxidation states (Zr^{4+} and $U^{5.5+}$, 5.5+ being a combination of 5+ and 6+).[62]

XPS was used to analyze the oxidation state of the metal and the surface composition of the dodecaboride system. There has been a single attempt to ascertain the oxidation state of the metal in a dodecaboride,[62] and thus, this is worth revisiting. **Figures 4-S16 and 4-S17** show XPS survey spectra of ($Zr_{1-x}Y_x$):13B and ($Zr_{1-x}U_x$):20B systems. The B 1s peak was observed at a binding energy of ∼187 eV along with the metal peaks for Zr, Y, and U depending on the sample. These spectra also contained O 1s and C 1s peaks due to possible oxidation and surface contaminants. Elemental composition was calculated (**Table 4-4**) for the metal and boron to compare the varying metal ratios within a system. The atomic percent may not be an accurate representation of the actual composition due to peak overlap of the B 1s and Zr 3d but can be used to verify relative ratios of the respective metals as already shown through EDS. To investigate the oxidation state of the metals, high-resolution XPS spectra (**Figures 4-S18 and 4-S19**) were obtained. As an example, ($Zr_{0.50}Y_{0.50}$):13B was analyzed using high-resolution scans for the Y 3d, B 1s, and Zr 3d peaks. The samples were sputtered with Ar^+ to clean off any surface contaminants prior to these high-resolution scans. A Shirley background was used for peak fitting with spin–orbit splitting

clearly observed for Y 3d and Zr 3d. The metallic Y $3d_{5/2}$ and Y $3d_{3/2}$ components at 155.3 and 157.4 eV were observed along with the Y^{3+} components observed at 157.8 and 160.1 eV for Y $3d_{5/2}$ and Y $3d_{3/2}$,[71,72] respectively. The Zr 3d peak also exhibited spin–orbit splitting with the Zr 3d5/2 and Zr 3d3/2 at 180.5 and 182.5 eV, respectively, corresponding to Zr^{4+}, and peaks at 178.8 and 181.5 eV corresponding to metallic Zr, which is similar to literature values.[73,74] The high-resolution scan was able to deconvolute B 1s from the Zr 3d peak even though the two peaks were not well resolved in the survey scan. In the instance of $(Zr_{0.25}U_{0.75})$:20B (**Figure 4-S19**), a simple peak fitting was carried out on a high resolution XPS spectrum of the U 4f peak showing spin–orbit splitting of the U $4f_{7/2}$ and U $4f_{5/2}$ peak. Sputtering of these samples was not needed. The oxidation state of U can be determined by observing the difference in binding energy between the satellite and U $4f_{5/2}$ peak.[75] Due to the low concentration of uranium, the satellite peaks were not easily determined. Our XPS spectra agrees with that of UB_{12} which has previously been analyzed.[76,77] The splitting within the main U $4f_{7/2}$ and U $4f_{5/2}$ peak signals a multivalent state for uranium. On the basis of previous calculations from high temperature TGA[62] of the oxidation states of uranium, +5 and +6 are the most likely charges on uranium within our system.

Another interesting property of metal dodecaborides is that these phases possess color (**Figures 4-3 to 4-5 and 4-7**). The color changes from blue for YB_{12} and violet for ZrB_{12} to metallic for UB_{12}. Although exhibiting color, all dodecaborides are considered to be metals and not semiconductors.[30,78] Therefore, the existence of color can be attributed to a charge-transfer (similar to $KMnO_4$, **Figure 4-S21**) from the boron cage to the metal and changes with the oxidation state of the metal: Y^{3+}, Zr^{4+}, and $U^{5+/6+}$(**Figure 4-S20**).[62] The diffuse-reflectance spectra for alloys with a composition of $(Zr_{1-x}Y_x)$:13B (**Figure 4-S20**) show a change in the maxima of pseudoabsorbance (after Kubelka–Munk transformation)[79–84] shift from 594 (ZrB_{12}, violet) to 730 (YB_{12}, blue) nm,

closely following Vegard's law[63] values (**Table 4-1 and Figures 4-4 and 4-S19**). For the alloys with a composition $(Zr_{1-x}U_x)$:20B, upon addition of 25 atom % U, the samples lose color and behave more like metals[30] (**Figures 4-S13 and 4-S20**).

Figure 4-10 presents the ^{11}B MAS NMR spectra of $Zr_{1-x}Y_xB_{12}$ compounds (prepared as $(Zr_{1-x}Y_x)$:13B) at ambient temperature. The spinning rate was 17 kHz, sufficient to narrow the line shapes and observe the isotropic shift. Different boron environments will have different chemical shifts and number of resonances in the NMR spectrum. The experimental (**Figure 4-10**, left) and simulated ^{11}B MAS (**Figure 4-10**, right) line shapes are presented in **Figure 4-10**, where good agreement between them can be observed. This indicates that in the case of ZrB_{12} and YB_{12} additional boron resonances (boron sites) arise at the upfield regime matching to the existence of ZrB_2 (−29 ppm) and YB_6 (2.9 ppm) secondary phases, respectively. Extra boron resonances were not detected in $Zr_{0.5}Y_{0.5}B_{12}$, which suggests that all the boron atoms in this material have similar chemical environments. As shown in the inset (**Figure 4-10**, left), a systematic ^{11}B resonance shift was detected with the increased yttrium content in the $Zr_{1-x}Y_xB_{12}$ series. In particular, our data show that the ^{11}B isotropic resonance position for ZrB_{12} that lies around 10 ppm progressively shifts to 16 ppm for $Zr_{0.5}Y_{0.5}B_{12}$ and finally reaches 25 ppm in the case of YB_{12}. The different resonance positions of each ^{11}B NMR spectrum verifies that the Y atoms are incorporated into the crystal lattice and, thus, affect the boron bonding environments (**Figure 4-10**, right). Moreover, the entire $Zr_{1-x}Y_xB_{12}$ series is metallic, and the downfield resonance shift can arise from the differences in the atomic orbital type (s, p, d states) contributions to the density-of-states at the Fermi level from ZrB_{12} to YB_{12}. Reported[85,86] and our (**Figure 4-S22**) electronic structure calculations for MB_{12} show that the dominant contributions to the states in the vicinity of the Fermi level are from B 2p and Y or Zr 4d orbitals, whereas the B 2s contribution is almost negligible.

The presence of d states amply polarizes the inner s shells, despite the fact that the 2p hyperfine interactions are weak compared to the s and d contributions.[87,88] Hence, the observed frequency shift is also proportional to the amount of unpaired d states around the Fermi level due to the admixture of s–d or p–d wave functions,[88,89] as seen in our case.

The ^{11}B and ^{10}B nuclear spin–lattice relaxation rate ($1/T_1$) measurements are able to explore the band structure and Fermi surface characteristics of the $Zr_{1-x}Y_xB_{12}$ series. The T_1 values were obtained by fitting the saturation recovery data to a single exponential function (**Figure 4-11**). The ^{11}B T_1 values were 3.12 ± 0.04 s (ZrB_{12}), 4.29 ± 0.01 s ($Zr_{0.5}Y_{0.5}B_{12}$), and 1.34 ± 0.02 s (YB_{12}) at ambient temperature. The metallic nature (as seen in NMR and resistivity measurements discussed below) of the $Zr_{1-x}Y_xB_{12}$ series allows, by using the isotropic shift as obtained from the MAS experiments and the T1 values at room temperature, us to estimate the Korringa ratio[90] as a function of the yttrium concentration. The experimental values of the Korringa ratios are equal to 0.036 (ZrB_{12}), 0.126 ($Zr_{0.5}Y_{0.5}B_{12}$), and 0.096 (YB_{12}) and are much smaller than unity (evidence for Fermi-contact interaction with s- states[90]). This is direct evidence that the detected frequency shift and relaxation process are not governed by s-type conduction carriers, but other contributions (p or d orbitals) play a dominant role.[88]

To investigate the origin of the relaxation mechanism (magnetic or quadrupolar relaxation), we also acquired the ^{10}B NMR spectrum (**Figure 4-12**, top) both at 10 and 17 kHz in order to identify the isotropic resonance as well as to obtain the ^{10}B T_1 value at ambient temperature (**Figure 4-12**, bottom). By using the ^{10}B and ^{11}B NMR nuclear spin–lattice relaxation data, we can determine the ratios of $\frac{10_{T1M}^{-1}}{11_{T1M}^{-1}}$ and $\frac{10_{T1Q}^{-1}}{11_{T1Q}^{-1}}$ where T_{1M}^{-1} and T_{1Q}^{-1} is the magnetic (related to the magnetic field fluctuations at the nuclear site) and quadrupolar (related to the electric field gradient fluctuations)

relaxation rates, respectively.[91,92] The $\frac{10_{T1M}^{-1}}{11_{T1M}^{-1}}$ is related to the square of the magnetogyric ratios $\left(\frac{\gamma_{10}}{\gamma_{11}}\right)^2$ that is approximately 0.112. On the other hand, the quadrupolar character as given by is $\frac{10_{T1Q}^{-1}}{11_{T1Q}^{-1}}$ related to the ratios of the quadrupole moments, $\frac{Q_{10}^2}{Q_{11}^2} = \frac{2I_{11}+3}{2I_{10}+3} \times \frac{I_{10}^2(2I_{10}-1)}{I_{11}^2(2I_{11}-1)} \times \frac{T_{1Q}(^{11}B)}{T_{1Q}(^{10}B)}$. The nuclear spin quantum numbers are $I_{10} = 3$ (^{10}B nucleus) and $I_{11} = \frac{3}{2}$ (^{11}B nucleus). Hence, the quadrupolar ratio $\frac{Q_{10}^2}{Q_{11}^2}$ is 4.297, and the $\frac{10_{T1Q}^{-1}}{11_{T1Q}^{-1}}$ is now estimated to be around 0.644. According to the experimental results obtained from the saturation recovery of ^{10}B (**Figure 4-12**, bottom) and ^{11}B NMR spectroscopic data for the $Zr_{0.5}Y_{0.5}B_{12}$ compound (**Figure 4-11**), the ratio of $\frac{10_{T1}^{-1}}{11_{T1}^{-1}}$ is equal to 0.089 (a value closer to $\left(\frac{\gamma_{10}}{\gamma_{11}}\right)^2$), verifying the magnetic character of the nuclear spin–lattice relaxation process. Based on all of the aforementioned results, the comparative analysis of the ratio for the two boron isotopes along with the experimental Korringa ratio value indicate that the boron relaxation process for $Zr_{0.5}Y_{0.5}B_{12}$ is mainly magnetic and driven by non-s states at the Fermi level. This result is in agreement with previously reported and our ab initio calculations[85,86] (**Figure 4-S22**), which predicted that the Fermi level is located in the region of a plateau in the density of states that is mainly formed by the boron 2p and metal 4d states, while B 2s contribution at the states near the Fermi level is 18–20 times lower than the B 2p contribution for YB_{12} and ZrB_{12} (**Figure 4-S22**). This is in accordance with the present NMR spectroscopic results, which also verified the major contribution of the non s-states at the Fermi level of the $Zr_{1-x}Y_xB_{12}$ series.

The superconducting properties and metallic character of these metal dodecaborides were assessed with electrical resistivity (**Figure 4-13**) and SQUID magnetometry (**Figure 4-S23**). Dodecaborides were reported to exhibit superconducting transition temperatures in the sub 6 K

range.[93–96] $(Zr_{0.5}Y_{0.5})B_{12}$ (synthesized as $(Zr_{0.5}Y_{0.5})$:13B, T_c = 2.5 K) does not fall between YB_{12} (synthesized as Y:13B, T_c ~ 4.5–5.0 K) and ZrB_{12} (synthesized as Zr:13B, Tc ~ 5.5–6.0 K) (**Figures 4-13 and Figure 4-S23**). This anomalous behavior of the solid solution transition is supported with both types of measurements. It should be noted that while superconductivity of the ZrB_{12} phase is well established, it appears that the YB_{12} phase does not superconduct above 2 K, and the observed T_c is due to the presence of YB_6 (T_c ~ 6–7 K) in the Y:13B sample.[97,98] This is evident when the samples of both dodecaborides are prepared at 1:20 boron ratio, which ensures no lower boride (ZrB_2 or YB_6) phases are present. In the case of ZrB_{12} prepared at both compositions (1:13 and 1:20), the value of T_c, stays the same, while for YB_{12}, prepared at high boron content, the T_c essentially disappears becoming lower than the measurement limit, 2 K (**Figure 4-S23**). Additionally, the residual resistivity at temperatures below T_c for the YB_{12} sample is substantially higher than the residual resistivity for ZrB_{12} and $Zr_{0.5}Y_{0.5}B_{12}$ indicating the presence of a secondary, non-superconducting phase in the Y–B sample, thus supporting the assumption that YB_6 and not YB_{12} is a superconducting phase. For $(Zr_{0.5}Y_{0.5})B_{12}$, the T_c suppression upon diluting Zr with another metal is similar to the one observed for the $Zr_{1-x}Lu_xB_{12}$ system, which was attributed to the presence of impurities.[94,96] Still, this is one of the rare cases where a known superhard material is also a superconductor, and $Zr_{0.5}Y_{0.5}B_{12}$ now joins $WB_{4.2}$[99] and FeB_4.[100]

CONCLUSIONS

A single-phase, as evident by PXRD, SEM, and solid-state NMR spectroscopy, metal dodecaboride, $Zr_{0.5}Y_{0.5}B_{12}$, has been synthesized via solid solution formation. Furthermore, a solid solution of ZrB_{12} and UB_{12} was prepared. The composition and phase purity were established by powder XRD, SEM/EDS, and XPS. The hardness of the $Zr_{0.5}Y_{0.5}B_{12}$ phase is 47.6 ± 1.7 GPa at

0.49 N load, which is ~17% higher compared to its parent compounds, ZrB_{12} and YB_{12}, having a hardness of 41.6 ± 2.6 and 37.5 ± 4.3 GPa, respectively. The hardness of $Zr_{0.5}U_{0.5}B_{12}$ is ~54% higher than that of the UB_{12} parent. In both cases, the hardness increase can be attributed to the solid solution hardening effects. In addition, carbon was added to the mixed dodecaboride system. It was found that carbon plays the role of an insoluble impurity and readily forms boron carbide, B_4C, playing a role in "templating" and patterning effects on the resulting surface morphology. Carbon causes the samples to cool down very rapidly and as such nucleates a large number of small grains. It was also found that the source of carbon generates similar results as far as phase composition and surface morphology. The metal oxidation states were investigated by means of XPS, as the previous determination was carried out only by fitting high-temperature TGA data. The metals were found to be in a +4 state for Zr, a +3 for Y and a +5/+6 state for U. Because dodecaborides are metals, their color phenomenon was investigated using diffuse-reflectance UV–vis spectroscopy, and their color was attributed to the charge-transfer from the 24 atom boron cage to the metal, similar to $KMnO_4$. The color of the $Zr_{1-x}Y_xB_{12}$ solid solution changed from violet for pure ZrB_{12} to blue for YB_{12}; however, for U it was found that upon the addition of 25 at% U, the color disappears and the sample starts to look metallic, suggesting that the corresponding transition has moved beyond the visible region. ^{10}B and ^{11}B solid-state NMR spectroscopy confirmed the cubic structure of the dodecaborides as well as the formation and phase purity of the 50/50 atom % Zr/Y solid solution. Furthermore, it confirmed the metallic character of the dodecaborides and showed that the boron relaxation process for $Zr_{0.5}Y_{0.5}B_{12}$ is mainly magnetic and driven by non-s states at the Fermi level. Metal dodecaborides are known superconductors, with a Tc of ~4.5–6.0 K for ZrB_{12} and YB_{12}, as determined by resistivity and SQUID measurements; however, it was found that the solid solution undergoes a suppression of T_c down to ~2.5 K.

ACKNOWLEDGEMENT

We thank Professor Chong Liu for helpful discussions. We also thank the National Science Foundation Division of Materials Research, Grant No. DMR-1506860, and the Dr. Myung Ki Hong Endowed Chair in Materials Innovation (R.B.K.), a UCLA Graduate Division Dissertation Year Fellowship (G.A.), Laboratory Research and Development Program of the Ames Laboratory under the U.S. Department of Energy Contract No. DE-AC02-07CH11358 (G.A. and K.K.), a UCLA Eugene V. Cota-Robles Fellowship (W.H.M.), the National Science Foundation Grant CHE-1809116 (P.L.D.), and the Virginia Commonwealth University Startup Grant 137422 (R.M.) for financial support. The NMR spectroscopic research is supported by the National Science Foundation MRI program Grant No. 1532232 (R.B.K.). We thank Zachary Hern for help with the uranium metal wire and Gourab Bhaskar for help with sample preparation for resistivity measurements.

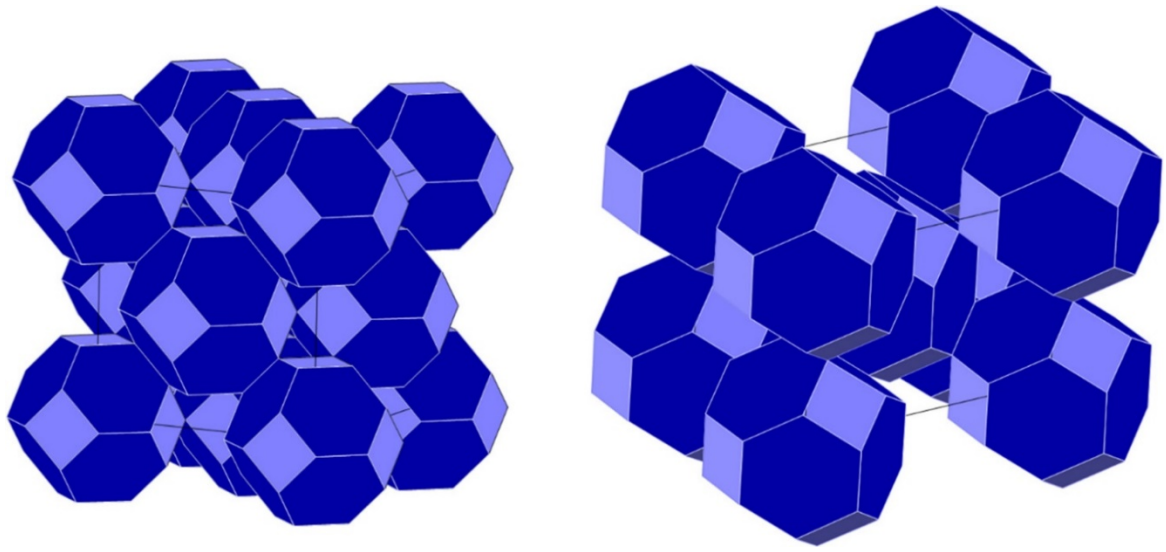

Figure 4-1. (Left) Polyhedra model of the unit cell of a cubic-UB_{12} (ZrB_{12}, $Fm\bar{3}m$, ICSD 409634)(101) structural type metal dodecaboride. (Right) Polyhedra model of the unit cell of a tetragonal-ScB_{12} (ScB_{12}, *I4/mmm*, JCPDS 00-024-1014)(103) structural type metal dodecaboride. Reprinted (adapted) with permission from ref (29).

Table 4-1. Unit Cell Parameters[a,b], Relative Concentration (EDS) of Y in $(Zr_{1-x}Y_x)$:13B and U in $(Zr_{1-x}U_x)$:20B Alloys, and Peak Maxima (Diffuse Reflectance) for $(Zr_{1-x}Y_x)$:13B

	$(Zr_{1-x}Y_x)$:13B					$(Zr_{1-x}U_x)$:20B		
nominal atom % of Y or U	$a_{(XRD)}$[a] (Å)	$a_{(Veg)}$[b] (Å)	atom % Y (EDS)	λ_{meas}[f] (nm)	λ_{veg} (nm)	$a_{(XRD)}$[a] (Å)	$a_{(Veg)}$[b] (Å)	atom % U (EDS)
0	7.411(6)	7.404[c]		594	594	7.409(7)	7.404[c]	
5	7.414(4)	7.409	5.0 ± 0.5	601	601	7.414(4)	7.407	8.1 ± 0.4
25	7.426(1)	7.428	25.8 ± 2.1	630	628	7.428(3)	7.421	31.8 ± 0.7
50	7.453(1)	7.452	49.1 ± 1.5	652	662	7.447(8)	7.439	56.1 ± 1.3
75	7.472(1)	7.476	73.4 ± 2.0	700	696	7.463(5)	7.456	79.2 ± 4.3
95	7.487(6)	7.495	91.0 ± 3.9	715	723	7.473(6)	7.470	95.3 ± 7.8
100	7.502(1)	7.500[d]		730	730	7.475(1)	7.473[e]	

[a]From cell refinement using Maud,(42−46) error in parentheses.

[b]Calculated using Vegard's Law.(63)

[c]Literature value for cell of ZrB12: a = 7.404 Å (ICSD (Inorganic Crystal Structure Database) 409634).(101)

[d]Literature value for cell of YB12: a = 7.500 Å (ICSD 23860).(102)

[e]Literature value for cell of UB12: a = 7.473 Å (ICSD 23862).(102)

[f]Determined from UV–vis diffuse-reflectance analysis

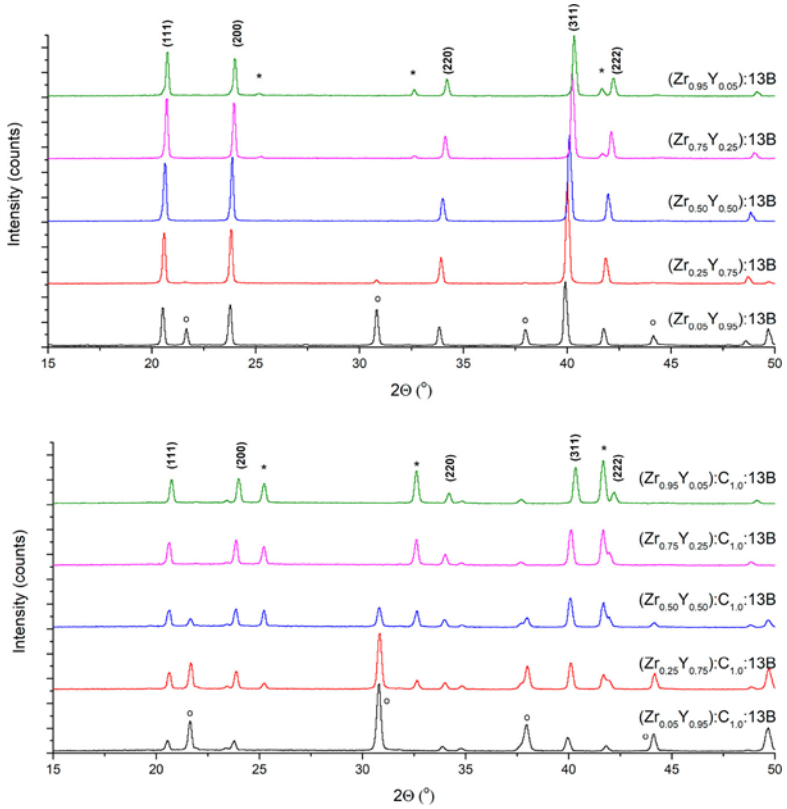

Figure 4-2. Powder XRD patterns of alloys with a composition of (top) $(Zr_{1-x}Y_x)$:13B and (bottom) $(Zr_{1-x}Y_x):C_{1.0}$:13B, where x = 0.05, 0.25, 0.50, 0.75, and 0.95. The peaks were assigned using YB_{12} ($Fm\bar{3}m$, JCPDS 01-073-1382), ZrB_2 (*P6/mmm*, JCPDS 00-034-0423, indicated by (*)), and YB_6 ($Pm\bar{3}m$, JCPDS 03–065–1827, indicated by (°)). The figure shows a 2Θ range from 15–50° (the full PXRD patterns are provided in the Supporting Information, **Figure 4-S2**).

Table 4-2. Phase Formation Scheme for the Alloys with a Nominal Composition of $(Zr_{1-x}Y_x):C_z:13B$[a]

<table>
<tr><td colspan="2"></td><td colspan="7">x</td></tr>
<tr><td colspan="2"></td><td>0</td><td>5</td><td>25</td><td>50</td><td>75</td><td>95</td><td>100</td></tr>
<tr><td rowspan="7">z</td><td>0.0</td><td>ZrB_{12} + ZrB_2</td><td colspan="2">$Zr_{1-x}Y_xB_{12}$ + ZrB_2</td><td>$Zr_{0.5}Y_{0.5}B_{12}$</td><td colspan="2">$Zr_{1-x}Y_xB_{12}$ + YB_6</td><td>YB_{12} + YB_6</td></tr>
<tr><td>0.2</td><td rowspan="5">ZrB_{12} + ZrB_2 + B_4C</td><td colspan="2" rowspan="5">$Zr_{1-x}Y_xB_{12}$ + ZrB_2 + B_4C</td><td>$Zr_{1-x}Y_xB_{12}$ ZrB_2 + B_4C</td><td colspan="2" rowspan="3">$Zr_{1-x}Y_xB_{12}$ + YB_6 + B_4C</td><td rowspan="3">YB_{12} + YB_6 + B_4C</td></tr>
<tr><td>0.4</td></tr>
<tr><td>0.5</td><td rowspan="3">$Zr_{1-x}Y_xB_{12}$ ZrB_2 + YB_6 + B_4C</td></tr>
<tr><td>0.6</td><td rowspan="2"></td></tr>
<tr><td>0.8</td></tr>
<tr><td>1.0</td><td></td><td>$Zr_{1-x}Y_xB_{12}$ YB_6 + B_4C</td><td>YB_{12} + YB_6 + B_4C</td></tr>
</table>

[a]Key: green, single-phase, light green, two-phase; blue, three-phase; and orange, four-phase compositions.

Table 4-3. Unit Cell Parameters[a] of MB_{12} Phase and Relative Concentration[b] (EDS) of Y in $Zr_{1-x}Y_xB_{12}$ for the Alloys with a Nominal Composition of $Zr_{1-x}Y_x$:C_z:13B

		x						
		0	5	25	50	75	95	100
z	0.0	7.411(6)	7.414(4)	7.426(1)	7.453(1)	7.472(1)	7.487(6)	7.502(1)
		-	5.0 ± 0.5	25.8 ± 2.1	49.1 ± 1.5	73.4 ± 2.0	91.0 ± 3.9	
	0.2	7.404(5)	7.417(7)	7.434(7)	7.460(8)	7.476(5)	7.499(5)	7.501(5)
		-	6.0 ± 0.4	27.3 ± 0.6	52.3 ± 1.1	73.7 ± 1.5	80.2 ± 2.2	
	0.4	7.405(2)	7.416(6)	7.442(1)	7.460(5)	7.463(1)	7.497(8)	7.500(1)
		-	8.4 ± 0.4	35.1 ± 0.6	49.4 ± 1.3	68.9 ± 1.3	86.1 ± 3.4	
	0.5	7.404(1)	7.410(7)	7.434(1)	7.461(2)	7.462(4)	7.490(3)	7.505(1)
		-	6.0 ± 0.4	25.3 ± 1.2	52.2 ± 0.6	56.3 ± 0.8	88.7 ± 5.1	
	0.6	7.411(1)	7.419(8)	7.445(2)	7.465(4)	7.454(5)	7.497(3)	7.500(2)
		-	7.4 ± 0.4	36.7 ± 0.8	49.2 ± 0.6	58.5 ± 1.6	90.7 ± 3.8	
	0.8	7.409(6)	7.416(7)	7.441(1)	7.459(4)	7.456(6)	7.490(6)	7.498(8)
		-	11.3 ± 0.3	36.7 ± 0.9	53.4 ± 2.0	52.3 ± 0.7	92.9 ± 2.7	
	1.0	7.405(1)	7.414(4)	7.454(1)	7.459(5)	7.454(1)	7.481(2)	7.496(1)
		-	11.1 ± 0.3	28.4 ± 1.6	49.7 ± 1.2	53.5 ± 3.3	95.1 ± 5.5	

[a]Top value in each cell; from cell refinement using *Maud*,(42−46) error in parentheses.

[b]Bottom value in each cell; error is given after the value.

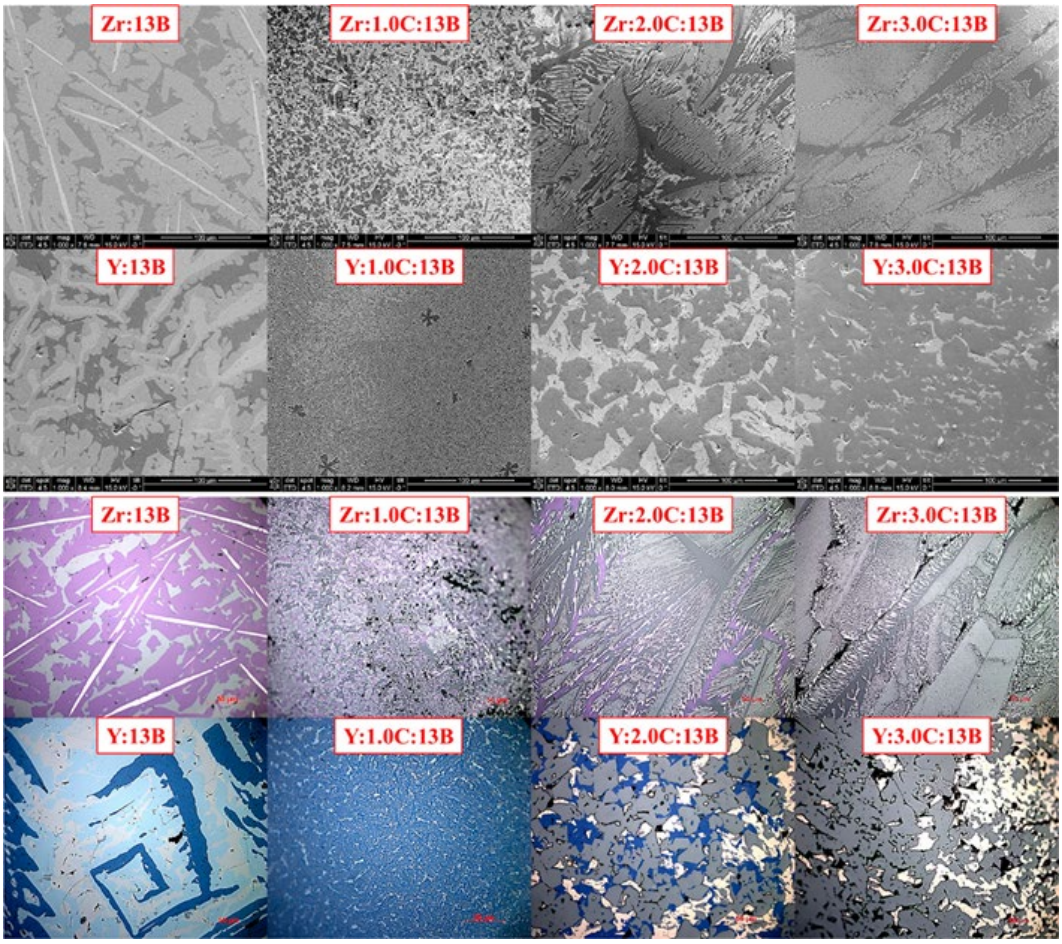

Figure 4-3. SEM and optical images of Zr:C_z:13B and Y:C_z:13B, where z = 0, 1, 2, and 3. All SEM images were taken at 1000× magnification; the scale bars are 100 µm. All optical images were taken at 500× magnification; the scale bars are 50 µm. The images show changes in morphology from "linear" and "spiral" to lamellar microstructures for ZrB_2 and ZrB_{12}(+4 metal oxidation state, violet color) and YB_6 (+3 metal oxidation state, dark blue color) and YB_{12}(+3 metal oxidation state, light blue color), respectively.

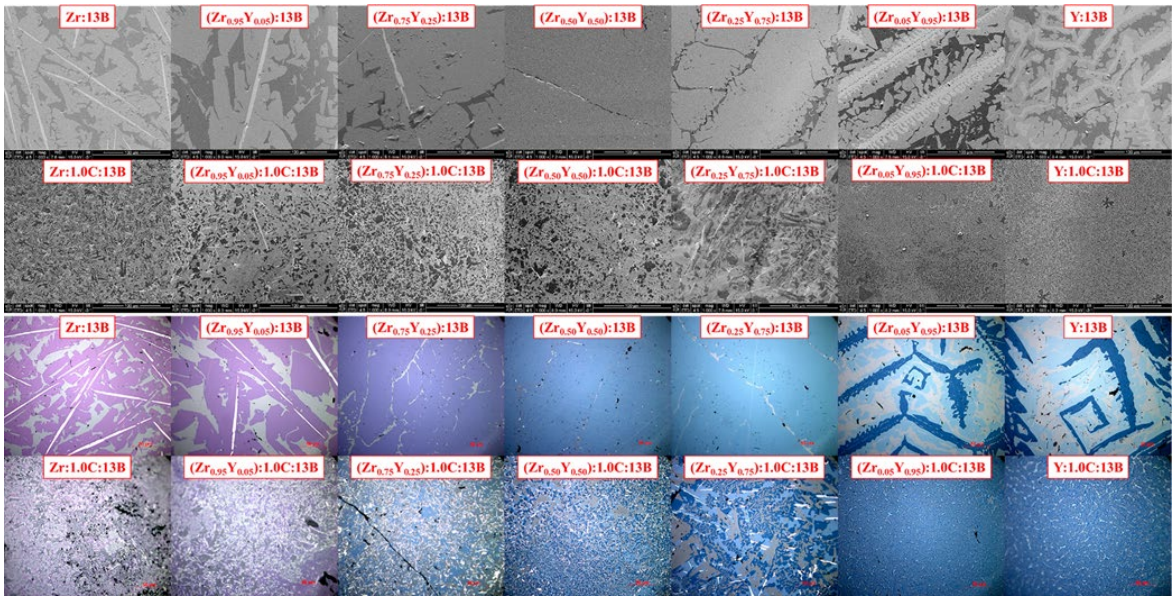

Figure 4-4. SEM and optical images of $(Zr_{1-x}Y_x)$:13B and $(Zr_{1-x}Y_x)$:C1.0:13B, where x = 0.00, 0.05, 0.25, 0.50, 0.75, 0.95, and 1.00. All SEM images were taken at 1000× magnification; the scale bars are 100 μm. All optical images were taken at 500× magnification; the scale bars are 50 μm. The images show the formation of a single-phase compound for $(Zr_{0.5}Y_{0.5})$:13B and the changes of morphology for the MB_{12}, ZrB_2 and YB_6 phases upon addition of carbon.

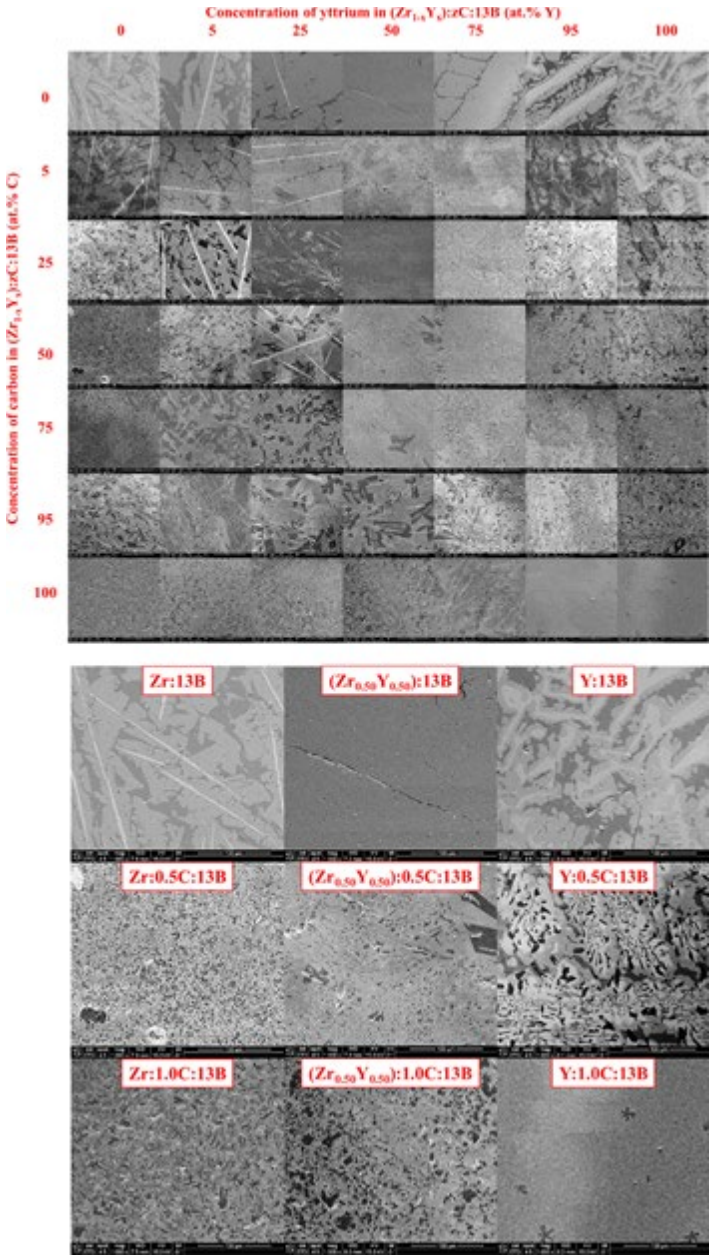

Figure 4-5. SEM images of $(Zr_{1-x}Y_x):C_z:13B$, where x = 0.00, 0.05, 0.25, 0.50, 0.75, and 0.95 and z = 0.0, 0.2, 0.4, 0.5, 0.6, 0.8, 1.0, and 3. All SEM images were taken at 1000× magnification; the scale bars are 100 μm. Bottom images are enlarged versions of the "pure alloys" and 50/50 atom % compositions. The images show the changes of morphology for the MB_{12}, ZrB_2 and YB_6 phases upon addition of carbon.

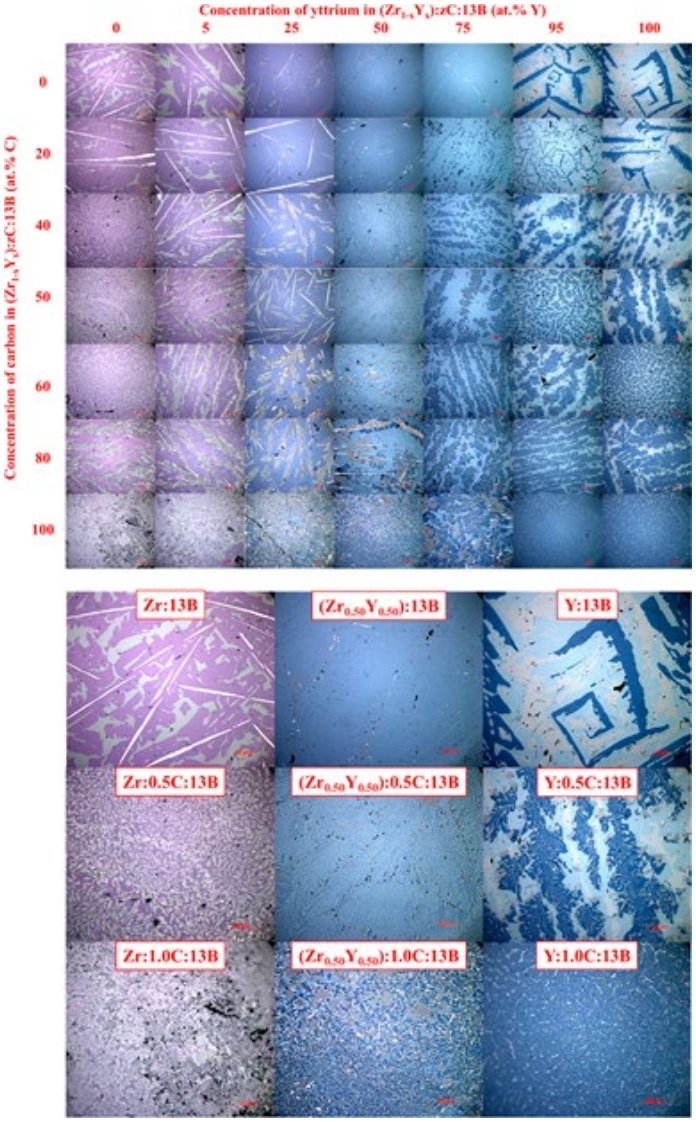

Figure 4-6. Optical images of $(Zr_{1-x}Y_x):C_z:13B$, where x = 0.00, 0.05, 0.25, 0.50, 0.75, and 0.95 and z = 0.0, 0.2, 0.4, 0.5, 0.6, 0.8, 1.0, and 3. All images were taken at 500× magnification; the scale bars are 50 μm. Bottom images are enlarged versions of the "pure alloys" and 50/50 atom % compositions. The images show the changes of morphology for the MB_{12}, ZrB_2 and YB_6 (dark-blue) phases upon addition of carbon as well as color changes for the solid solution on going from ZrB_{12} (+4 metal oxidation state, violet color) to YB_{12} (+3 metal oxidation state, light blue color).

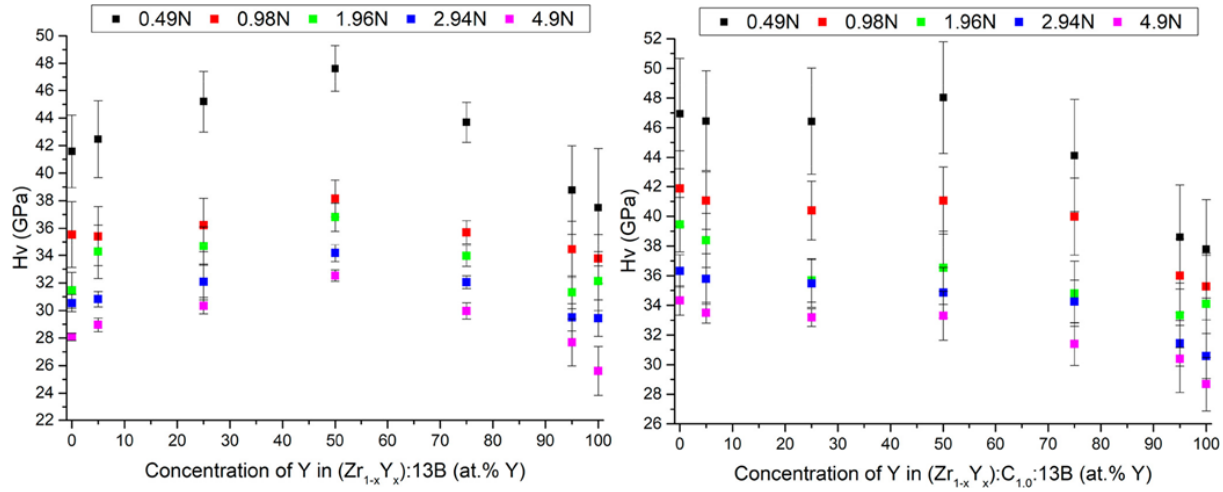

Figure 4-7. Vickers microindentation hardness of alloys with a nominal compositions of (left) $(Zr_{1-x}Y_x)$:13B and (right) $(Zr_{1-x}Y_x)$:C_z:13B, where x = 0.00, 0.05, 0.25, 0.50, 0.75, 0.95, and 1.00 and z = 1.0 at low (0.49 N) to high (4.9 N) applied loads.

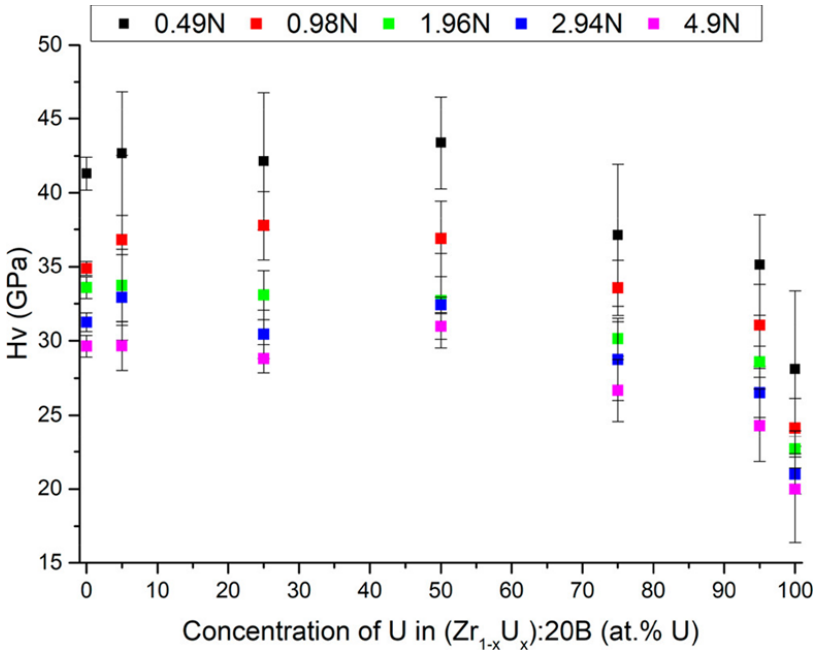

Figure 4-8. Vickers microindentation hardness of alloys with a nominal compositions of $(Zr_{1-x}U_x)$:20B, where x = 0.00, 0.05, 0.25, 0.50, 0.75, 0.95, and 1.00 at low (0.49 N) to high (4.9 N) applied loads.

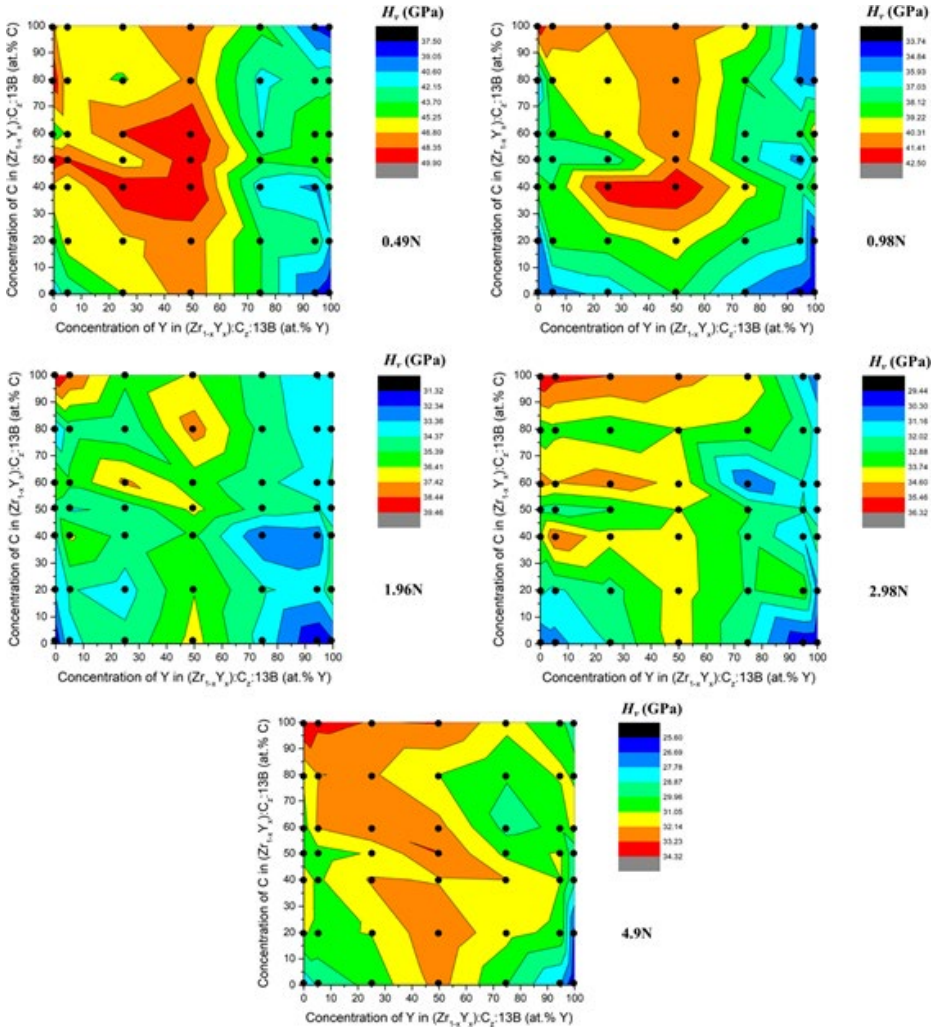

Figure 4-9. Colored contour plots of Vickers microindentation hardness of alloys with a nominal compositions of $(Zr_{1-x}Y_x):C_Z$:13B, where x = 0.00, 0.05, 0.25, 0.50, 0.75, 0.95, and 1.00 and z = 0.0, 0.2, 0.4, 0.5, 0.6, 0.8, and 1.0 at low (0.49 N) to high (4.9 N) applied loads. Black circles represent the data points. The error is within 5.6, 5.9, 5.2, 4.6, and 3.3 GPa for the loads of 0.49, 0.98, 1.96, 2.98, and 4.9 N, respectively. **Table 4-S1** contains all numeric values for the hardness and error values used to make the contour plots.

Table 4-4. Concentration (XPS) of Y in $(Zr_{1-x}Y_x)$:13B and U in $(Zr_{1-x}U_x)$:20B Alloys

	Absolute composition					Absolute composition			
nominal composition	Zr 3p (atom %)	Y 3p (atom %)	B 1s (atom %)	Y 3p (rel[b] atom %)	nominal composition	Zr 3p (atom %)	U 4f (atom %)	B 1s (atom %)	U 4f (rel[b] atom %)
Zr:13B	3.39		96.61						
$(Zr_{0.95}Y_{0.05})$:13B	3.49	[a]	96.51	[a]	$(Zr_{0.95}U_{0.05})$:20B	2.50	0.52	96.98	17.2
$(Zr_{0.75}Y_{0.25})$:13B	2.83	1.14	96.03	28.7	$(Zr_{0.75}U_{0.25})$:20B	2.41	1.17	96.41	32.6
$(Zr_{0.50}Y_{0.50})$:13B	2.17	2.36	95.47	52.1	$(Zr_{0.50}U_{0.50})$:20B	2.40	1.61	95.99	40.1
$(Zr_{0.25}Y_{0.75})$:13B	1.68	4.47	93.85	72.6	$(Zr_{0.25}U_{0.75})$:20B	0.92	1.67	97.40	64.5
$(Zr_{0.05}Y_{0.95})$:13B	[a]	5.57	94.43	[a]	$(Zr_{0.05}U_{0.95})$:20B	[a]	5.35	94.65	[a]
Y:13B		9.26	90.74		U:20B		6.04	93.96	

[a]Peak not visible due to low concentration.

[b]Calculated from the absolute metal composition.

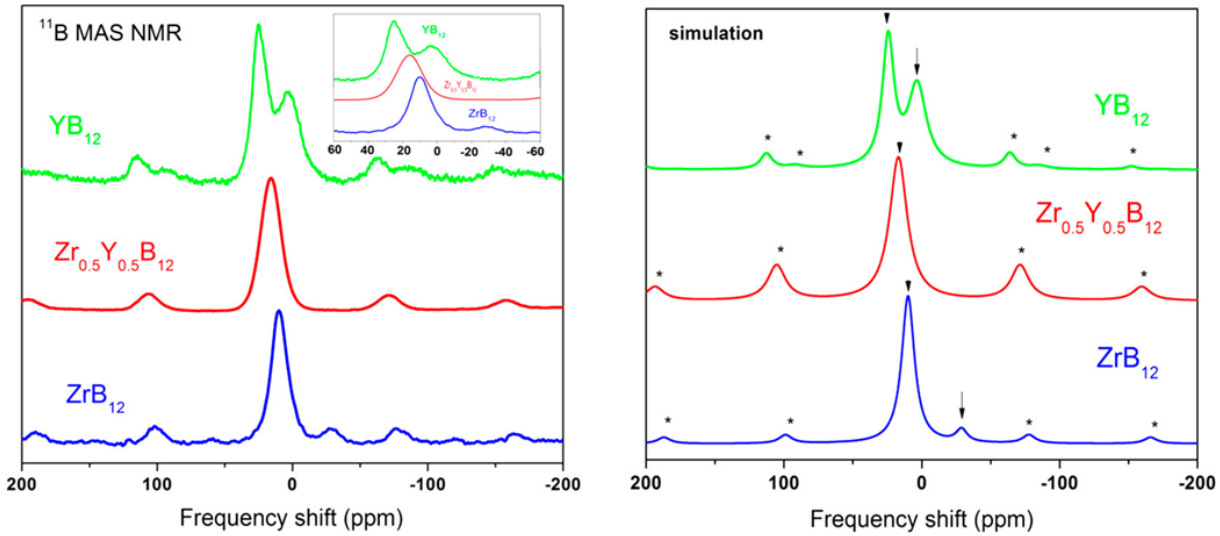

Figure 4-10. ^{11}BMAS NMR experimental and simulated spectra for $Zr_{1-x}Y_xB_{12}$ series (prepared as $(Zr_{1-x}Y_x)$:13B). The spinning rate is 17 kHz. Asterisks indicate spinning sidebands. There is a systematic downfield resonance shift going from ZrB_{12} (blue line) to YB_{12} (green line) accompanied by a substantial line broadening, as shown in the inset. The simulated NMR spectra identify the spinning sidebands and the isotropic resonances. The additional boron resonances in case of YB_{12} and ZrB_{12} confirm the presence of YB_6 and ZrB_2, respectively.

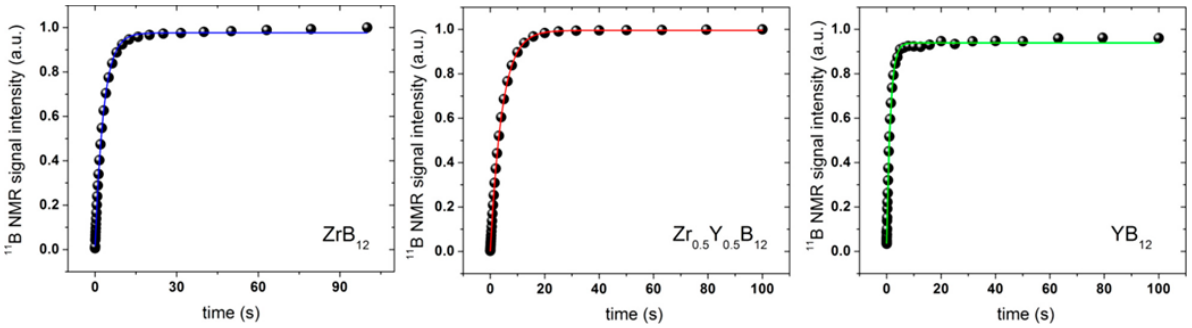

Figure 4-11. ^{11}B NMR saturation recovery results for (left) ZrB_{12}(prepared as Zr:13B), (middle) $Zr_{0.5}Y_{0.5}B_{12}$(prepared as $(Zr_{0.5}Y_{0.5})$:13B), and (right) YB_{12}(prepared as Y:13B) at ambient temperature. The solid smooth lines represent the fittings of single exponential functions to the data.

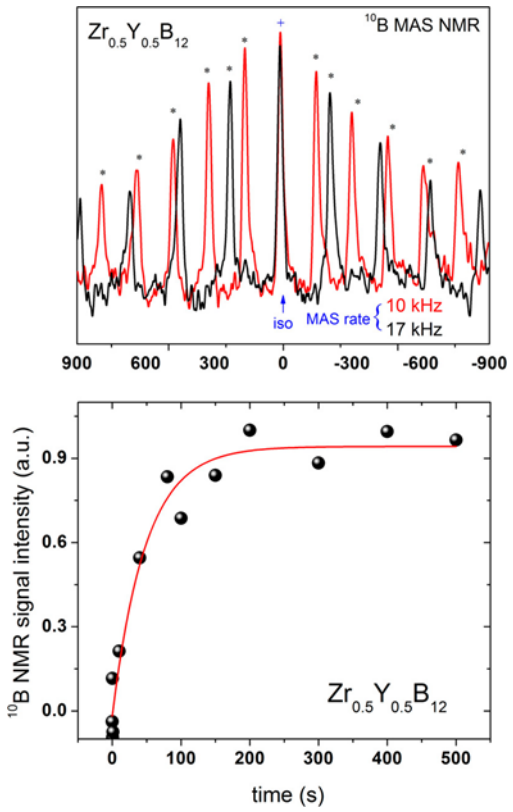

Figure 4-12. ^{10}B MAS NMR spectra at 10 kHz and 17 kHz spin rates. The spinning side bands are indicated by asterisks (black) and the isotropic shift by a star (blue). The ^{10}B NMR saturation recovery data for $Zr_{0.5}Y_{0.5}B_{12}$ (prepared as $(Zr_{0.5}Y_{0.5})$:13B) at room temperature are shown as black bullets. The red smooth line is a single exponential fit function to the experimental results.

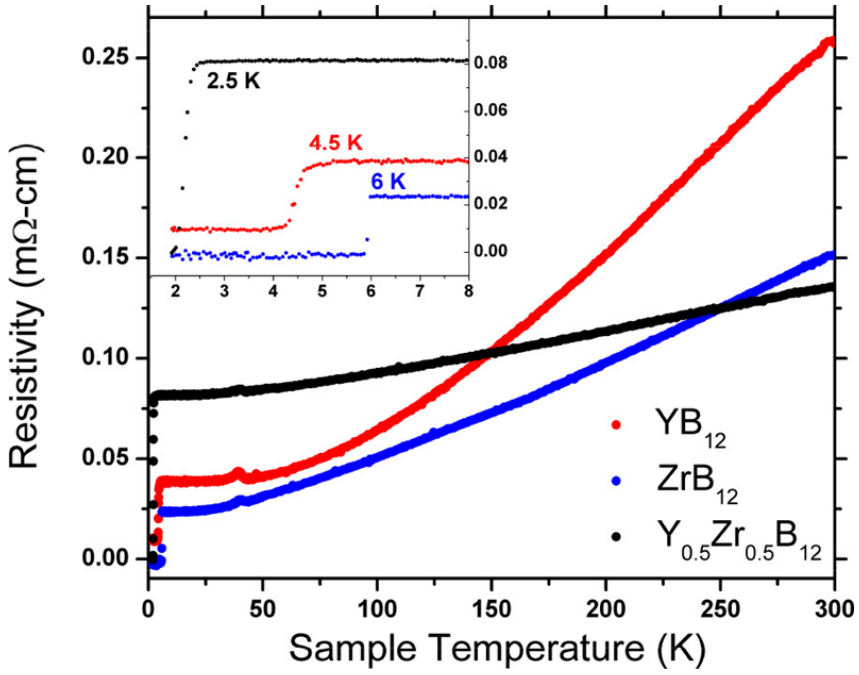

Figure 4-13. Electrical resistivity of YB_{12}, ZrB_{12}, and $Zr_{0.5}Y_{0.5}B_{12}$, prepared at 1:13 metal to boron ratio, from 1.9 to 300 K. Inset shows low temperature region from 1.9 to 8 K.

Table 4-S1. Vickers Hardness[a] (H_v, GPa) of Alloys of the Nominal Composition of $(Zr_{1-x}Y_x):C_z:13B$[b]

at. % Y	at. % C	0.49 N		0.98 N		1.96 N		2.98 N		4.9 N	
		H_v	ΔH_v	H_v	ΔH_v	H_v	ΔH_v	H_v	ΔHv	Hv	ΔHv
0	0	41.6	2.6	35.5	2.4	31.5	1.3	30.5	0.6	28.1	0.3
0	20	43.7	5.0	34.9	4.0	33.7	1.0	32.2	1.4	31.1	1.4
0	40	46.4	3.3	38.7	4.4	34.4	1.5	33.7	1.1	31.5	0.7
0	50	49.4	4.4	37.5	2.0	34.8	4.6	32.6	3.1	30.7	1.1
0	60	44.2	4.0	37.8	1.4	36.6	2.1	34.9	1.7	30.6	1.7
0	80	49.4	4.8	36.3	5.3	33.4	2.1	33.2	3.1	31.2	0.4
0	100	46.9	3.7	41.9	2.6	39.5	1.8	36.3	1.1	34.3	1.0
5	0	42.5	2.8	35.4	2.2	34.3	2.0	30.8	0.6	29.0	0.5
5	20	46.2	5.6	38.4	2.9	34.4	3.0	31.9	1.8	30.9	1.1
5	40	45.4	3.8	38.2	1.1	36.6	5.2	35.4	1.7	30.9	2.0
5	50	48.5	4.2	37.3	2.6	34.3	5.2	32.4	1.9	30.6	1.9
5	60	45.5	4.0	38.4	1.6	35.6	3.5	34.6	1.4	32.2	2.1
5	80	45.8	3.3	39.3	3.3	34.9	1.5	33.5	4.6	32.1	0.4
5	100	46.5	3.4	41.1	1.9	38.4	1.8	35.8	1.7	33.5	0.7
25	0	45.2	2.2	36.2	2.0	34.7	1.4	32.1	1.3	30.4	0.6
25	20	46.4	4.4	38.7	2.9	34.0	1.3	32.5	2.7	31.1	1.3
25	40	49.6	3.8	42.4	2.6	35.0	1.4	34.0	1.8	32.3	1.7
25	50	45.7	3.8	37.3	2.7	34.5	2.6	32.8	3.3	31.2	1.4
25	60	48.4	5.2	39.6	2.1	37.6	1.7	35.0	2.0	33.2	2.1
25	80	45.1	3.5	39.5	2.6	34.5	4.3	33.2	3.5	32.3	2.2
25	100	46.4	3.6	40.4	2.0	35.7	1.5	35.5	1.6	33.2	0.6
50	0	47.6	1.7	38.2	1.3	36.8	1.0	34.2	0.6	32.5	0.4
50	20	47.5	4.4	39.8	1.4	36.4	1.5	34.1	1.7	33.0	1.1
50	40	49.8	3.2	42.5	1.1	35.5	2.8	34.1	2.3	32.0	0.7
50	50	49.4	4.1	40.9	3.2	36.7	2.1	33.8	1.4	33.3	1.4
50	60	49.9	4.8	41.2	2.2	35.8	2.6	34.4	3.1	32.5	1.5
50	80	47.1	4.6	41.4	2.2	37.9	2.6	33.8	2.5	31.0	1.4
50	100	48.0	3.8	41.1	2.3	36.5	2.5	34.9	1.7	33.3	1.7
75	0	43.7	1.5	35.7	0.8	34.0	0.8	32.1	0.5	30.0	0.6
75	20	43.7	5.3	37.8	1.5	34.5	0.8	32.8	1.9	31.4	1.6
75	40	41.3	4.5	39.6	3.2	32.4	0.5	32.7	1.6	32.1	1.5
75	50	44.0	4.7	37.4	2.2	34.9	2.1	33.0	1.5	30.8	1.1
75	60	42.1	4.8	37.6	4.7	34.5	2.5	30.4	2.3	29.6	2.9
75	80	41.6	4.5	38.2	5.9	35.0	1.5	33.5	0.9	30.0	2.9
75	100	44.1	3.8	40.0	2.6	34.8	2.2	34.3	1.4	31.4	1.4
95	0	38.8	3.2	34.5	2.1	31.3	1.2	29.5	1.0	27.7	1.7
95	20	43.2	5.1	37.1	1.4	33.9	2.8	33.5	2.4	30.7	1.5
95	40	40.3	5.1	37.5	2.3	32.7	1.9	31.2	1.3	31.0	1.6
0	0	41.6	2.6	35.5	2.4	31.5	1.3	30.5	0.6	28.1	0.3
0	20	43.7	5.0	34.9	4.0	33.7	1.0	32.2	1.4	31.1	1.4

0	40	46.4	3.3	38.7	4.4	34.4	1.5	33.7	1.1	31.5	0.7
0	50	49.4	4.4	37.5	2.0	34.8	4.6	32.6	3.1	30.7	1.1
0	60	44.2	4.0	37.8	1.4	36.6	2.1	34.9	1.7	30.6	1.7
0	80	49.4	4.8	36.3	5.3	33.4	2.1	33.2	3.1	31.2	0.4
0	100	46.9	3.7	41.9	2.6	39.5	1.8	36.3	1.1	34.3	1.0
5	0	42.5	2.8	35.4	2.2	34.3	2.0	30.8	0.6	29.0	0.5
5	20	46.2	5.6	38.4	2.9	34.4	3.0	31.9	1.8	30.9	1.1
5	40	45.4	3.8	38.2	1.1	36.6	5.2	35.4	1.7	30.9	2.0
5	50	48.5	4.2	37.3	2.6	34.3	5.2	32.4	1.9	30.6	1.9

[a]Error is given as ΔH_v (GPa);

[b]x = 0.00, 0.05, 0.25, 0.50, 0.75, 0.95 and 1.00 and z = 0.0, 0.2, 0.4, 0.5, 0.6, 0.8 and 1.0.

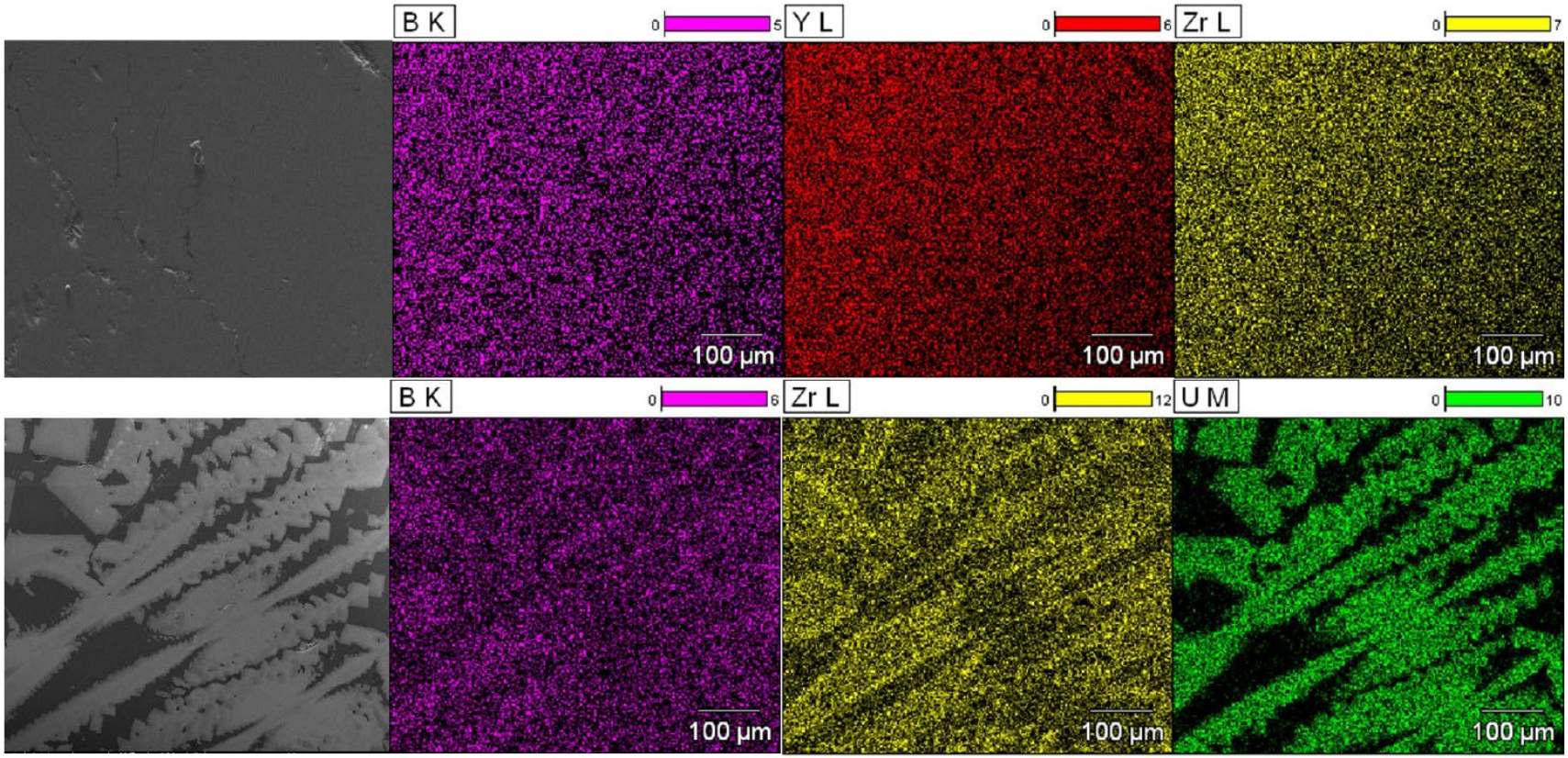

Figure 4-S1. Elemental maps for boron (K line), zirconium (L line), yttrium (L line) and uranium (M line). The thick horizontal bars represent the intensity as a color legend. The maps for the $Zr_{0.5}Y_{0.5}B_{12}$ (prepared as M : B = 1 : 13) shows a single phase compound, while the maps for the $Zr_{0.5}U_{0.5}B_{12}$ (prepared as M : B = 1 : 20) shows the metal dodecaboride phase and β-rhombohedral boron phase.

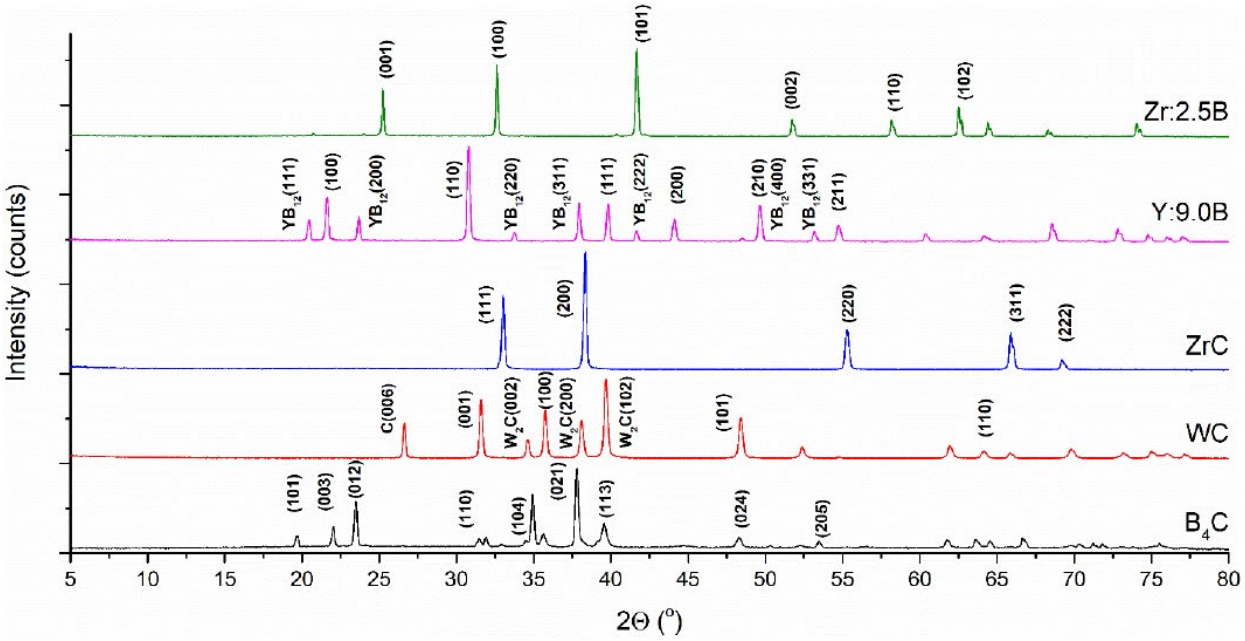

Figure 4-S2. Powder XRD patterns of carbides and borides: ZrB_2 (prepared as Zr:2.5B), YB_6 (Y:9.0B), ZrC (purchased), WC (purchased) and B4C (purchased). The peaks were assigned using ZrB_2 (P6/mmm, JCPDS 00-034-0423); YB_6 ($Pm\bar{3}m$, JCPDS 03-065-1827); ZrC ($Fm\bar{3}m$, JCPDS 00-035-0784); WC ($P\bar{6}m2$, JCPDS 00-051-0939), W_2C (Pbcn, JCPDS 00-020-1315) and carbon (graphite) ($P\bar{6}m2$, JCPDS 00-026-1076) for WC; and B_4C ($R\bar{3}m$, JCPDS 00-035-0798).

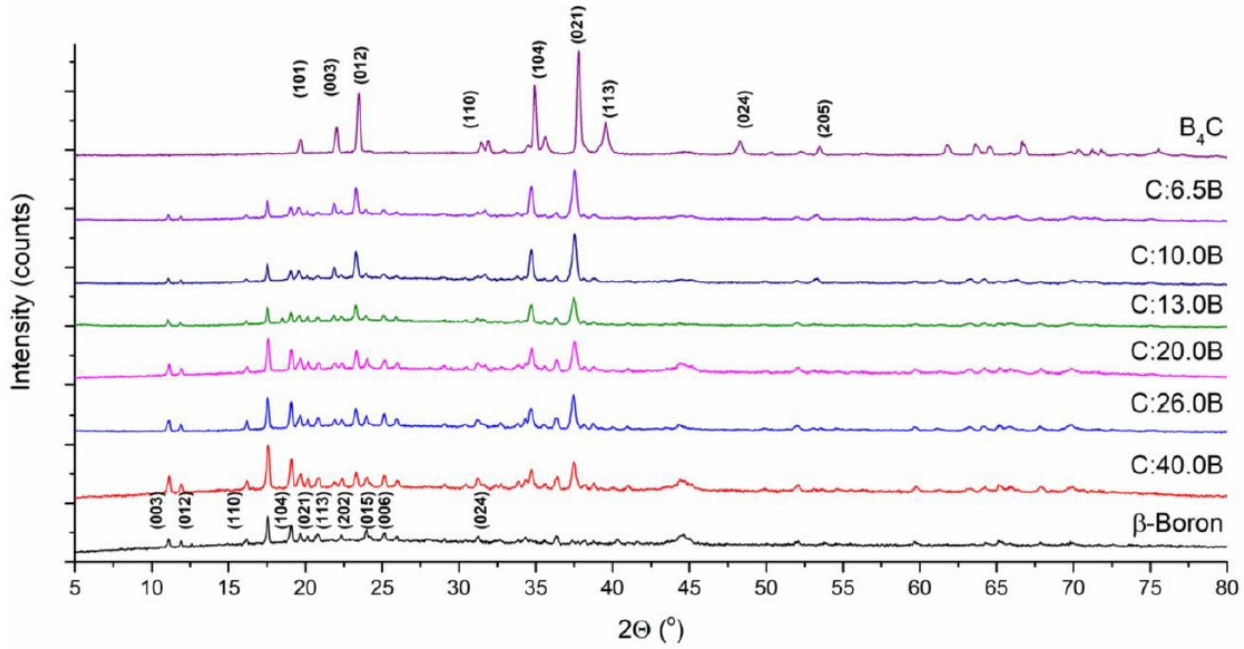

Figure 4-S3. Powder XRD patterns of pure B_4C, B_4C with a boron addition of: 6.5, 10.0, 13.0, 20.0, 26.0, 40.0 and pure β-rhombohedral boron. The peaks were assigned using B_4C ($R\bar{3}m$, JCPDS 00-035-0798) and β-rhombohedral boron ($R\bar{3}m$, JCPDS 00-011-0618).

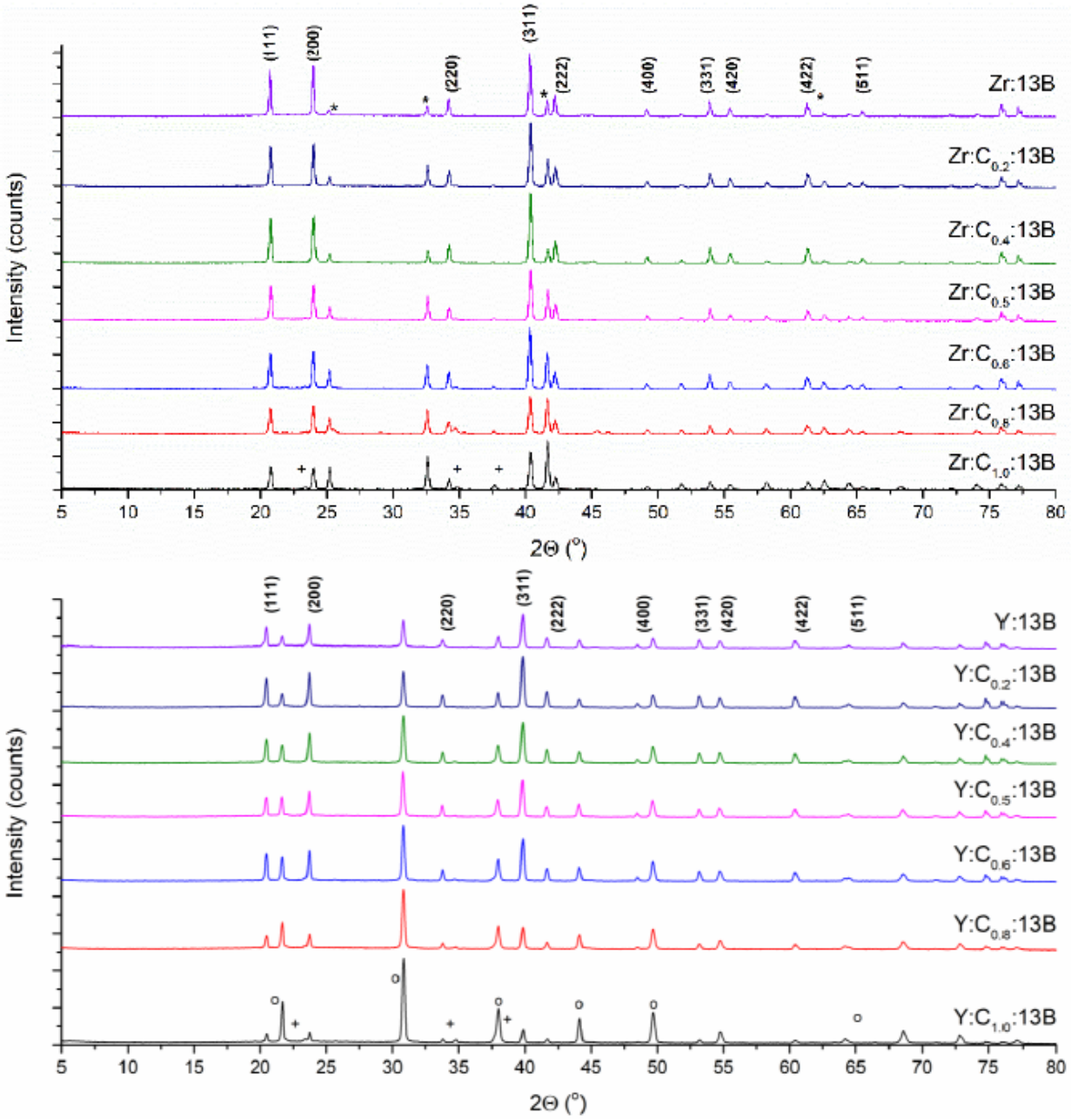

Figure 4-S4. Powder XRD patterns of alloys with a composition of: Zr:C_z:13B and Y:C_z:13B, where z = 0.0, 0.2, 0.4, 0.5, 0.6, 0.8 and 1.0. The peaks were assigned using YB_{12} ($Fm\bar{3}m$, JCPDS 01-073-1382), ZrB_2 (P6/mmm, JCPDS 00-034-0423, shown as (*)), YB_6 ($Pm\bar{3}m$, JCPDS 03-065-1827, shown as (^{o})), and B_4C ($R\bar{3}m$, JCPDS 00-035-0798, shown as ($^+$)).

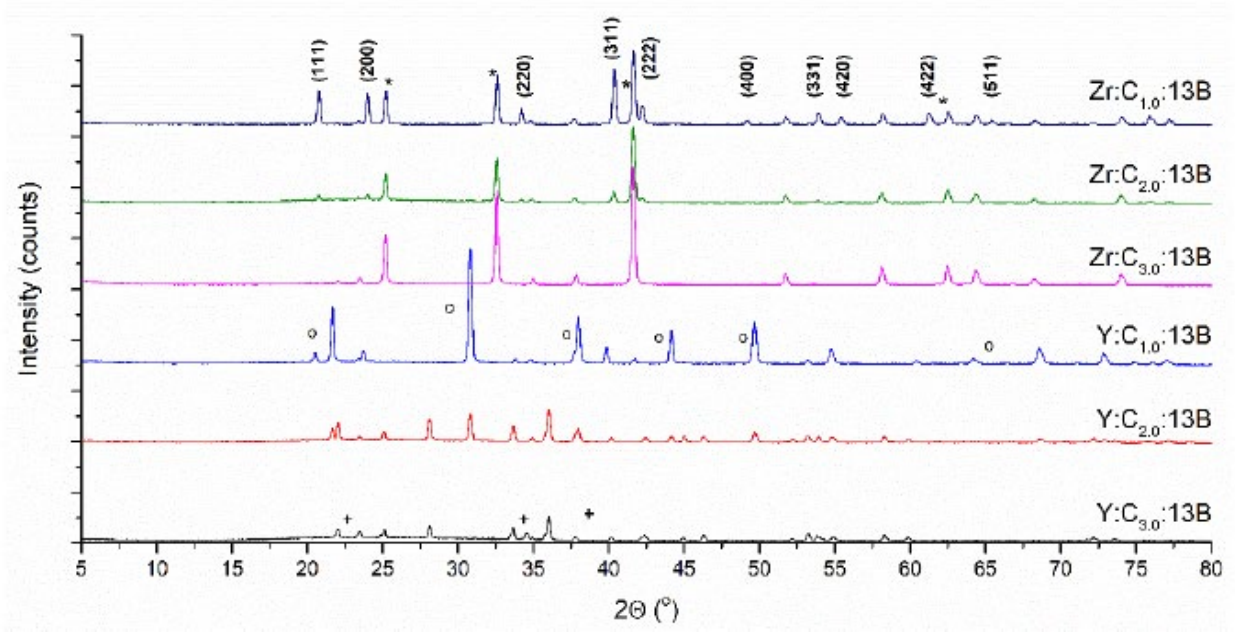

Figure 4-S5. Powder XRD patterns of alloys with a composition of: $Zr:C_z:13B$ and $Y:C_z:13B$, where z = 1.0, 2.0 and 3.0. The peaks were assigned using YB_{12} ($Fm\bar{3}m$, JCPDS 01-073-1382), ZrB_2 (P6/mmm, JCPDS 00-034-0423, shown as (*)), YB_6 ($Pm\bar{3}m$, JCPDS 03-065-1827, shown as (^{o})), and B_4C ($R\bar{3}m$, JCPDS 00-035-0798, shown as ($^+$)).

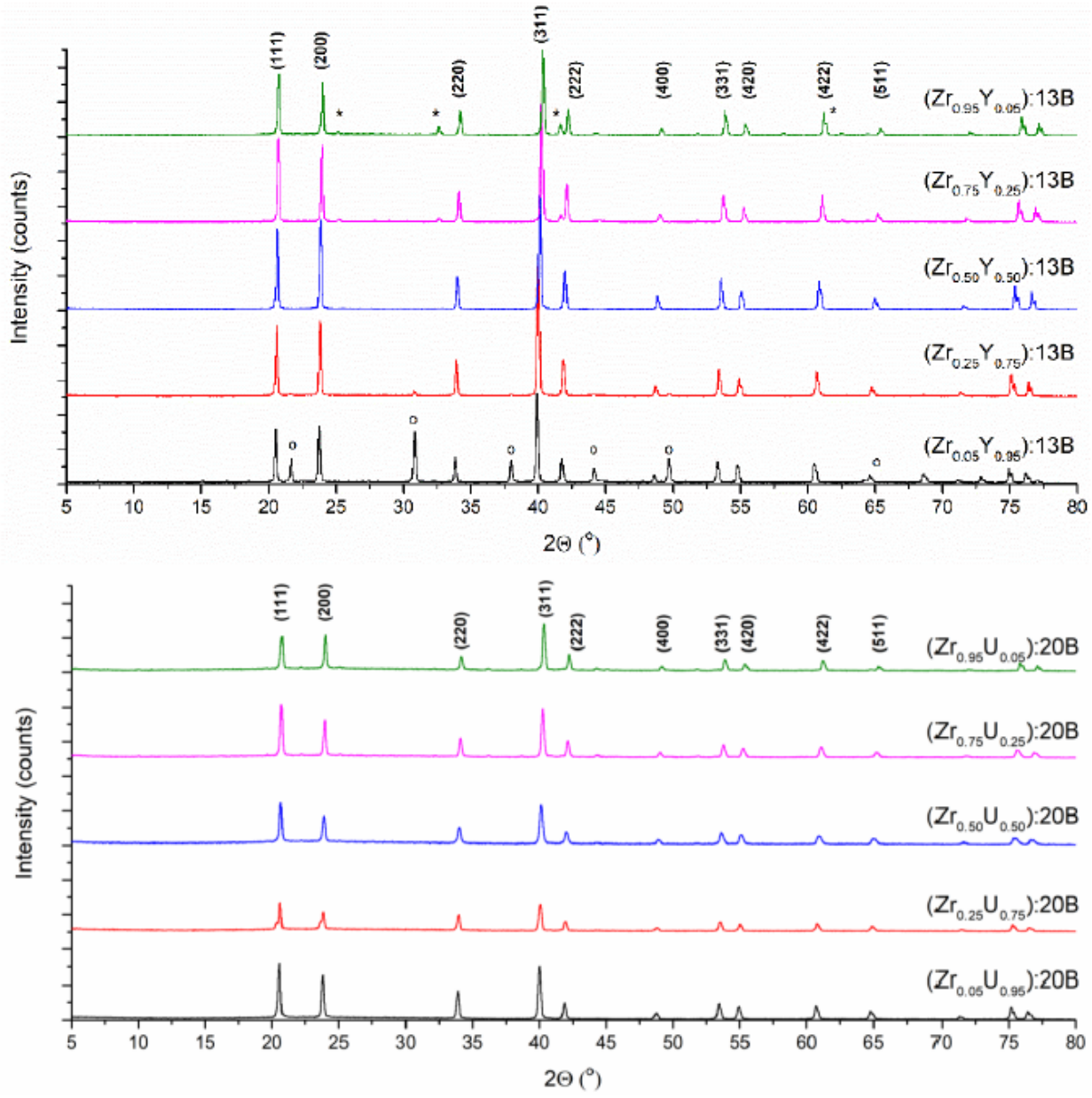

Figure 4-S6. Powder XRD patterns of alloys with a composition of: (top) $(Zr_{1-x}Y_x)$:13B and (bottom) $(Zr_{1-x}U_x)$:20B, where x = 0.05, 0.25, 0.50, 0.75 and 0.95. The peaks were assigned using YB_{12} ($Fm\bar{3}m$, JCPDS 01-073-1382), ZrB_2 (P6/mmm, JCPDS 00-034-0423, shown as (*)), YB_6 ($Pm\bar{3}m$, JCPDS 03-065-1827, shown as (o)).

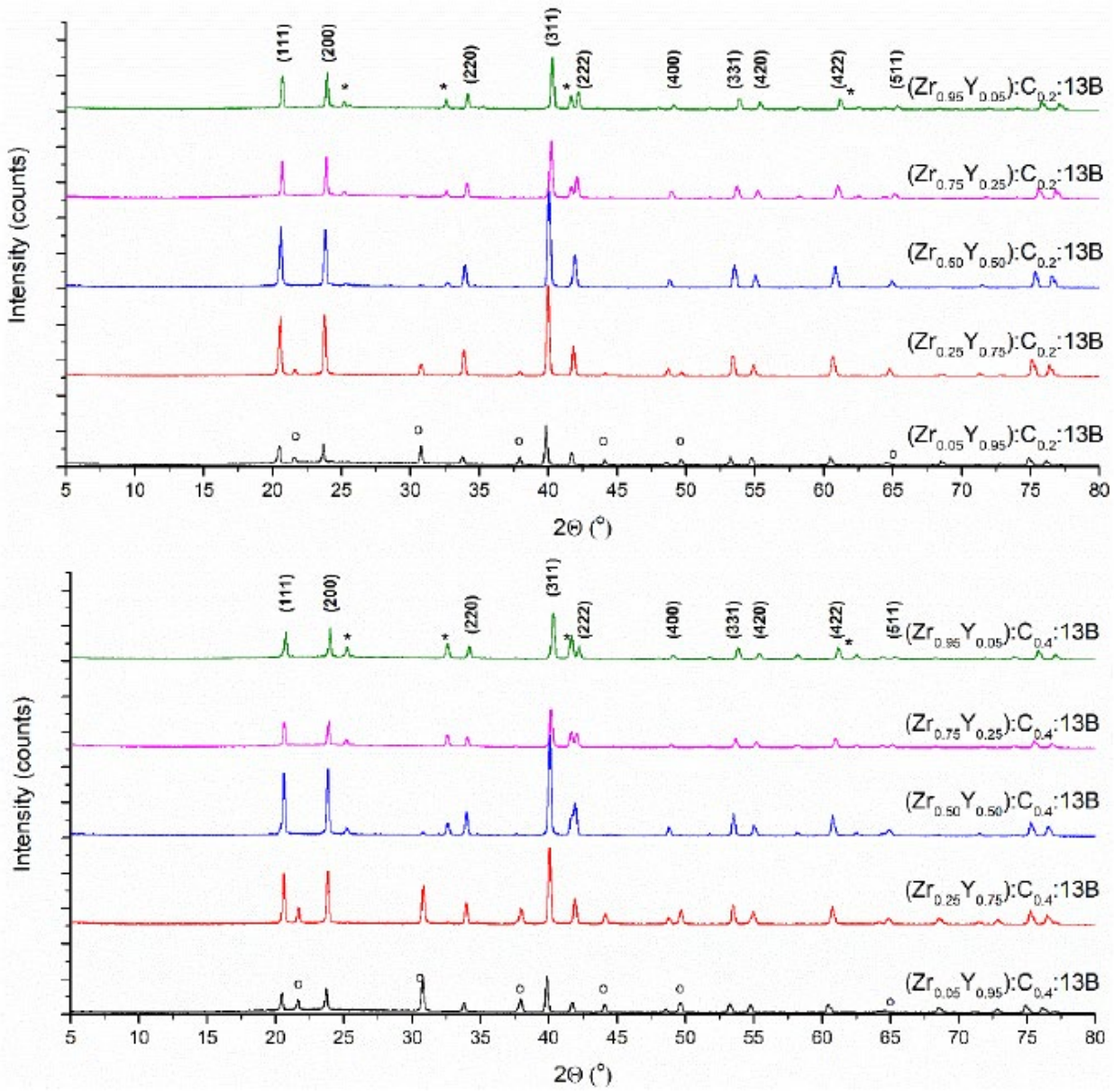

Figure 4-S7. Powder XRD patterns of alloys with a composition of: (top) $(Zr_{1-x}Y_x):C_{0.2}$:13B and (bottom) $(Zr_{1-x}Y_x):C_{0.4}$:13 B, where x = 0.05, 0.25, 0.50, 0.75 and 0.95. The peaks were assigned using YB_{12} ($Fm\bar{3}m$, JCPDS 01-073-1382), ZrB_2 (P6/mmm, JCPDS 00-034-0423, shown as (*)), YB_6 ($Pm\bar{3}m$, JCPDS 03-065-1827, shown as (°)).

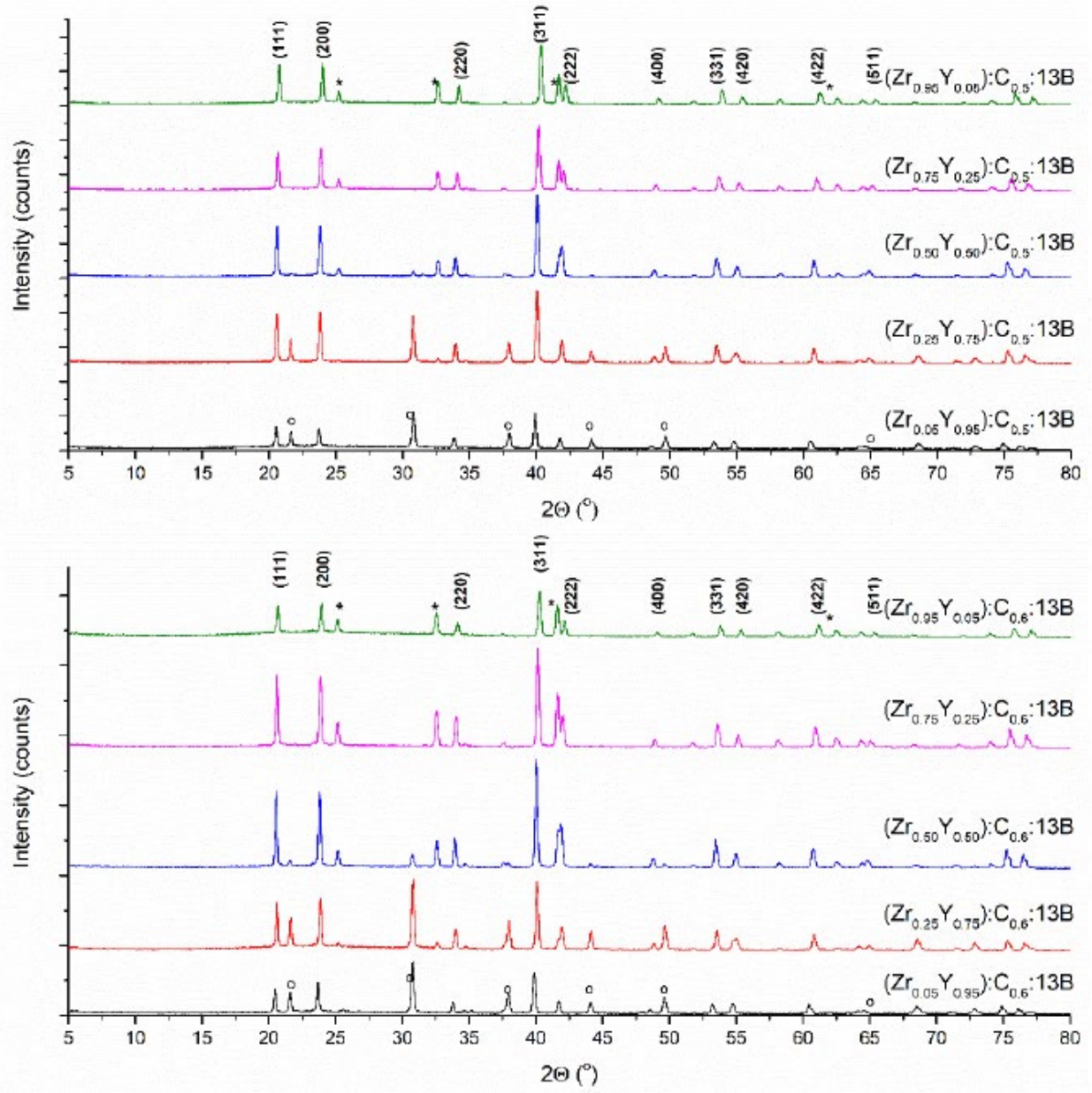

Figure 4-S8. Powder XRD patterns of alloys with a composition of: (top) $(Zr_{1-x}Y_x):C_{0.5}$:13B and (bottom) $(Zr_{1-x}Y_x):C_{0.6}$:13 B, where x = 0.05, 0.25, 0.50, 0.75 and 0.95. The peaks were assigned using YB_{12} ($Fm\bar{3}m$, JCPDS 01-073-1382), ZrB_2 (P6/mmm, JCPDS 00-034-0423, shown as (*)), YB_6 ($Pm\bar{3}m$, JCPDS 03-065-1827, shown as (°)).

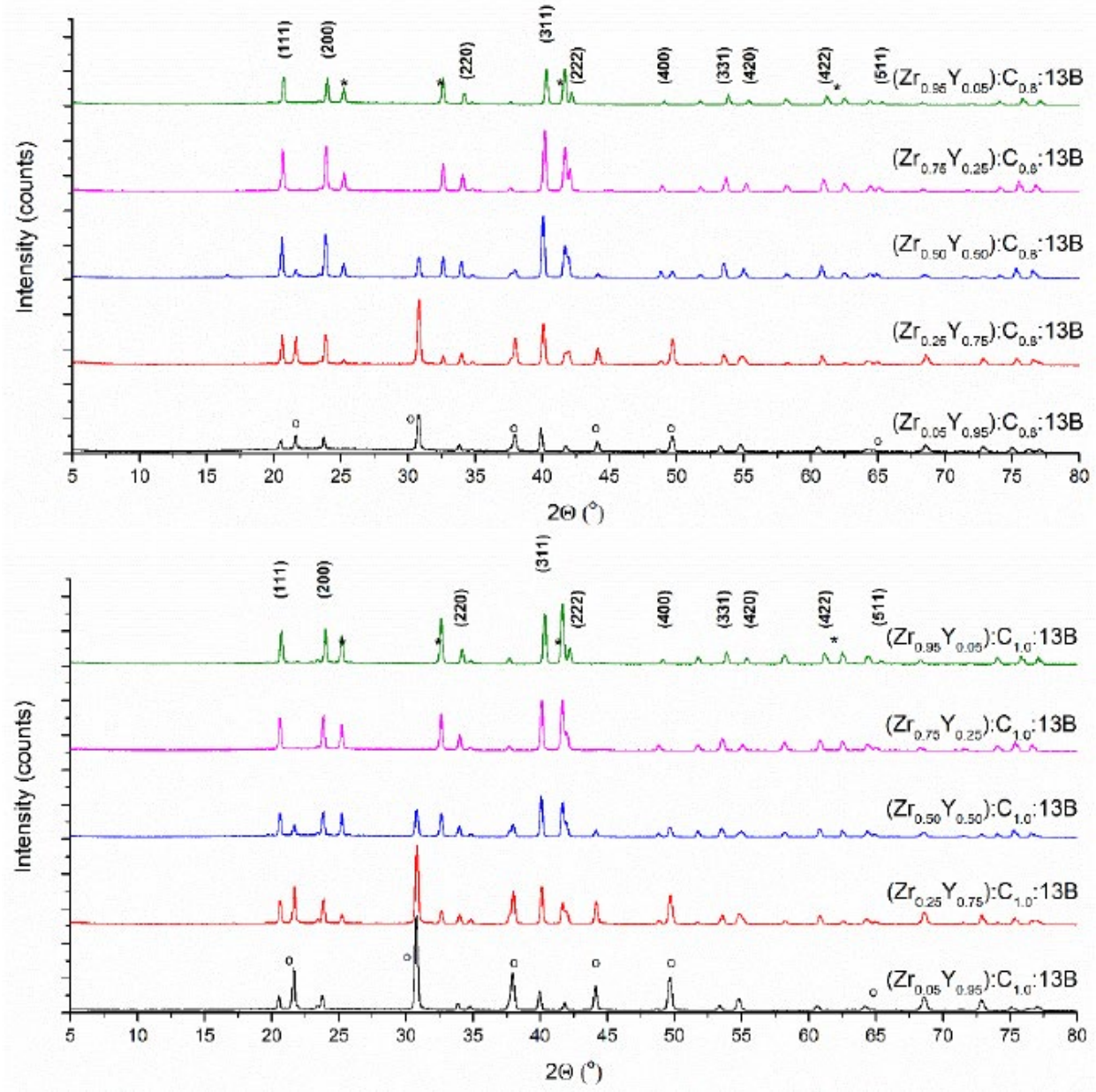

Figure 4-S9. Powder XRD patterns of alloys with a composition of: (top) $(Zr_{1-x}Y_x):C_{0.8}$:13B and (bottom) $(Zr_{1-x}Y_x):C_{1.0}$:13 B, where x = 0.05, 0.25, 0.50, 0.75 and 0.95. The peaks were assigned using YB_{12} ($Fm\bar{3}m$, JCPDS 01-073-1382), ZrB_2 (P6/mmm, JCPDS 00-034-0423, shown as (*)), YB_6 ($Pm\bar{3}m$, JCPDS 03-065-1827, shown as (°)).

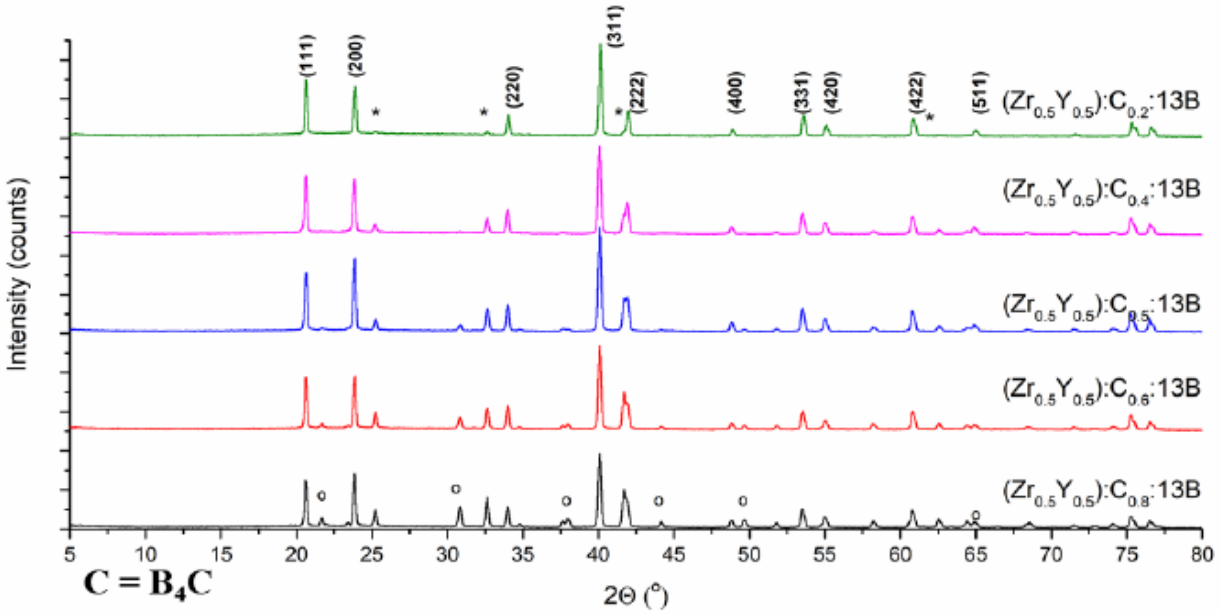
(111)
(200)
(220)
(311)
(222)
(400)
(331)
(420)
(422)
(511)
(Zr0.5Y0.5):C0.2:13B
(Zr0.5Y0.5):C0.4:13B
(Zr0.5Y0.5):C0.5:13B
(Zr0.5Y0.5):C0.6:13B
(Zr0.5Y0.5):C0.8:13B
Intensity (counts)
2Θ (°)
C = B4C

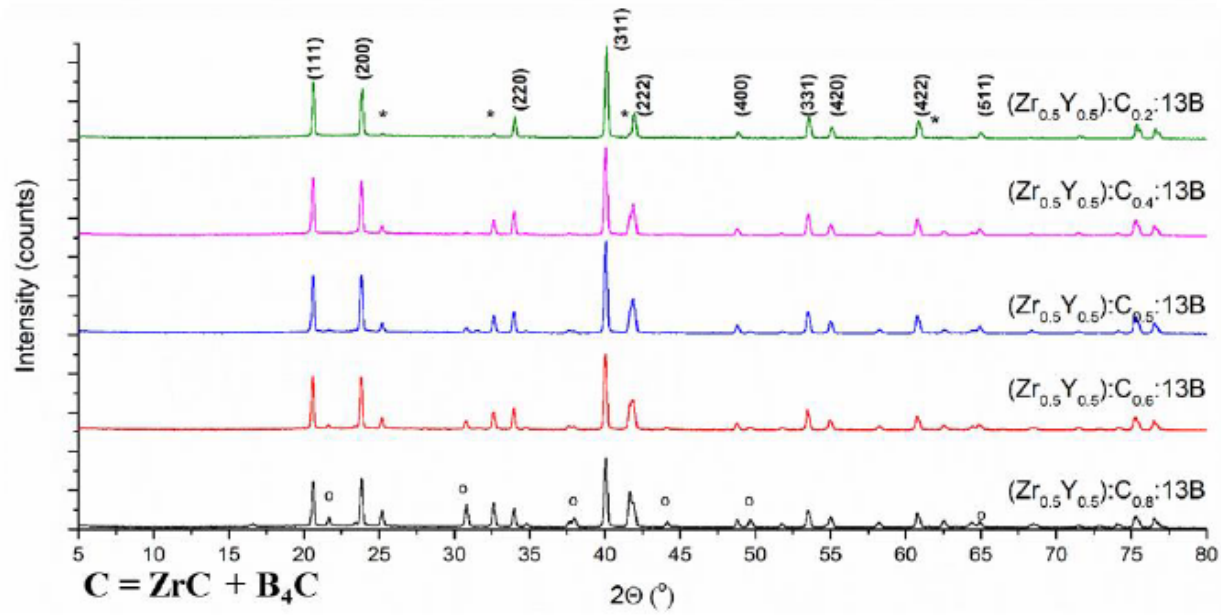
(111)
(200)
(220)
(311)
(222)
(400)
(331)
(420)
(422)
(511)
(Zr0.5Y0.5):C0.2:13B
(Zr0.5Y0.5):C0.4:13B
(Zr0.5Y0.5):C0.5:13B
(Zr0.5Y0.5):C0.6:13B
(Zr0.5Y0.5):C0.8:13B
Intensity (counts)
2Θ (°)
C = ZrC + B4C

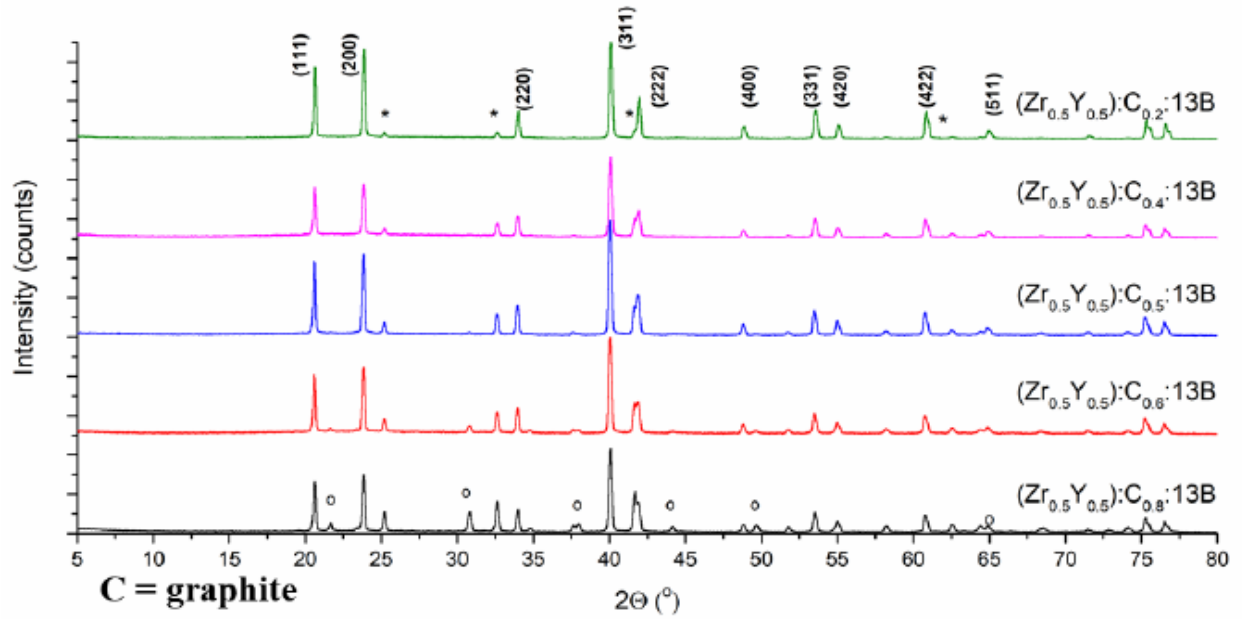

Figure 4-S10. Powder XRD patterns of alloys with a composition of $(Zr_{0.5}Y_{0.5})$:C_x:13B, where x = 0.05, 0.25, 0.50, 0.75 and 0.95. The carbon sources are: (top) B_4C, (middle) ZrC and B_4C, (bottom) graphite. The peaks were assigned using YB_{12} ($Fm\bar{3}m$, JCPDS 01-073-1382), ZrB_2 (P6/mmm, JCPDS 00-034-0423, shown as (*)), YB_6 ($Pm\bar{3}m$, JCPDS 03-065-1827, shown as (°)). In all three cases the phase formation is similar.

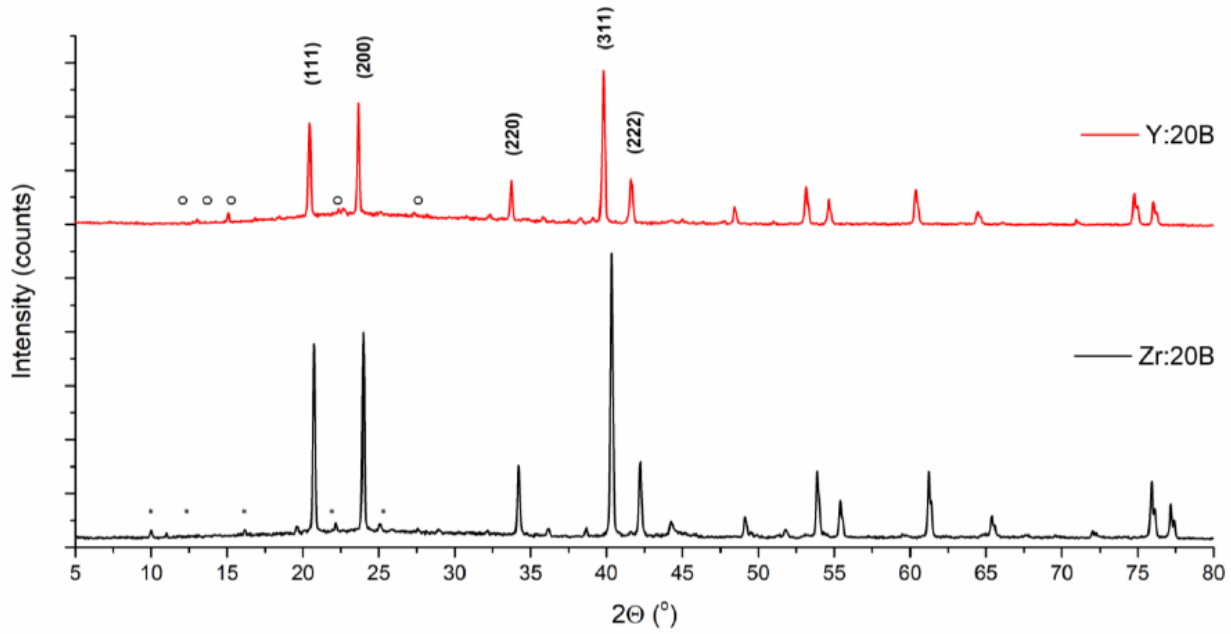

Figure 4-S11. Powder XRD patterns of alloys with a composition of Y:20B and Zr:20B. The peaks were assigned using YB_{12} ($Fm\bar{3}m$, JCPDS 01-073-1382), ZrB_{50} ($R\bar{3}m$, JCPDS 03-065-2184, shown as (*)), YB_{66} ($Fm\bar{3}c$, JCPDS 01-073-0759, shown as (°)).

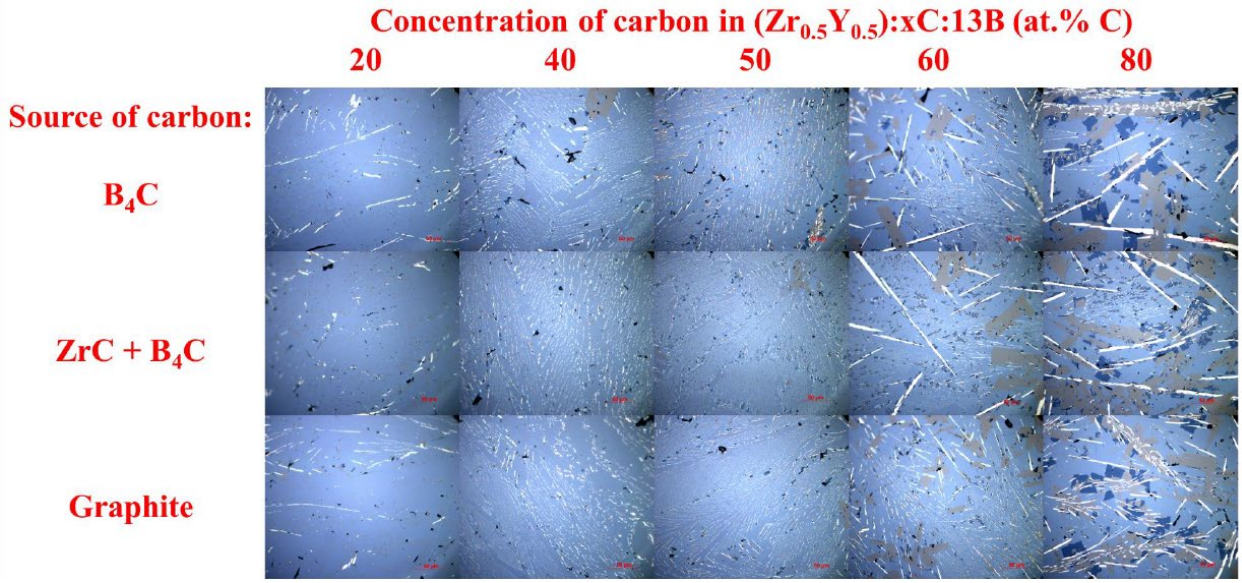

Figure 4-S12. Optical images of $(Zr_{0.5}Y_{0.5})$:C_x:13B, where x = 0.2, 0.4, 0.5, 0.6 and 0.8 synthesized with different sources of carbon. All images were taken at 500× magnification; the scale bars are 50 μm. The images show that regardless of carbon source, the morphology remains the same: as the amount of carbon increases, the amount of lower borides (ZrB_2 (white) and YB_6 (dark-blue)) and boron carbide increases (grey). Dodecaboride phase is light blue.

Figure 4-S13. SEM images and optical images of $(Zr_{1-x}U_x)$:20B, where x = 0.00, 0.05, 0.25, 0.50, 0.75, 0.95 and 1.00. All SEM images were taken at 1000× magnification; the scale bars are 100 μm. All optical images were taken at 500× magnification; the scale bars are 50 μm. The images show the formation of a single phase solid solutions of $Zr_{1-x}U_xB_{12}$, and the changes of color on going from a zirconium rich dodecaboride (+4 metal oxidation state, violet color) to a more uranium rich (+5/+6 metal oxidation state, metallic color).

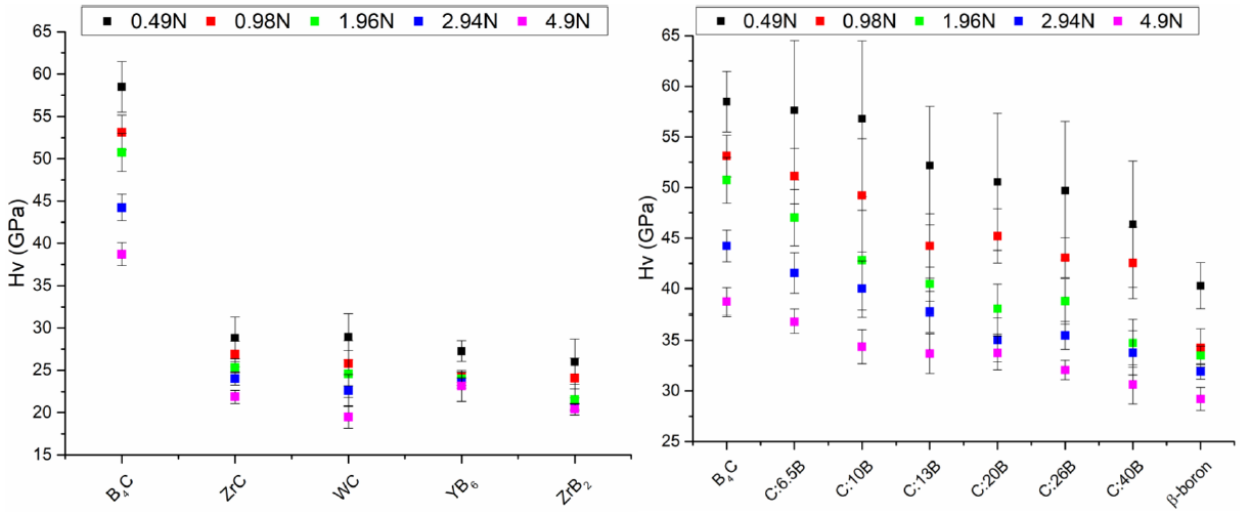

Figure 4-S14. Vickers micro-indentation hardness of: (left) carbides (B_4C, ZrC and WC) and borides (ZrB_2 and YB_6), (right) B_4C in boron at low (0.49 N) to high (4.9 N) applied loads.

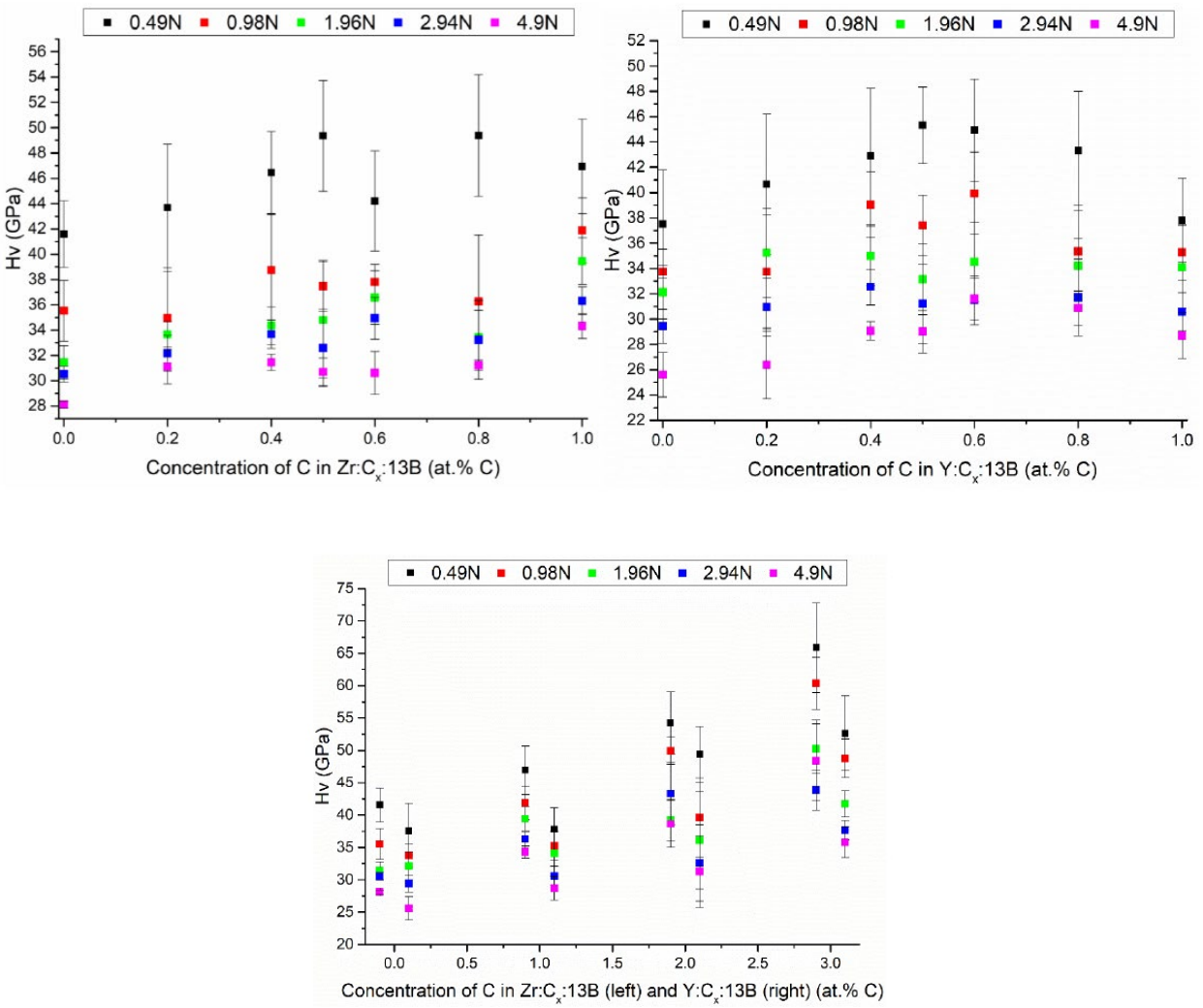

Figure 4-S15. Vickers micro-indentation hardness of: (top left) Zr:C_x:13B, (top right) Y:C_x:13B, where x = 0.0, 0.2, 0.4, 0.5, 0.6, 0.8, 1.0, and (bottom) Zr:C_z:13B and Y:C_z:13B, where z = 0.0, 1.0, 2.0 and 3.0 at low (0.49 N) to high (4.9 N) applied loads.

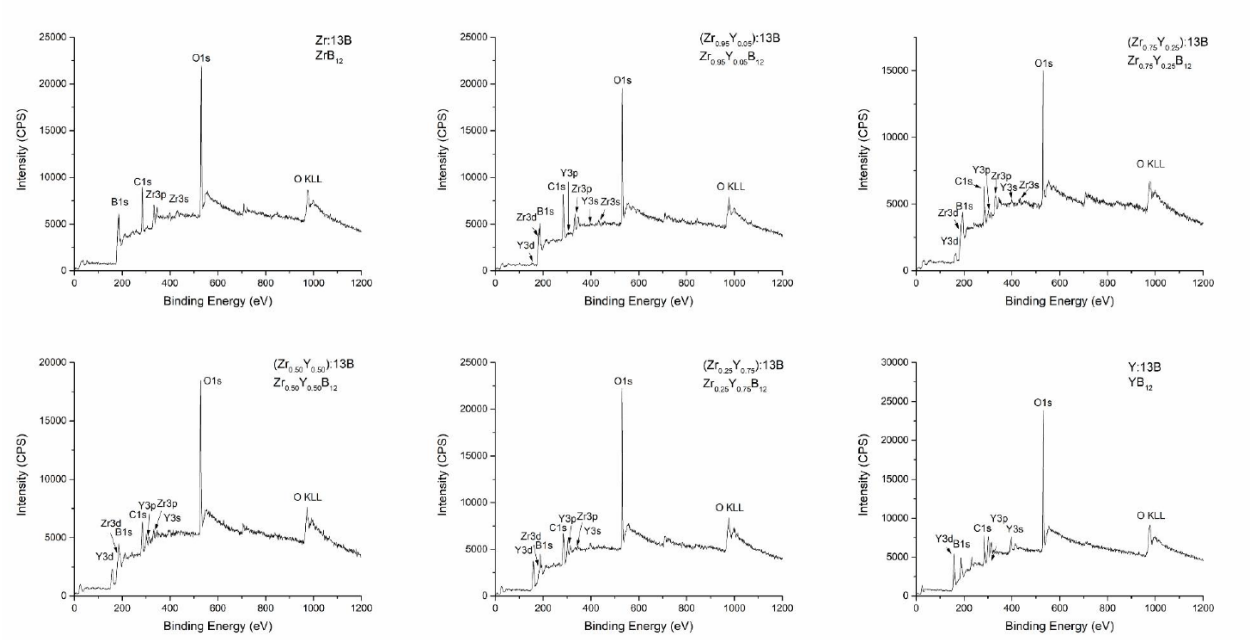

Figure 4-S16. XPS survey for the alloys with a nominal composition of $(Zr_{1-x}Y_x)$:13B corresponding to the $Zr_{1-x}Y_xB_{12}$ solid solution, showing B 1s, Y 3d (5/2 and 3/2) and Zr 3d (5/2 and 3/2) peaks. Peaks corresponding to the O 1s and C 1s are due to possible oxidation and surface contamination.

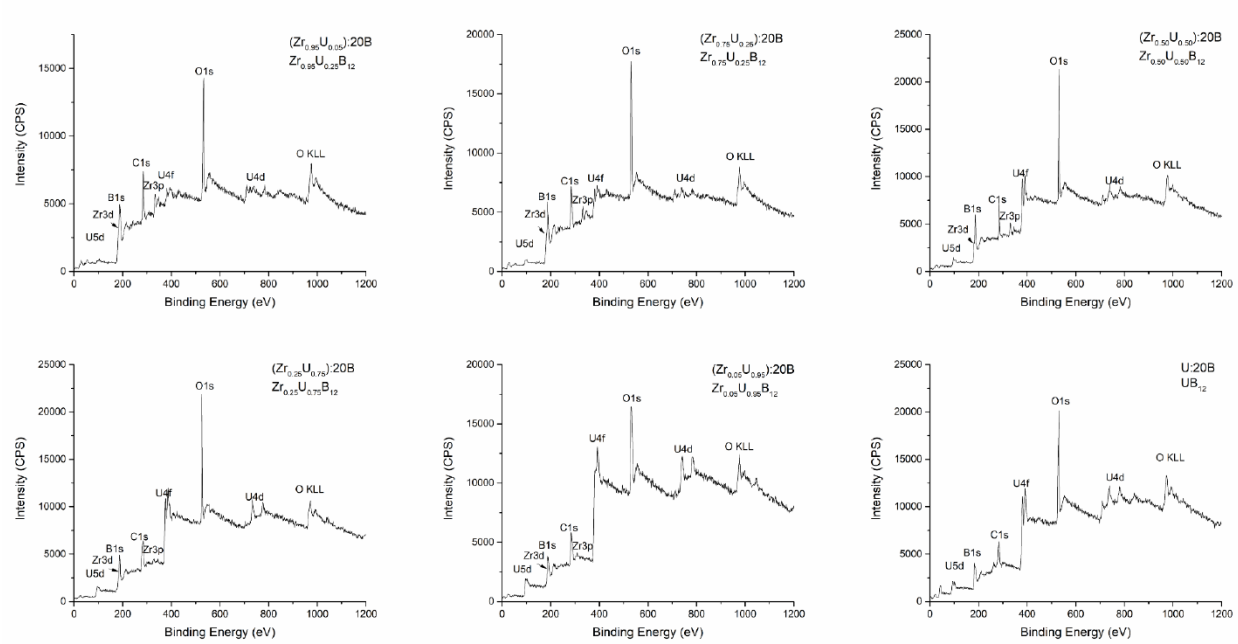

Figure 4-S17. XPS survey for the alloys with a nominal composition of $(Zr_{1-x}U_x)$:20B corresponding to the $Zr_{1-x}U_xB_{12}$ solid solution, showing B 1s, U 4f (7/2 and 5/2) and Zr 3d (5/2 and 3/2) peaks. Peaks corresponding to the O 1s and C 1s are due to possible oxidation and surface contamination.

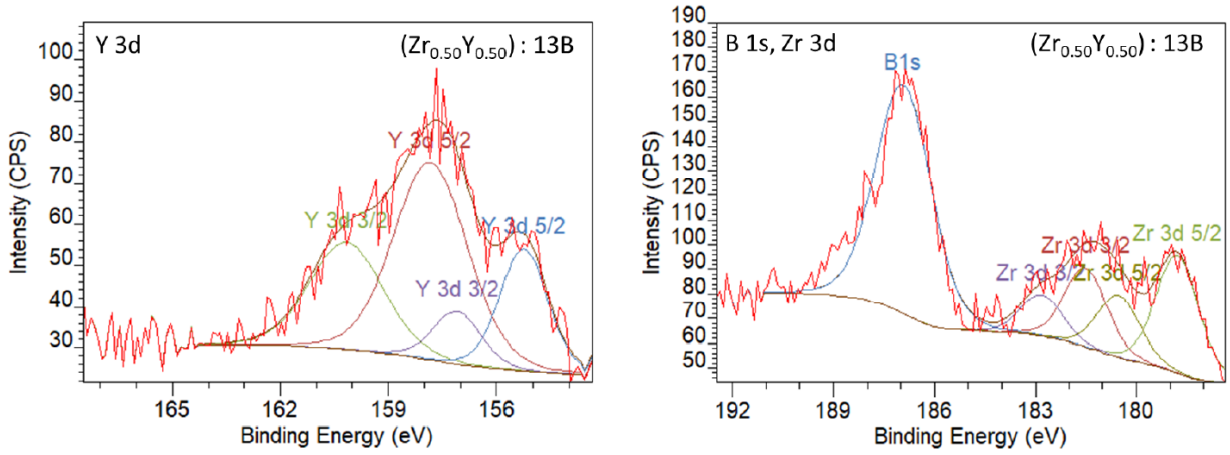

Figure 4-S18. High-resolution XPS spectra and peak fittings for Y3d (left) and Zr3d and B1s (right).

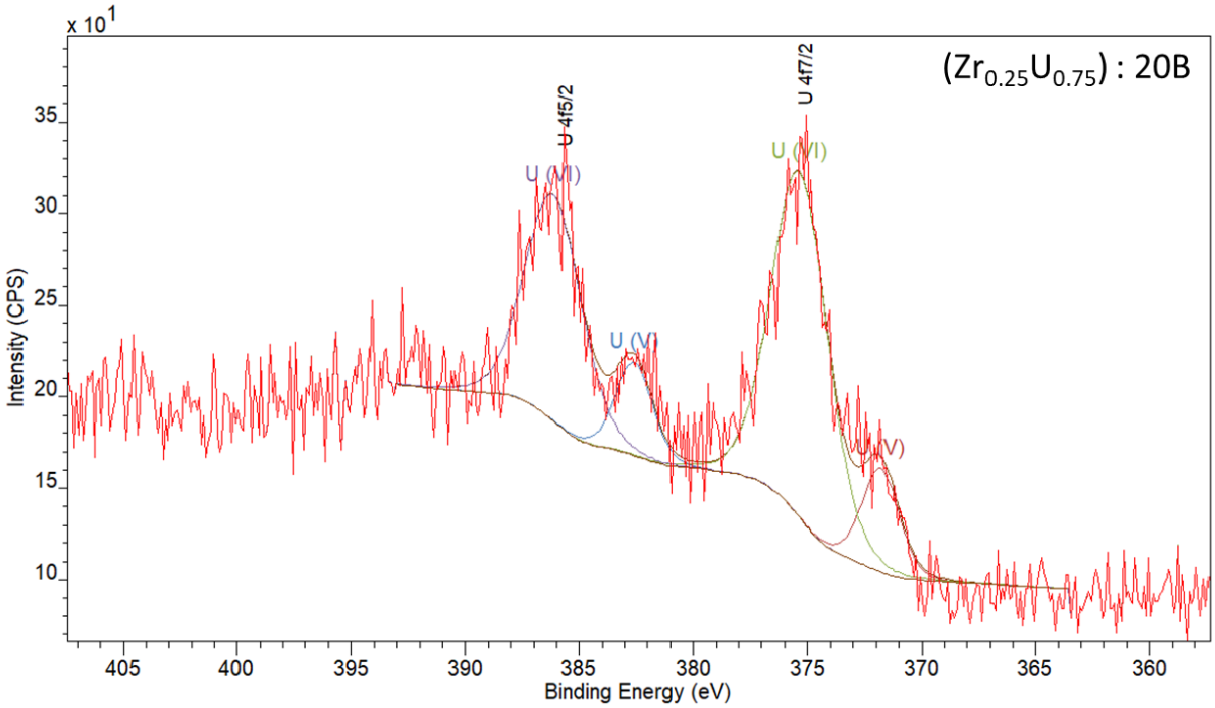

Figure 4-S19. High-resolution XPS spectra and peak fittings for U4f.

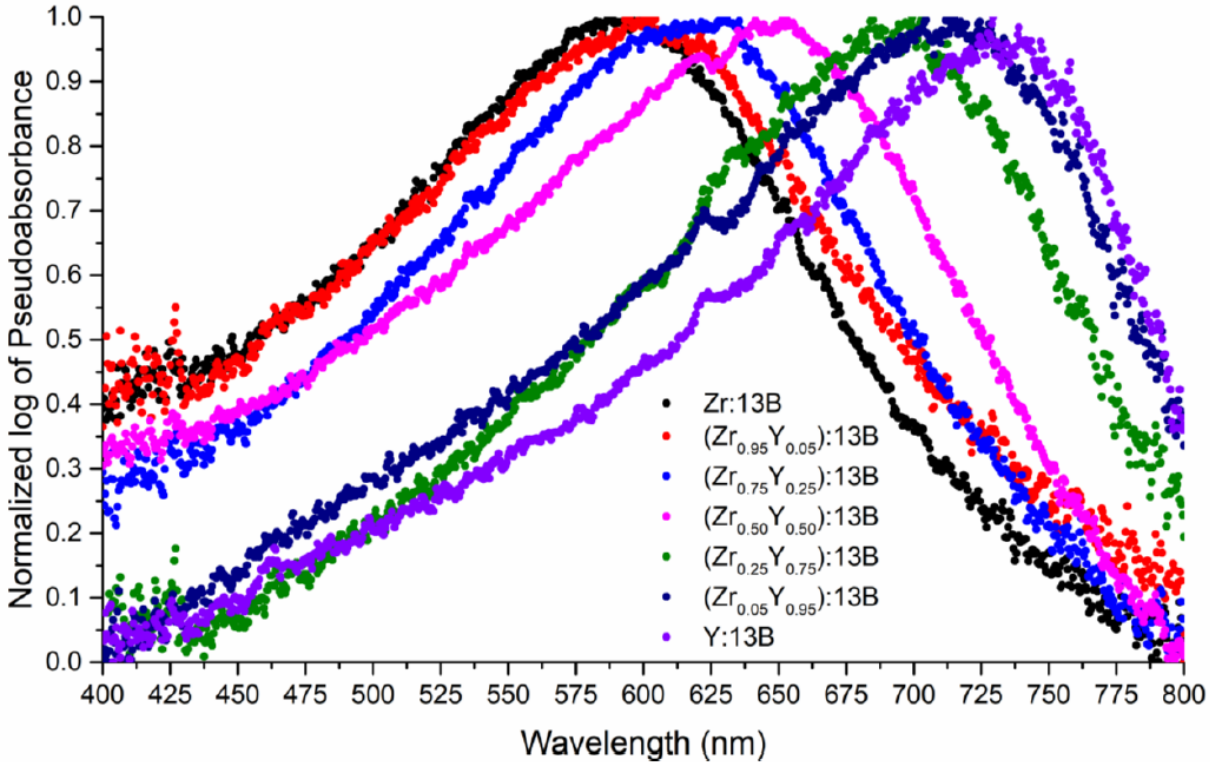
Normalized log of Pseudoabsorbance
Wavelength (nm)
Zr:13B
(Zr0.95Y0.05):13B
(Zr0.75Y0.25):13B
(Zr0.50Y0.50):13B
(Zr0.25Y0.75):13B
(Zr0.05Y0.95):13B
Y:13B

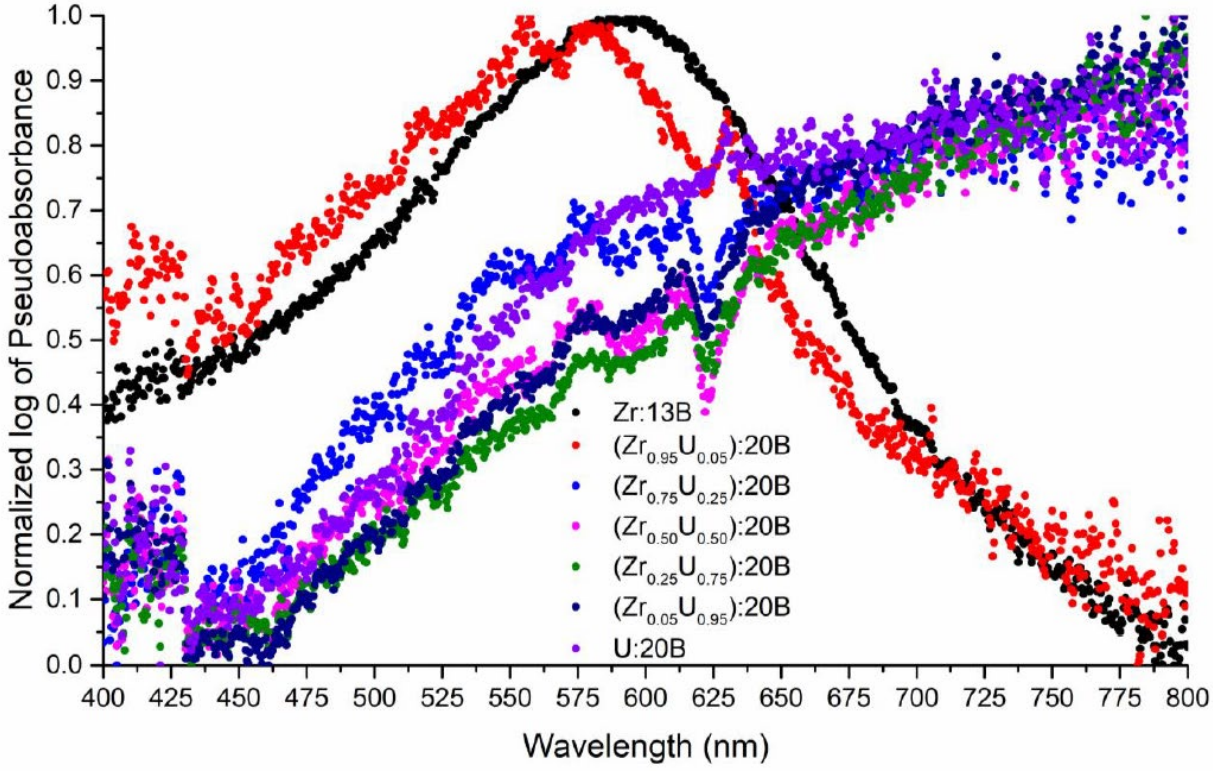

Figure 4-S20. Diffuse-reflectance UV-Vis spectra for (top) $(Zr_{1-x}Y_x)$:13 B and (bottom) $(Zr_{1-x}U_x)$:20 B showing a peak shift on going from ZrB_{12} (+4 metal oxidation state, violet color) to YB_{12} (+3 metal oxidation state, light-blue color); and from a zirconium rich dodecaboride (+4 metal oxidation state, violet color) to a more uranium rich (+5/+6 metal oxidation state, metallic color).

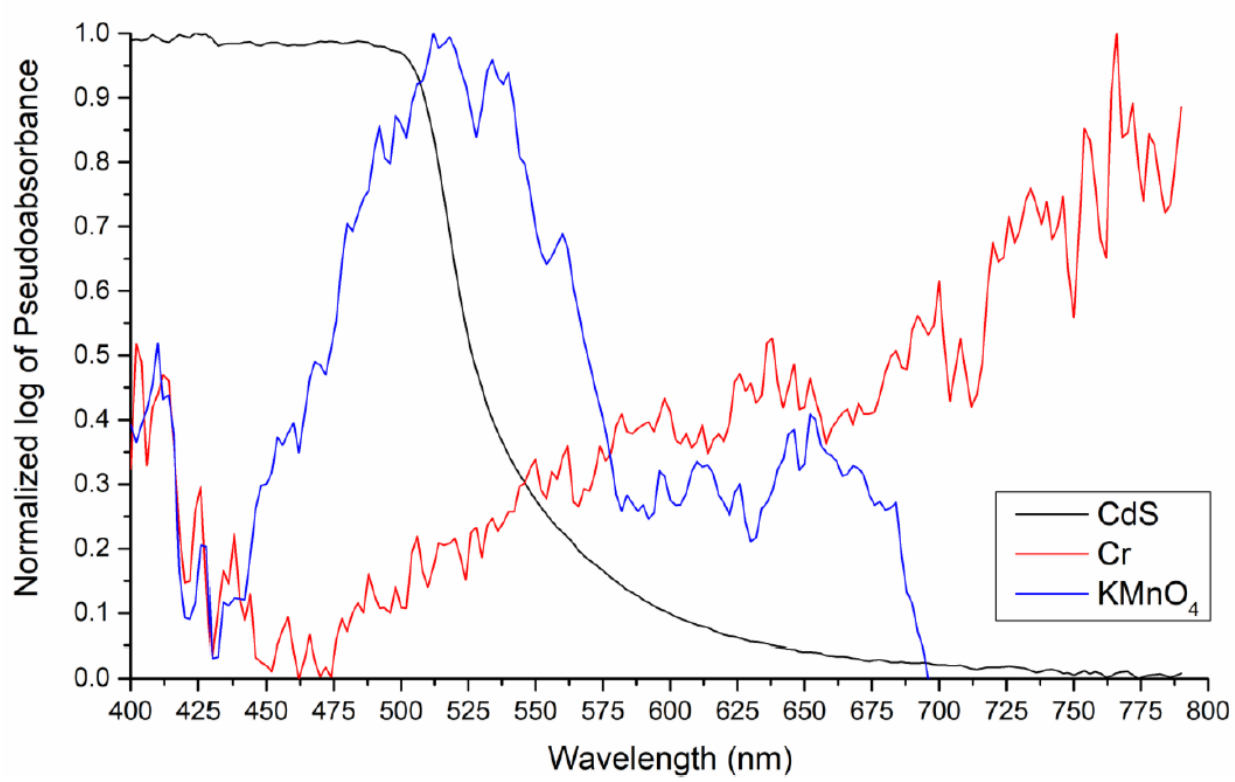

Figure 4-S21. Diffuse-reflectance UV-vis spectra for CdS, $KMnO_4$ and Cr metal. CdS and $KMnO_4$ represent two compounds that possess color, but due to different underlying nature: CdS being a semiconductor, and $KMnO_4$ being a charge-transfer complex.

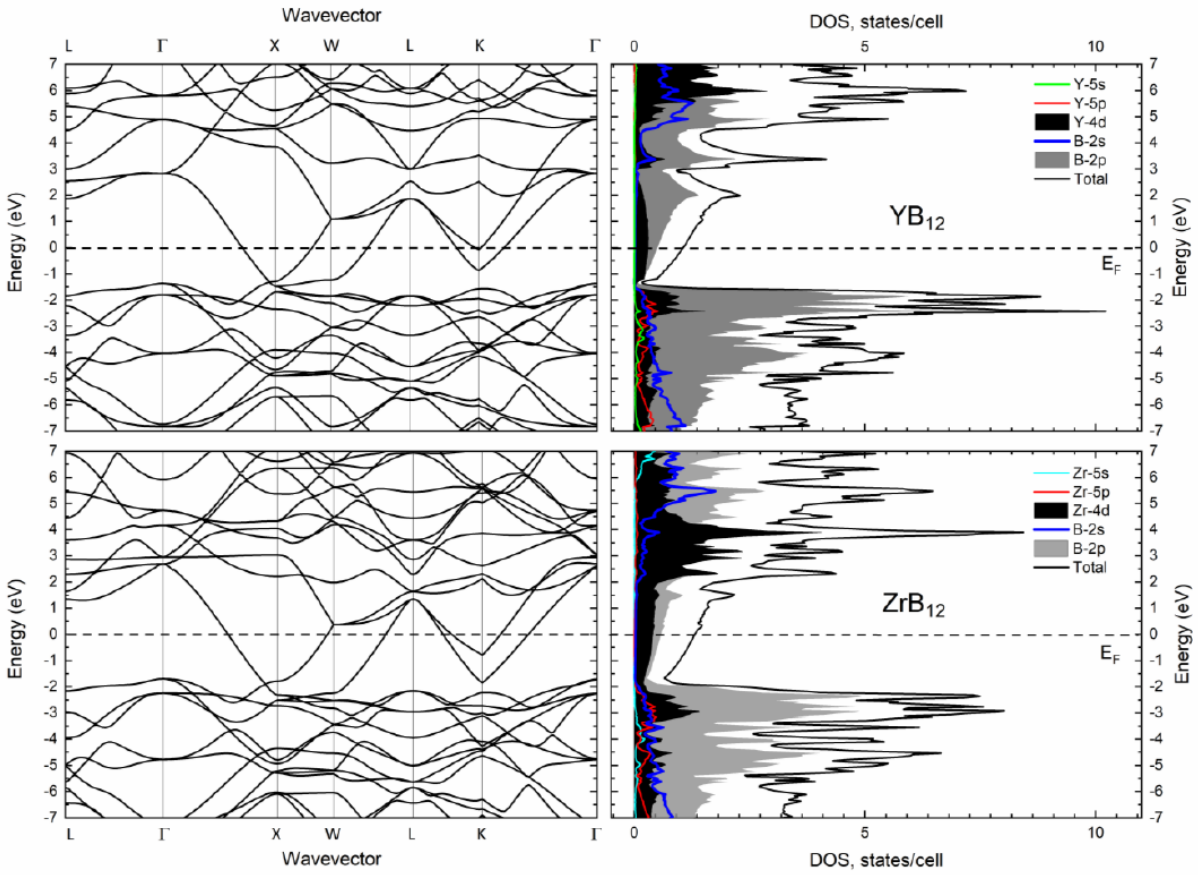

Figure 4-S22. Calculated band structures and density of states with partial orbital contributions outlined for YB_{12} (top) and ZrB_{12} (bottom) using TB-LMTO-ASA.

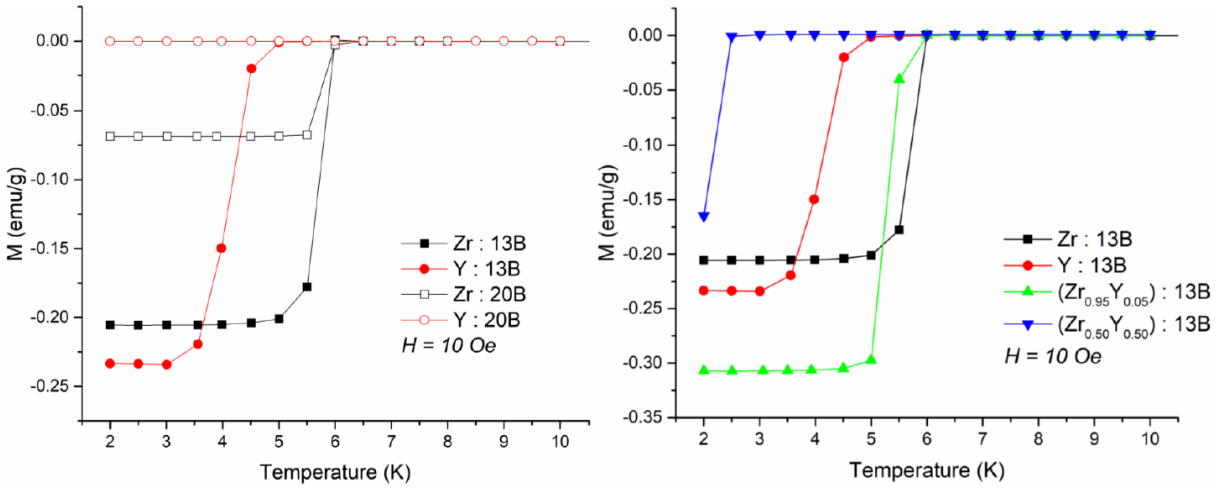

Figure 4-S23. SQUID magnetometry data for: (left) YB_{12} and ZrB_{12} prepared at two different metal to boron ratios: 1 : 13 and 1 : 20), showing that the $T_{c(Zr:13B)} \sim T_{c(Zr:20B)} \sim 5.5 – 6.0$ K, while $T_{c(Y:13B)} \sim 4.5 – 5.0$ K and $T_{c(Y:20B)} < 2$ K, suggesting that superconductivity is due to the main dodecaboride phase in Zr:13B and Zr:20B and due to YB_6 in Y:13B; and (right) ZrB_{12}, YB_{12}, $Zr_{0.95}Y_{0.05}B_{12}$ and $Zr_{0.50}Y_{0.50}B_{12}$ prepared at 1 : 13 metal to boron ratio, showing a decrease in $T_c \sim 2.5 – 3.0$ K for the 50/50 at.% solid solution. Data in the 2 – 10 K range are shown, all measurements were done at 10^{-3} Tesla (10 Oersted) applied magnetic fields.[1]

SUPPORTING INFORMATION REFERENCES

(1) Renosto, S. T.; Corrêa, L. E.; da Luz, M. S.; Rosa, P. F. S.; Fisk, Z.; Albino-Aguiar, J.; Machado, A. J. S. Superconductivity in the Th0.93Zr0.07B12 Compound with UB12 Prototype Structure. Phys. Lett. A 2015, 379, 2498–2501.

REFERENCES

(1) Akopov, G.; Yeung, M. T.; Kaner, R. B. *Adv. Mater.* **2017**, *29* (21), 1604506.

(2) Lundström, T. *Encycl. Inorg. Bioinorg. Chem.* **2011**.

(3) Samsonov, G. V.; Markovskii, L. Y.; Zhigach, A. F.; Valyashko, M. G. *Boron, Its Compounds and Alloys [in Russian]*; House of the Academy of the Sciences Ukrainian SSR: Kiev, 1960.

(4) Samsonov, G. V.; Vinitskii, I. M. *Refractory Compounds [in Russian]*; Atomizdat: Moscow, 1975.

(5) Samsonov, G. V.; Serebriakova, T. I.; Neronov, V. A. *Borides [in Russian]*; Atomizdat: Moscow, 1975.

(6) Buschow, K. H. J. *Magnetic Properties of Borides*; In Boron and Refractory Borides; Matkovich, V. I., Ed.; Springer: Berlin, 1977.

(7) Scheifers, J. P.; Zhang, Y.; Fokwa, B. P. T. *Acc. Chem. Res.* **2017**, *50* (9), 2317–2325.

(8) Park, H.; Encinas, A.; Scheifers, J. P.; Zhang, Y.; Fokwa, B. P. T. *Angew. Chemie - Int. Ed.* **2017**, *56* (20), 5575–5578.

(9) Jothi, P. R.; Zhang, Y.; Yubuta, K.; Culver, D. B.; Conley, M.; Fokwa, B. P. T. *ACS Appl. Energy Mater.* **2019**, *2* (1), 176–181.

(10) Fokwa, B. P. T. *Encycl. Inorg. Bioinorg. Chem.* **2014**, 1–14.

(11) Akopov, G.; Pangilinan, L. E.; Mohammadi, R.; Kaner, R. B. *APL Mater.* **2018**, *6* (7), 070901.

(12) Yeung, M. T.; Mohammadi, R.; Kaner, R. B. *Annu. Rev. Mater. Res.* **2016**, *46* (1), 465–485.

(13) Tergenius, L. E. *J. Less Common Met.* **1981**, *82*, 335–340.

(14) Yeung, M. T.; Akopov, G.; Lin, C. W.; King, D. J.; Li, R. L.; Sobell, Z. C.; Mohammadi, R.; Kaner, R. B. *Appl. Phys. Lett.* **2016**, *109* (20), 203107.

(15) Yeung, M. T.; Lei, J.; Mohammadi, R.; Turner, C. L.; Wang, Y.; Tolbert, S. H.; Kaner, R. B. *Adv. Mater.* **2016**, *28* (32), 6993–6998.

(16) Post, B.; Glaser, F. W.; Moskowitz, D. *Acta Metall.* **1954**, *2* (1), 20–25.

(17) Pangilinan, L. E.; Turner, C. L.; Akopov, G.; Anderson, M.; Mohammadi, R.; Kaner, R. B. *Inorg. Chem.* **2018**, *57* (24), 15305–15313.

(18) Knappschneider, A.; Litterscheid, C.; Brgoch, J.; George, N. C.; Henke, S.; Cheetham, A. K.; Hu, J. G.; Seshadri, R.; Albert, B. *Chem. - A Eur. J.* **2015**, *21* (22), 8177–8181.

(19) Akopov, G.; Roh, I.; Sobell, Z. C.; Yeung, M. T.; Pangilinan, L.; Turner, C. L.; Kaner, R. B. *J. Am. Chem. Soc.* **2017**, *139* (47), 17120–17127.

(20) Akopov, G.; Yeung, M. T.; Roh, I.; Sobell, Z. C.; Yin, H.; Mak, W. H.; Khan, S. I.; Kaner, R. B. *Chem. Mater.* **2018**, *30* (10), 3559–3570.

(21) La Placa, S.; Binder, I.; Post, B. *J. Inorg. Nucl. Chem.* **1961**, *18* (C), 113–117.

(22) Tanaka, T.; Otani, S.; Ishizawa, Y. *J. Cryst. Growth* **1985**, *73* (1), 31–36.

(23) Crespo, A. J.; Tergenius, L. E.; Lundström, T. *J. Less-Common Met.* **1981**, *77* (1), 147–150.

(24) Andersson, S.; Lundström, T. *J. Solid State Chem.* **1970**, *2* (4), 603–611.

(25) Akopov, G.; Yin, H.; Roh, I.; Pangilinan, L. E.; Kaner, R. B. *Chem. Mater.* **2018**, *30* (18), 6494–6502.

(26) Akopov, G.; Yeung, M. T.; Sobell, Z. C.; Turner, C. L.; Lin, C. W.; Kaner, R. B. *Chem. Mater.* **2016**, *28* (18), 6605–6612.

(27) Akopov, G.; Yeung, M. T.; Turner, C. L.; Li, R. L.; Kaner, R. B. *Inorg. Chem.* **2016**, *55* (10), 5051–5055.

(28) Akopov, G.; Roh, I.; Sobell, Z. C.; Yeung, M. T.; Kaner, R. B. *Dalt. Trans.* **2018**, *47* (19), 6683–6691.

(29) Akopov, G.; Sobell, Z. C.; Yeung, M. T.; Kaner, R. B. *Inorg. Chem.* **2016**, *55* (23), 12419–12426.

(30) Troć, R.; Wawryk, R.; Pikul, A.; Shitsevalova, N. *Philos. Mag.* **2015**, *95* (21), 2343–2363.

(31) Liang, Y.; Zhang, Y.; Jiang, H.; Wu, L.; Zhang, W.; Heckenberger, K.; Hofmann, K.; Reitz, A.; Stober, F. C.; Albert, B. *Chem. Mater.* **2019**, *31* (3), 1075–1083.

(32) Paderno, Y.; Shitsevalova, N. *J. Alloys Compd.* **1995**, *219* (1–2), 119–123.

(33) Hamada, K.; Wakata, M.; Sugii, N.; Matsuura, K.; Kubo, K.; Yamauchi, H. *Phys. Rev. B* **1993**, *48* (10), 6892–6898.

(34) Cannon, J. F.; Cannon, D. M.; Tracy Hall, H. *J. Less-Common Met.* **1977**, *56* (1), 83–90.

(35) Cannon, J. F.; Farnsworth, P. B. *J. Less-Common Met.* **1983**, *92* (2), 359–368.

(36) Portnoi, K. I.; Romashov, V. M.; Burobina, L. N. *Sov. Powder Metall. Met. Ceram.* **1970**,

9 (7), 577–580.

(37) Liao, P. K.; Spear, K. E. *J. Phase Equilibria* **1995**, *16* (6), 521–524.

(38) Paderno, Y. B.; Adamovskii, A. A.; Lyashchenko, A. B.; Paderno, V. N.; Fillipov, V. B.; Naydich, Y. V. *Powder Metall. Met. Ceram.* **2004**, *43* (9–10), 546–548.

(39) Okamoto, H. *J. Phase Equilibria* **1992**, *13* (4), 436.

(40) Sologub, O.; Michiue, Y.; Mori, T. *Acta Crystallogr. Sect. E Struct. Reports Online* **2012**, *68* (8), 1–6.

(41) Okamoto, H. *J. Phase Equilibria* **1996**, *17* (2), 162.

(42) Lutterotti, L.; Matthies, S.; Wenk, H. R.; Schultz, A. S.; Richardson, J. W. *J. Appl. Phys.* **1997**, *81* (2), 594–600.

(43) Lutterotti, L.; Chateigner, D.; Ferrari, S.; Ricote, J. *Thin Solid Films* **2004**, *450* (1), 34–41.

(44) Lutterotti, L.; Bortolotti, M.; Ischia, G.; Lonardelli, I.; Wenk, H. R. *Zeitschrift fur Krist. Suppl.* **2007**, *1* (26), 125–130.

(45) Lutterotti, L. *Maud Rev. 2.55 Univ. Trento-Italy, Dep. Ind. Eng. Trento, Italy.; Univ.*; Univ. Trento Italy, Trento, Italy, 2015.

(46) Lutterotti, L. *Nucl. Instruments Methods Phys. Res. Sect. B Beam Interact. with Mater. Atoms* **2010**, *268* (3–4), 334–340.

(47) Turner, C. L.; Zujovic, Z.; Koumoulis, D.; Taylor, R. E.; Kaner, R. B. *J. Mater. Sci.* **2019**, *54* (4), 3547–3557.

(48) Jaeger, C.; Hemmann, F. *Solid State Nucl. Magn. Reson.* **2014**, *63*, 13– 19.

(49) Yesinowski, J. P. *J. Magn. Reson.* **2015**, *252*, 135–144.

(50) Harris, R. K.; Becker, E. D.; Cabral De Menezes, S. M.; Goodfellow, R.; Granger, P. *Concepts Magn. Reson. Part A Bridg. Educ. Res.* **2002**, *14* (5), 326–346.

(51) Bishop, M.; Shahid, N.; Yang, J.; Barron, A. R. *Dalt. Trans.* **2004**, No. 17, 2621–2634.

(52) Jepsen, O.; Burkhardt, A.; Andersen, O. K. *The Program TB-LMTO-ASA, Version 4.7*; Max-Planck-Institut fur Festkorperforschung: Stuttgart, Germany, 1999.

(53) Renosto, S. T.; Corrêa, L. E.; Da Luz, M. S.; Rosa, P. F. S.; Fisk, Z.; Albino-Aguiar, J.; Machado, A. J. S. *Phys. Lett. Sect. A Gen. At. Solid State Phys.* **2015**, *379* (39), 2498–2501.

(54) Akopov, G.; Yeung, M. T.; Turner, C. L.; Mohammadi, R.; Kaner, R. B. *J. Am. Chem. Soc.* **2016**, *138* (17), 5714–5721.

(55) Mohammadi, R.; Xie, M.; Lech, A. T.; Turner, C. L.; Kavner, A.; Tolbert, S. H.; Kaner, R. B. *J. Am. Chem. Soc.* **2012**, *134* (51), 20660–20668.

(56) Hume-Rothery, W.; Powell, H. M. *Zeitschrift für Krist. - Cryst. Mater.* **1935**, *91*, 23.

(57) Hume-Rothery, W. Smallman, R. W.; Haworth, C. W. *The Structure of Metals and Alloys*; The Institute of Metals: London, 1969.

(58) Hume-Rothery, W. *Atomic Theory for Students of Metallurgy*, 5th ed.; The Institute of Metals: London, 1969.

(59) Slater, J. C. *J. Chem. Phys.* **1964**, *41* (10), 3199–3204.

(60) Pauling, L. *J. Am. Chem. Soc.* **1932**, *54* (9), 3570–3582.

(61) Pauling, L. *Nature of the Chemical Bond*, 3rd ed.; Cornell University Press: Ithaca, 1960.

(62) Mar, R. W.; Stout, N. D. *J. Chem. Phys.* **1972**, *57* (12), 5342–5349.

(63) Vegard, L. *Eur. Phys. J. A* **1921**, *5*, 17– 26.

(64) Mansouri Tehrani, A.; Oliynyk, A. O.; Parry, M.; Rizvi, Z.; Couper, S.; Lin, F.; Miyagi, L.; Sparks, T. D.; Brgoch, J. *J. Am. Chem. Soc.* **2018**, *140* (31), 9844–9853.

(65) McCaughey, C.; Tsakiropoulos, P. *Materials (Basel).* **2018**, *11* (6), 967.

(66) Lei, J.; Akopov, G.; Yeung, M. T.; Yan, J.; Kaner, R. B.; Tolbert, S. H. *Adv. Funct. Mater.* **2019**, *29* (22), 1900293.

(67) Li, Y.; Bushby, A. J.; Dunstan, D. J. *Proc. R. Soc. A* **2016**, *472*, 20150890.

(68) Petch, N. J. *J. Iron Steel Inst.* **1953**, *174*, 25–28.

(69) Bundy, F. P.; Hall, H. T.; Strong, H. M.; Wentorf, R. H. *Nature* **1955**, *176*, 51–55.

(70) Bovenkerk, H. P.; Bundy, F. P.; Hall, H. T.; Strong, H. M.; Wentorf, R. H. *Nature* **1959**, *1*, 1094–1098.

(71) Uwamino, Y.; Ishizuka, T.; Yamatera, H. *J. Electron Spectros. Relat. Phenomena* **1984**, *34*, 67–78.

(72) Baba, Y.; Sasaki, T. A. *Surf. Interface Anal.* **1984**, *6* (4), 171–173.

(73) Anderson, J. A.; Fierro, J. L. G. *Journal of Solid State Chemistry*. 1994, pp 305–313.

(74) Nishino, Y.; Krauss, A. R.; Lin, Y.; Gruen, D. M. *J. Nucl. Mater.* **1996**, *228* (3), 346–353.

(75) Ilton, E. S.; Bagus, P. S. *Surf. Interface Anal.* **2011**, *43* (13), 1549–1560.

(76) Samsel-Czekała, M.; Talik, E.; Troć, R.; Shitsevalova, N. *J. Alloys Compd.* **2014**, *615*, 446–450.

(77) Ejima, T.; Sato, S.; Suzuki, S.; Saito, Y.; Fujimori, S.; Sato, N.; Kasaya, M.; Komatsubara, T.; Kasuya, T.; Ōnuki, Y. *Phys. Rev. B - Condens. Matter Mater. Phys.* **1996**, *53* (4), 1806–1813.

(78) Ma, T.; Li, H.; Zheng, X.; Wang, S.; Wang, X.; Zhao, H.; Han, S.; Liu, J.; Zhang, R.; Zhu, P.; Long, Y.; Cheng, J.; Ma, Y.; Zhao, Y.; Jin, C.; Yu, X. *Adv. Mater.* **2017**, *29* (3), 1–7.

(79) Tauc, J.; Menth, A. *J. Non. Cryst. Solids* **1972**, *8–10* (C), 569–585.

(80) Tauc, J. *Mater. Res. Bull.* **1968**, *3*, 37–46.

(81) Tauc, J.; Grigorovici, R.; Vancu, A. *Phys. Status Solidi* **1966**, *15* (2), 627–637.

(82) Hecht, H. G. *J. Res. Natl. Bur. Stand., Sect. A* **1976**, *80*, 567–583.

(83) Kubelka, P. *J. Opt. Soc. Am.* **1954**, *44* (4), 330–335.

(84) Kubelka, P.; Munk, F. *Z. Techn. Phys.* **1931**, *12*, 593–601.

(85) Korozlu, N.; Surucu, G. *Phys. Scr.* **2013**, *87* (1), 015702.

(86) Shein, I. R.; Ivanovskiĭ, A. L. *Phys. Solid State* **2003**, *45* (8), 1429–1434.

(87) Papavassiliou, G.; Pissas, M.; Karayanni, M.; Fardis, M.; Koutandos, S.; Prassides, K. *Phys. Rev. B - Condens. Matter Mater. Phys.* **2002**, *66* (14), 1–4.

(88) Winter, J. *Magnetic Resonance in Metals*, Vol. xiii.; Claredon Press: Oxford, 1971.

(89) Carter, G. C.; Bennett, L. H.; Kahan, D. J. *Metallic Shifts in NMR:: A Review of the Theory and Comprehensive Critical Data Compilation of Metallic Materials: Part 2,*

Progress in Materials Science (Book 20), 1st ed.; Pergamon Press: Oxford, 1977.

(90) Suh, B. J.; Zong, X.; Singh, Y.; Niazi, A.; Johnston, D. C. *Phys. Rev. B - Condens. Matter Mater. Phys.* **2007**, *76*, 1–4.

(91) Balz, R.; Brändie, U.; Kammerer, E.; Köhnlein, D.; Lutz, O.; Nolle, A.; Schafitel, R.; Veil, E. *Zeitschrift fur Naturforsch. - Sect. A J. Phys. Sci.* **1986**, *41* (5), 737–742.

(92) Brinkmann, D. *Zeitschrift fur Naturforsch. - Sect. A J. Phys. Sci.* **2000**, *55* (1–2), 323–326.

(93) Ge, J. Y.; Gladilin, V. N.; Sluchanko, N. E.; Lyashenko, A.; Filipov, V. B.; Indekeu, J. O.; Moshchalkov, V. V. *New J. Phys.* **2017**, *19* (9), 0–9.

(94) Sluchanko, N. E.; Azarevich, A. N.; Anisimov, M. A.; Bogach, A. V.; Gavrilkin, S. Y.; Gilmanov, M. I.; Glushkov, V. V.; Demishev, S. V.; Khoroshilov, A. L.; Dukhnenko, A. V.; Mitsen, K. V.; Shitsevalova, N. Y.; Filippov, V. B.; Voronov, V. V.; Flachbart, K. *Phys. Rev. B* **2016**, *93* (8), 1–7.

(95) Thakur, S.; Biswas, D.; Sahadev, N.; Biswas, P. K.; Balakrishnan, G.; Maiti, K. *Sci. Rep.* **2013**, *3*, 3–8.

(96) Teyssier, J.; Lortz, R.; Petrovic, A.; Van Der Marel, D.; Filippov, V.; Shitsevalova, N. *Phys. Rev. B - Condens. Matter Mater. Phys.* **2008**, *78* (13), 1–7.

(97) Czopnik, A.; Shitsevalova, N.; Pluzhnikov, V.; Krivchikov, A.; Paderno, Y.; Onuki, Y. *J. Phys. Condens. Matter* **2005**, *17* (38), 5971–5985.

(98) Szabó, P.; Kačmarčík, J.; Samuely, P.; Girovský, J.; Gabáni, S.; Flachbart, K.; Mori, T. *Phys. C Supercond. its Appl.* **2007**, *460-462 I* (SPEC. ISS.), 626–627.

(99) Carnicom, E. M.; Strychalska-Nowak, J.; Wiśniewski, P.; Kaczorowski, D.; Xie, W.;

Klimczuk, T.; Cava, R. J. *Supercond. Sci. Technol.* **2018**, *31*, 115005.

(100) Gou, H.; Dubrovinskaia, N.; Bykova, E.; Tsirlin, A. A.; Kasinathan, D.; Schnelle, W.; Richter, A.; Merlini, M.; Hanfland, M.; Abakumov, A. M.; Batuk, D.; Van Tendeloo, G.; Nakajima, Y.; Kolmogorov, A. N.; Dubrovinsky, L. *Phys. Rev. Lett.* **2013**, *111* (15), 157002.

(101) Leithe-Jasper, A.; Sato, A.; Tanaka, T. *Kristallogr. - New Cryst. Struct.* **2002**, *217*, 319-320.

(102) Matkovich, V. I.; Economy, J.; Giese, R. F.; Barrett, R. *Acta Crystallogr.* **1965**, *19*, 1056–1058.

(103) Callmer, B. *J. Solid State Chem.* **1978**, *23*, 391– 398.